Development of an image guidance system for laparoscopic liver surgery and evaluation of optical and computer vision techniques for the assessment of liver tissue

A thesis submitted for the degree of

Doctor of Philosophy (PhD)

Dr. Crispin Schneider

MD, MRCS

University College London

Division of Surgery & Interventional Science

2017

Declaration

I, Crispin Schneider confirm that the work presented in this thesis is my own. Where information has been derived from other sources, I confirm that this has been indicated in the thesis.

.....

Dedication

I would like to dedicate this thesis to my wife Fiona and our son Moritz for their support and understanding.

Abstract

Introduction

Liver resection is increasingly being carried out via the laparoscopic approach (keyhole surgery) because there is mounting evidence that it benefits patients by reducing pain and length of hospitalisation. There are however ongoing concerns about oncological radicality (i.e. ability to completely remove cancer) and an inability to control massive haemorrhage. These issues can partially be attributed to a loss of sensation such as depth perception, tactile feedback and a reduced field of view. Utilisation of optical imaging and computer vision may be able to compensate for some of the lost sensory input because these modalities can facilitate visualisation of liver tissue and structural anatomy. Their use in laparoscopy is attractive because it is easy to adapt or integrate with existing technology. The aim of this thesis is to explore to what extent this technology can aid in the detection of normal and abnormal liver tissue and structures.

Methods

The current state of the art for optical imaging and computer vision in laparoscopic liver surgery is assessed in a systematic review. Evaluation of confocal laser endomicroscopy is carried out on a murine and porcine model of liver disease. Multispectral near infrared imaging is evaluated on *ex-vivo* liver specimen. Video magnification is assessed on a mechanical flow phantom and a porcine model of liver disease. The latter model was also employed to develop a computer vision based image guidance system for laparoscopic liver surgery. This image guidance system is further evaluated in a clinical feasibility study. Where appropriate, experimental findings are substantiated with statistical analysis.

Results

Use of confocal laser endomicroscopy enabled discrimination between cancer and normal liver tissue with a sub-millimetre precision. This technology also made it possible to verify the adequacy of thermal liver ablation. Multispectral imaging, at specific wavelengths was shown to have the potential to highlight the presence of colorectal and hepatocellular cancer. An image reprocessing algorithm is proposed to simplify visual interpretation of the resulting images. It is shown that video magnification can determine the presence of pulsatile motion but that it cannot reliably determine the extent of motion. Development and performance metrics of an image guidance system for laparoscopic liver surgery are outlined. The system was found to improve intraoperative orientation more development work is however required to enable reliable prediction of oncological margins.

Discussion

The results in this thesis indicate that confocal laser endomicroscopy and image guidance systems have reached a development stage where their intraoperative use may benefit surgeons by visualising features of liver anatomy and tissue characteristics. Video magnification and multispectral imaging require more development and suggestions are made to direct this work. It is also highlighted that it is crucial to standardise assessment methods for these technologies which will allow a more direct comparison between the outcomes of different groups. Limited imaging depth is a major restriction of these technologies but this may be overcome by combining them with preoperatively obtained imaging data. Just like laparoscopy, optical imaging and computer vision use functions of light, a shared characteristic that makes their combined use complementary.

Impact statement

This thesis focuses on laparoscopic liver surgery which is a form of minimal invasive surgery. It benefits patients by reducing surgical trauma which may improve recovery time and complication rates. Laparoscopic liver surgery is not widely practised because it is technically challenging. Some of these challenges relate to the fact that surgeons cannot palpate the liver or visualise it directly. In other words, the sense of touch and vision is impaired during laparoscopic surgery.

The aim of this work is to explore technologies that enhance surgical vision to compensate for these shortcomings. The potential benefit of improving surgical sensing is firstly to enable the complete removal of liver cancer, which reduces the cancer recurrence rate, and secondly to avoid potentially fatal injury to vulnerable liver structures. The potential beneficiaries of this work are surgeons and by natural extension their patients. It also benefits researchers who are investigating imaging of liver disease. The results of this work are being disseminated through peer reviewed publications and presentations at scientific conferences. To maximise public visibility of this research, publication in an open access format has been pursued whenever possible.

Some of the findings of this work and their potential impact are outlined below.

It has been demonstrated that confocal laser endomicroscopy can discriminate between cancerous and non-cancerous liver tissue. This method may enhance intraoperative decision making by determining if a liver lesion needs to be excised and how extensive the excision needs to be. Avoiding unnecessary excisions can help in reducing surgical complications. This methodology is already being applied to the diagnosis of solid cancer in other organs and it is hoped that the findings in this work will contribute to ongoing clinical research in this field.

Multispectral imaging is an imaging modality that can utilise alterations in the light absorption behaviour to elucidate the biological composition of tissue. In this thesis a novel, remote approach to acquire and analyse multispectral images of liver tissue has been developed. Subsequently it has been shown that this method can predict the presence of liver cancer. Pending further research, this imaging method could also be applied to assess other liver pathologies.

Augmented reality based image guidance utilises 3D organ models that contain a virtual representation of patient specific anatomy and tumour locations. These organ models can be projected onto the surgical field (e.g. laparoscopic monitor) hence creating an augmented reality environment. The development and evaluation of such a system forms part of this thesis and highlights the potential of this technology to improve precision and safety of

laparoscopic liver surgery. However, before this can be realised, further improvements focusing on the accuracy and usability of this imaging modality are required.

In conclusion the research in this thesis has demonstrated how technologically enhanced vision may improve the assessment of liver tissue and guide laparoscopic liver surgery. The methods evaluated in this work can be expanded to other organs and therefore the findings are generalisable and may therefore benefit research and clinical care in other medical specialties.

Table of Contents

List of figures

List of tables

Acknowledgements

For making this research possible I would particularly like to thank the following people:

First and foremost my supervisor Professor Brian Davidson and my co-supervisors Dr Kurinchi Gurusamy and Dr Adrien Desjardins for providing guidance, mentoring, support and inspiration throughout my PhD.

Professor David Hawkes (UCL, Centre for Medical Image Computing) and Dr Richard Cook (Kings College London, Dental Institute) for providing access to CLE systems and guidance on image interpretation.

Dr Matt Clarkson and Dr Stephen Thompson (UCL, Centre for Medical Image Computing) for their support in acquiring and analysing IGS and CLE data.

Dr Simon Walker-Samuel (UCL, Centre for Advanced Biomedical Imaging) for providing access to imaging and histological facilities at CABI and for his aid in CLE image analysis.

Dr Peter Johnson (UCL, Centre for Advanced Biomedical Imaging) for his help in murine and porcine CLE studies.

Dr Daniil Nikitichev and Dr Wenfeng Xia (UCL, Department of Medical Physics and Bioengineering) for their help in setting up and operating the OPO equipment platform.

Dr Amir Gander (UCL, Tissue Access for Patient Benefits) for his help in providing access to the UCL tissue bank.

List of Prizes, Publications and Presentations

Prize

Association of Laparoscopic Surgeons of Great Britain and Ireland, David Dunn Medal, Prize for best oral presentation at ALSGBI Annual Scientific Meeting 2015, Southport, UK

Publications Arising from Research

Schneider C, Johnson SP, Gurusamy K, Cook RJ, Desjardins AE, Hawkes DJ, Davidson BR, Walker-Samuel S. Identification of liver metastases with probe-based confocal laser endomicroscopy at two excitation wavelengths. Lasers Surg Med. 2017 Mar;49(3):280-292. doi: 10.1002/lsm.22617.

Gibson E, Robu MR, Thompson S, Edwards PE, **Schneider C**, Gurusamy K, Davidson B, Hawkes DJ, Barratt DC, Clarkson MJ. Deep residual networks for automatic segmentation of laparoscopic videos of the liver. -Conference paper- SPIE Medical Imaging 2017 Mar 3 (pp. 101351M-101351M). International Society for Optics and Photonics.

Ramalhinho J, Robu M, Thompson S, Edwards P, **Schneider C**, Gurusamy K, Hawkes D, Davidson B, Barratt D, Clarkson MJ. Breathing motion compensated registration of laparoscopic liver ultrasound to CT. -Conference paper- InSPIE Medical Imaging 2017 Mar 3 (pp. 101352V-101352V). International Society for Optics and Photonics.

Thompson S, Stoyanov D, **Schneider C**, Gurusamy K, Ourselin S,·Davidson B,·Hawkes D, Clarkson MJ. Hand-eye calibration for rigid laparoscopes using an invariant point. Int J Comput Assist Radiol Surg. 2016 Mar 19. [Epub ahead of print] PMID: 26995597

Schneider C, Johnson SP, Walker-Samuel S, Gurusamy K, Clarkson MJ, Thompson S, Song Y, Totz J, Cook RJ, Desjardins AE, Hawkes DJ, Davidson BR. Utilizing confocal laser endomicroscopy for evaluating the adequacy of laparoscopic liver ablation.Lasers Surg Med. 2015 Dec 31. doi: 10.1002/lsm.22464.

Song Y, Totz J, Thompson S, Johnsen S, Barratt D, **Schneider C**, Gurusamy K, Davidson B, Ourselin S, Hawkes D, Clarkson MJ. Locally rigid, vessel-based registration for laparoscopic liver surgery. Int J Comput Assist Radiol Surg. 2015 Dec;10(12):1951-61. doi: 10.1007/s11548-015-1236-8. Epub 2015 Jun 20. PMID: 26092658

Schneider C, Desjardins AE, Gurusamy K, Hawkes DJ, Davidson BR. Laparoscopic manipulation of a probe-based confocal laser endomicroscope using a steerable intravascular catheter. Surg Laparosc Endosc Percutan Tech. 2015 Apr;25(2):e83-5. doi: 10.1097/SLE.0000000000000139.

Thompson S, Totz J, Song Y, Johnsen S, Stoyanov D, Ourselin S, Gurusamy K, **Schneider C**, Davidson B, Hawkes D, Clarkson MJ. Accuracy validation of an image guided laparoscopy system for liver resection. Conference paper- Proc. SPIE 9415, Medical Imaging 2015: Image-Guided Procedures, Robotic Interventions, and Modeling, 941509 (March 18, 2015); doi: 10.1117/12.2080974

Abstracts

Schneider C, Thompson S, Gurusamy K, Clarkson M, Davidson B. Use of enhanced visualisation methods to decrease the effect of organ motion in image guided laparoscopic liver surgery. BRITISH JOURNAL OF SURGERY 2017 Jul 1 (Vol. 104, pp. 73-73).

Schneider C, Thompson S, Totz J, Song Y, Desjardins A, Stoyanov D, , Gurusamy K, Davidson B,·Hawkes D, Clarkson MJ. Preliminary Results from a Clinical Study evaluating a novel Image Guidance System for Laparoscopic Liver Surgery. HPB. 2016 Apr 1;18:e99.

Schneider C, Thompson S, Clarkson MJ, Hawkes D, Davidson B. A novel approach to image guidance in laparoscopic liver surgery. Surg Endosc. 2016;30:S185-210.

Schneider C, Thompson S, Totz J, Song Y, Johnsen S, Stoyanov D, Ourselin S, Gurusamy K, Hawkes D, Clarkson M, Davidson B. “Evaluation of a novel system for image guided laparoscopic liver surgery in an animal model and first clinical experience”. Gut 2015;64:A453-A454 doi:10.1136/gutjnl-2015-309861.991

Johnson SP, **Schneider C**, Desjardins A, Walker-Samuel S, Hawkes D. “Confocal fluorescence endomicroscopy for the in-vivo detection of tumour microenvironment and healthy tissue margin”. EUROPEAN JOURNAL OF CANCER Volume: 50 Supplement: 5 Pages: S168-S169 Meeting Abstract: 700 Published: JUL 2014 doi:10.1016/S0959-8049(14)50618-1

Book chapters

Schneider C., Davidson B. Hepatocellular Cancer. In: Ajithkumar T, Barrett A, Hatcher H, Jefferies SJ, editors. Oxford Desk Reference: Oncology, Second Edition. Oxford University Press 2017 – accepted

Schneider C., Davidson B. Biliary tract tumours. In: Ajithkumar T, Barrett A, Hatcher H, Jefferies SJ, editors. Oxford Desk Reference: Oncology, Second Edition. Oxford University Press 2017 – accepted

Key presentations

Schneider C, Thompson S, Gurusamy K, Clarkson M, Davidson B. Evaluation of an augmented reality based image guidance system for laparoscopic liver surgery. E-AHPBA 2017, Mainz, Germany

Schneider C. An augmented reality image guidance system for laparoscopic liver resection -surgical perception of benefits and limitations. 5th ECALSS as part of E-AHPBA 2017, Mainz, Germany

Schneider C, Thompson S, Gurusamy K, Clarkson M, Davidson B. Use of enhanced visualisation methods to decrease the effect of organ motion in image guided laparoscopic liver surgery. ASGBI 2017, Glasgow

Schneider C, Thompson S, Totz J, Song Y, Desjardins A, Stoyanov D, , Gurusamy K, Davidson B,·Hawkes D, Clarkson MJ Preliminary Results from a Clinical Study evaluating a novel Image Guidance System for Laparoscopic Liver Surgery. 12th World Congress of the International Hepato-Pancreato-Biliary Association, Sao Paolo, Brazil

Schneider, Thompson S, Clarkson MJ, Hawkes D, Davidson B. A novel approach to image guidance in laparoscopic liver surgery. Association of Laparoscopic Surgeons of Great Britain and Ireland ASM, 2015, Southport, UK

Abbreviations

2D – Two dimensional

3D – Three dimensional

A – Amplitude (for video magnification settings)

ALPPS – Associated liver partition with portal vein ligation for staged hepatectomy

AIC – Akaike information criteria

AR – Augmented reality

AUC – Area under the curve

BAP – Bland-Altman plot

Bpm – Beats per minute

CCA - Cholangiocarcinoma

CBCT – Cone beam computer tomography

CBD – Common bile duct

CI – Confidence interval

CLE – Probe based confocal laser endomicroscopy

CPU – Central processing unit

CRLM – Colorectal cancer liver metastasis

CT – Computer tomography

FLR – Future liver remnant

Fps – Frames per second

GLCM – Gray-level co-occurrence matrix

GLIMMIX – Generalised linear mixed model analysis mode in SAS™

GPU – Graphic processing unit

GUI – Graphic user interface

HBV – Hepatitis B virus

HCV – Hepatitis C virus

HCC – Hepatocellular carcinoma

HD – High definition

H&E – Haematoxylin & Eosin staining for histology

ICG – Indocyanine green

IGS – Image guidance system

InGaAs - Indium-Gallium-Arsenide

IOUS – Intraoperative ultrasound

IQR – Inter quartile range

IVC – Inferior vena cava

KPS-1 – Kidney perfusion solution 1

L – Lambda

LCTF – Liquid crystal tuneable filters

LIFI – Laparoscopic ICG based fluorescence imaging

LMSI – laparoscopic multispectral imaging

LLR – Laparoscopic liver resection

LLS – Laparoscopic liver surgery

LUS – Laparoscopic ultrasound

MB – Methylene blue

MSI – Multispectral imaging

MRI – Magnetic resonance imaging

Nd-Yag – Neodymium-doped yttrium aluminium garnet

NIR – Near infrared

NOTES – Natural orifice endoscopic transluminal surgery

NP – No pulse present

OCT – Optical coherence tomography

OP1 / OP2 – Operating day 1 / 2

OPO - Optical parametric oscillator

PAI – Photoacoustic imaging

PP – Pulse present

PVCP - Polyvinyl chloride plastisol

PVE – Portal vein embolisation

RCT – Randomised controlled trial

RFA – Radiofrequency ablation

RFU – Relative fluorescence unit

RGB – Red green blue space

RMS – Root mean square

ROC – Receiver operating characteristic

ROI – Region of interest

SEM – Standard error of the mean

SLAM - Simultaneous localization and mapping

SNR – Signal to noise ratio

SRC – Spectral response curve

SSR – Stereoscopic surface reconstruction

TRE – Target registration error

Uint8 / 16 – Unsigned integer 8bit or 16bit

US – Ultrasound

VM – Eulerian video magnification

VR – Virtual reality

Glossary

Absorption spectrum also Spectral response curve

Fraction of incident radiation absorbed by the material (or tissue) over a range of frequencies or simplified how much light is absorbed at certain wavelength. In this thesis the tissue absorption is plotted against wavelengths of light.

Augmented reality

A technology that superimposes a computer-generated image on a user's view of the real world, thus providing a composite view.

Band-pass filter

A band-pass filter is a device that passes frequencies within a certain range and rejects (attenuates) frequencies outside that range. In this work it describes devices that filter certain wavelengths of light.

Bandwidth

A range of frequencies within a given band, in particular that used for transmitting a signal.

Codec

A codec is a device or computer program for encoding or decoding a digital data stream or signal.

Confocal laser endomicroscopy

Probe based variant of confocal laser microscopy imaging.

Data smoothing

Creation of an approximating function that attempts to capture important patterns in the data, while leaving out noise.

Fluorophore

A fluorescent chemical compound.

Gray-level co-occurrence matrix

A texture based statistical representation of image data.

Gray-level co-occurrence matrix statistics

Described as Energy, Contrast, Correlation and Homogeneity which are statistics that provide information about the texture of an image.

Hepatectomy

Resection of liver tissue.

Image guided surgery

General term for using images to guide surgical therapy. In the context of this thesis only used for computer navigated surgery i.e. using a 3D organ model to reflect *in-vivo* anatomy.

Intensity

In this work used to describe luminous intensity which is a measure of the wavelength-weighted power emitted by a light source.

Multispectral imaging

An imaging method that captures image data within specific wavelength ranges across the electromagnetic spectrum.

Parenchymal sparing resection

A method of liver resection with the intention of preserving a maximum volume for the future liver remnant.

Registration

In image guided surgery it describes the process of aligning a 3D organ model in an anatomically correct position with the corresponding organ of the patient (e.g. liver).

Segmentectomy

Resection of a functional liver segment.

SmartLiver

An image guidance system for laparoscopic liver surgery that is being developed by a team of surgeons and computer scientists at UCL.

Steatosis

Fatty change or degeneration (used in the context of liver steatosis in this work).

Sub-segmentectomy / wedge resection / non-anatomical resection

Resection of less than a segment of liver.

Tracking

In laparoscopic image guided surgery it describes the process of following the position of the laparoscope or laparoscopic instrument.

Video magnification

A video processing algorithm that enhances subtle motion or colour variation.

Virtual reality

The computer-generated simulation of a three-dimensional image or environment.

1. General introduction

1.1. Introduction to liver surgery

1.1.1 Liver function

The liver is the largest solid organ in the body and weighs between 1200-1500g. It is situated in the right upper portion of the abdominal cavity where it is sheltered by the ribs. The upper border of the liver lies approximately at the height of the nipples (1). Major organs that border onto the liver are the right kidney, stomach, duodenum and colon.

The liver fulfils many diverse functions and can perhaps be regarded as the body's "power plant and manufacturing site". It fulfils a variety of roles that include metabolic-, synthetic-, excretory-, endocrine- and immunological functions. More specifically the liver plays a central role in the metabolism of carbohydrates, fats and proteins (2). It is essential for the metabolism and conjugation of many drugs whose excretion depends on a normal liver function. The liver accumulates fat soluble vitamins and glycogen which is a storage carbohydrate. Proteins that are crucial for coagulation, immune response and transport and bloodstream mediated transport are all synthesised in the liver as is bile. The main excretory functions involve the excretion of drug metabolites and bile(2). The liver performs an important endocrine function by breaking down hormones and activates vitamin D via hydroxylation. As a crucial component of the immune system, it removes circulating immune complexes, aids in the fetal development of B-lymphocytes, hosts the majority of the bodies macrophage population in the form of Kupffer cells and it is one of the main sources for cytokine release (3,4).

Because of this diversity which sets it apart from organs with one main function such as the heart (pump) or the kidney (filter) it has so far not been possible to create an artificial liver device. In contrast to most other solid organs the liver has a striking capacity for self-regeneration. In animal models it has been proven that it is possible to remove two-thirds of the liver up to 12 times. Hepatocytes have the ability to replenish liver volume but when they eventually lose this ability, then so called oval cells, a population of pluripotent stem cells that dwell in small bile ducts, can proliferate and differentiate into hepatocytes and biliary cells (5).

1.1.2 Liver anatomy

1.1.2.1 External liver anatomy

As described above, most of the liver bulk lies in the right upper abdomen, there is however a smaller portion that constitutes about a sixth of the livers volume which protrudes to the left of the midline, between the diaphragm and the anterior surface of the stomach. The superior portion of the liver is convex and is moulded to the diaphragm. At the front it slopes down straight lying against the lower right ribcage and the abdominal wall. At the back it extends

down to a posterior surface which is triangular in outline. The liver is invested in peritoneum except at the back where the peritoneum reflects onto the diaphragm and thus forms the left and right triangular ligaments. These ligaments in conjunction with the falciform ligament also provide attachments to the anterior convexity of the diaphragm. The falciform ligament is the landmark for the border between the right and left liver lobe. The anterior and posterior liver surface meet inferiorly at a sharp angle to form the lower liver border (6). The liver has a dual blood supply, the portal vein brings venous blood from the intestines and spleen and the hepatic artery carries arterial blood from the coeliac trunk. Both blood vessels enter the liver through the porta hepatis which is a fissure in the inferior portion of the right lobe. The bile ducts follow the course of the hepatic artery within the liver. With the exception of its left main trunk, which has an unusual morphology due to its need to perform different functions in the foetus, this is also true of the portal vein. Because the smaller subdivisions of the hepatic artery, portal vein and bile ducts run alongside each other, surrounded by a fibrous sheath, they are also referred to as portal triad or portal pedicles. Blood drains directly into the inferior vena cava (IVC) via three main hepatic veins (right, middle and left) and a number of smaller hepatic veins that originate from the posterior surface of the liver where it lies adjacent to the IVC.

1.1.2.2 Functional liver anatomy

The classical description of the liver anatomy above hides a more intricate internal liver anatomy, also sometimes called functional anatomy. The knowledge of this functional anatomy which is based on the teachings of Couinaud (7) with a later amendment introduced by a consensus conference in 2000 Brisbane classification (8), is essential to carry out precise hepatectomies (liver resections). A simplified description of the functional liver anatomy is given below (Figure 1.1). This is intended to stress the central role that imaging plays in the correct interpretation of liver anatomy.

Couinaud divided the liver into 2 livers, 4 sectors and 8 segments founded on the distribution of the portal vessels and the main hepatic veins. The first division of the proper hepatic artery divides the liver into the right and left liver. The course of the three main hepatic veins separates the liver into 4 sectors, two each in the right and left liver, respectively. The sectors are supplied by the second order division of the hepatic artery (right anterior, right posterior, left medial and left lateral section). Each liver segment is supplied by the third order division of the hepatic artery. As a simplification it can be said that the course of the portal vessel along the horizontal plan subdivides the sectors into cranial and caudal segments. Segment 4 is divided by its course into segment 4a and 4b. The caudate lobe (segment 1) lies posterior to the liver and embraces the retrohepatic IVC. It is surrounded by major vascular structures such as the IVC, left portal vein and the main middle hepatic vein. A detailed anatomical description of the caudate lobe goes beyond the scope of this chapter. The interested reader is referred to here (6).

Knowledge of the functional anatomy is key to describing the location of surgical liver pathology and to planning its resection. Because there is little correlation between the livers surface anatomy and its functional anatomy it is crucial to employ intraoperative imaging to guide surgical resection.

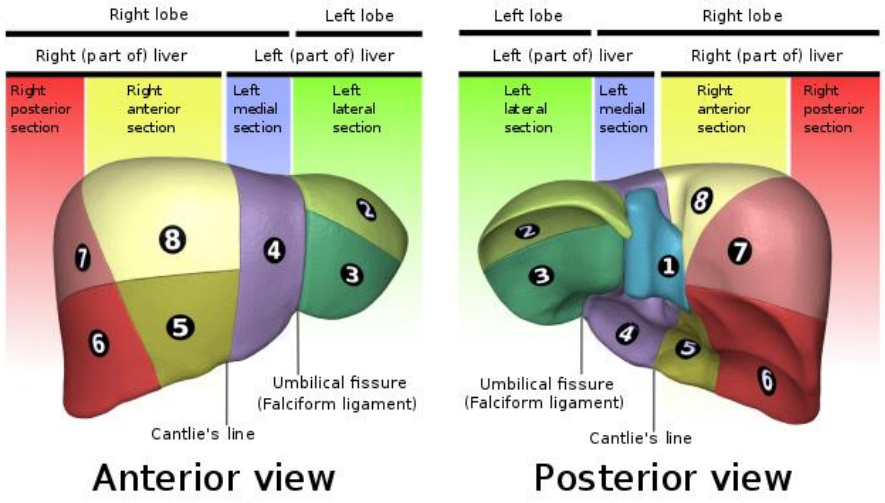

Figure 1.1 Illustration of functional liver anatomy after Couinaud. (reprinted with permission from : BodyParts3D, © The Database Center for Life Science licensed under CC Attribution-Share Alike 2.1 Japan.")

1.1.3 History of liver surgery

1.1.3.1 Pre-modern medicine

A report on gallbladder calculi found in a mummy from Theben (1.500 B.C.) is the only evidence of biliary disease that survived from antiquity. Alexander the Great is also thought to have succumbed to biliary tract disease culminating in peritonitis in 323 B.C. Translations from the works of Hippocrates (5th century B.C.) indicate that he had knowledge of the clinical signs of biliary sepsis and malignant obstructive jaundice (9). A few centuries later (1st century A.D.), Galen decreed that the liver, alongside the heart and brain, is one of the main organs of the body and as such is chiefly involved with governing the nutritive facility. Many of his teachings surrounding the balance and imbalance of bodily humours being the cause of disease persisted up to the middle of the 17th century. The advent of the renaissance saw further advances founded on the autopsies of patients who succumbed to the complications of gallstone disease (6). The publication of “Anatomia Hepatis” by Francis Glisson, in 1654 was a milestone in the study of liver disease (10). In it he clearly described the liver anatomy, in particular its capsule which invests the portal structures and the distribution of the bile ducts. He also deduced that the venous blood entering from the portal vein traverses through capillaries before entering the vena cava. Some of his illustrations bear a striking similarity to those of Couinaud and to modern computer tomography (CT) based 3D reconstruction of liver anatomy (6). The liver capsule and fibrous sheath

surrounding the portal vessels is named after him. In the 18th century, Morgagni published a seminal work which revolutionised the understanding of liver and biliary disease. In it he presented symptoms in a logical sequence and combined knowledge of pathology and physiology to formulate theories on the causes of disease. From the 18th century onwards the theories around humoral imbalances were disproved and modern scientific medicine was born (6).

1.1.3.2 Advent of biliary surgery

The first surgical interventions for liver disease were all centred on the gallbladder and biliary system. This is hardly surprising as the disease burden related to gallstones is vastly greater than other liver diseases and in addition it was technically safer to operate on the biliary system than on the substance of the liver itself. The first lithotomy, meaning opening of the gallbladder and extraction of stones was carried out by Bobbs in 1867. This was an incidental procedure as Bobbs was expecting to find an ovarian tumour (6). The first planned gallbladder procedures in the modern era were cholecystostomies which were performed by Simms, Koch and Tait around the same time. In this historic form of cholecystostomy, the gallbladder is opened to extract pus and stones and it is left open, draining onto the skin to prevent biliary peritonitis. The first excision of the gallbladder (cholecystectomy) was performed by Langenbuch in 1882, who correctly identified that “others busied themselves with the product of the disease (gallstones), not with the disease itself”. This was an important step as it was observed that gallstones would frequently reoccur (6). Soon after the first cholecystectomy, techniques to remove stones from the common bile duct were invented. These were initially unpopular because of the risk of biliary peritonitis, until Kehr introduced the technique of biliary intubation. Kehr was also credited with performing the first hepatico-enteric anastomosis and resection of a hepatic tumour (11).

1.1.3.3 The role of imaging in the development of hepato-biliary surgery

Progress in biliary surgery was supported by new developments in imaging, especially in the 20th century when it became possible to image the gallbladder via oral cholecystography (1924) and the bile duct via cholangiography (1932). Much later in the 1970’s ultrasound imaging, CT and magnetic resonance imaging (MRI) were added to the imaging armamentarium (12,13). The first successful percutaneous interventions on the liver such as percutaneous transhepatic cholangiography for the relief of jaundice and the dilatation of strictures were also described in this decade. The refinement of selective arteriography led to the invention first hepatic artery embolisation for the treatment of liver tumours (14). Modern surgeons have seen their world transformed by advancements in imaging and it is fair to say that these have enabled the rapid progress in the management of biliary and hepatic disease (6).

1.1.3.4 Advent of liver surgery

"...the liver is so friable, so full of gaping vessels and so evidently incapable of being sutured that it seems impossible to successfully manage large wounds of its substance."

JW Elliot 1897 (15)

This description by Elliot, in a case report on liver resection, highlights why liver surgery was virtually non-existent, until the middle of the last century. There is the oft cited Greek myth of Prometheus who was chained to the Caucasus Mountain as a punishment by Zeus for showing humans how to make fire. Every day an eagle descends and eats his liver, which miraculously re-grows over night (Figure 1.2). If this myth can be regarded as proof that the ancient Greeks knew about the livers regenerative capabilities is uncertain.
Nevertheless, with the exception of one report form 1716 where part of the liver which was protruding from the wound was amputated, no hepatic resections were attempted until the advent of anaesthesia. As mentioned above, Langenbuch described the first liver resection in 1888 and other surgeons soon followed. At around this time Rex (1888) and later Cantlie (1897) further enhanced the understanding of lobar and segmental liver anatomy and brought to light the existence of planes within the liver parenchyma that are devoid of major vascular and biliary structures. These findings were complemented by studies which revealed that blood vessels in the liver parenchym (liver tissue) could be compressed by suture ligation if the sutures were passed in sufficient distance from the wound.

Figure 1.2 Prometheus depicted in a sculpture by Nicolas-Sébastien Adam, 1762. (from https://en.wikipedia.org/wiki/Prometheus#/media/File:Prometheus_Adam_Louvre_MR1745_edit_atoma.jpg, image rights released)

More adjuncts to control hepatic bleeding were introduced in quick succession. In 1907, Garre emphasised the importance of packing for the management of liver injuries and indeed even in modern times this approach remains the mainstay of liver trauma management. Pringle contributed another milestone in the management of hepatic bleeding in 1908 by describing a method of compressing the hepatic inflow vessels.
The first major hepatectomy was carried out by Wendell (1911) who realised that blood loss could be reduced by ligating the portal pedicle that supplied the side of the liver that was to be removed. Unfortunately this discovery was lost to the surgical community so that the next major hepatectomy was not performed until 1949. As this was not reported in the English literature until 1955, another case of major hepatectomy carried out by Lortat-Jacob in 1952 gained publicity instead. Initially a thoraco-laparotomy incision (opening chest and abdomen) was popularised because it allowed good access to vascular structures, although this came at the cost of increased morbidity. The introduction of coastal rib retractors made opening of the chest unnecessary. A variety of methods for parenchymal transection have been advocated such as electrocautery, microwave tissue coagulation, water jet, ultrasonic aspiration dissector and the harmonic scalpel to name a few. Many of these remain still in use today as does the original method of parenchymal transection, the clamp-crush technique.

1.1.4 Common indications for liver surgery

Following is a brief summary of common indications for liver resection. Diseases where only part of the biliary system is excised (e.g. cholecystectomy) will not be discussed here because it is not relevant for the research proposed in this work. There is a significant discrepancy in surgical liver disease patterns between the West (Europe and the Americas) and the East (East Asia). A detailed description of global variations in presentation and practice however is beyond the scope of this chapter and hence the focus is on western practice and in particular the UK.

1.1.4.1 Primary liver cancer

The majority of liver resections are carried out for malignant tumours. These can be categorised into primary (originating in the liver) and secondary liver cancers (i.e. metastatic). More than 90% of primary liver cancers are hepatocellular carcinomas (HCC) which is the fifth most common cancer worldwide and the third most common cause of cancer related mortality (16). In the majority of cases HCC arises in cirrhotic livers. It constitutes the bulk of hepatic cancer resections in the East Asia because of the endemic presence of hepatitis B virus (HBV) infection which is one of the globally leading causes for liver cirrhosis (17). HCC in the West usually presents late, as a large and/or multifocal cancer and hence is often not amenable for surgical resection. The main limitation for resection of HCC is liver function, because a removal of even small amounts of liver tissue may precipitate liver failure. Another issue is that development of de-novo HCC in cirrhotic livers is common after resection. Since the 1990's liver transplantation has been shown to be an effective therapy for small HCC in patients with liver failure (18).

Cholangiocarcinoma (CCA) accounts for approximately 3% of all GI cancers and is the second most common hepatobiliary cancer after HCC (19,20). On the basis of anatomical distribution of the involved bile ducts, CCA has been classified as intrahepatic, perihilar or distal. Usually only intrahepatic and perihilar CCA are treated with liver resection. There are number of risk factors for CCA with primary sclerosing cholangitis being the best known one. Most cases of CCA are however sporadic. Intrahepatic CCA is treated with liver resection whereas perihilar CCA requires additional excision of the common bile duct and not infrequently also of hilar blood vessels that have been invaded by cancer. The preponderance of vascular invasion and extensive spread along the bile ducts means that most perihilar CCA are unresectable. Some centres have demonstrated good survival rates for patients with perihilar CCA who were treated with liver transplantation (20).

1.1.4.2 Secondary liver cancer

Colorectal cancer is the commonest gastrointestinal malignancy and causes an estimated 17,000 cancer deaths in the UK each year. Approximately 25% of patients with colorectal cancer present with liver metastasis at the time of diagnosis. A further 40-50% will develop colorectal cancer liver metastasis (CRLM) later on (21). The minority of these patients (around 20%) present with resectable disease (22). If resection is undertaken approximately

40% of patients are alive after 5 years, without surgery it is <1% (23). The definition and limits of what is deemed resectable have undergone tremendous evolution over the last two decades. The main criteria for resection with curative intent are considered if 1) all disease can be cleared 2) the remaining liver volume is adequate to prevent liver failure 3) there is no extrahepatic disease that cannot be removed (24,25). In unresectable CRLM, preoperative (neoadjuvant) chemotherapy is often employed to reduce the size of the cancer in an attempt to make it potentially amenable to resection. If cancer reoccurs in the liver without concomitant extrahepatic disease, it can be re-resected with outcomes being comparable to the primary resection (23,26). Surgeons in western countries carry out the majority of liver resections for metastatic disease (6).

The success in treating CRLM with hepatic resection has created interested in treating other forms of metastatic cancer the same way. In patient with metastatic gastrointestinal neuroendocrine tumour, liver resection has been shown to be a viable curative option. If all disease can be removed the 5 year survival rates approach 85% (27). In a non-curative setting liver resection may be carried out to reduce tumour burden (debulking) which is thought to have a beneficial impact on survival (28). Debulking for metastatic ovarian cancer may also necessitate hepatectomy to reduce the burden of disease prior to intraperitoneal chemotherapy, which has been shown to convey a survival advantage (29). There are some reports about the benefit of liver resection in a number of other cancers (e.g. melanoma, breast cancer, renal cell cancer), but due to the heterogeneous biology of these cancer types more data is needed to establish a clear role for hepatic surgery (30).

1.1.4.3 Benign indications for liver resection

There a variety of benign liver tumours, with the most common ones of epithelial origin being hepatocellular adenoma and focal nodular hyperplasia whereas the most common tumours of mesenchymal origin are haemangiomas and angiomyolipomas. Diagnosis is frequently made based on imaging criteria because percutaneous biopsy is only indicated in selected cases. If lesions become symptomatic they are usually excised while asymptomatic lesions are kept under surveillance. Lesions with an increased risk for malignant transformation (e.g. hepatic adenoma >5cm) or lesions that are indeterminate are usually also excised (31). Other benign diseases that may require hepatic resection include intrahepatic gallstones, intrahepatic biliary strictures and hydatid cysts (6).

1.1.5 Current state of liver surgery

Morbidity and mortality associated with liver resection has vastly improved over the last few decades. The first ever reported operative mortality from a multicentre series of liver resections was 25% (32). Compared to this recent series frequently quote mortality rates of 2-3% for CRLM and <5% for HCC resection routinely (33,34). The reasons for these improvements are multifactorial and include advances in pre- and postoperative diagnostics, preoperative planning and patient selection, perioperative care, interventional procedures and specialised surgical instruments (6).

The majority of newly developed instruments are dedicated towards the division of liver tissue which is also called parenchymal transection. The gold standard for parenchymal transection is the Crush-Clamp technique, where a standard surgical metal clamp is used to fracture parenchym around bile ducts and blood vessels which subsequently can be divided in a controlled fashion (35). The Cavitron Ultrasonic Suction Aspirator (CUSA) is used in a similar fashion; the removal of parenchym however is achieved by inducing a cavitation effect through tiny oscillating motions. Stapled hepatectomy employs devices that simultaneously cut and seal liver tissue via small metallic staples. Finally there are a number of energy devices that employ various methods (e.g. radiofrequency ablation, bipolar coagulation, ultrasonic vibration) to create heat that divides and seals liver tissue.

Numerous clinical trials have been conducted to establish the optimal parenchymal transection method. Some RCT's have compared more recently developed transection technologies with each other and found some to be more advantageous (36,37). So far however there is no evidence that any method has advantages over the traditional clamp-crush technique. A network analysis found an increased rate of adverse events with use of the radiofrequency dissecting sealer compared to clamp-crush transection. The majority of novel transection methods however have been shown to be non-inferior or to have no significant benefits compared to the gold standard (38,39).

At present the majority of liver resections are carried out in highly specialised centres that have the necessary support network to provide optimal care (40,41). Surgical education has evolved alongside these rapid developments and in most countries surgeons require a dedicated period of subspecialty training in liver surgery before they can obtain accreditation as hepato-biliary surgeons.

Concomitant with improved patient outcomes the indications for liver surgery have expanded significantly. In its early beginnings, liver resection for metastatic disease was contentious whereas in current practice in constitutes the bulk of resected liver lesions in western countries (1.1.4.) The introduction of novel technologies has expanded the surgical armamentarium for parenchymal transection and haemostasis (42,43).

Thermal ablation of liver tumours, which can be performed via a percutaneous, laparoscopic or open (laparotomy) approach, has been shown to be a viable alternative to surgical resection. In some case it can be used as a complementary modality alongside resection. Ablation is based on the principle of destroying tumour tissue via induced liver necrosis. It involves insertion of one or more metal probes into the liver tumour (44,45). During ablation, USS, MRI or CT guidance is used for the adequate localization and monitoring of the ablation process. At present thermal ablation via radiofrequency or microwave ablation is the most widely practised method with the latter, more novel method having the advantage achieving higher temperatures in a shorter time frame thus allowing more extensive ablation procedures to be carried out (46).

An important limitation of ablation is the heatsink effect which cools down tumours that are close to larger blood vessels. A reduction in maximum temperature may result in incomplete tumour destruction. Furthermore, thermal ablation carried out close to blood vessels or bile ducts may damage these vulnerable structures which can lead to complications such as bile leak, bile duct strictures, bleeding and thrombosis. To address this limitation, a new technology called irreversible electroporation (IRE) has been introduced. IRE employs multiple, rapid, high voltage pulses that disrupts cell membranes which ultimately leads to loss of homeostasis and cell death (47–49). Ablation of small solitary liver cancers may produce comparable results to liver resection with a reduced morbidity and mortality (50).The main concern regarding thermal ablation is the high incidence of local recurrence. To avoid recurrence it is crucial to destroy not only the cancer harbouring tissue but also a 5-10mm safety margin to include any local satellite lesions.

Neoadjuvant chemotherapy is frequently utilised in an attempt to downsize unresectable CRLM to such an extent that they become amenable for curative resection. Another approach to improve resectability is the use of portal vein embolisation (PVE) which is used to block the blood flow to the part of part of the liver (right or left) that carries the majority of disease burden. This leads to a decrease in the affected part of the liver and a compensatory growth in the contralateral side (51,52). The two-staged hepatectomy approach is used in conjunction with PVE or surgical portal vein ligation to improve outcomes in bi-lobar disease (affecting right and left liver). The first stage involves localised resection (e.g. segmentectomy) of disease from the less affected side of the liver. This is followed by PVE or surgical ligation to the contralateral side to induce growth in the side that has been rendered disease free. Once sufficient liver regeneration has taken place the previously embolised side is resected (53).

The method of associated liver partition and portal vein ligation for staged hepatectomy (ALPPS) has evolved from the two staged hepatectomy recently with the main difference being that the liver is transected during the first stage. This induces more rapid regeneration but also increases operative morbidity and mortality (54,55). In a recent attempt to improve the safety profile of ALPPS, some authors have advocated the less invasive partial -ALPPS where liver transection is limited to 50-80% of the whole transection surface. The mini-ALPPS procedure combines partial transection with a portal vein embolisation instead of portal vein ligation. Both modifications of ALPPS have the aim of reducing the complication rates during the first stage of ALPPS (e.g. bile leaks, bleeding) (56,57). For liver cancers with extensive involvement of vascular structures an *ex-vivo* dissection approach has been first propagated by Pichlmayr (58). Although this has been replicated by other groups its applicability remains reserved for a few select cases (59,60).

Two staged hepatectomy, ALPPS and *ex-vivo* dissection are aggressive surgical solutions for advanced and complex disease. The disadvantage of utilising these techniques is an increase in surgical morbidity and mortality (54,59). At the other end of the spectrum novel

approaches are being developed with the aim of minimising invasiveness and surgical trauma. Parenchyma sparing resections such as segmentectomies have long been popularised for HCC in cirrhotic livers but are also now being introduced for CRLM resection in the form of sub-segmentectomies. The benefit of parenchyma sparing surgery is that a greater future liver remnant can be preserved which reduces the risk of postoperative liver failure and enhances the feasibility of carrying out further liver resections should the cancer reoccur (23,61,62). Correctly identifying segmental anatomy relies heavily on imaging by intraoperative ultrasound whose use and visual interpretation has been accordingly refined (63,64). Virtual three dimensional (3D) reconstruction of the liver has been introduced to aid in the planning of liver resection and to accurately predict the future liver remnant (FLR) (65). More recently 3D organ models have been integrated into image guidance systems that can provide intraoperative image guidance in real-time (66,67). Laparoscopic (keyhole) surgery was introduced in the early 1990's into the field of oncological surgery and has since undergone a rapid expansion. Minimising the size of abdominal incision has been shown to benefit patients by reducing pain, blood loss, length of stay and postoperative complications. In certain procedures (e.g. cholecystectomy, anti-reflux surgery) the impact of laparoscopy has been so significant that it has become the approach of 1st choice (68,69). In contrast to this liver surgeons have been relatively slow to adapt the laparoscopic approach. The reasons behind this will be elaborated on in the following section.

1.2. Introduction to laparoscopic liver surgery

1.2.1 The concept of laparoscopy

The aim of laparoscopic surgery is to reduce the size of the surgical incision and hence the associated surgical trauma (Figure 1.3). The semantic origins of “laparoscopy” stems from the Greek words ‘lapar’ meaning ‘flank’ or ‘abdomen’ and ‘scop’ meaning ‘see’. It is essentially a medical procedure initially developed to look inside the abdomen for diagnostic purposes which later on has evolved to enable therapeutic interventions (e.g. organ resection) as well. To perform laparoscopy the first step is to distend the abdominal cavity by insufflating it with carbon dioxide, which subsequently creates the space required for the manoeuvring surgical instruments. The now established pneumoperitoneum is accessed via laparoscopic ports. These ports are essentially 5-15mm diameter tubes with an integrated air lock that enables introduction of specialised laparoscopic instruments without the loss of intraabdominal pressure. The first port is used is to introduce a laparoscopic camera called ‘laparoscope’. The view of the laparoscope is projected on a screen that is placed in a convenient position close to the patient. Depending on the requirements of the intended procedure a varying number of additional ports is subsequently introduced (Figure 1.4).

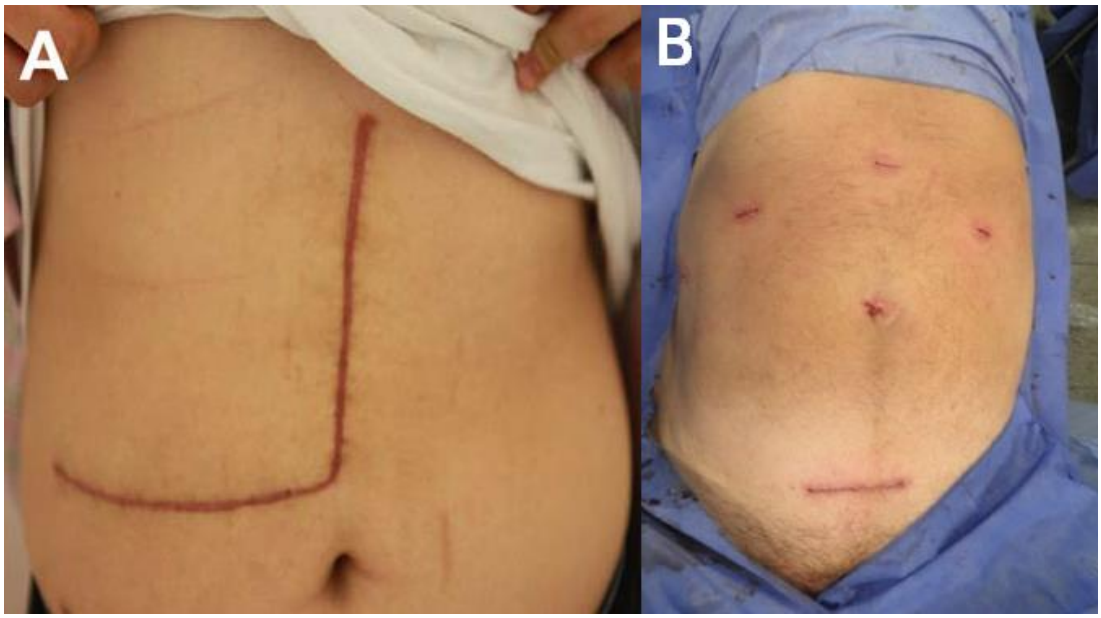

Figure 1.3 Comparison between conventional and laparoscopic scars.

a) Open liver resection (70) **and b) Laparoscopic liver resection** (71)**. (reprinted with permission from: a - Wiley copyright 2014, b - CC BY-NC 4.0 from Ingenta Connect)**

There are a vast and steadily increasing number of laparoscopic instruments that amongst many other things can be utilised to manipulate, cut, coagulate, irrigate and suture tissues. Many of these are adaptations of instruments used in open surgery such as laparoscopic diathermy, needle holders or staplers. Others instruments have been specifically designed

for laparoscopic surgery, tissue graspers for example have been introduced to hold and manipulate tissues with the aim of replacing the surgeon's hands. Laparoscopic surgeons are becoming increasingly skilful in substituting the motor function of the hand with tissue graspers. The issue is that graspers cannot convey the feel of touch and hence surgeons are deprived of their second most important sense, the sense of touch.

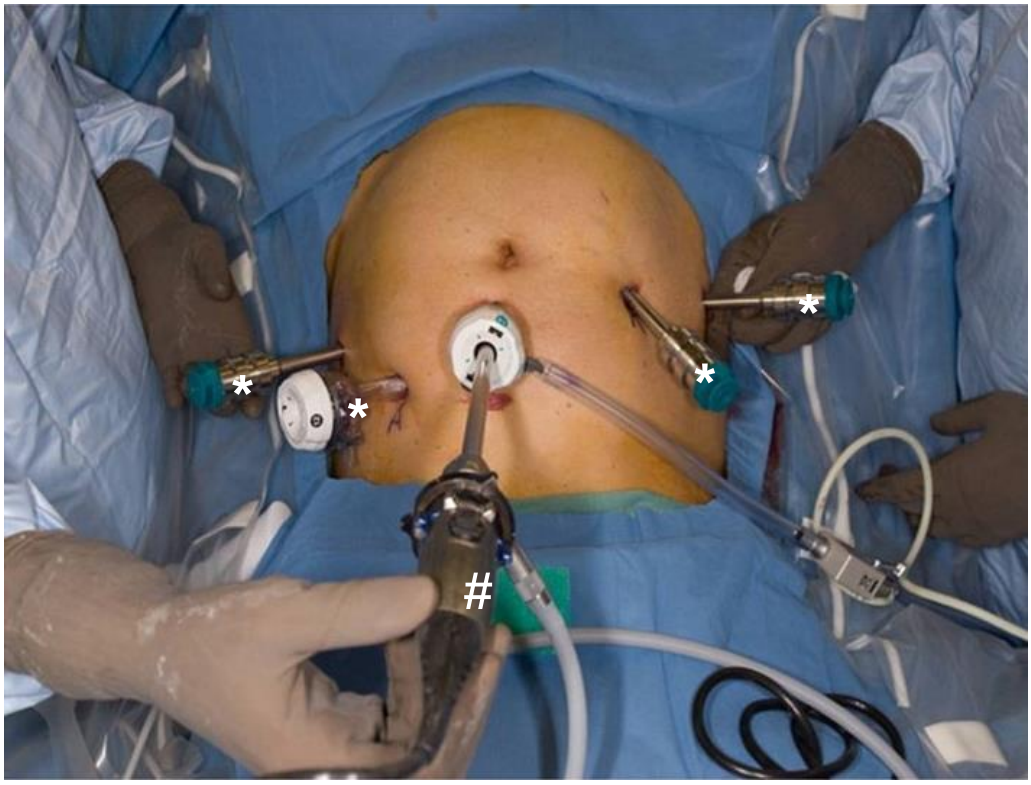

Figure 1.4 Laparoscopic port placement.

The ports (*) allow the insertion of a laparoscopic camera (#) and instruments (72)**. (reprinted with CC BY-NC 4.0 from Intechopen)**

1.2.2 Adaptations specific to liver surgery

The majority of the laparoscopic instruments used for liver resections are also used in other laparoscopic procedures. These 'general purpose' instruments include graspers for tissue manipulation, diathermy or thermal tissue sealing systems for dissection and haemostasis (stopping bleeding), scissors for cutting, needle holders for suturing, suction to evacuate fluid, laparoscopic staplers to divide and seal structures and to perform an anastomosis between two hollow viscus. Laparoscopic retractors either held by hand or fixed to the operating table by a pole, can be used to hold the liver in place while a resection is carried out. There are many other instruments in use which cannot all be named here.

Some instruments however have been developed for specific use in liver surgery. These include the argon beam coagulator used for haemostasis, the ultrasonic suction aspirator for parenchymal transection and laparoscopic ablation probes for thermal ablation. Although also employed by other surgical specialties, laparoscopic ultrasound is an essential tool for the visualisation of functional liver anatomy and has therefore found widespread uptake for laparoscopic liver resection (73–77).

1.2.3 Historical development of laparoscopic liver surgery

The first report of a laparoscopic procedure in the field of hepato-biliary surgery was that of a laparoscopic cholecystectomy carried out by Muhe in 1985 (78). This was performed using a side-viewing endoscope without video connectivity. In this first report the surgeon visualised the abdominal cavity directly without the aid of a video screen. The procedure was soon adapted to be used in conjunction with a video-laparoscope that projected its views onto a screen, much like it is performed in this day and age (79). It took several years until this approach was extended to the resection of a parenchymal liver lesion in order to remove a focal nodular hyperplastic nodule (80). The first liver resection for malignancy (CRLM) was carried out soon after this report (81). As the international surgical community took note of these advances which is reflected by a number of case series of laparoscopic liver resection (LLR) that were published in rapid succession (82–85). These studies conducted on different continents, populations and pathologies demonstrated the repeatability and safety of this new approach. Due to concerns about oncological adequacy of LLR, many groups gained experience in benign cases first before embarking on resection of malignancy. Not unlike laparoscopic liver surgery today, a variety of methods for parenchymal transection such as hydro jet dissector, thermal ablation, clamp crush technique and ultrasonic scalpel were proposed in these studies(82,84–88). Many authors advocated the use of laparoscopic ultrasound to identify landmarks of functional liver anatomy intraoperatively (85,86,88). In this early period very few authors attempted major liver resections (>2 segments) via the laparoscopic approach were reported. The first series containing major hepatectomies via the laparoscopic approach was published in 1997 and the authors concluded that it was a feasible alternative in selected patients (83).

Several of these pioneers of LLR continued to refine their operative techniques and publish them in the literature. Other centres emulated these techniques and started to introduce LLR into their repertoire. This process started a standardisation of several laparoscopic techniques (e.g. ‘French position’, caudal approach), which are still in use today (74,76,83,85,89,90).

In parallel with increasing sophistication, the laparoscopic approach was extended to technically more demanding and complex procedures such as caudate lobe resection (91) or resection of the right posterior liver segments (92). The confidence of some authors in the safety of LLR is reflected by the first report of laparoscopic left lateral sectionectomy for the purpose of living donor transplantation (93) (harvest of partial liver for liver transplantation). In living donor transplantation, donor safety is of the utmost importance and the willingness to apply LLR to this patient cohort heralded a big step in the evolution of laparoscopic liver surgery.

With increasing certainty about the technical feasibility and safety of LLR (76,94–96), the focus of publications extended to studying the potential benefits of this technique for patient outcomes. Outcome parameters that were thought to improve with the minimal invasive approach included postoperative pain, length of hospital stay and intraoperative blood loss (75,76,97). Over the last decade evidence of a decrease in postoperative complications for patients undergoing LLR vs. open liver resection has been accumulating (98,99). However due to the paucity of standardised registries, randomised controlled trials (RCT) or a large volume meta-analysis, there remained some uncertainty about the exact nature of benefits conveyed by the laparoscopic approach (94,100,101).

In 2008 and 2014 two consensus conferences on the international position on laparoscopic liver surgery were held in Louisville and Morioka, respectively. During the Louisville conference it was concluded that LLR is safe and effective if performed by surgeons with experience in traditional (open) liver- and laparoscopic surgery. A recommendation to establish an international registry for LLR was issued (94). The second conference in Morioka postulated that minor (i.e. resection of ≤2 segments) LLR has made the transition from experimental treatment to standard of care whereas major LLR is still an innovative procedure that requires further evaluation (74).

1.2.4 Current state of the art in laparoscopic liver surgery

The uptake of LLR has exponentially increased over the last decade. The estimate of globally reported procedures has increased from approximately 3000 to over 9000 in the span of 6 years (96,102). The majority of laparoscopic liver surgeons are carrying out minor LLR such as left lateral sectionectomies or wedge resections; more complex surgery (e.g. major hepatectomy, caudate lobe, right posterior sectionectomy) however has not been taken up widely so far. Complex LLR are performed in a relatively small number of highly specialised centres that have driven the innovation of novel laparoscopic techniques in the recent past (74,102).

Laparoscopic resection of hilar cholangiocarcinoma for example had not been attempted until a few years ago because it required a concomitant reconstruction of biliary drainage (hepatico-jejunostomy). Although technically challenging, the feasibility of performing this laparoscopically with acceptable outcomes has been demonstrated recently (103). Because a significant number of hilar cholangiocarcinomas also require resection and reconstruction of blood vessels that have been infiltrated by cancer (20), it is likely that the laparoscopic approach will only be applicable for a small cohort of these patients.

It has been recognised that the difficulty of a laparoscopic resection does not exclusively depend on the extent of resected liver tissue but also and perhaps to a greater degree on its location. In this context it is particularly difficult to perform a segmentectomy of liver segments 7 and 8, on the superior right aspects of the liver. It is simpler to carry out a right hepatectomy and remove segment 7 or 8 together with segments 5 and 6. This however has the disadvantage of unnecessarily removing healthy parenchyma which can affect postoperative liver function in diseased livers (e.g. cirrhosis) and restrict surgical options if a cancer recurrence in the liver requires resection at a later stage (23,74). Technical aspects to performing parenchyma-sparing segmentectomies throughout segment 1-8 have been described previously (73). In this report it was suggested to place laparoscopic ports traversing through the chest and diaphragm into the abdominal cavity to access the most challenging superior portions of the liver (segment 7&8). A more aggressive trans-diaphragmatic access facilitated by a thoracoscopic (minimal invasive chest surgery) approach that requires incision and repair of the diaphragm, has been advocated by a different group. For preoperative planning and simulation a 3D liver model (Figure 1.5) was utilised in this report (104).

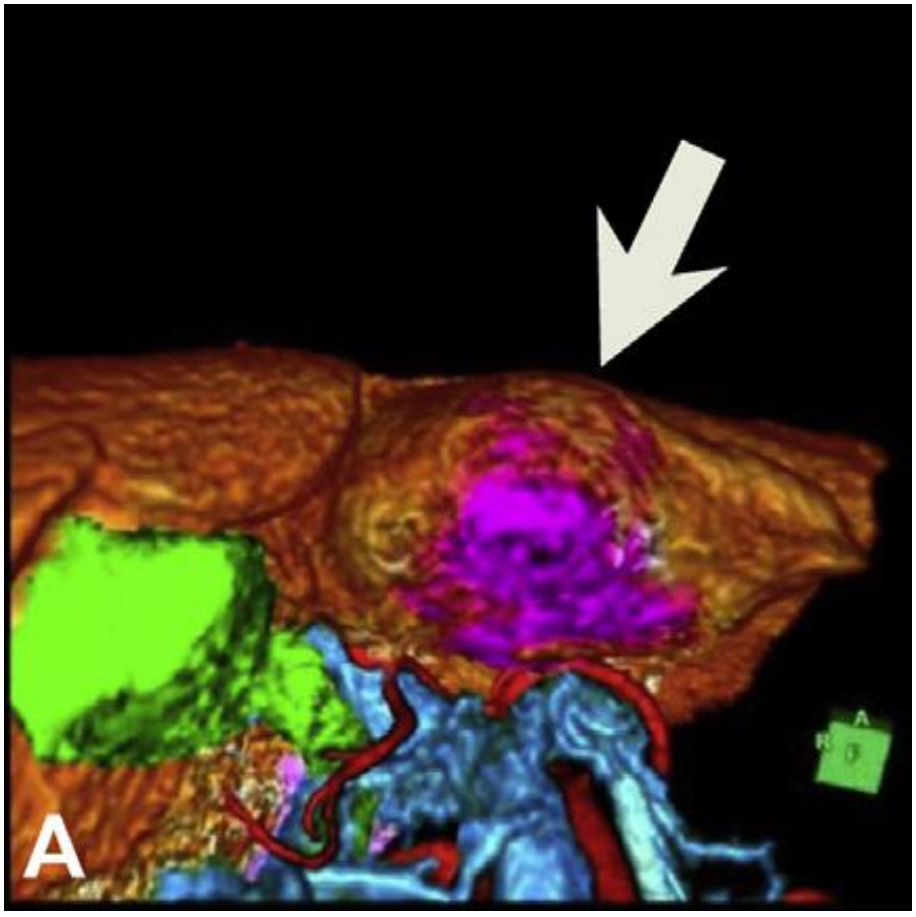

Figure 1.5 A 3D liver model for preoperative simulation.

The 3D model was used to visualise the position of the liver lesion (arrow). At the lower half of the image the hilar vessels can be seen (blue - portal vein; red - hepatic artery). The gallbladder is shown as a green structure on the left (105)**. (Reprinted with CC BY-NC 4.0 from Elsevier)**

An alternative to hilar dissection and control was suggested by an author who invented the 'Glissonian approach' (106). Instead of controlling hepatic inflow vessels at the hilum, they (the hepatic inflow vessels) are transected with a stapler device inside the liver parenchyma. The same group that initially proposed laparoscopic donor hepatectomy on the left liver, has more recently described this approach for the right liver in adult-to-adult donation (107).

Not all research is focused on improving the technical aspects of LLR though. It has long been stressed that better levels of evidence or needed to verify the benefits of the laparoscopic approach. The highest level of evidence up to date has been provided by meta-analysis of comparative studies (102). The relatively low number of patients suitable for LLR and their heterogeneous pathologies is thought to be a major obstacle for the instigation of a RCT (94). The Orange II study, which compared open vs. laparoscopic left lateral sectionectomy for example was forced to close prematurely due to slow recruitment accrual (108). Its sister trial, the Orange II Plus study which investigates outcome differences

between laparoscopic vs. open major hepatectomies (right or left hepatectomy) is still recruiting patients. So far only one RCT investigating the differences in postoperative morbidity in open vs. laparoscopic liver resections for CRLM (Oslo-CoMet trial) has been completed and its results published (109). In this trial, patients undergoing LLR were found to have a lower complication rate and better quality of life after surgery.

Laparoscopic resection was also shown to be more cost effective than open surgery. Although the costs of the operation were higher in the LLR group, this was more than compensated for by a decreased length of hospital stay. Other parameters of intraoperative performance such as operating time, blood loss and oncological resection margins were found to be equivalent between both types of surgery (109). The results of this RCT add to the steadily accruing evidence that LLR is safe in the right hands, has a positive impact on short-term patient outcomes and is non-inferior to open liver resection with regards to long-term outcomes (98,99,102,109–111).

1.2.4.1 Robotic liver resection

Robotic surgery in the abdomen can perhaps best be described as a subcategory of laparoscopic surgery where the motion of surgical instruments is finely controlled by robotic limbs. The first report on a successful telerobotic operation, a cholecystectomy, was published 1997 (112). The aim of robotic surgery is to negate some of the inherent motor limitations of laparoscopic surgery such as limited range of movement, tremor magnification and the fulcrum effect against the laparoscopic port. An additional advantage is the ability to obtain a three dimensional view of the operating site which is thought to improve spatial awareness (113). Because the surgical robot is controlled remotely by a surgeon who is seated in front of a control module, these procedures were initially described as ‘telerobotic surgery’. Over time the terminology has been simplified into ‘robotic surgery’.

A large variety of abdominal operations has been performed robotically including anti-reflux surgery, Heller myotomy, Roux-en-Y gastric bypass, and, more recently, colorectal surgery (114,115). The most enthusiastic and enduring uptake of the robotic approach however has occurred in prostate and gynaecological surgery (116). A recent meta-analysis comparing laparoscopic vs. robotic radical prostatectomy postulated a lower operative blood loss and improved outcomes in terms of continence and erectile function for the robotic approach (117).

Robotic liver resection has been compared to LLR in a number comparative studies that found a comparable safety profile, similar short term outcomes but also an increased operating time (118–120). The disadvantages of robotic surgery in general are a steep learning curve, complete lack of tactile feedback and near prohibitive costs (114). Currently it remains unclear whether there is any added patient benefit when compared to laparoscopic procedures (114,121). Some advocates of robotic surgery argue that it is essentially an aid

to expand minimal invasive surgery to procedures that are too challenging to carry out via the standard laparoscopic approach (119,120).

1.2.5 Challenges in laparoscopic liver surgery

Compared to other surgical specialties, the uptake of LLR has been relatively slow. This is thought to be due to concerns about the ability to control haemorrhage and to achieve complete oncological clearance (remove all cancer tissue)during LLR (102,122). Some surgeons are also reluctant to embark on laparoscopic resections because the acquisition of the necessary skills is associated with a steep learning curve (123–126).

These concerns may be ultimately related to the inherent technical limitations of laparoscopic surgery. Potential patient benefits from a laparoscopic liver resection have to be balanced against these limitations that the surgeon must overcome in order to carry out the operation successfully. These disadvantages can perhaps be categorised into motor limitations (i.e. how to do something) and sensory limitations (i.e. we do not know what a structure is). Innovations in laparoscopic instruments and robotic surgery may be a possible solution to overcome the motor limitations of laparoscopic surgery but generally they do not address the sensory deficits. Of the 5 senses, vision is arguably the most important with the sense of touch coming second and the remaining three senses bearing relatively little importance. There are several limitations to both vision and touch in LLR or laparoscopy in general. The laparoscopic view is displayed in two dimensions (2D) and a limited field of view, which impedes spatial- awareness and orientation with subsequent effects on fine motor skills and interpretation of anatomy (127–131). The lack of haptic feedback (i.e. feeling tissue) has been well documented for laparoscopic surgery (128,132). An additional issue in LLR is that bi-manual palpation in conjunction with intraoperative ultrasound is important for the detection of liver lesions (33,133,134). It has therefore been postulated that recovering or perhaps even extending some of the lost sensory information could help in the location of vulnerable structures (e.g. blood vessels) and liver lesion during LLR. Improving identification of these structures and lesions would in turn lessen the risk of causing inadvertent damage or leaving pathological tissue behind. As an additional benefit, an enhanced sensory input may also improve the surgical learning curve associated with LLR (123).

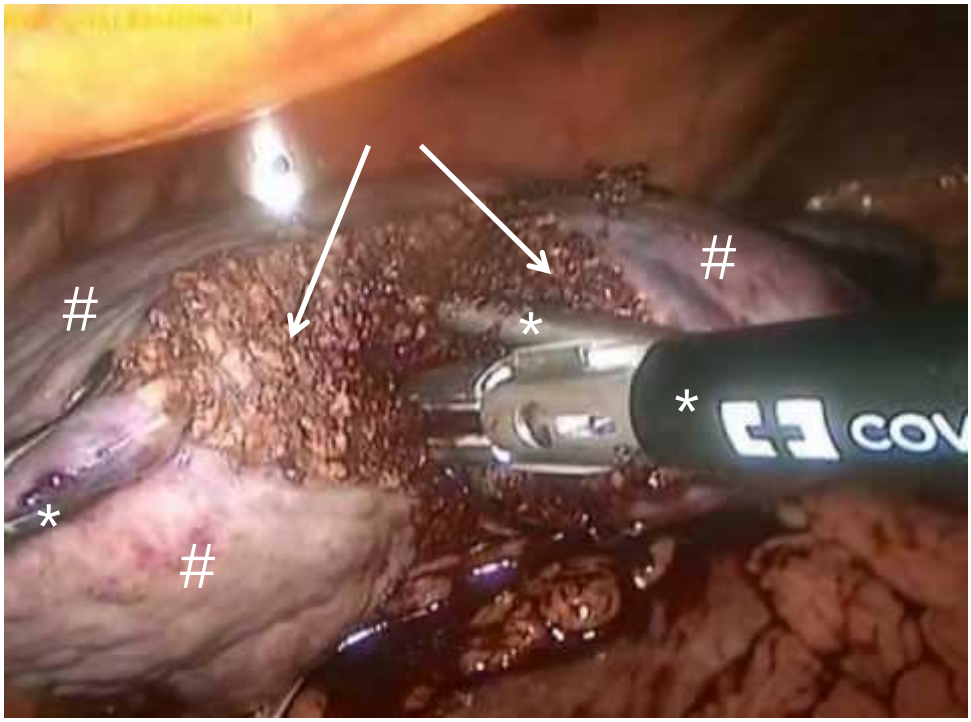

Figure 1.6 Laparoscopic view during liver resection.

Note how bleeding and line of sight occlusion from laparoscopic instruments (*) further impair the view. The transected liver tissue (transection plane – arrows) can be seen centrally whereas the liver surface (#) is visible on either side.

The work in this thesis aims to explore methods of enhancing the sensory information during LLR by utilising optical imaging and computer vision. These technologies are based on functions of light and as such there are natural advantages of applying them in a laparoscopic environment because they can extract additional sensory data, not perceivable with the human eye directly through a laparoscopic camera (135,136). If additional equipment requires insertion into the abdominal cavity, this can usually be adapted to fit through laparoscopic ports without great difficulties (127,137,138).

1.3. Thesis hypothesis

It is hypothesised that optical imaging and computer vision technologies have the ability to extract sensory information from the liver that is useful for guiding laparoscopic liver surgery.

1.4. Objectives of the thesis

1) To elucidate the ability of confocal laser endomicroscopy to characterise normal and pathological liver tissue
2) To investigate how multispectral imaging may be applied to evaluate the composition of liver tissue and its implication on disease states.
3) To develop and test a quantification method for motion magnified signals in video.
4) To evaluate the feasibility of using a novel image guidance system for laparoscopic liver surgery in a clinical setting and assess its performance.

In the following chapter the existing literature on *in-vivo* optical imaging and computer vision of the liver will be reviewed.

2. Literature review

To better evaluate the current state of the art in optical imaging and computer vision of the liver in a laparoscopic environment, a systematic literature search that combined the terms “liver” and “laparoscopy” with optical imaging- or computer vision terms was performed using the Medline and Embase databases. Generic and mesh terms used for the search were, “optical imaging” and “image guided surgery”. A detailed description of the search strategy is outlined in the methods section under “electronic search strategy” below. To complement the initial search, each Medline search term indexed under “Diagnostic Techniques and Procedures” was screened for relevant optical imaging modalities and included as a separate search term if appropriate.

2.1. Introduction

A background on liver surgery and laparoscopic liver surgery has been provided in the general introduction of this thesis. The introduction to this chapter focuses on providing background information on imaging modalities relevant to this work.

The use of laparoscopic ultrasound (LUS) prior to parenchymal transection is recommended by some surgeons to identify liver lesions and delineate the hepatic vasculature during LLR (95,96,123,139,140). Once transection has started however the use of LUS is challenging and non-intuitive because it only provides 2D images which are difficult to interpret and do not offer much orientation within a 3D space. Additional limitation of LUS is that its diagnostic accuracy is decreased in the case of small or vanishing liver lesions or when background changes in the liver such as steatosis or cirrhosis are present (141–144). Finally it may be difficult to discriminate between benign or malignant liver lesions that are incidentally found on LUS and therefore the decision on whether to resect such a lesion depends on clinical judgment (134).

The issues around anatomical orientation have led to research efforts into developing image guidance systems (IGS) that enable visualisation of 3D liver anatomy during LLR. Further research is directed at creating laparoscopic imaging modalities that enhance the visualisation of liver tissues with the intention of enabling surgeons to discriminate between different types or normal and pathologic liver tissues. These combined efforts can be regarded as an initiative to substitute for a decreased sensory input that is inherent to laparoscopic surgery, by enriching and maximising the data that is obtainable in the visual domain. Optical imaging and computer vision technology forms the foundation of the majority of emerging systems that are being developed to provide enhanced visualisation or image guidance (128,135,145).

Medical optical imaging is an emerging non-invasive modality that is used in conjunction with endogenous or exogenous contrast agents. The latter, also known as fluorophores can be selected according to disease processes or tissue type of interest. This approach confers a high specificity which is unrivalled by conventional radiological imaging modalities. In contrast to X-Ray based modalities, optical imaging utilises non-ionising radiation to interpret information and transform them into images .i.e. light at visible and invisible wavelengths. The former mainly focuses on regular white light illumination whereas the latter includes ultraviolet, near-infrared and infrared light. This has the advantage that patients are not exposed to harmful radiation and therefore imaging can be repeated multiple times.

Computer vision is closely related to optical imaging because it utilises image information in the visible light spectrum, usually in the form of video. The difference to conventional video or other forms of optical imaging is that processing and interpretation of these images is carried out by computer algorithms. This approach conveys the advantage of being able to

detect subtle details in a large volume of information or performing complex image analysis procedures that would be beyond the abilities of a human user.

Some examples for optical imaging modalities are spectral imaging, laser microscopy, optical coherence tomography and fluorescence imaging all of which share common characteristics such as excellent spatial resolution, high specificity, real-time image processing, lack of ionising radiation and the wide availability of miniaturised equipment which facilitates its use in minimal invasive procedures. Most of these traits also apply to computer vision which is inherently related to optical imaging because they rely on the optics within camera and because they are frequently used in conjunction with other optical modalities (e.g. laser range scanner). Viewed within this wider context, computer vision can be referred to as an optical imaging modality for the purpose of this article.

Technical background of common imaging modalities

Microscopic fluorescence imaging

Probe based confocal laser endomicroscopy (CLE) is a relatively well established microscopic fluorescence imaging technique that utilises a fibre-optic bundle to emit and receive light signals which are subsequently processed into µm-scale resolution images. Light emission is generated by a laser scanning unit that is situated at the proximal end of the fibre (i.e. further away from the tissue). The optical lenses required to focus the light at a specific imaging plane and to collect the resulting fluorescence emissions can be located at the distal or proximal end of the fibre. The former solution generally results in a more bulky, rigid endomicroscope design because the lenses have to be incorporated within the tip of the probe but this may be offset by a better image resolution (146). Systems that combine the laser scanning unit and optics at the proximal end of the fibre on the other hand enable use of miniaturised, flexible probes with a minimal diameter of between 0.3 mm whereas their rigid counterparts have a minimum diameter of 6.3 mm (147). Either design can readily be introduced through a standard laparoscopic port but flexible probes have also been deployed trans-gastric and trans–vaginally during natural orifice transluminal endoscopic surgery (148,149). To facilitate image acquisition via laparoscopic or natural orifice route, the probe is gently pressed on the area of interest with the resulting image visible on a screen in real-time.

Generally fluorescence signals may originate from endogenous or exogenous fluorophores but in CLE imaging of the liver only the latter are of relevance (146). Fluorophores can be regarded as “contrast agents” that respond to illumination by emitting light at a specific wavelength. Most CLE systems are therefore designed to operate a single specific wavelength although more recently “dual wavelength” systems with the ability to simultaneously acquire images at two separate spectra of light have been developed (150). There is a plethora of fluorophores available but for CLE imaging of the liver fluorescein and

indocyanine green (ICG) have been employed most frequently. Both have the advantage of being licensed for clinical use and as an additional benefit, ICG is exclusively excreted into bile, a property which is desirable because it results in a strong and selective contrast in the biliary system and healthy parenchym (151,152). It has to be noted however that patients with congenital non-haemolytic hyperbilirubinemia (e.g. Gilbert's and Rotor syndrome) may exhibit altered ICG fluorescence characteristics (153).

Wide field fluorescence imaging

Parallel to CLE imaging, fluorescence can also be used for the macroscopic visualisation of anatomical structures. To facilitate this, the laparoscope needs the ability to view a specific wavelength range that corresponds to the fluorophore(s) of interest. This is achieved by either filtering undesired wavelengths, using light sources tuned to a certain wavelength range or a combination thereof (144,151,152,154–156).

Endogenous fluorophores have been used for controlling the effectiveness of photodynamic therapy in the peritoneum and liver (157) and they are a viable source of fluorescence in some organs (158). For hepatic imaging however exogenous fluorophores including methylene blue, fluorescein conjugated bile acids and ICG are preferred for experimental use (151,154,159). Out of these only ICG has been evaluated clinically so far, most likely due to the same above mentioned reasons that made it a popular fluorophore for CLE imaging of the liver.

Multispectral imaging

The absorption of light within the visible and invisible spectrum can be altered by pathological processes that affect cellular composition or tissue structure (160). This effect can also be exploited to obtain anatomical and physiological information that is subsequently transformed into images. Although there are variations in the names attributed to this methodology such as hyperspectral-, multispectral- or narrow band imaging, the basic principle remains the same. Tissues are illuminated at one or more specific wavelengths and the amount of absorbed and reflected light can consequently be used to infer its composition. In contrast to fluorescence imaging and CLE this modality is frequently used with endogenous fluorophores. In this context haemoglobin and tissue oxygenation have been widely studied but other substances such as fat, water or bile can also be quantified in absolute or relative terms (137,161–163). It is possible to obtain information on particular tissue components using a single spectrum but the simultaneous or sequential acquisition of multiple spectra has the potential to reflect tissue composition in greater detail.

Enhanced white light vision

Traditionally laparoscopic vision relies on a monocular scope that views the surgical site at a 0˚ or 30˚ angle. Regular vision has been improved by the introduction of digital video,

automatic focus, and high definition video (164). Above and beyond imaging modalities that utilise magnification or invisible spectra of light, there may be an advantage in enhancing the laparoscopic view within the visible spectrum. This may be achieved by increasing the laparoscopic angle of view through the use of wedge prism (165). A completely different approach is to improve the mobility and versatility of laparoscopic equipment by amalgamating laparoscope, instrument port and laparoscopic screen into one single piece of equipment (166).

The most widely used example of enhanced white light vision in minimal invasive surgery is stereoscopic- or 3D laparoscopy. It is well established that lack of tactile feedback and depth perception are the two major drawbacks of laparoscopic surgery. Since stereoscopic vision is the main contributor to depth perception, it is unsurprising that the introduction of 3D laparoscopy has been repeatedly attempted in the past. Unfortunately previous attempts of introduction have been hindered by concerns about cumbersome equipment that induced dizziness, fatigue and headaches in the surgical users (167). Driven by the entertainment industry, stereoscopic or 3D technology has greatly matured over the last decade and is now employed in a number of commercially available laparoscopy systems that do not suffer from the disadvantages of their predecessors (137). The laparoscopic camera itself differs from its conventional counterparts in that it has two separate, slightly set apart video channels instead of one. The right and left video channel are only shown to the corresponding eye of the surgeon which creates an effect that simulates true 3D vision to the human visual cortex (168).

Intraoperative image guidance

A common limitation of optics and vision based approaches is their short penetration depth which rarely exceeds 5mm (144). This restriction may be overcome with the use of image guidance systems (IGS) where optical technology can be used to project or display anatomical data from preoperative scans integrated into the operative site. Use of IGS in LLR is particularly appealing because the display of the highly variable vascular and tumour anatomy may aid in identifying tumour dimensions, vascular and biliary structures (169,170).

An IGS is based on three essential components, a 3D model, positional tracking and intraoperative registration. Initially a 3D representation of the individual patient anatomy (henceforth called 3D model) is created from CT or MRI images. Positional tracking is a method that enables the spatial correlation of patient anatomy, surgical view and/or surgical instrument. The most frequently employed tracking methods in image guided surgery are based on optical markers or electromagnetic signals. Both technologies are in routine clinical use and have been extensively investigated (128). For this reason, articles reporting solely on the use of optical marker tracking have not been included in this review. Finally the precise alignment of 3D model and patient anatomy is carried out in a process called registration. It is unsurprising that various methods of registration have been proposed as it

is by far the most error-prone and difficult component of an IGS (128,141). Optics and computer vision based registration concepts are popular because they offer advantages in terms of excellent spatial resolution, high update frequency, lack of invasiveness, comparatively low costs, portability and are relatively easy to integrate into existing operating equipment (141,171,172). Other non-optical solutions for registration exist (e.g. LUS or MRI based) but will not be discussed as this is beyond the scope of this review.

Although IGS are currently widely used in neurosurgery, orthopaedic surgery and otolaryngology, the development of solutions for abdominal surgery has been slow (173). The main obstacles preventing a meaningful implementation of this technology are the significant mobility of abdominal organs, lack of fixed bony landmarks for orientation and cyclical organ motion secondary to diaphragmatic and cardiac movement (141,173,174). Further difficulties that have to be addressed by IGS for hepatic surgery are the paucity of liver surface features, the inability of viewing the complete organ with a laparoscope and the significant deformation that the liver undergoes due to the increased intraabdominal pressure from the pneumoperitoneum and surgical manipulation (174).

Because of these latter issues, AR solutions for retroperitoneally fixed organs such as the pancreas or kidney are thought to be somewhat simpler (173). Despite these difficulties, researchers have keenly pursued the advancement of AR for LLR because the innate drawbacks of laparoscopy such as lack of touch, depth perception and orientation are thought to be main factors in delaying the uptake of the laparoscopic liver surgery in the international community (122).

The aim of this systematic review is to provide a comprehensive overview of the potential and limitations of minimal invasive optical imaging technology that has been evaluated on the liver. To ensure immediate- to mid-term clinical relevance, this review focuses exclusively on modalities that have been tested in *in-vivo* experiments or clinical studies. Finally a number of promising optical imaging concepts that have not advanced to this stage yet are discussed and key areas for future research focus are highlighted.

2.2. Methods

A systematic literature search that included the free text and corresponding controlled vocabulary terms for “liver” and “laparoscopy” combined with those for optical imaging, computer vision terms, or “image guided surgery” was performed using the Medline and Embase databases. A detailed description of the search strategy is stated in Appendix 1. To complement the initial search, each Medline search term indexed under “Diagnostic Techniques and Procedures” was screened for relevant optical imaging modalities and included as a separate search term if appropriate.

Full text articles, conference proceedings and conference abstracts describing *in-vivo* basic science or clinical research on optical imaging modalities in laparoscopic liver surgery or

laparoscopic liver ablation were retrieved. The time period for article retrieval was set to 15 years from June 2001 to June 2016. In total 750 articles were identified and their titles and abstracts were subsequently screened for inclusion. The reference flow is outlined in Figure 2.1.

Exclusion criteria were image guidance based on non optical methods (e.g. CT), image guidance for radiotherapy purposes, ex-vivo research, non-primary research and articles not written in English. Articles reporting on imaging in open liver resection or laparoscopic cholecystectomy were excluded as well. Screening of the titles and abstracts of retrieved references was carried out by the author.

Full texts for eligible articles were retrieved and read. A qualitative summary of the findings is given in the results section. Due to the heterogeneous nature of available research no quantitative analysis or meta-analysis could be conducted.

2.2.1 Electronic search strategy

Given below is a list of search terms and Boolean operators used for conducting a systematic review of optical imaging technology in laparoscopic liver surgery.

Pubmed

#1 ("Surgery, Computer-Assisted"[Mesh:NoExp]

#2 "Optical Imaging"[Mesh] OR Optical imaging*

#3 fluorescence imaging* OR autofluorescence imaging*

#4 "Spectroscopy, Near-Infrared"[Mesh] OR NIR Spectroscop*

#5 NIR spectrometr* OR near-infrared Spectrometr* OR Near Infrared Spectrometr* OR near-infrared spectroscop* OR near infrared spectroscop* OR infrared spectroscop* OR "Photoelectron Spectroscopy"[Mesh] OR photoelectron spectroscop* OR "Spectrometry, Fluorescence"[Mesh] OR spectrophotometr* OR spectrofluo* OR fluorescence spectroscop* OR "Spectrophotometry"[Mesh] OR spectrophotometr* OR spectroscopic photometry OR "Spectrum Analysis, Raman"[Mesh] OR Raman Spectroscop* OR Raman Scatter* OR laser raman spectroscop* OR raman resonance spectroscop* OR Absorption spectroscop* OR diffuse reflect* OR spectroscopy reflect* OR ellipsometry OR fluorescence correlation spectroscop* OR scanning fluorescence correlation spectroscop* OR infrared spectroscop* OR ir spectroscop* OR transmission infrared spectroscop* OR fourier transform infrared spectroscop* OR near infrared reflect* OR near-infrared reflect*

#6 "Microscopy, confocal"[Mesh] OR confocal microscop* OR laser scanning microscop* OR laser microscop*

#7 "Intravital microscopy"[Mesh] OR Intravital Microscop* OR in vivo microscop*

#8 "Microscopy, Fluorescence"[Mesh] OR fluorescence microscop* OR Immunofluorescence microscop*

#9 "Microscopy, Interference"[Mesh] OR phase contrast microscop* OR interference reflection microscop* OR interferometry* OR interference microscop* OR microinterferometry* OR differential Interference Contrast microscop* OR nomarski interference contrast microscop*

#10 "Microscopy, Polarization"[Mesh] OR polarized light microscop* OR polarization microscop*

#11 "Microscopy, Ultraviolet"[Mesh] OR Ultraviolet Microscop*

#12 "Photoacoustic Techniques "[Mesh] OR Photoacoustic* OR Optoacoustic*

#13 "Stroboscopy"[Mesh] OR Stroboscop*

#14 "Holography"[Mesh] OR Holography

15 image guided surger* OR image guidance* OR image guided* OR Image-guided*

#16 "Artificial Intelligence"[Mesh] OR artificial intelligence*

#17 computer vision* OR machine vision*

#18 surface reconstruction*

#19 3D laparoscop* OR three dimensional laparoscop* OR three-dimensional laparoscop*

#20 virtual reality* OR augmented reality*

#21 hyperspectral* OR multispectr*

#22 #1 or #2 or #3 or #4 or #5 or #6 or #7 or #8 or #9 or #10 or #11 or #12 or #13 or #14 or #15 or #16 or #17 or #18 or #19 or #20 or #21

#23 "Laparoscopy"[Mesh] OR laparoscop* OR peritoneoscop* OR celioscopy OR peritoneoscop* OR celioscop*

#24 "Robotic Surgical Procedures"[Mesh] OR robotic surgery OR robotic surgical procedure* OR robotic surgery OR robotic assisted* OR robot surgery OR robot assisted surgery

#25 #23 or #24

#26 #22 and #25

Embase

#1 spectrometry/ OR (Raman Spectr* OR Raman Scatter* OR laser raman spectr* OR raman resonance spectr*).af.

#2 exp holography/ OR (hologra*).af.

#3 exp fluorescence imaging/ OR (Optical imaging* OR fluorescence imaging* OR autofluorescence imaging*).af.

#4 (hyperspectral* or multispectr*).af.

#5 (intravital microscop* OR in vivo microscop*).af.

#6 exp confocal microscopy/ OR (confocal microscop* OR laser scanning microscop* OR laser microscop*).af. OR exp fluorescence microscopy/ OR (fluorescence microscop* OR Immunofluorescence microscop*).af.

#7 exp phase contrast microscopy/ OR (phase contrast microscop* OR interference reflection microscop* OR interferometry* OR interference microscop* OR microinterferometry* OR differential Interference Contrast microscop* OR nomarski interference contrast microscop*).af.

#8 exp polarization microscopy/ OR (polarized light microscop* OR polari* microscop*).af.

#9 (ultraviolet microscop*).af.

#10 exp stroboscopy/ OR (Stroboscop*).af.

#11 exp photoacoustics/ OR (Photoacoustic* OR Optoacoustic*).af.

#12 *computer assisted surgery/ OR (image guided surger* OR image guidance* OR image guided* OR Image-guided*).af.

#13 exp virtual reality/ OR (virtual reality* OR augmented reality*).af.

#14 exp artificial intelligence/ OR (artificial intelligence* OR computer vision* OR machine vision* OR surface reconstruction*).af.

#15 (3D laparoscop* OR three dimensional laparoscop* OR three-dimensional laparoscop*).af.

#16 #1 or #2 or #3 or #4 or #5 or #6 or #7 or #8 or #9 or #10 or #11 or #12 or #13 or #14 or #15

#17 exp laparoscopy/ OR exp robot assisted surgery/ OR (laparoscop* OR peritoneoscop* OR celioscop* OR robotic surg* OR robotic surg* procedure* OR robotic assisted*).af.

#18 exp liver/ OR exp liver surgery/ OR (liver OR hepat*).af.

#19 #17 and #18

#20 #16 and #19

2.3. Results

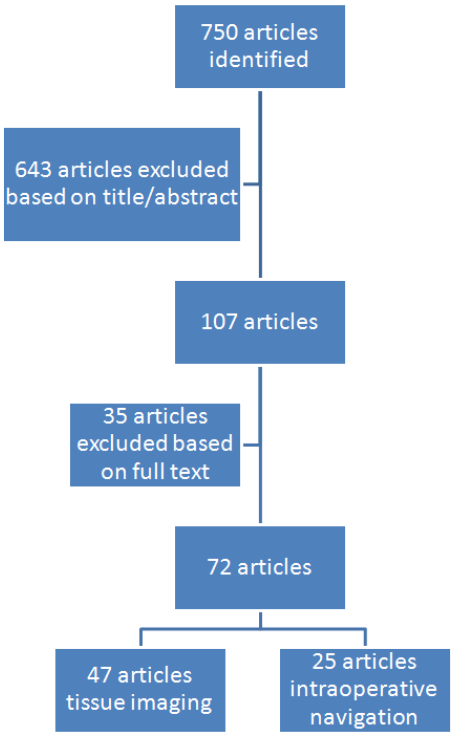

Figure 2.1 Flowchart showing the selection of relevant articles for the literature review

2.3.1 Optical imaging

Microscopic fluorescence imaging

Use of CLE has been shown to enable visualisation of liver anatomy and physiology at a microscopic level, with a lateral resolution ranging between 0.7-3.5µm and a maximum imaging depth of 0-350µm (147,175). Some systems allow the user to adjust the imaging depth which raises the potential for 3D reconstruction of tissue volumes (146). This imaging modality has previously been termed" virtual histology" due to its ability to not only visualise liver lobules, microscopic vasculature and bile ducts but also individual hepatocytes and stroma cells. In addition to static histological details, physiological parameters such as blood flow velocity and cell apoptosis have also be observed (176,177). Large animal studies have demonstrated the feasibility of laparoscopic use (148,149). One group has employed CLE imaging in the near-infrared (NIR) and blue light spectrum during mini-laparoscopy to

diagnose and quantify liver steatosis and cirrhosis in patients (Figure 2.2). Taking into account variations due to different imaging wavelengths and pathologies, a good diagnostic correlation with histopathology of 81-90% was demonstrated (177,178). The use of CLE for the clinical evaluation of hepato-biliary malignancy has until recently been restricted to endoscopic retrograde cholangio- pancreatography based diagnosis of biliary cancer (179).

The “Persee Project” aims to transfer this technology to a laparoscopic setting by demonstrating the use of CLE to diagnose malignancy on peritoneum, lymph nodes and abdominal organs including the liver (180,181).

To maximise the CLE’s real-time potential, this group uses an audio-visual conference with a pathologist which enables them to receive immediate feedback in-vivo images.

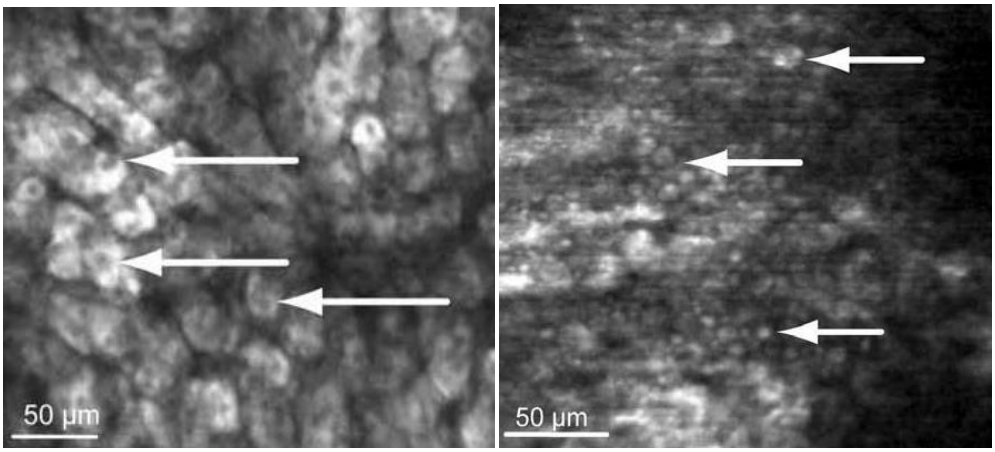

Figure 2.2 CLE visualisation of normal and steatotic liver.

a) normal hepatic architecture in healthy human liver, dark intracellular structures represent nuclei b) mixed micro & macrovesicular fat inclusions in liver steatosis (177)**. (reprinted with permission from Elsevier, copyright 2010)**

To achieve good quality images, a stable contact needs to be made with the tissue of interest, ideally at a 90˚ angle while exerting constant pressure to prevent slippage. Conversely excessive pressure may reduce microcirculation and thus impair fluorescence signals in some organs. To view larger areas of tissue, a smooth and finely controlled motion of the CLE probe tip has to be asserted. Addressing all these requirements during laparoscopy can be technically challenging (182). Robotic control of the CLE probe or the use of a modified intravascular steerable catheter, have been proposed as a possible solution to this issue (150,175). A further drawback of CLE is its small field of view which for flexible CLE probes rarely exceeds 600µm^2 (146,175). A technique called mosaicing can enhance the field of view by incorporating multiple adjacent images together into one larger image (175).

Of all the imaging modalities discussed in this review, CLE has the highest resolution and magnification, thus allowing visualisation of cellular and sub-cellular details. Another advantage is that a clinically licensed, commercial solution exists. Although licensing is currently restricted to luminal endoscopy, the probes can be sterilised to a surgical standard which makes a transfer to a laparoscopic application simple (150,183). The main challenge to laparoscopic application consists of providing a technical solution that will allow controlled and stable acquisition of images in a meaningful field of view and a reproducible method of objectively evaluating CLE images.

Wide field fluorescence imaging

One of the first groups to investigate wide field fluorescence imaging of the liver used a rabbit model to demonstrate that fluorescein conjugated bile acids elicit selective fluorescence in hepatocytes and bile ducts with the latter being easy to distinguish from blood vessels (151). A non-bolus injection of methylene blue reduces the risk of adverse events and in combination with ICG provides good delineation of bile duct anatomy in a porcine model. The drawback of using this combination of fluorophores is that repeat imaging is difficult because ICG causes strong and prolonged background fluorescence in the liver (184). For single fluorophore use, laparoscopic ICG-mediated fluorescence imaging (LIFI) has been investigated extensively in experimental and clinical studies. Its advantages are rapid hepatic uptake, exclusive biliary excretion and a good safety profile (151). ICG has been routinely used for decades to test the preoperative hepatic function (185). Due to its propensity of exhibiting residual fluorescence around hepatocellular cancer and liver metastasis for up to two weeks, any patient who underwent hepatic function testing can potentially undergo LIFI without requiring additional medication (133,152). The emission peak for ICG and methylene blue are in the near-infrared range around 800nm and 700nm wavelength respectively. In contrast the emission peak of fluorescein and its derivates is within the visible light spectrum at around 520nm.

To the best of our knowledge, only ICG has been studied clinically in the context of laparoscopic fluorescence imaging. So far four indications for its clinical application have been proposed, namely: the identification of liver malignancy, visualisation of bile ducts, delineation of liver segment borders, and as a test for bile leaks. ICG exhibits a selective uptake by hepatocytes which results in enhanced fluorescence throughout perfused liver tissue (159,186). Excretion into bile starts almost immediately and can last for up to 20 hours (187). It has been well documented however that this behaviour deviates in the presence of primary and secondary liver malignancy. Hepatocellular carcinoma can either appear as an area with globally increased fluorescence intensity or as a rim enhancing lesion (Figure 2.3). This phenomenon is thought to be related to the grade of malignant differentiation because high grade HCC cells can take up ICG via membrane transport proteins that are also found in normal hepatocytes but at the same time they cannot excrete ICG due to concomitant

biliary excretion disorders. In contrast to this finding, low grade HCC cells often seem to lack the required transport proteins to take up ICG and are therefore more likely to exhibit a rim enhancing fluorescence that is also seen with secondary liver metastasis (188). Rim enhancing type fluorescence (Figure 2.3) is purportedly caused by pressure induced biliary excretion disorders in normal hepatocytes that are adjacent to a liver lesion (189). Based on the knowledge of fluorescence patterns, liver lesions can be localised during LLR. In some cases this may reveal additional lesions which were not visualised on preoperative CT or LUS with subsequent implications on patient management (144,190). One study of 12 patients comparing preoperative CT and MRI and intraoperative LUS and LIFI reported that LIFI had the best sensitivity (190). Another potential benefit of this technique is the identification of malignancy on the background of altered liver tissue (e.g. previous RFA) which may be difficult to visualise on conventional white light laparoscopy (133). Sensitivity is probably related to distance from the surface and lesion size with smaller and deeper lesions being harder to detect. One group reported detection of lesions up to 8mm from the surface and down to a size of 3mm (152).

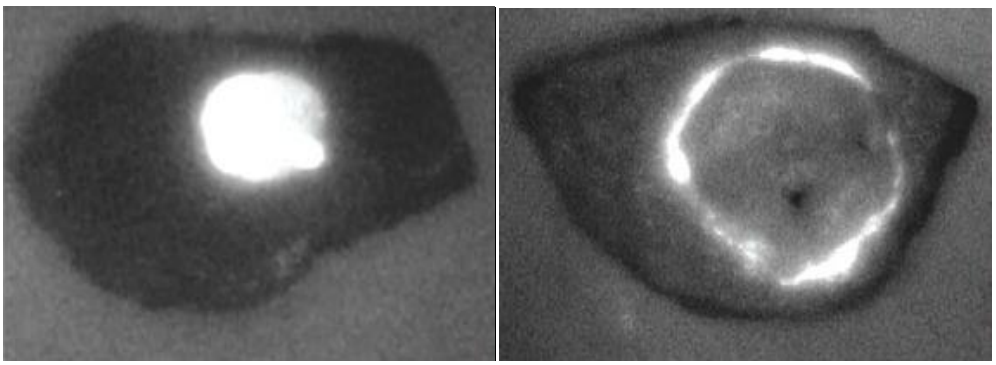

Figure 2.3 ICG fluorescence of HCC on LIFI.

a) HCC exhibiting fluorescence throughout the lesion b) HCC exhibiting rim enhancing fluorescence (189)**. (reprinted with CC BY-NC 4.0 from Wiley)**

Fluorescence based imaging of bile ducts has mainly been studied with the aim of delineating common bile duct (CBD) anatomy during laparoscopic cholecystectomies but its utility for LLR and laparoscopic liver cyst fenestration has also been investigated (191–194). During laparoscopic cyst fenestration bile ducts may be severely displaced secondary to cyst growth. Utilisation of fluorescence imaging enables visualisation of common bile duct (CBD), hepatic ducts and smaller bile ducts in the vicinity of liver cyst a feature which may aid surgeons in avoiding inadvertent injury to these structures. One group investigating ICG mediated fluorescence imaging in 24 patients undergoing LLR demonstrated that all surgically relevant bile ducts could be visualised. Because anatomical guidance can be provided in real-time throughout parenchymal transection, this modality may be more valuable for LLR than for laparoscopic cholecystectomy, where it is mainly employed prior to dissection (191).

Postoperative bile leak is a relatively common complication of liver resection and a cause of major morbidity. Detection of bile leaks with standard laparoscopy is difficult because bile is frequently mixed with blood, making its distinctive green-yellow colour harder to detect (195). To enhance detection of bile leaks one group injected diluted ICG into the cystic duct and observed any resulting signs of increased fluorescence at the liver resection surface. If leakage was observed an abdominal drain was placed in the proximity of the resection surface (196). Other groups advocated suture repair of detected bile leaks (197) or employed naso-biliary drains for injecting ICG into the biliary system. In contrast to radiographic cholangiography, ICG cholangiography may be more attractive because it saves time and does not carry a risk of bile duct injury secondary to insertion of a cholangiogram catheter (191).

Anatomical hepatic resection may offer advantages in terms of preserved hepatic volume and improved recurrence rates in HCC but is technically more challenging than carrying out atypical resections or major hepatectomies (73). LIFI has been proposed as a method of delineating liver segment anatomy intraoperatively. Fundamentally there are two different approaches called positive and negative staining which are respectively based on either increasing or decreasing fluorescence intensity in the segment of interest. Positive staining provides clearer delineation of segmental borders but is technically more challenging because it requires injection of ICG into the segmental portal vein branch (198). This may be facilitated by LUS probes that have a channel for guiding needle insertion (159,186). Alternatively, selective arterial cannulation of segmental branches via a percutaneous approach from the femoral artery may be an option for positive staining but this has so far only been demonstrated in an animal model (198). For negative staining protocols the segmental vessels are clamped and subsequently ICG is injected systemically which leads to strong fluorescence intensity in all remaining segments (159). Although methylene blue has historically been used for positive staining in open liver resection, it is less practical for laparoscopic surgery because simultaneous clamping of the segmental artery is required to avoid fluorophore washout (159).

An important technical consideration when employing LIFI is the time of systemic ICG injection because this will strongly impact on how fluorescence is observed. For visualisation of bile ducts and bile leaks an injection time of at least 20-30 minutes prior to imaging has been proposed (191) because ICG excretion into bile starts within minutes and peaks around two hours (133). As outlined above, fluorescence related to malignancy can be observed within a two week timeframe (133,152,197) but opinions about the optimal injection time vary between authors (133,144). Simultaneous imaging of biliary anatomy and liver malignancy is not feasible because ICG injections immediately before surgery can lead to high fluorescence intensity in both normal liver and tumours (133).

The concept of LIFI has become more user friendly over recent years with commercial products becoming widely available (144,152,193). One solution allows swift change

between standard white light and NIR fluoroscopy (144) whereas another system employs an overlay display function that integrates white light and NIR spectra into the same image (193,199). An important limitation to consider is that penetration depth is thought to be in the range of 5mm (144). Deeper lying lesions may be visualised but sensitivity is probably decreased (152).

Multispectral imaging

A variety of technical solutions has been developed to facilitate laparoscopic multispectral imaging (LMSI) of the liver, with no single system being popularised over another so far. One of the more complex approaches is the utilisation of a liquid crystal filter which offers a spectral range of 650-1100nm. In their study a principal component analysis was carried out to establish the variations in absorption profiles between the different anatomical structures in a porcine model. The bile duct for example exhibited absorption peaks that could be attributed to water and fat whereas in contrast the hepatic artery had absorption peaks attributed to oxygenated haemoglobin and water. With this information it was possible to enhance image contrasts based on the underlying chemical mixture thus enabling visualisation of hepatic artery, portal vein and common bile duct without prior dissection of the hepatoduodenal ligament (155). (Figure 2.4)

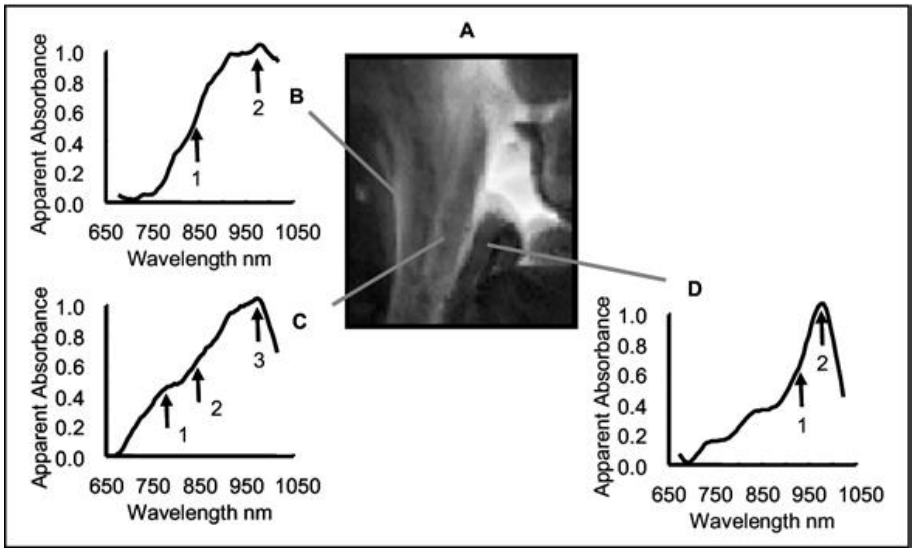

Figure 2.4 LMSI of the hepatoduodenal ligament in a porcine model.

The three different gray levels are based on specific absorption spectra for oxygenated haemoglobin in the hepatic artery (B - light); oxygenated and deoxygenated haemoglobin in the portal vein (C - gray); lipids and water in the common bile duct (D – dark) (200)**. (reprinted with permission from Elsevier, copyright 2008)**

Spectroscopic autofluorescence was successfully used in a patient to demarcate a recurrent HCC from surrounding cirrhotic liver tissue. Illumination in the blue spectrum was shown to

reveal decreased autofluorescence and haemoglobin associated absorption within the tumour (156). The detection of bile leaks may be facilitated by a commercial narrow band LMSI system focused at a single spectrum of 415-540nm. Bile may be difficult to detect because it is mixed with blood but at this spectrum red substances are filtered from view, a feature which enabled surgeon to clearly identify bile as yellow fluid (195). Away from classical areas of surgical therapy there has been interest in utilising laparoscopy for the diagnosis of chronic liver disease (177,178). One group has evaluated single fibre NIR spectroscopy to evaluate liver fibrosis using diffuse reflectance- and fluorescence spectroscopy in a laparoscopic rat model. In contrast to the other LMSI systems described above however a direct contact between probe and liver tissue is required. Higher levels of fluorescence and diffuse reflection were found to correlate with increasing levels of liver fibrosis with the latter parameter proving to be more effective. Fluorescence and diffuse reflection changes were hypothesised to be caused by alterations in NADH and elastin concentration and structural tissue changes respectively (160).

Enhanced white light vision

In an attempt to increase the field of view of a laparoscopic camera, one group reported on a custom made design which was characterised by a wide angle view endoscope system with two wedge prisms. This setup enabled visualisation of almost the entire liver surface in a single field of view during a porcine experiment (165). It was hypothesised that a larger field of view may result in improved visualisation within a confined surgical space.

Advances in optical technology are not limited to improving intraoperative imaging but instead can be employed to miniaturise laparoscopy systems which may positively impact on versatility, mobility and cost effectiveness. An article describing a system that integrated camera port, working port and laparoscopic monitor in one piece of equipment was previously published. In their article the authors described the feasibility of employing this single port, battery powered system for a liver biopsy in a large animal study.

In addition to decreased invasiveness, portability and lower costs, the system was claimed to have ergonomical advantages over conventional laparoscopic setups because it enabled in-line working by aligning monitor, surgical work space and instrument along the same axis (Figure 2.5) (166).

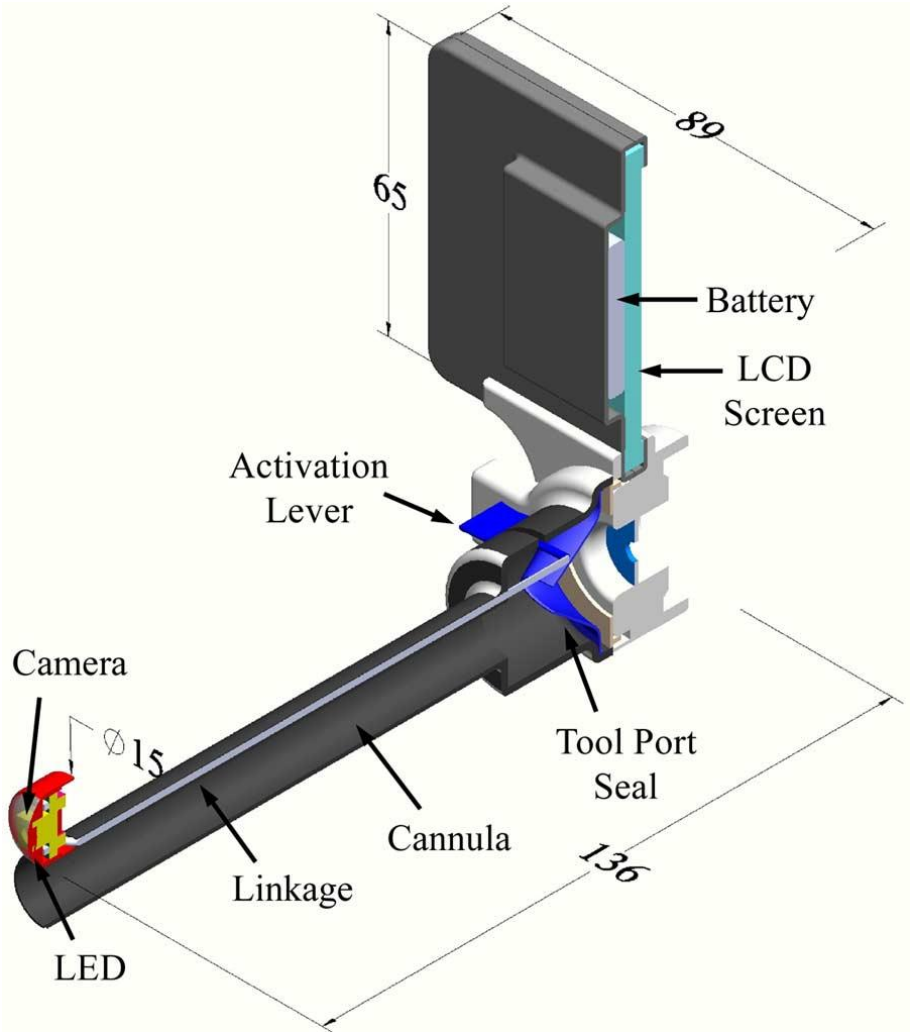

Figure 2.5 Amalgamation of laparoscopic- camera, port and monitor in a single piece of equipment (166)**. (reprinted with permission from IEEE, copyright 2010)**

The reports on 3D laparoscopy in liver surgery have been in the main, limited to case reports and case series which have studied its application to liver cyst excision, the Glissonian approach and to extended right donor hepatectomy (192,201,202). Anecdotally it was found that stereoscopic vision enhanced precision and speed of dissection. One of the authors hypothesised that 3D laparoscopy was particularly useful in advanced laparoscopic manoeuvres such as suturing and knot tying (202). In a recent case-control study a historic patient group of conventional LLR's was matched with LLR's that were carried out with the aid of a 3D laparoscope. In this article it was demonstrated that utilisation of 3D laparoscopy lead to significantly reduced operating times. No adverse effects on the surgeon were found and an influence of the learning curve effect was felt to be unlikely since all procedures were carried out by a single expert for laparoscopic liver surgery within a four year period (203). A summary of selected optical imaging modalities is shown in Table 2.1.

Technology	Application	Maturity	Resolution (max)	Imaging depth (max)
probe based confocal laser endomicroscopy	Diagnosis: malignancy; steatosis; fibrosis	clinical study	1024x1024	350µm
Wide field fluorescence	Locate: malignancy; bile leaks Visualise anatomy: Bile ducts; Liver segments	clinical licence	HD	≈5mm
Multispectral imaging	Locate: malignancy; bile leaks Visualise anatomy: Bile ducts; blood vessels Diagnosis: Fibrosis	preclinical study clinical licence (narrow band)	HD	≈5mm
3D laparoscopy	Reduce operating time Improve laparoscopic learning curve	clinical licence	HD	surface only

Table 2.1 Summary of selected optical imaging modalities.

2.3.2 Intraoperative image guidance

Intraoperative image guidance is based on three key components or processes which are: 1) 3D modelling and planning - to create a virtual representation of individual patient anatomy 2) registration and tracking - to align “virtual” and real anatomy and 3) Visualisation - to make the information interpretable to the surgeon. Optical technology mainly contributes to registration and tracking but in order to provide a comprehensive overview of intraoperative image guidance, the other two processes are covered here as well. The usefulness of intraoperative image guidance does heavily depend on the quality of the registration which can be expressed as accuracy. As an understanding of accuracy is essential for comparing the performance of different image guidance systems, the methodology for accuracy analysis and the accuracy results reported from relevant research groups are also highlighted in this section.

Registration

To facilitate registration it is necessary to obtain geometrical liver features during surgery that can be precisely aligned with corresponding features on the 3D model. These features may consist of only a handful of points or they may represent a complete surface representation of the liver (141). In optics or vision based IGS, an approach called surface reconstruction is used which entails the acquisition of intraoperative liver surface points

which are subsequently used to reconstruct geometrical features that will allow a registration to the preoperative 3D model (135).

Initial attempts at recording the liver surface where made with devices that use laser beams and their reflections to obtain the structure of solid objects. The basic structure of these devices is a source that emits laser beams which are reflected from the liver surface and a camera that records and measures the distances of the reflected beams (204). During robotic surgery in a porcine model, an IGS based on a laser range scanner (also called laser pointing endoscope) has demonstrated its capability of acquiring up to 50 surface points/cm^2 at a rate of 5-6 frames per second. One group demonstrated that these characteristics could be used to obtain live updates on liver deformation which facilitated subsequent overlay of a 3D model onto live video data (205). This approach has been successfully applied to a commercial IGS for open hepatic surgery (141) but because its bulky design seriously disadvantages laparoscopic deployment, no further studies on its use in LLR have been made for over a decade (206). Although this concept has recently been refined and employed in an ex-vivo study (127), it has not been applied to LLR in patients yet.

The visual assessment of the liver anatomy may be used as a simplistic but highly translatable method of surface reconstruction. This may be based on the subjective identification of corresponding anatomical liver landmarks which allows surgeons to manually align 3D model and *in situ* anatomy (207). For some IGS the registration can be done automatically with an algorithm that computes the optimal 3D model position by minimising the distance between *in situ* and virtual landmarks (143,171). In the latter studies an optically tracked stylus is used to assign a few landmarks per patient but this approach may also be employed to obtain several hundred landmarks in a dense area. This data can subsequently be transformed into a surface representation of the liver which enables a registration based on the alignment of surfaces instead of singular points (141).

The camera optics integrated within a laparoscope form the corner stone of any laparoscopic or robotic surgical procedure. It is therefore an attractive prospect to utilise computer vision techniques to facilitate surface reconstruction. Different methods have been proposed, but the only approach that has been investigate *in vivo*, makes use of a 3D camera also known as a stereoscope. This method also known as stereoscopic surface reconstruction (SSR) utilises the individual right and left video channels to triangulate points on the liver surface (Figure 2.6). These points are subsequently amalgamated together into a point cloud that represents the liver surface. A well established process called iterative closest point (ICP) matching is subsequently used to find the optimal alignment position between 3D model and intraoperative point clouds. Intensive research and development has matured SSR and ICP technology to a stage where it can be applied to laparoscopic video feeds in real-time (208). Stereoscopic camera systems are an essential component of SSR and have been first introduced to the field of minimally invasive surgery with the arrival of the DaVinci™ surgical robot (135). Because SSR can be adapted to work with any type of

stereoscope, it is anticipated that the more recent commercialisation of high definition 3D laparoscopes (129) will make this form of IGS even more accessible to the surgical community.

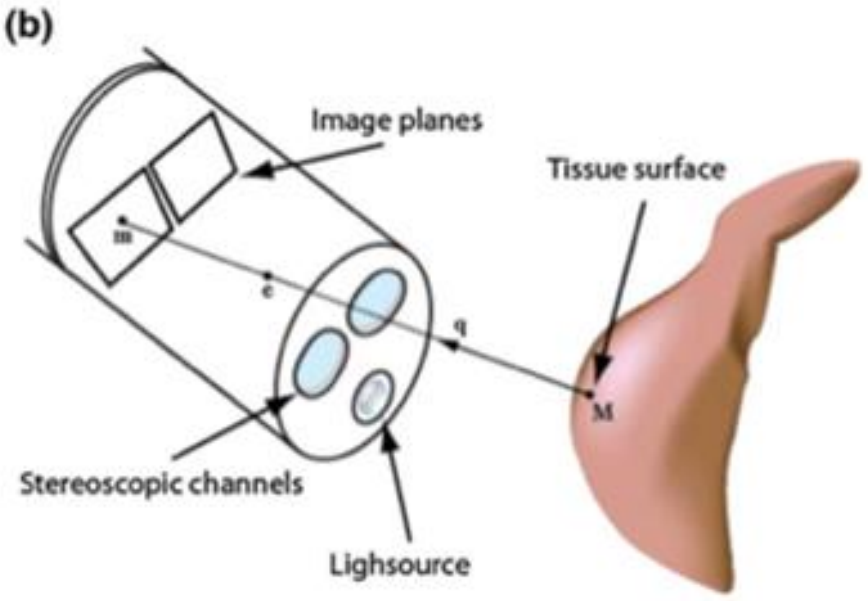

Figure 2.6 Principle of stereoscopic surface reconstruction.

Viewing the same point through two different spatially fixed video channels allows calculation of the point-to-camera distance (135)**. (reprinted with permission from Springer, copyright 2012)**

The first published report on SSR of the liver investigated a computational model of surgical liver deformation. In this first instance stereoscopic video data was retrieved and evaluated in a retrospective fashion (209). Real-time application of SSR was first reported in a porcine model with the aim of developing an AR environment that integrates LUS and 3D video images within the same display. The spatial correlation of LUS and video images was facilitated by employing optical tracking markers on a rigid LUS probe and a stereo-laparoscope (210).

Tracking

It has been purported that factors contributing to poor registration are inaccuracies secondary to tracking, internal camera configuration, organ motion and soft tissue deformation (211). Errors from optical tracking are minimal (210) but this modality requires a free line of sight which is not always achievable during surgery and can only be used in conjunction with rigid instruments or cameras. Electromagnetic tracking does not suffer from this restriction but it is more difficult to implement as a tracking sensor has to be integrated in the tip of the camera. A novel approach to tracking uses an ICP matching based technique.

With the aid of a stereo-laparoscope, an intraoperative liver surface point cloud is matched to the most likely corresponding locations on a point cloud from the preoperative 3D model. Because specific video frames and point cloud locations are co-registered, it is possible to estimate the laparoscope position in relation to the 3D model. This method currently has only been functional for static scenes and furthermore it has been shown that ICP tracking is inferior to optical tracking or a combination of ICP and optical tracking which achieved the best results (129). A robust calibration process is used to adjust the IGS to negate errors caused by the internal camera optics configuration.

Imaging accuracy

Although the number of reports on new methods to image guided surgery in LLR has significantly increased over the last few years, many groups have only presented minimal data on imaging accuracy or completely neglected this aspect (143,171,212). Accuracy also called the target registration error (TRE) and stated in millimetre (mm) is a measure of how well the 3D model represents *in-vivo* anatomy. There is no consensus on what the limits for an acceptable TRE are but it has been advocated that it should be guided by surgical need. Some authors have purported that a TRE of 3-5mm is sufficient but it is crucial to verify this assumption in clinical practice (213,214).

It is however important to consider that if a TRE for a certain IGS is known than this will give the surgeon the opportunity to increase his resection margin based on this knowledge. For other, less forgiving IGS applications such as intracranial surgery a TRE of several mm would be less acceptable (141). The methodology of TRE assessment employed by different groups has varied widely. In one approach used for VR based IGS, the geometrical constellation of intraoperatively acquired anatomical landmarks (141,171,215) or mesh of surface points (141,206) is compared to the constellation on the 3D model. This method does not actually analyse discrepancies of spatial coordinates between the *in-situ* and virtual space but rather analyses each space individually. As such it can perhaps be regarded as a reflection of intraoperative soft tissue deformation rather than an absolute measure of accuracy. In AR based IGS, accuracy assessment appears more intuitive as it can be subjectively appreciated subjectively when viewing the discrepancy between laparoscopic view and superimposed 3D model. For objective TRE evaluation one group has proposed to measure the distance between corresponding landmarks on the laparoscopic view and the 3D model, using a mesh of points that represent the liver surface *in-situ* (174,216). In this scenario the position of landmarks on the laparoscopic video can be regarded as the gold standard because without a measurable TRE both the real organ and 3D model should match each other perfectly. A better gold standard maybe provided by direct comparison to intraoperative surface points that are obtained via a CT scan or a laser range scanner. The validity of this method has been a demonstrated by different groups but due to the practicalities and ethical implications of employing either modality in patients this approach

has so far been restricted to large animal and ex-vivo experiments (216,217). Laparoscopic ultrasound may also be used in a similar fashion (210,218) but this has proven a less popular method because LUS is more suited to visualise deep lying structures than to the recording of surface points or landmarks. An overview of the accuracy performance that has been reported in the literature is given in Table 2.2. It is important to note that different methods of TRE evaluation have been used by each group and therefore the stated values are not comparable.

Group	Mean TRE in mm	Reconstruction method	Maturity
Hayashibe et al. 2006	1.0-1.5	Laser range scanner	Preclinical study
Kingham et al. 2013	5.0	Tracked probe	Clinical study
Kang et al. 2014	3.0	LUS on 3D video	Preclinical study
Pessaux et al. 2014	2.0	manual alignment	Clinical study
Reichard et al. 2016	13	SSR	Preclinical study
Plantefeve et al. 2016	<3	SSR	Clinical data

Table 2.2 Listed are published TRE's for IGS studied in the context of LLS.

Due to significant variation in the methodology of TRE calculation the measures cannot be compared to each other. If several publications exist from the same group, then only the most recent TRE are stated.

Soft tissue deformation

Compared to tracking and calibration, inaccuracies related to organ- shift and deformation are thought to be more problematic and are harder to address. Liver shift is caused mainly by diaphragmatic and cardiac motion whereas liver deformation is mainly caused by surgical manipulation and increased intraabdominal pressure secondary to pneumoperitoneum (172,216). Although computational algorithms with the capability of simulating liver shift and deformation have been successfully applied to ex-vivo experiments and retrospectively to laparoscopic video, a functional real-time implementation has so far proved elusive (174,216,219). For this reason clinical IGS applications have relied on rigid (141,171,220) or one-off deformable 3D models (221).

This figures show that considerable more research efforts are required to offer excellent and reproducible accuracy in the area of 3-5mm. Only one group has reported TRE's in patients undergoing LLR with values of app 10mm RMS. While this may be sufficient for improving

better intraoperative orientation it is not comparable to precise surgical navigation that can be achieved in rigid compartments such as during intracranial surgery.

Display

Different methods of displaying data during surgery have been described in the past but in the main they can be categorised as either virtual reality or augmented reality displays which either shows a standalone 3D model or a composite image of 3D model and real world, respectively (Fig. 2.7). Virtual reality configurations make use of two monitors that provide the laparoscopic view and 3D model view side-by-side. A tracked object such as an ablation probe or surgical instrument is visualised simultaneously in both screens to facilitate intraoperative image guidance (141,171,218,222). Augmented reality displays can be achieved through a variety of methods including a robotic binocular camera a 3D screen or a standard 2D screen (143,210).

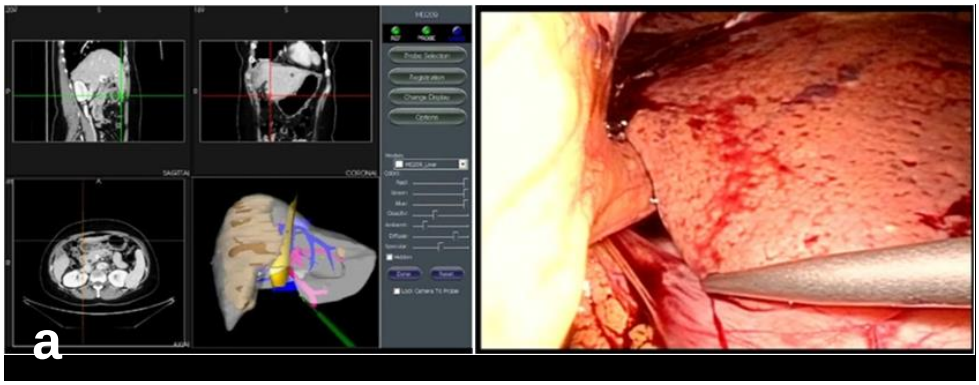

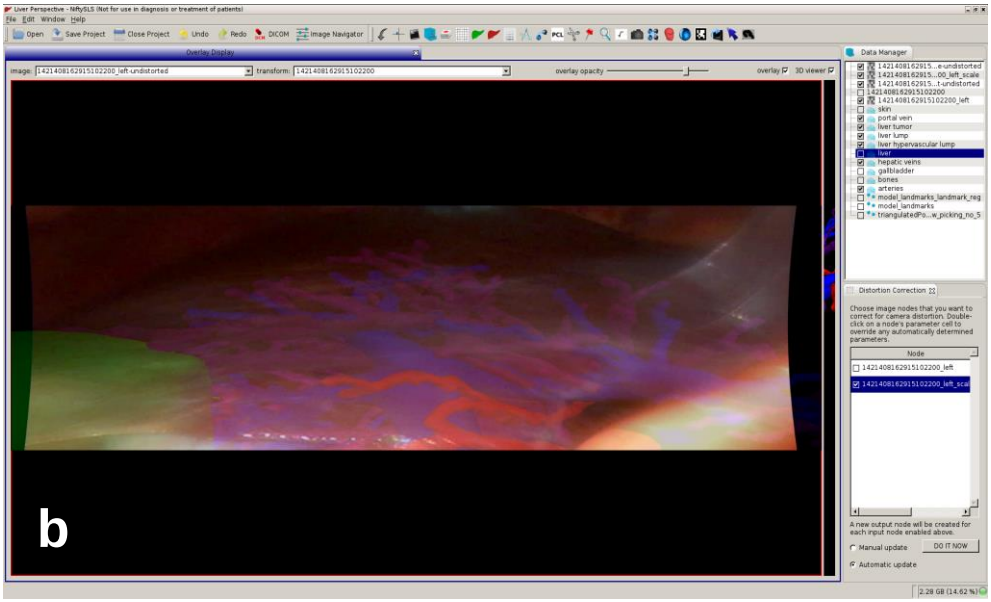

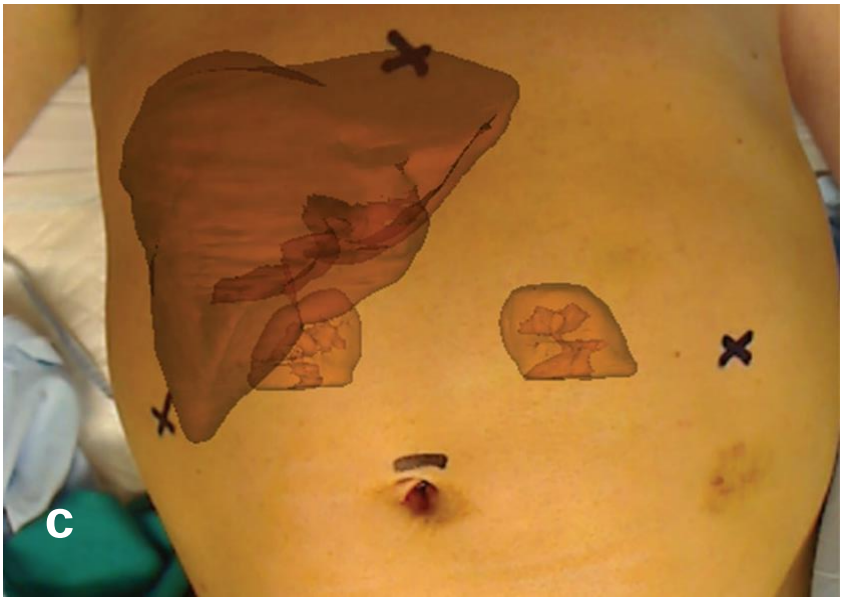

2.7 Comparison of different IGS display methods.

a) **VR display showing 3D model and operative site in parallel b) AR display showing an overlay of 3D model onto the operative site c) Projector display using a beamer projection of a 3D liver model onto the skin** (211)**.**

(reprinted with permission from a- Springer, copyright 2013; b - with CC BY-NC 4.0 from Hindawi)

An alternative screen-less application for an AR overlay display has been proposed by several groups that investigated its utility in guiding laparoscopic port placement. The correct placement of ports is crucial to facilitate good hand-eye coordination and economy of movement during laparoscopic or robotic surgery. Patient obesity or positional changes caused by abdominal gas insufflation can make the estimation of the optimal port position difficult. To overcome this issue several groups have used a standard commercial beamer to project a 3D model of the intraabdominal compartment onto the patients skin prior to port insertion. Visual alignment of landmarks such as the umbilicus, the costal margin and the anterior superior iliac spine which are visible on preoperative scans and on physical examination or standard video, have been used for registration (211,221,223). It was demonstrated that using this method accuracy and variability of port placement could be improved by 33% and 63% respectively (211). Use of a beam projected 3D model for intraoperative guidance is not feasible because of the interference cause by ports, instruments, robotic arms and the uneven outline of the distended abdomen (223). The use of virtual reality head-mounted displays or glasses has been suggested as a further display option but up to date has not been evaluated in image guided LLS (128).

2.4. Discussion

In this review a number of optical technologies that can enhance the sense of vision and orientation during laparoscopic liver surgery have been evaluated. The employed selection criteria ensured that all modalities are non-invasive, have been evaluated *in-vivo* and if required can be used in conjunction with safe and clinically licensed fluorophores. This combination of factors means that clinical translation should not be greatly impeded by concerns about safety of intraoperative use.

Although they all rely on functions of light, their distinct properties make them useful for a variety of different applications. Microscopic tissue examination during LLR using confocal laser endomicroscopy (CLE) for example has been shown to provide real-time histological evaluation. Concerns about the training required to properly interpret microscopic images may be addressed by establishing live video links with trained histopathologists (150). Due to the small field of view it is challenging to examine larger areas of tissue (175) and therefore this modality may be better suited to investigate or confirm the histological nature of small and well defined areas of interest that have been previously identified with other imaging techniques.

One potential option for “screening” the liver surface for areas that warrant a closer microscopic examination is the use of laparoscopic ICG based fluorescence imaging (LIFI). It has been shown that this imaging modality can identify superficial liver lesions that have not been detected on preoperative scans or laparoscopic ultrasound (144,199). There

appears to be a correlation between the type of LIFI fluorescence and the nature of some liver lesion (188,189) but as this link as of yet lacks specificity, it appears to be justified to advocate a more detailed microscopic examination of suspicious areas. In addition to the detection of malignancy, LIFI has been employed in clinical studies to stain liver segments, visualise bile ducts and to detect bile leaks from the liver resection surface (196). Out of these three indications the detection of bile leaks seems to be the most widely applicable and straight forward to use as it is relevant for any type of resection and does not require prior identification of vascular branches as is the case for liver segment staining. Furthermore LIFI may allow visualisation of intra-parenchymal bile ducts which are close to the dissection plane but in the main this option appears to be most useful as an alternative approach to intraoperative cholangiography during cholecystectomy (191).

In parallel to LIFI, multispectral imaging appears to be an imaging modality that is well suited for the examination of macroscopic tissue areas and anatomical structures. Its advantage over wide field fluorescence techniques is that a plethora of endogenous tissue components can be visualised and therefore LMSI may be tailored to specific clinical areas of interest such as the evaluation of metabolic variations and histopathological changes over a wider area. This flexibility however comes at the expense of more complex imaging equipment and analysis algorithms, which is perhaps the reason why LMSI has not been clinically studied to the same extent as LIFI. Although different LMSI systems with fixed wavelength spectra have been successfully utilised in the diagnosis of liver fibrosis, HCC or bile leaks (156,160,195), it is conceivable that a system with an adjustable wavelength spectrum (200) will be more desirable for clinical use as it can be employed in a much broader context. The drawback of a LMSI system with an adjustable and broad wavelength spectrum however is, that it is technically more complex. For the purpose of imaging it is sufficient to utilise relative tissue component concentrations which are subsequently translated into colours, shades and contrast. Tissue components exhibit distinct absorption spectra which can be regarded as a relationship between light absorption and excitation wavelength. If the absorption spectrum for a specific tissue component such as lipids or oxygenated haemoglobin is known it is possible to calculate the absolute concentration of the substance (161,224). Although this approach has yet to be demonstrated on the liver in a laparoscopic setting, it presents, a potential opportunity for future research (162,225).

An inherent weakness of optical imaging is its lack of depth penetration which is ≈5mm in the NIR spectrum but may be less at other wavelengths (144). For this reason it is an attractive option to integrate it with other imaging modalities that offer good depth penetration such as CT, MRI or occasionally LUS. Within this context IGS for LLS represent an amalgamation of imaging techniques with the opportunity to combine the best of both worlds with excellent resolution, high specificity, non-invasiveness, portability, good update speed and miniaturised equipment being provided by optics whereas depth penetration and 3D reconstruction are provided by preoperative scans or LUS. The main aims of utilising IGS

during LLS are improved oncological safety and a reduced risk of vascular injury. Unfortunately the development of an IGS for LLS has been slow and although two commercial systems have been built for open liver surgery (67,226) there is no clinically licensed laparoscopic alternative yet. A variety of optical registration methods have been explored previously but SSR is currently the most widely studied approach. This method however requires a 3D laparoscope which at this time is significantly more expensive than comparable 2D equipment. As 3D technology becomes disseminated into the mainstream, prices for stereo-laparoscopes will likely decrease but nonetheless, if liver surface reconstruction based on other methods (e.g. shading and motion) becomes feasible in the future, then cheaper monocular scopes could be used instead (129,137). The way that IGS integrate image guidance information into the surgical workflow is crucial to harness maximal benefits. A number of options including beamer-projection, VR and AR displays have been shown to be feasible. More recently however AR based displays have been more frequently represented in research efforts and on balance this display method would appear to be more intuitive to use (216,220,227).

Alternative registration methods for LLS that have been studied *in*-vivo include cone beam CT (CBCT), MRI and LUS. One clinical team utilised repeated CBCT registration in conjunction with a 3D model from a preoperative MRI scan to carry out an image guided HCC resection in segment 7. No accuracy measurements for the *in-vivo* case were reported but the authors felt that CBCT image guidance was useful for complex resections. Despite having been established as an essential tool for image guidance in endovascular surgery, CBCT suffers from several disadvantages including a low resolution, ionising radiation, high costs, lack of portability and an inability to allow spatial correlation between instruments and 3D model in real time (228,229). With the exception of ionising radiation and low resolution, MRI based IGS do share most of the shortcomings of their CBCT based IGS with costs being an even more relevant factor. MRI also has a slower image acquisition than CBCT but the most significant obstacle to utilising it for image guidance during laparoscopy is its incompatibility with metallic equipment. This restriction makes the use of custom built metal free surgical equipment mandatory (230,231). In contrast to MRI and CBCT, LUS shares many practical characteristics with optical image guidance such as portability, miniaturisation potential, relatively low costs and good registration update speed. The main differences are that LUS offers better depth penetration whereas optical imaging has a higher specificity (232). Another issue with LUS is that positional tracking of flexible LUS probes is difficult and has yet to be applied in clinical studies (233). LUS acquired images can be integrated into a 3D model or projected onto the laparoscopic video stream (234,235) but this data may also be employed as a method of registration. One group demonstrated how LUS could be utilised to reconstruct the highly individual pattern of hepatic vasculature which was then subsequently registered to the corresponding vascular pattern on a 3D liver model (236). It remains to be seen whether LUS or optics based registration will prove to more

advantageous during LLR and perhaps there may be a benefits to combining aspects of both methods.

There are various reports on the utilisation of modern 3D laparoscopy systems for laparoscopic surgery but experience in LLS is limited (237–239). Results from a cohort study hint towards shorter operating times and it was hypothesised that 3D laparoscopy may flatten out the learning curve for “open surgeons” who embark on laparoscopic procedures. The authors of a case series suggested that stereoscopic vision is of particular benefit for complex laparoscopic manoeuvres such as suturing (202). These finding are supported by studies from other surgical specialties (237–239). In the cohort study however, all operations were carried out by a single laparoscopic expert and therefore further studies are warranted to evaluate how applicable these findings are to other surgical centres.

Due to the selection criteria applied in this review some promising imaging techniques that may become relevant for LLS in the near future were not mentioned. One such an example is photoacoustic imaging, a modality that uses ultrasound waves which are created by laser light induced excitation of tissue expansion and relaxation. This so called photoacoustic effect combines the best of both worlds, optical and acoustic imaging and thus can provide images with better specificity and penetration depth than ultrasound or optical imaging, respectively (232). The capability of photoacoustic imaging to identify liver fibrosis and steatosis has been demonstrated previously (240). When used in conjunction with ICG, PAI can been utilised to detect superficial CRLM and HCC tumours (241). The main hurdle for a laparoscopic application is the need for a miniaturised laparoscopic probe design that is capable of simultaneously delivering light and acquiring ultrasound waves (242). Another more recently developed technique is based on the processing of standard RGB video data, an approach that makes it innately attractive for laparoscopic imaging. Video magnification for example utilises computer algorithms to analyse imperceptible changes in video colour. These colour variations are subsequently enhanced to make them visible to the naked eye. The potential of this work was demonstrated on real life examples e.g. by visualising the percutaneous pulsation of the ulnar artery and the pulse dependent change of facial colour (136). In clinical research, video magnification has been proposed as a method to monitor the effectiveness of regional anaesthesia (243) and to localise blood vessels during minimal invasive kidney and prostate surgery (244,245). Analysis of colour variation can be expanded onto stereoscopic video which has the advantage of enabling estimation of tissue haemoglobin concentration and oxygen saturation in near real-time (246).

In conclusion there are a number of optical imaging techniques available that can enhance surgical sensing by enabling different degrees of tissue examination or intraoperative image guidance during LLS. The individual strengths, limitations and outstanding development needs for each imaging modality were highlighted in this review. Despite the specific nature of development needs there are perhaps three key areas that warrant focus for future research which are: standardisation, integration and clinical translation. To allow effective

comparison and evaluation of potential clinical benefit a standardised image acquisition and interpretation approach in tissue examination and a consensus on the evaluation of accuracy in IGS studies would appear to be beneficial. The diversity of available optical technologies and their respective indications seems extensive but it is perhaps useful to take a more holistic approach and analyse how individual modalities could supplement each other to improve laparoscopic “sensing”. One existing example is how stereoscopic vision is used to facilitate surface reconstruction in SSR. The feasibility of integrating co-registered LUS images into AR based IGS has already been demonstrated (210,236) and it is conceivable that this approach can be replicated for optical modalities such as CLE or MIS. Ultimately any advances in optics based tissue examination and laparoscopic image guidance should focus on improving patient outcomes and safety by enhancing the surgeon’s perception and awareness of the intraoperative field.

3. General methods

3.1. Confocal laser endomicroscopy

The ability of confocal laser microscopy to discriminate between normal (i.e. healthy) and pathological liver tissue was explored in two separate animal models. Initially a murine model was used to look at discrimination between normal and cancerous tissue. Subsequently a porcine mode was employed to evaluate discrimination between normal and ablated liver tissue. In addition this model was also thought to reflect realistic conditions of laparoscopic surgery that would be encountered in a clinical scenario. Because the same system was utilised for murine and porcine experiments, a general description of the technology and equipment is given first before the specifics of each model are outlined.

3.1.1 General description of confocal laser endomicroscopy

Confocal laser endomicroscopy (CLE) is a novel optical imaging technology that enables accurate microscopic assessment of in-vivo histopathology. Its utilisation in a variety of experimental and clinical scenarios has been increasingly reported. CLE utilises a fibre optic element as its objective lens, allowing confocal microscopy with a micron-scale resolution that enables visualisation of sub-cellular details using endogenous or exogenous fluorescence. Exogenous fluorescence is provided by fluorescent dyes which can be applied in a systemic (e.g. intravenous) or topical fashion and are commonly referred to as fluorophores. They enhance CLE image contrast by absorbing and emitting light at wavelengths that are specific for each individual agent and circumstance (146,247).

CLE during laparoscopy or NOTES (Natural Orifice Transluminal Endoscopic Surgery) has been performed either with a rigid endomicroscope which contains the scanning optics in its tip (146) or with a slim, flexible optical fibre bundle which transmits light signals to laser scanning equipment situated at the far (e.g. extra-corporeal) end of the intrusive fibre (177,248). An example for a fibre based CLE system is Cellvizio™ (Mauna Kea Technologies, Paris, France) which is CE-marked for clinical use in luminal endoscopy and can be operated with probes that have a diameter range of 0.3-4.5mm. During endoscopy, Cellvizio™ can reveal histopathological cellular changes and has been shown to enhance accuracy in the diagnosis of malignancy and dysplasia (146,249).

3.1.2 CLE Equipment

Experiments were performed sequentially in a “dual wave length approach” using both 488nm (blue) and 660nm (red) laser lines which were connected to separate CLE imaging systems (Cellvizio™ 488nm & Cellvizio™ 660nm, Mauna Kea Technologies, Paris). For CLE image acquisition 0.5-1.5mm, flexible confocal probes (MiniZ, Ultra MiniO and S1500, Mauna Kea Technologies, Paris, France) were used, all compatible with conventional endoscopic instrument channels. The CLE imaging systems control laser illumination and fibre scanning, delivering12 frames per second which enables near real-time image

acquisition. Images at different wavelengths were recorded “in turn”, meaning without parallel co-registration of the red- and blue-light laser systems. Imaging parameters were probe dependent with 1.4-3.5µm lateral resolution, 10-30µm axial resolution, 0-70µm imaging depth and a 240-600µm² fields of view.

3.1.3 Murine experiments

A murine model of colorectal cancer liver metastasis was evaluated to study the ability of CLE to distinguish between normal and cancerous tissue.

3.1.3.1 Orthotopic murine model of colorectal cancer liver metastasis

The human colorectal carcinoma cell line SW1222 was cultured under aseptic technique in Dulbecco’s Modified Eagles Medium containing 5mM L-glutamine and 10% v/v Foetal bovine serum. All animal studies were conducted in accordance with UK home office regulations and the guidelines for the welfare and use of animals in cancer research. The liver metastasis model used has been previously described (250). Briefly, eight (n=8) MF1 *nu/nu* mice (female, 6-8 weeks old, 25-30g) underwent a laparotomy in order to directly inject $1x10^6$ cells in to the spleen. Splenectomy was performed after 5 minutes to stop formation of a primary tumour at the site of injection, with cells that had been carried by the blood flow through to the liver forming the solid tumours of the metastatic model. At conclusion of the procedure the laparotomy incision was closed and animals were recovered. In the described animal model, female mice are exclusively used due to their better compliance. Liver tumour maturation took between 5-6 weeks. The progression of metastatic disease was monitored once per week with non-invasive magnetic resonance imaging under general anaesthesia. The evolving disease pattern showed a heterogeneous distribution of distinct solid tumour nodules of varying sizes (app. 2-12mm) throughout the lobes of the liver. Typically disease burden comprised of 10-20 tumour nodules that could be visualised on magnetic resonance imaging.

3.1.3.2 CLE Image acquisition murine model

A transverse laparotomy was carried out under general anaesthesia to allow unrestricted access to the liver. CLE imaging at 488nm and 660nm was performed with two different CLE imaging stacks with separate laser scanning units, probes and image processing computers. Both systems were initialised and calibrated at the start of each experiment. Switching between wavelengths simply required imaging probes to be swapped over. Due to the inability of CLE to visualise tissues beyond 100µm depth, images were exclusively acquired from superficial tissue, while the probes were manually maintained in contact with the liver surface. Images were acquired with the Z-probe at 488nm and the miniZ probe at 660nm wavelength. Probe characteristics were the following: probe diameter 18 or 9.4mm; lateral resolution 3.9µm, axial resolution 44 or 13µm, working distance 80 or 65µm, maximal field of view 426x302µm or 323x323µm.for the Z probe or mini-Z probe, respectively.

The liver was macroscopically categorised into normal and cancerous tissue areas based on its respective brown or white appearance. This approach was made possible by the radically different appearance of normal liver vs. CRLM. No attempt was made to identify microscopic disease because the aim was to establish reproducible CLE criteria of CRLM which could then be translated to the detection of microscopic disease in future studies. Baseline CLE images were recorded over a representative area prior to fluorophore administration. To provide exogenous fluorescence for CLE imaging at 488nm and 660nm excitation, fluorescein sodium (molecular weight 376.27g/mol – henceforth called “fluorescein”) and ICG (molecular weight 774.96g/mol) were mixed with 0.9% sodium chloride or 5% dextrose respectively. Subsequently, fluorescein (4-7mg/kg) and indocyanine green (0.3-0.5mg/kg) were sequentially injected into the tail vein with a delay of 20-40 minutes between injections to allow adequate time for imaging. In preliminary experiments it was confirmed that neither fluorescein nor ICG elicited unintentional “cross”-fluorescence signals.

An initial image sequence of 1-3 minutes was recorded to monitor and confirm distribution of the fluorophores in the liver. Several short sequences ranging from 10-20s were taken from normal and malignant tissue in different locations. It was not possible to co-register tissue areas between 488nm and 660nm CLE imaging. But due to the relatively small size of mouse livers it was hypothesised that approximately the same areas were imaged at both wavelength. For statistical analysis which is described below, all values for individual animals were pooled into one group and hence co-registration is less relevant than for the visual comparison of image features. The mean fluorescence values for each image frame from these sequences were subsequently analysed.

3.1.3.3 Preparation and examination of murine liver tissue samples

Following termination of the animals, the livers were resected, fixed in 10% formalin and embedded in paraffin blocks. Tissue samples were sliced at 4µm thickness with a microtome and sections mounted on glass slides. The presence of colorectal cancer metastases was confirmed by using a standard structural Haematoxylin and Eosin stain. Because areas of normal liver and CRLM in this disease model looked radically different, histological examination enabled us to confirm infiltration of adenocarcinoma cells in representative liver areas which previously underwent CLE *in-vivo* examination.

3.1.3.4 Statistical analysis of murine CLE data

Cellvizio™ is packaged with image analysis software (Imagecell™) that records and displays basic values termed relative fluorescence units (RFU), from which the maximum, minimum, median and mean were calculated and exported for each image frame. Relative fluorescence units are based on a reconstruction of single fibre fluorescence intensity at a given point in time. A number of factors such as fibre injection rate, fibre collection rate, fibre auto-fluorescence, biological sample fluorescence and laser source intensity influence fluorescence intensity. These variables are factors in an equation that allows the real time reconstruction of fluorescence intensity in individual fibres each of which corresponds to an

image pixel of the CLE image. A detailed description of the equation and other relevant methodology has been published previously (251). At the start of each imaging session a calibration is carried out using solution that provides a uniform value of background fluorescence. The calibration procedure results in homogenisation of the individual probe fibres to give them uniform detection sensitivity (which corresponds to a measured light intensity) (252). This process enables comparison of fluorescence values between individual fibres (i.e. pixels) of the probe, for a given calibration. However, whilst the absolute background fluorescence value in the calibration solution is uniform it may change between repeated calibrations and different solution containers, meaning that fluorescence units have to be regarded as relative, as opposed to absolute values. Thus, imaging data were only compared within the same animal.

Negative RFU values either correspond to image noise or can be caused by a reduction in fibre autofluorescence due to prolonged illumination. To avoid misinterpretation, negative RFU values were thresholded at zero. All RFU values underwent a square root transformation to reduce data skew and kurtosis.

Routine statistical comparison e.g. by paired Wilcoxon rank sum test (individual animal paired with RFU) was not possible due to specific constraints of the acquired data which were: 1) unequal number of frame counts for normal and CRLM tissue and 2) potential introduction of a repeat sampling error. These circumstances lead us to choose a generalised linear mixed model (GLIMMIX) analysis which can accommodate for the described data constraints by estimating the interaction of fixed and random effects.

Fixed effects in GLIMMIX work in analogy to a regular linear or logistic regression analysis in that a covariate (e.g. age) is assigned a fixed coefficient that determines its impact on the dependent or response variable(e.g. morbidity) in the statistical model. A random effect in contrast to this can have different coefficients that are depending on a subgroup (e.g. ward on hospital) within a dataset. Combination of fixed and random effects may allow elucidation of a better statistical model fit in some circumstances. The difference between linear mixed models and generalised linear mixed models is that the relationship between the dependent variable and the effect terms is non-linear. This non-linearity is expressed via a link function which utilises a transformation (e.g. logit, probit, gaussian) between the effect terms and dependents in the equation. For the data in this study for example a binominal distribution with a logit link function was used to conduct the GLIMMIX analysis.

The GLIMMIX analysis enabled modelling of the probability of the acquired images corresponding to normal liver parenchyma. The measured RFU value and animal ID were set up as fixed effect and random effect for this model, respectively.

Different estimation methods such as Pseudo Likelihood, Laplace and Gauss-Hermite quadrature can be used for GLIMMIX analysis. For the purpose of this study, the Laplace method was chosen because it exhibited satisfactory convergence and the best fit characteristics as assessed by Akaike information criterion (AIC). GLIMMIX analysis results are given as the change in odds ratio for an increase in RFU at a standardised value. For example, an odds ratio of 2 at a standardised RFU increase of 100 to 101 means that the odds ratio of liver parenchyma being normal increases by 2 if the RFU value increased by one from 100 to 101.

To test the validity of the GLIMMIX model resulting from the study data, a ROC analysis was performed. The covariates and intercepts provided by the GLIMMIX analysis were used to calculate the log odds, odds and finally the probability of identifying normal liver tissue. Each single probability value corresponded to a single observation (mean RFU per frame), a specific animal ID and a tissue type which enabled us to perform a ROC analysis based on this data. Because animal ID was a random effect due to the difference in probe calibrations between experiments, the same RFU value would result in different probability values for individual animals.

To determine if a probability based threshold value could be used to distinguish between normal and malignant tissue random sample cross validation was carried out. To this end, all observations were randomised into a training and a validation dataset. The training set was used to build a GLIMMIX prediction model whose output subsequently underwent ROC analysis. A threshold value with an optimal sensitivity and specificity for identifying normal liver tissue was then chosen from the ROC curve coordinates. This threshold probability value was subsequently applied to the validation set, to evaluate its performance in distinguishing between normal and malignant liver tissue and calculate the resulting sensitivity, specificity and accuracy for this test.

An estimation of erythrocyte flow velocity calculated from the available image data was also carried out. To calculate flow velocity (in mm/s), the distance travelled by a single erythrocytes in the time period between two image frames (=41.7ms at 24 frames per second) was measured. Depending on the amount of available data, 5-10 individual erythrocytes were assessed per tissue type and animal ID.

Statistically significant differences were assumed if $p<0.05$. Statistical analysis was performed using SPSS™ Version 21 (IBM, Armonk, NY, USA) with exception of the GLIMMIX analysis which was carried out with SAS™ Version 9.4 (SAS Institute, Cary, NC,

USA). Quantitative data (RFU and erythrocyte flow velocity) is given as median and interquartile range. Odds ratios are stated together with their 95% confidence intervals (CI).

The author of this thesis was not involved in: establishing the animal model, pre-operative imaging (to confirm cancer seeding) or in the operative procedure required for image acquisition or preparation of histology. The author did help with CLE image acquisition itself and performed subsequent image analysis and data evaluation.

3.1.4 Porcine experiments

A porcine model of laparoscopic liver resection and liver ablation was used to study the CLE imaging characteristics of normal and ablated liver tissue and assess the feasibility of using this imaging modality during laparoscopy. These experiments were conducted as part of a series of experiments that in addition to CLE also evaluated an image guidance system and video magnification studies (see below). Establishing the model and image data acquisition was done on separate days to accommodate requirements for the image guidance experiments. To illustrate this, a detailed description of the experimental steps involved is given below.

3.1.4.1 Porcine model of laparoscopic liver surgery

3.1.4.1.1. Sequence of events

The experimental flow of the model is listed below, sequentially:

Laparoscopic microwave ablation – OP1.

Recovery period of 7 to 10 days.

Laparoscopic CLE image acquisition (following laparoscopic liver resection in 2 cases) and intraoperative image guidance experiments OP2.

Post mortem liver biopsies.

3.1.4.1.2. Study animals

Following approval by the local animal ethics committee, experiments were performed at Northwick Park Institute for Medical Research (London). A total of 4 female landrace mini-pigs with a bodyweight ranging between 50-80kg were studied. Following best practice husbandry, the animals were acclimatised to their surroundings with free access to food and water at least one week prior to experiments. To avoid intestinal distension animals were fasted 24 hours prior to surgery but continued to have access to water. Each animal underwent two procedures under general anaesthesia on separate days with a 7-10 day recovery period in between. On the first procedure, laparoscopic liver ablation zones were produced (Medical microwave systems research group, Bangor University, UK). During the second procedure CLE images, intraoperative image guidance data and liver biopsies were obtained. In two animals a laparoscopic left hemi-hepatectomy was carried out to simulate intraoperative conditions and to allow CLE examination of the surgical resection margin.

3.1.4.1.3. Preparation and Anaesthesia

Following best practice animal husbandry, the mini-pigs were acclimatised to their surroundings with free access to food and water at least one week prior to experiments. To avoid intestinal distension animals were fasted 24 hours prior to surgery but had continual access to water. Oral endotracheal intubation facilitated general anaesthesia with 2% Isoflurane in oxygen in a recovery (ablation) or non-recovery (CLE imaging and

intraoperative image guidance) algorithm with 200mg Pentobarbitone euthanasia at termination of surgery. Orogastric intubation decompressed the stomach during laparoscopy. All procedures were carried out with the animals in a supine position.

3.1.4.1.4. Liver ablation

Thermal ablation of the liver was carried out to create an experimental model that supported two different experimental designs. Firstly microscopic imaging using CLE was carried out with the aim of studying ablation induced changes on a cellular level. Secondly intraoperative image guidance experiments using an image guidance system were performed where ablation zones were treated as substitutes for liver tumours. The simulation of liver tumours was necessary because there is no suitable porcine model of liver malignancy and research towards such a model has so far not produced any convincing results (253). The ablated liver lesions could be visualised by a CT scan and therefore they could be subsequently incorporated into a 3D liver model.

Laparoscopic liver ablation was performed under general anaesthetic on OP1. Sterile conditions were created by cleaning the abdominal wall with Chlorhexidine solution and placement of sterile operating drapes. To facilitate laparoscopy, a pneumoperitoneum was established using port insertion under direct vision. A periumbilical 10mm port was used for the laparoscopic Viking 3DHD Visions System™ (Viking Systems, Inc., Westborough, MA, USA) with one additional 5mm port inserted in the right subcostal region to facilitate microwave liver ablation. Liver ablation was performed using a custom made microwave ablation system (Medical microwave systems research group, Bangor University, UK). The ablation probe was inserted through the anterior surface of the liver with the utmost caution to avoid injury to organs lying behind the liver. Due to the relative thinness of the porcine liver this step can be technically challenging. Ablation zones of approximately 1cm were created at different locations in the liver. Number of ablations ranged between 3-6, with care being taken to ensure a sufficient distance between ablations. This was necessary so that they could be individually distinguished on CT. If lesions were too close together they would erroneously be displayed as one lesion on CT. Because a number of lesions were induced superficially, they had the benefit of functioning as additional anatomical landmarks which was an important feature in the determination of IGS accuracy as described below. After completion of ablation the abdominal cavity was examined for any signs of inadvertent organ injury. Laparoscopic ports were left in-situ while the pig was moved to the CT scanner still under general anaesthesia. On return from the CT scanner ports were removed and the fascia closed with 1-0 Vicryl at the periumbilical port-site. Skin incisions were closed with 3-0 Vicryl and subsequently all port sites were dressed. The animals were woken up, extubated and returned to postoperative intensive monitoring.

3.1.4.1.5. Operative technique

Pneumoperitoneum was established using either the Veress technique or port insertion under direct vision. A periumbilical 10mm port was used for the laparoscopic camera with

additional 5mm and 12mm ports inserted in the right and left upper quadrants. For ablation, one additional 5mm port was inserted in the right subcostal region. Liver resection was performed using four ports in addition to the camera port; three in the right upper and one in the left upper abdomen. Pneumoperitoneum was constantly monitored and maintained at 8-12mmHg. The porcine equivalent of a left hemi-hepatectomy was carried out without vascular inflow occlusion. A portable ultrasonic scalpel (Sonicision™, Covidien, Dublin, Ireland) was used for transection of the liver parenchyma. Small vessels were controlled with ultrasonic scalpel or metal clips, whereas major vessels were divided with a laparoscopic stapling device (Echelon Endopath™, Ethicon Endo-Surgery, Blue Ash, USA).

3.1.4.2 In-vivo image acquisition in the porcine model

Following establishment of the pneumoperitoneum, abdominal contents were visually inspected for potential ablation induced collateral injuries. All imaging experiments were recorded with the laparoscopic camera and stored as digital files. Position of the Cellvizio™ probe tip in relation to the ablation zones examined could be identified on video and correlated with the recorded CLE images for future analysis. Immediately before liver imaging, a standardised Cellvizio™ system calibration procedure (251) was carried out in theatre. Baseline CLE images were recorded over normal and ablated liver, respectively. Fluorescein sodium (molecular weight 376.27g/mol – henceforth called “fluorescein”) and ICG (molecular weight 774.96g/mol) were mixed with 50 ml 0.9% sodium chloride or 5% dextrose respectively just prior to intravenous injection. Intravenous injection of fluorescein (at 4-7mg/kg) and indocyanine green (at 0.3-0.5mg/kg) was carried out sequentially with an interval of 30-60 minutes between injections. Fluorescein and ICG acted as fluorophores for CLE imaging at 488nm and 660nm wavelength, respectively. CLE image acquisition was carried out with separate systems for each individual wavelength (Cellvizio™ 488nm & Cellvizio™ 660nm, Mauna Kea Technologies, Paris). In addition to this protocol, two animals underwent fluorophore injection 15 minutes prior to ablation therapy to determine if the time point of injection impacted on CLE imaging characteristics. In preliminary bench experiments, it was confirmed that the illumination – emission spectra were so widely separated, that there was no cross-talk between the 488-fluorescein and the 660-ICG systems. An initial image sequence was recorded to monitor and confirm distribution of the fluorophores in the liver. This was followed by several short sequence acquisitions taken in equal numbers from normal parenchyma and ablated regions. Short sequences ranged from 10-20s and were later analysed to determine variations of relative fluorescence between healthy and ablated liver tissue.

When visualisation became impeded by blood or other detritus that had attached itself to the tip of the probe, it was cleaned with normal saline. This reflects the value of an imaging scheme rather than a single fibre spectrometer. In the latter case a low signal could represent either a lack of fluorophore or a fouled fibre tip – enhancing the risk of a false reading from a given sampling site.

Before experiments commenced, a training session was conducted to familiarise surgeons with CLE probe handling during laparoscopy. Particular attention was paid to probe tip pressure because too little pressure resulted in insufficient tissue contact, whereas too much pressure severely diminished fluorescence intensity. Both extremes resulted in the loss of any measurable fluorescence intensity and hence a black image which again demonstrates the value of an imaging system rather than a spectrometer fibre. The training session allowed surgeons to find a narrow range of tip pressure that enabled image acquisition at a visibly stable fluorescence level. From a surgical technique point of view, deliberate adjustment of pressure within this narrow window was very challenging, without haptic feedback so no formal quantification of probe tip pressure was undertaken. None of the image data acquired during the training session was used for analysis.

The confocal probes were inserted into the peritoneal cavity through the lumen of a steerable catheter (Agilis™ St. Jude Medical, Saint Paul, MN, USA) which was itself introduced through a 5mm laparoscopic port. The steerable catheter, designed for intra-vascular use, allowed subtle manipulation of the probe tip during laparoscopy (Figure 3.1). A technical note on this approach to probe manipulation has been reported elsewhere (254).

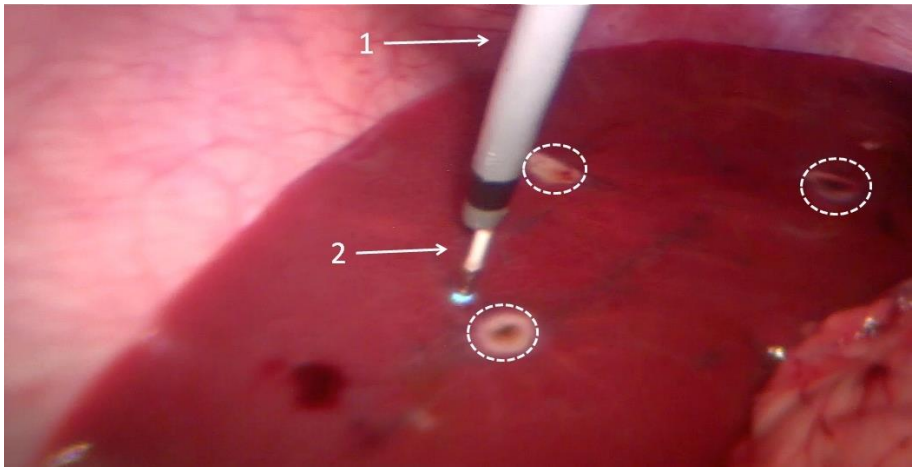

Figure 3.1 Laparoscopic CLE imaging of porcine liver with fluorescein/488 nm.

The ablated regions are highlighted with dashed circles. (1) Steerable catheter inserted through a laparoscopic port; (2) CLE probe with blue light reflex at the tip.

3.1.4.3 Preparation and examination of porcine liver tissue samples

Following termination of the animals, the ablation zones and the surrounding healthy liver were resected for histological analysis. During surgery, if more than one ablation zone was examined, they were assigned numbers and their anatomical position was recorded during laparoscopy with the intention to facilitate postoperative CLE image analysis for each individual lesion. No attempt was made to perform a more detailed spatial correlation between CLE- and histopathological images because the CLE probe's field of view

(<300µm^2) was too small to accurately localise with markings that would have been visible on laparoscopy.

Samples were fixed in formalin and then embedded in paraffin. Tissue samples were sliced with a histiotome in a direction parallel to the liver surface. These slices were placed on glass slips and stained according to a standard Haematoxylin & Eosin protocol.

3.1.4.4 Statistical analysis of porcine CLE data

The statistical analysis of the porcine model liver ablation model was conducted along similar principles as the analysis of normal and CRLM liver tissue which has already been described (3.1.3.4). Further details are outlined here to describe where this process differed from the above.

Image acquisition was more difficult during laparoscopy and hence some of the CLE images had to be discarded. To adjust the data for erratic probe movement all laparoscopic videos were reviewed. If there was a clear disconnection between the probe tip and the liver surface the relevant data sequence was excluded from analysis. Due to the difficulty in keeping constant contact between CLE probe and liver surface, it was not feasible to measure erythrocyte velocity as was done in the murine CRLM model. In contrast to the murine CRLM model, the GLIMMIX analysis was set up to model the probability of the probe being on normal (i.e. non-ablated) liver parenchyma. Fixed and random effects were handled in a similar fashion as described already.

To test the validity of the GLIMMIX model a receiver operating characteristic (ROC) analysis was performed. The covariates and intercepts provided by the GLIMMIX analysis were used to calculate the log odds, odds and finally the probability of identifying non-ablated tissue. Each single probability value corresponded to a single observation (mean RFU per frame), a specific animal ID and a tissue type, which enabled us to perform a ROC analysis based on this data. Because animal ID was a random effect, the same RFU value would result in different probability values for the individual animals. This relationship explains why based on our data, no single RFU cut-off value can be estimated as an optimal threshold to distinguish ablated from non-ablated tissue. No cross validation was carried out on the ablation model because there was insufficient data to facilitate randomisation into a training and validation dataset. The workflow for the statistical analysis is shown in Figure 3.2.

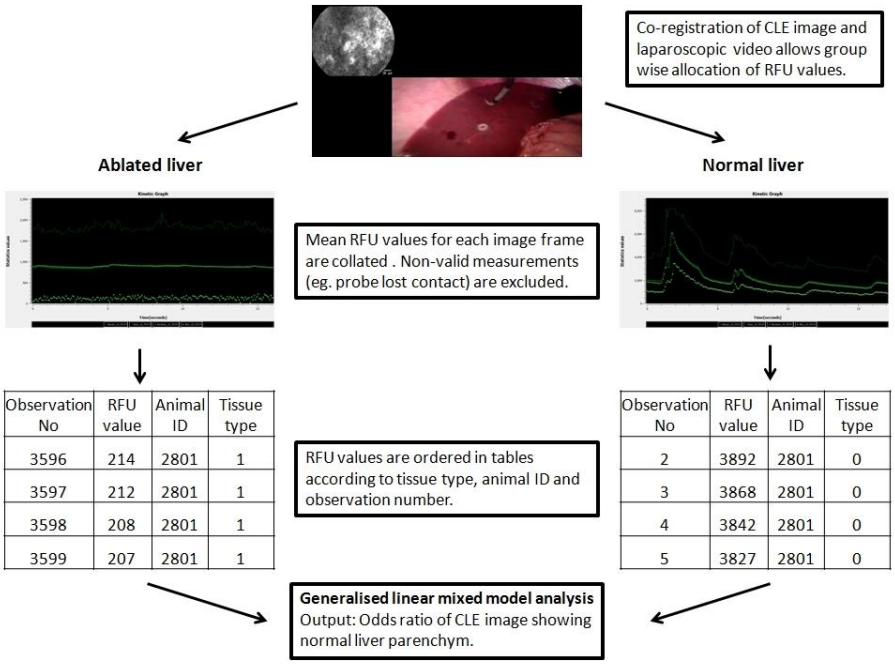

Observation No	RFU value	Animal ID	Tissue type
3596	214	2801	1
3597	212	2801	1
3598	208	2801	1
3599	207	2801	1

Observation No	RFU value	Animal ID	Tissue type
2	3892	2801	0
3	3868	2801	0
4	3842	2801	0
5	3827	2801	0

Figure 3.2 Workflow of statistical analysis of porcine CLE data.

The workflow depicted here was also used for the murine model.

The author of this thesis was not involved in the preparation of histology. The author helped during establishment of the animal model and during laparoscopic surgery, carried out CLE image acquisition and performed subsequent image analysis and data evaluation.

3.2. Digital image processing techniques used in this work

The analysis methodologies used in the chapters on multispectral imaging and video magnification make extensive use of image and video processing techniques. All colour images and video material was processed in the 8bit RGB colour space. Images from multispectral experiments were processed in an arbitrary grayscale format based on the camera recording characteristics as described below (3.3.4). A detailed description of digital image processing basics is beyond the scope of this chapter. For detailed background information please see here (255).

3.3. Multispectral imaging

Multispectral imaging experiments were conducted with the aim to develop an imaging platform that enabled examination of tissue spectra. This platform was consequently utilised to evaluate spectra from normal and pathological liver tissues.

3.3.1 General principle

The principle behind this imaging modality is that the chemical and physical composition of tissue alters the way that light is absorbed. This property is a function of light spectrum i.e. tissues absorption changes depending on light wavelength. This behaviour is reflected in the absorption coefficient which is specific for individual substance compounds such as lipids or haemoglobin. Tissue characteristics can therefore be inferred by exposing it to light of different wavelengths.

Absorption coefficients for specific substances can be plotted against wavelength in a spectral response curve which exhibits a typical pattern that depends on the underlying substance. The shape of the curve can be used to infer not only the presence of a substance but also in some cases its concentration. In biomedical science the substances that are most relevant are oxyhaemoglobin, deoxyhaemoglobin, lipids and water. Other substances such as collagen and bilirubin have been studied as well but to a lesser extent as they are not as ubiquitous. Typical spectral response curves for these substances are shown in (Figure 3.3).

3.3.2 *Ex-vivo* tissues for multispectral evaluation

To develop the imaging platform, animal tissue intended for consumption was purchased and tested. Animal tissue was more readily available than human tissue and hence was more attractive for preliminary testing. When the development phase was concluded, experiments continued with liver tissue excised from patients undergoing liver resection and from discarded donor livers. The aim was to get at least 2-3 samples (161,163) for any pathological condition (i.e. CRLM, steatosis), but ideally > 6 samples (256,257). Ultimately the number of specimen was limited by clinical availability. The former tissues were chosen to examine liver malignancy and the latter tissues to examine liver steatosis because explanted livers are frequently discarded because they are too fatty. Imaging was conducted

on *ex-vivo* liver tissue as previously described by other authors (162,256). These samples had the advantage of being more representative of clinical disease then tissue from cell cultures or animal models. Additionally it was technically not feasible to move the imaging platform to animal labs or to hospital facilities at this early development stage because of concerns about laser safety and the fragility of the system.

3.3.2.1 Animal tissue

For preliminary experiments on some of the imaging modalities, commercially available animal tissues marketed for consumption were purchased from food stores. The type of animal product depended on the tissue of interest. To study multispectral imaging (MSI) on lipids for example goose fat was found to be useful whereas beef liver was frequently used to obtain preliminary confocal laser endomicroscopy data. The interchange between muscle- (red part of the bacon) and fat tissue in bacon proved useful to study the spatial resolution of MSI imaging. The composition of these tissues was not quantified because preliminary experiments served towards testing of equipment and refining of image acquisition system. Experiments were not used to correlate image data with tissue constitution. For transport to the laboratory, no additional cold storage precautions were made. In the lab, specimen were cut into dimensions appropriate to the imaging modalities field of view. Subsequently they were placed on a stationary platform for examination. For MIS studies a translation stage was used whereas tissue for CLE examination was simply placed on a plastic tray.

3.3.2.2 Patient tissue

Ethical approval for the research use of patient tissues from the Royal Free Hospital, London was granted by the UCL Biobank Ethical Review Committee (Reference number NC2015.012). Tissue from patients undergoing liver resection for malignancy was collected during surgery. Following resection of the cancer and surrounding normal liver the specimen was placed in a bowl. Specimen were then taken for further analysis. During excision of liver samples for experiments, it was crucial that the oncological resection margins i.e. the area where the diseased liver was transected from the healthy liver during surgery was not compromised as this would have affected the histopathological evaluation. The maximal size of the specimen was tailored to fit under microscope glass slides (75 x 25mm). Frequently however the maximal size was limited by the available liver tissue especially in minor liver resections which are of a smaller resection volume. The number of excised specimen again was mainly dependent on the size of the resected specimen (i.e. less in smaller specimen).

The main goal of tissue acquisition was to obtain at least one sample of healthy and cancerous tissue for each patient. If there was a large resection specimen or multiple tumour nodules, the aim was to take multiple biopsies representative of different tumour nodules and areas of normal liver tissue. In some patients it was not feasible to excise tissue without compromising the resection margin and in these cases only normal liver tissue was excised. For transport, biopsies were placed in a container filled with cooled (app. 4 ˚C) organ storage solution (KPS-1). After transport the liver samples were removed and placed on a

dry gauze swabs to remove excess fluid and prevent smearing between tissue and glass cover slip. For image acquisition samples were then placed on a translation stage that was covered with an incontinence sheet (dry gauze on top with water proof sheet at the bottom) commonly used in hospitals. Smaller samples were placed in a row and covered with one glass slip whereas larger samples were covered with individual glass slips (Figure 3.4)

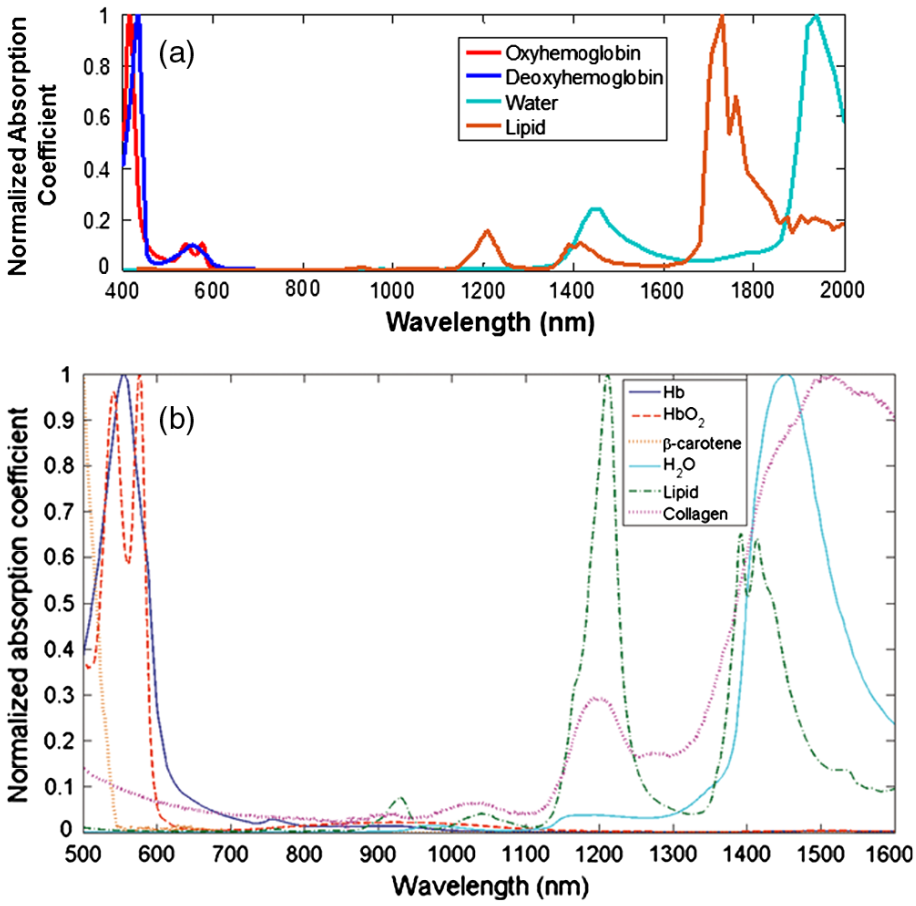

Figure 3.3 Absorption spectra of endogenous chromophores.

Plots of absorption coefficients on the y-axis against excitation wavelengths on the x-axis for common endogenous chromophores.

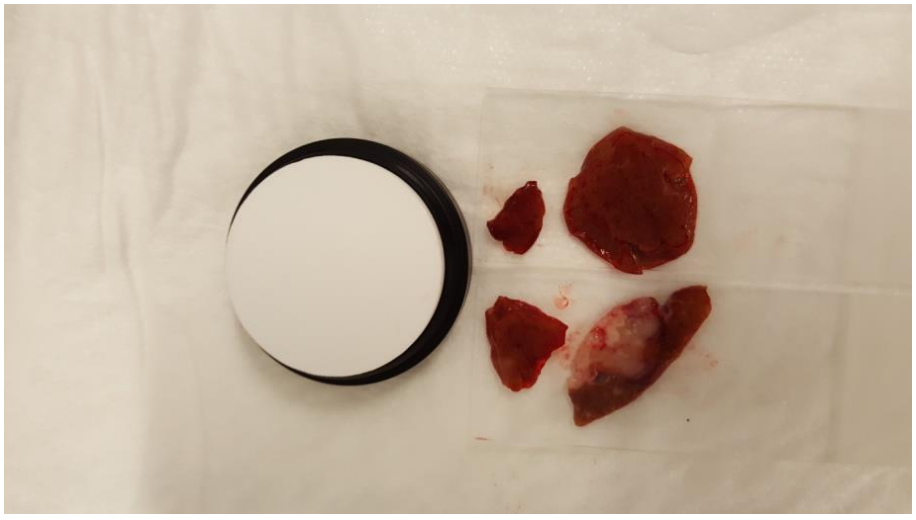

Figure 3.4 Placement of ex-vivo specimen for MSI studies.

On the right 4 liver specimen which are covered with glass slides can be seen. On the left is a white reflectance standard which is used as reference point for image processing.

There are two technical challenges to accurate multispectral image acquisition (MSI). Firstly the wavelength used for recording, needs to be precisely controlled. Secondly a camera sensor which is sensitive to the wavelengths used, which are often within the invisible spectrum, needs to be used. For wavelength control unwanted spectra can be filtered out by interposing a filter between camera lens and light sensor. Alternatively an excitation source that emits light at a specific wavelength can be used. The type of camera sensor depends on the desired imaging spectrum.

3.3.3 Specific setup of the multispectral imaging platform

Light excitation was conferred via an optical parametric oscillator (OPO) laser that is tuneable within a wavelength range of 700nm-2000nm. The light signal itself was conducted through an optical fiber with silica-core/silica-cladding and a core diameter of 910 μm. For acquisition of multispectral images the wavelength was changed at 5-10 nanometre (nm) intervals while images were taken. An Indium-Gallium-Arsenide (InGaAs) sensor camera (C10633-23, Hamamatsu, Welwyn Garden City, UK) with the capability of viewing images in the near-infrared (NIR) spectrum with a sensitivity ranging from 950-1700nm (henceforth called NIR camera) was used to record images. Images were saved on the hard drive of a Windows 8™ laptop for subsequent processing and analysis.

3.3.3.1 Laser excitation and tuning

As a light excitation source the optical parametric oscillator (OPO) (VersaScan L-532, GWU-Lasertechnik) was used. This type of laser uses a fixed laser as input source which is being fed into an oscillating crystal. As the oscillating speed is adjustable, the output wavelengths of the laser can be tuned to a desired wavelength. This OPO was pumped by a frequency-doubled Q-switched Nd-YAG laser frequency with a wavelength of 532 nm, a repetition rate of 10 Hz, and a pulse width duration of 6-10 ns (Quanta-Ray INDI-40-10, Spectra-Physics). The idler beam of the OPO was coupled to a silica-silica optical fibre with a core diameter of 910 µm (FG910LEC, Thorlabs). The idler wavelengths were varied by motorised rotation of the nonlinear crystal in the OPO.

At maximum light intensity the laser produced an over illumination in the camera sensor (i.e. a completely white image). Therefore additional optical filters of 6 optical densities were positioned between laser source and optical output fibre to reduce light intensity. Before experimental use the OPO was calibrated to ensure an accurate wavelength output with an error margin of approximately 5nm. The robustness and validity of the calibration was checked at regular intervals with a spectrometer that was connected to the optical fibre. The calibration was renewed if there was evidence of misalignment.

3.3.3.2 NIR camera and specimen placement

The camera was fixed to a 150 mm x 150 mm x 12.7 mm breadboard (metal plate with holes) with a 25mm x 100mm optical post (Thorlabs, Newton, NJ, USA). The same breadboard also carried the post which held the optical fibre through which the excitation

laser was emitted. The breadboard itself was installed onto a 1.5” x 300mm optical post which enabled adjustment of the distance between camera and the specimen. The NIR camera connected to a Windows 8 laptop via an USB 2 port. NIR camera control and image recording was controlled with custom build code written in Labview™ Professional, a high level programming language which is widely used for the purpose of controlling physics instruments in a experimental environment.

The camera was fitted with a low magnification lens (machine vision lens - Navitar, Rochester, NY, USA) whose focus was adjusted to achieve optimal image sharpness. The lens aperture was varied to identify a threshold where maximal light intensity was achieved while simultaneously avoiding over illumination (i.e. too much brightness). To study absorption behaviour of tissues it is important to reduce the amount of light that is directly reflected back from the tissue surface at the same angle at which the excitation light hit the surface. To reduce these so called specular reflections (Figure 3.5) a microscope glass slide was placed over specimen as described above.

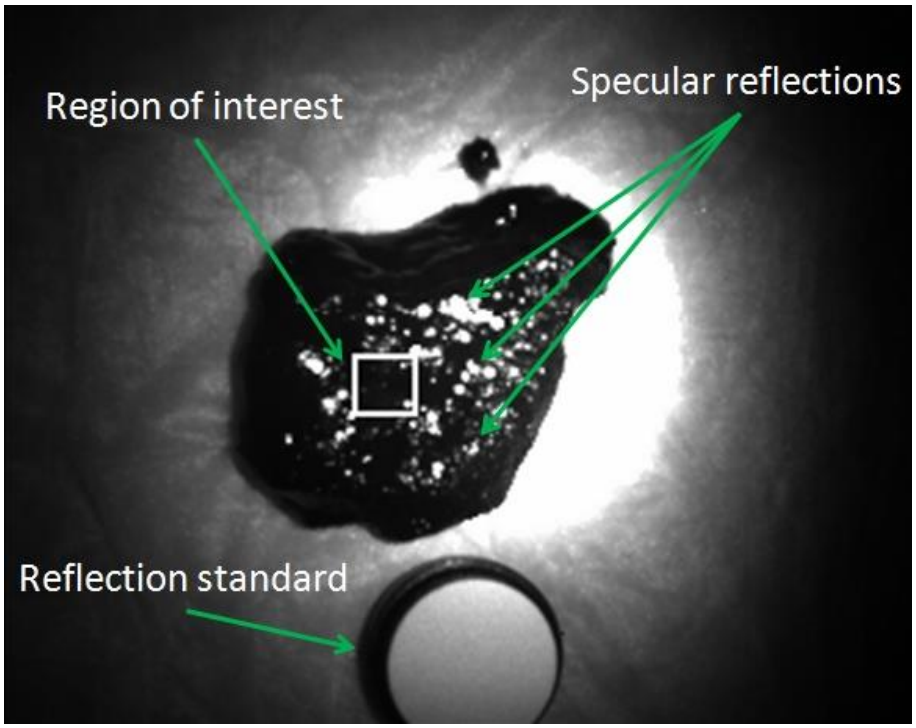

Figure 3.5 Example of specular reflections during MSI experiments.

The liver specimen can be seen centrally. Specular reflections cause over saturation of the camera sensor which results in data loss. To standardise absorption coefficients a white reflection normalise was placed in proximity to the liver specimen.

3.3.3.3 Laser and camera synchronisation

The NIR camera operated with a maximal and variable rate of 50 frames per second. The OPO had a fixed pulse rate (i.e. the frequency that the laser was admitted with) of 10 Hz. The exposure time of the camera could be varied between 0.1-15ms whereas the duration of the OPO light emission was fixed at 10ns. This means that synchronisation of NIR camera exposure and light emission was necessary to ensure that the timing of light emission coincided with the exposure time of the NIR camera in a reliable fashion. The OPO generated an output signal in the form of an electrical voltage signal which can be used to trigger other devices e.g. initiate image acquisition. Unfortunately the NIR camera could not be triggered through such a voltage signal but instead could be triggered through a software generated signal which had the disadvantage of being slower than a hardware signal.

To enable a synchronisation of image acquisition and laser pulse it was therefore important to transform the voltage signal from the OPO into a software signal that could be recognised by the camera. Transformation of the voltage signal i.e. hardware trigger to a software trigger was facilitated by a digital input/output box (henceforth called I/O box; National Instruments™, Austin, TX, USA) that received the hardware signal in the form of a voltage threshold through BNC connectors and send the software signal in the form of a binary signal (on or off) to the controlling computer. Because the incoming hardware trigger voltage was below the 2.2 Volt (V) limit required by the I/O box, the signal was amplified via an oscilloscope (DPO3032, Tektronix, Beaverton, OR, USA) to raise it above the 2.2V threshold. The connections, signals and equipment activity was controlled and monitored through custom written Labview code. The Oscilloscopes 2nd channel was used to visualise the timing of the camera software trigger to aid in evaluating delays between hardware to software signal transformation (Figure 3.6).

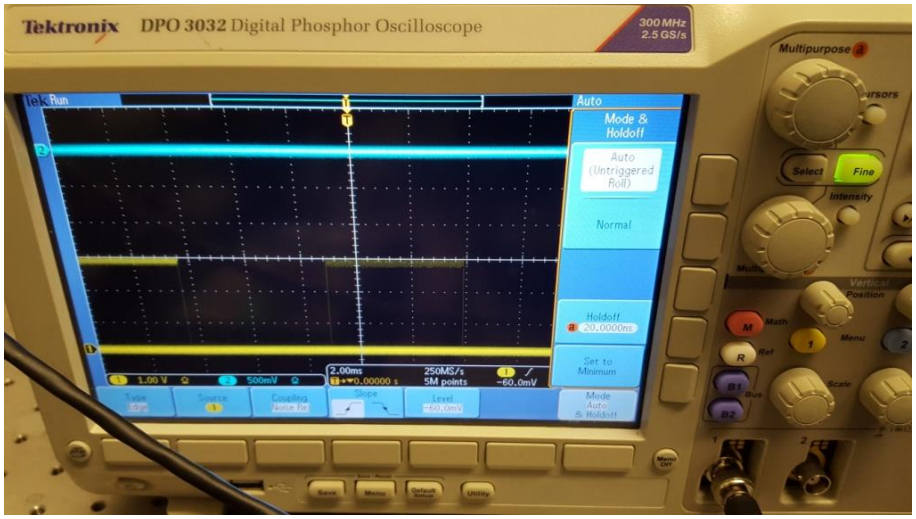

Figure 3.6 Oscilloscope for OPO light source and NIR camera synchronisation.

Oscilloscope screen showing the OPO trigger in yellow and the NIR camera trigger in blue. Good synchronisation between both signals was crucial for successful image acquisition.

The transformation of hardware to software signal in addition to the execution of one cycle of the image acquisition algorithm took in the range of 0.4s. To accommodate for this delay, the maximum rate of camera triggering was forcibly reduced to 1s. This ensured that the preceding image was recorded and that the NIR camera was ready for the next image acquisition. As opposed to the Labview code, the delay caused by the signal transformation was inconsistent at times which lead to an approximate 15-25% loss of synchronisation and hence image data. Desynchronised images were under illuminated i.e. virtually black. To avoid recording and processing of desynchronised images, an algorithm was implemented into the Labview code to automatically delete images where the maximal light intensity per pixel fell below a certain light intensity threshold that indicated lack of illumination. The threshold was set at 4.000-7.000 depending on the running time of the NIR camera and operating wavelength of the OPO because both factors positively correlated with the intensity of black pixels (i.e. at higher wavelength and after longer running time black pixels had a higher intensity). A photo of the experimental setup is shown below to illustrate the workflow and components of the system (Figure 3.7).

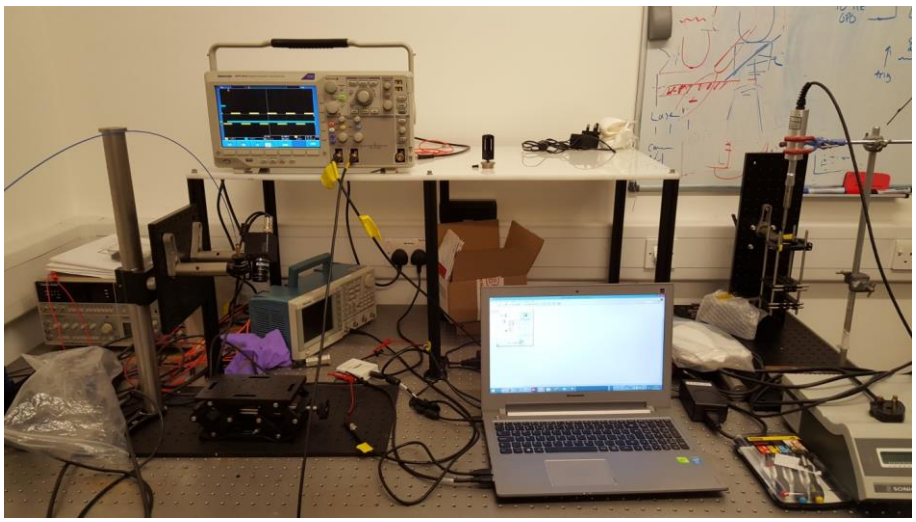

Figure 3.7 Experimental setup for MSI studies.

Signal control and storage is controlled via the laptop. To the left the fibre holder and NIR camera can be seen placed above the black translation table that normally holds the specimens,

3.3.4 Image processing

Images were recorded as grayscale pictures in the uint16 format. This commonly used 16-bit deep format enables depiction of 65.536 different gray levels in an image. The image size was 320x256 pixels but the NIR camera originally saved image data in bytes (i.e. pixels) in single 81.920 long sequence of Little-endian order. The order (Big-endian vs. Little-endian) describes in which order the sequence must be read correctly when transforming it to other formats i.e. a 2D image, as was the case in these experiments. Image data was transferred

to MATLAB™ (MathWorks™, Natick, MA, USA) for transformation, processing and subsequent analysis. The sequence of pixels was initially transformed to a corresponding 320x256 pixel image with 65.536 gray levels (uint16). Essentially the gray levels of zero and 65.536 represented the lowest (i.e. black) and highest (i.e. white) possible pixel intensity. In the experimental design described here, high pixel intensity correlates with a low absorption in the corresponding tissue and vice versa. Because each image acquisition was repeated at different wavelength, the change in pixel intensity can be plotted against wavelength to evaluate changes in tissue absorption. This form of representing absorption coefficients, can also be called spectral response curve (Figure 3.8). Generally this approach could be applied to a region of interest that may consist of a small tissue area or the whole image. Alternatively a spectral response curve may be studied for a single pixel that represents a minute tissue area of <1mm^2 (Figure 3.9).

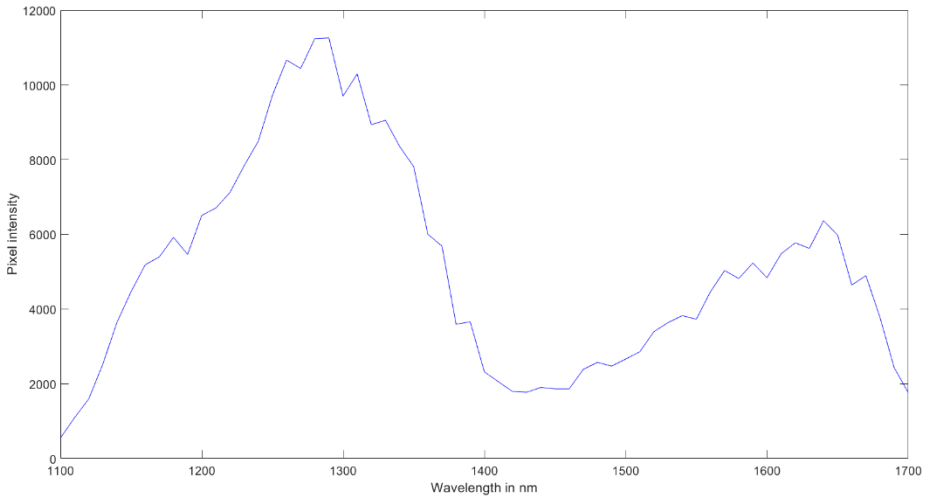

Figure 3.8 Example of a spectral response curve (SRC).

Tissue light absorption on the y-axis is plotted against excitation wavelength on the x-axis to reveal the spectral response curve of a tissue specimen.

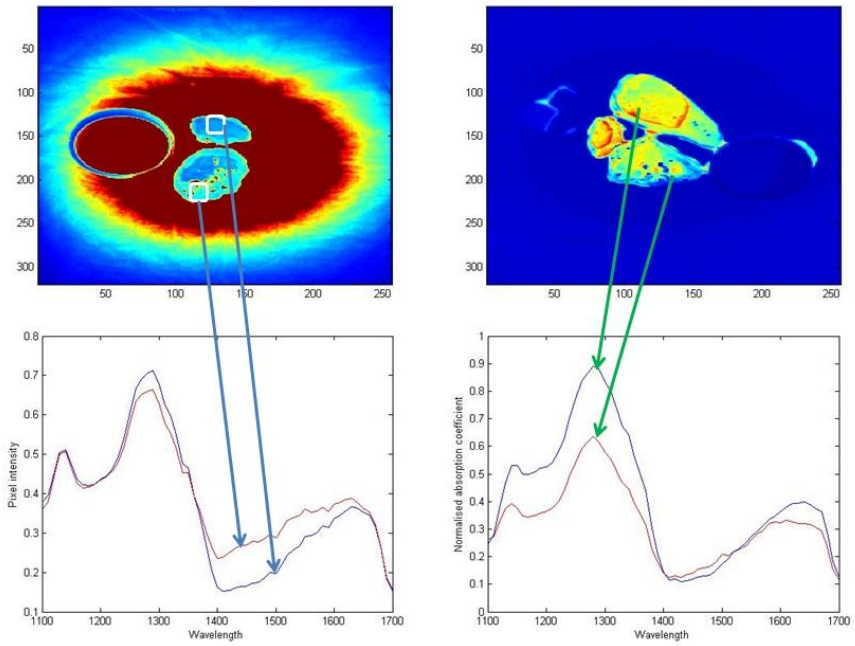

Figure 3.9 Spectral response curve from ROI vs. single pixel.

Spectral response curves can be plotted from larger tissue areas consisting of multiple pixels or the whole image (left). Alternatively a spectral response may be plotted for single pixels (right).

3.3.5 Image recording

Specimen were placed on an incontinence sheet. As described above specimen were covered with microscope glass slides to reduce specular reflections. A white reflection standard was placed close to the specimen to ensure that it was exposed to the excitation laser to the same extent that the liver specimen were.

Initially single images were recorded to ensure that specimen were placed centrally in the field of view. Following this the lens aperture was adjusted so that the maximum intensity in the images stayed below 16.383 intensity units (maximum of arbitrary units used by NIR camera). Beyond this value over-illumination (i.e. white out) occurs which results in loss of data. Finally background images were recorded without any illumination to determine the background values that were needed for the normalisation process. Once background values were recorded, MSI acquisition commenced. For each wavelength step at least 20 frames were recorded to reduce the impact of outliers. Once the desired complement of frames was recorded, the acquisition was paused to allow a manual change of the excitation wavelength. This process was repeated until the pre-determined wavelength range required to create a spectral response curve was covered.

3.3.6 Colour representation of multiple spectra

It is possible to visualise the single spectrum images in a variety of ways in an attempt to improve comprehensibility and mental integration of the observer. The simplest form of visualisation is to translate the recorded intensities and therefore the absorption characteristics into a gray scale image. This is straightforward and also the default option of the NIR camera's standard issue software package. For improved visualisation the gray levels can be converted to a variety of colours and their corresponding hues. For this purpose, colourmaps can be employed which assign colours to numerical values, which in this specific case correlate with intensity levels. When using the MATLAB™ colourmap jet for example low and high intensities are assigned to blue and red respectively (Figure 3.10).

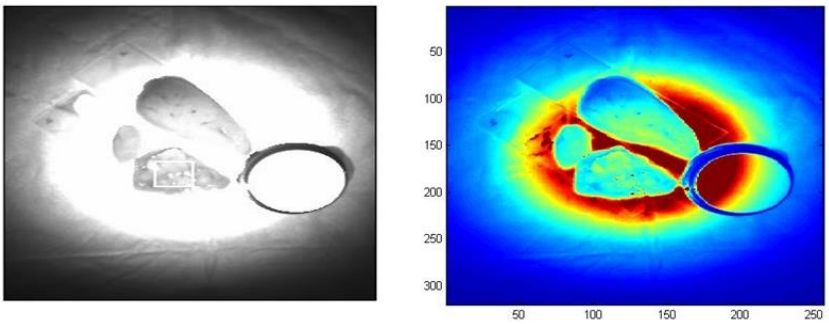

Figure 3.10 Example of different colour maps used for MSI.

Grayscale 16 bit image representation (left) and the equivalent image shown in colour (jet colourmap).

Transformation into colour can perhaps be regarded as a 1:1 conversion where no additional data is available to the observer. It is however possible to integrate data from multiple spectra (Figure 3.11) into the same two dimensional image to increase the amount of data visualised. The only factor changing over time during MSI experiments with individual specimen is the wavelength (i.e. single spectra) whereas the tissues are completely stationary.

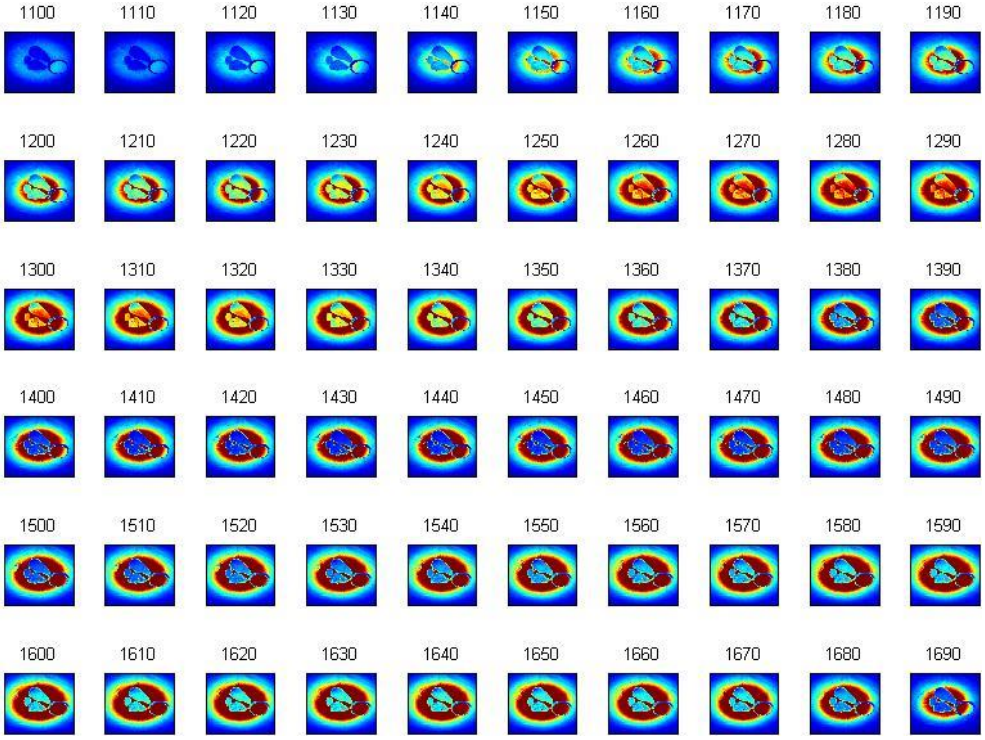

Figure 3.11 Variations in pixel intensity according to wavelength.

Each thumbnail image shows a colour representation of the changing light absorption of three liver specimen at wavelengths from 1100-1690nm.

It is therefore possible to combine information pertaining to multiple absorption spectra of the same pixel (i.e. tissue area) into a single two-dimensional (2D) image. In a perhaps simplified way this could be described as “squeezing” the data contained in a spectral response curve into a single pixel colour. There are almost limitless possibilities of combining the various spectra, starting with the number of wavelengths to include which could range from only two wavelengths up to the maximum number of 61 wavelengths used in these experiments. Perhaps even more important is the method of combining intensities from different wavelengths. Values can be combined with simple arithmetic operations such as addition or division (Figure 3.12). The area under the spectral response curve can be determined and used for false colour representation. In a perhaps more complex approach, intensity values at particular wavelengths could be employed as variables in an equation or regression analysis.

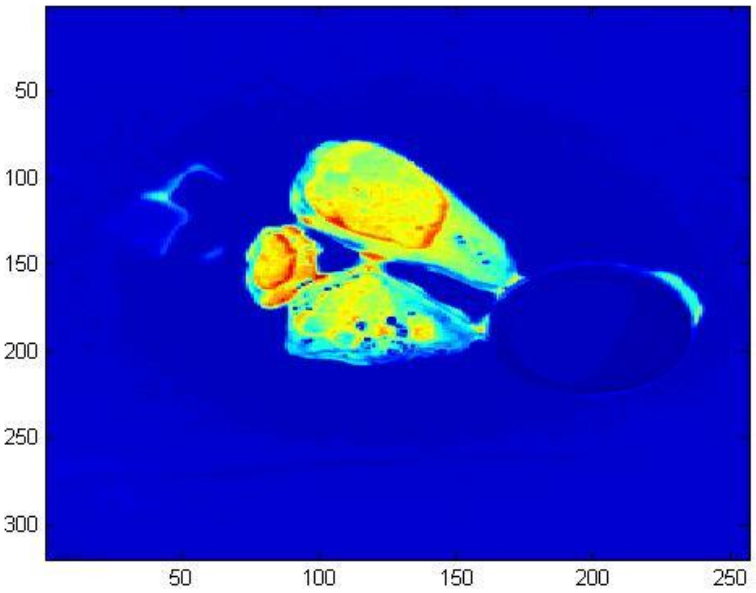

Figure 3.12 Example of 'false colour' visualisation.

The same specimen as in figure 3.10 & 3.11 are shown here. Pixel intensities (jet colourmap) have been derived by dividing absorption at 1290nm/1450nm hence the pixel intensities can be regarded as a function of the two respective wavelengths.

An approach optimised according to a statistical analysis is of utilising different false colour options are described in the results section. To systematically assess which wavelengths are the most relevant for discriminating normal liver tissue from malignant liver tissue, multiple wavelengths absorption coefficients have been evaluated statistically using Bland-Altman plotting to determine the wavelengths with the greatest discriminatory power and subsequently using these as covariates for inclusion into a generalised linear mixed model analysis The statistical methodology is further described in the Statistics part of the relevant results chapter.

3.3.7 Statistical analysis

Tissue spectra are compared by plotting pixel intensity which is inversely related to absorption, against changes in wavelength. As indicated either mean values or scatter plots are used. To facilitate statistical comparability between different experiments the intensity values were normalised as described in the relevant chapter (6.3.4). Normalised intensity values were visualised on a Bland-Altman plot to evaluate if any intensities lying outside the limits of agreement were associated with any particular wavelengths. Consequently, the normalised pixel intensities are then analysed in a generalised linear mixed model analysis to elucidate if intensity variations at particular wavelengths are indicative of pathological tissue states. The model used normalised intensity and wavelength as fixed terms whereas patient ID and cancer type were used as random terms. Further details about the statistical

model can be found below (6.3.4). Statistical analysis was performed using SPSS™ Version 21 (IBM, Armonk, NY, USA). Statistical significance was assumed for $p<0.05$.

With the exception of histological preparation of liver biopsies, all aspects of this research were carried out by the author.

3.4. Video magnification

The experiments in this section were conducted to evaluate a video processing technique called Eulerian video magnification. Initially a method is developed to analyse and compare the signals that result from applying this technology to video. This method is then applied to a mechanical flow phantom and subsequently to a porcine model of laparoscopy that has already been described above (3.1.4.1).

3.4.1 General concept

The experiments outlined in this chapter are based on a work of Wu et.al (136) who have created a video processing algorithm called Eularian Video Magnification (VM) that was designed to reveal subtle changes in colour or motion that are invisible to the naked eye. In brief, the algorithm partitions the field of view into different sections (spatial decomposition) to make location of changes possible. The video then undergoes temporal filtering which essentially means that only signals that repeatedly occur at a given range of frequencies (e.g. physiologic heart rate) are selected for amplification.

Although algorithms with similar capabilities have been developed in the past, the VM algorithm has the advantage of being less computationally expensive (i.e. runs faster) and it therefore can process videos in real time on a personal computer. This is made possible by measuring and amplifying changes in pixel values such as colour and brightness whereas previous algorithms relied on accurate motion estimation (e.g. Lagrangian method), a process that requires more computing power and is more prone to errors. A detailed description of the work underlying VM can be found here (136).

The VM algorithm has been written in MATLAB™ (MathWorks, Natick, MA, USA) and is freely available from the authors (CSAIL, Massachusetts Institute of Technology). A regular video in MP4 or AVI format is used as input and following processing a MP4 video that visualises the VM induced changes is stored in MP4 format. A number of parameters can be adjusted within the supplied MATLAB code to control the VM processing in detail. Two frequency values in Hertz (Hz) determine the frequency bandwidth for video signals which will undergo amplification. This means that only signals that occur at a given repetitive rate will be amplified by the algorithm.

A spatial frequency variable determines the level of detail that the VM (henceforth called video magnification - VM) algorithm will analyse. Spatial frequency can be described as the level of detail from a stimulus (e.g. light or contrast) that is present per degree of visual angle. In other words a high spatial frequency translates into a greater level of details in an image and vice versa. In regards to the VM algorithm a higher spatial frequency value (e.g. 100) means that signals that fall below this level of detail are excluded from the magnification process. The use of filters suppresses video signals outside the selected spatial frequency bandwidth which has the benefit of reducing the video noise in the final product. The magnification factor α determines the factor with which signals within the

bandwidth are multiplied. In practice, higher amplification factors are able to highlight subtler signals but this also results in an overall noisier (i.e. more grainy) output video.

The choice of temporal band pass filters affects the way that signals outside the selected frequency bandwidth are handled. These should be selected based on the desired application of VM. A broad band pass filter like the Butterworth filter for example exhibits a mildly attenuated amplification for frequencies that are adjacent to the selected frequency bandwidth. Amplification is increasingly attenuated the farther away the frequency lies from the selected bandwidth. Narrow temporal bandwidth filters like the ideal filter on the other hand almost completely suppress magnification of signals outside the selected bandwidth. In terms of application, broad temporal band pass filters are well suited for magnification of motion signals whereas their narrow counterparts are superior when applied to colour change signals. All temporal band pass filters were tested initially to select the most suitable filters for motion and colour magnification respectively. Filters were chosen depending on optimal visual results and on the fastest processing time as further described in the results chapter.

Colour clipping artefacts result when colour intensity is outside the level that can be displayed within a frame which may be caused by excessive magnification. Some artefacts may be reduced by increasing the chrominance attenuation in the VM algorithm. For standardisation purposes the same chrominance attenuation was used for an individual set of image data (e.g. all videos from on patient).

3.4.2 Flow phantom

Flow phantoms are normally constructed from a pump that circulates fluid, a channel or several channels through which fluid flows, and a tissue-mimicking phantom that surrounds the channels (258). Below is a description of how the was constructed. The construction of the flow phantom for the purpose of experimenting with video magnification signals in a controlled environment is described in the following sections.

3.4.2.1 Tissue component and flow channels

Tissue mimicking models with internal structures as a substitute for blood vessels have been extensively used for experimental and training purposes. These models can be further subdivided into flow phantoms that have vessels with or without walls (wall-less vessels). A variety of construction methods have been described (259).

Limitations of wall-less phantoms is their fragility e.g. they are less able to withstand higher pressures from flow (258,260). Because it was intended to conduct some experiments with high pressures, a vessel mimicking phantom that could withstand higher pressures was chosen for this study. Limitations for vessel mimicking phantom mostly pertain to their use in conjunction with ultrasound. The border between flow channel and tissue mimicking substance may have an unrealistic appearance on ultrasound and may impede image

analysis. If the model is used as a training phantom for percutaneous needle interventions then repeat penetrations with a needle may damage the integrity of the flow channels (260).

Flow channels for the phantom used in this study were created by Foley catheters (hollow silicone tubes). The tissue mimicking substance was built from polyvinyl chloride plastisol (PVCP) a deformable plastic substance. PVCP has the advantage that its consistency and colour can be altered during the production phase.

Urinary Foley catheters (medical use for draining the urinary bladder) were purchased from commercial suppliers (Tiga-Med, Ronneburg, Germany). A catheter size of 12Fr was chosen to construct the flow channels because preliminary tests showed that at this size catheters were able to withstand pressures of >400mmHg, and because their diameter (3-4mm) is similar to medium sized liver vessels. Smaller sizes such as 10Fr were considered as well but they turned out to be too fragile for manipulation during the building of the model. Clear catheters were used so that they could blend into the PVCP which was also of a clear colour.

The PVCP used for these experiments can be treated with additives that can make it harder, softer or change its colour. To establish a consistency and stiffness reflects that of human liver tissue, 3 surgeons were asked to rank 4 mixtures of PVCP that differed in stiffness. The mixture that all three surgeons opted for unanimously was chosen for all experiments.

The PVCP (Lure factors, Doncaster, UK) was purchased in its liquid form. For solidification the PVCP was heated at 200˚-250˚ C for 20-30 minutes. During this process its colour changes from a milky opaque to a colourless translucent appearance. Heating was carried out on a laboratory heater-stirrer under a fume hood. On completion the liquid was poured into a rectangular plastic container for cooling. Once cooled sufficiently, holes were drilled at corresponding heights at either end of the plastic container to prepare it for insertion of the silicone catheters. A tract for the catheter was created by pushing a knitting needle through opposing holes. A guidewire was then inserted into the catheters to provide some stiffness and steerability during insertion. Subsequently catheters were inserted along the previously created needle tract crossing over from one end of the container to the other. In some cases the surface of the tissue model was inadvertently damaged while advancing the catheters. Smaller defects were repaired by adding an additional layer of PVCP onto the disrupted area (Figure 3.13).

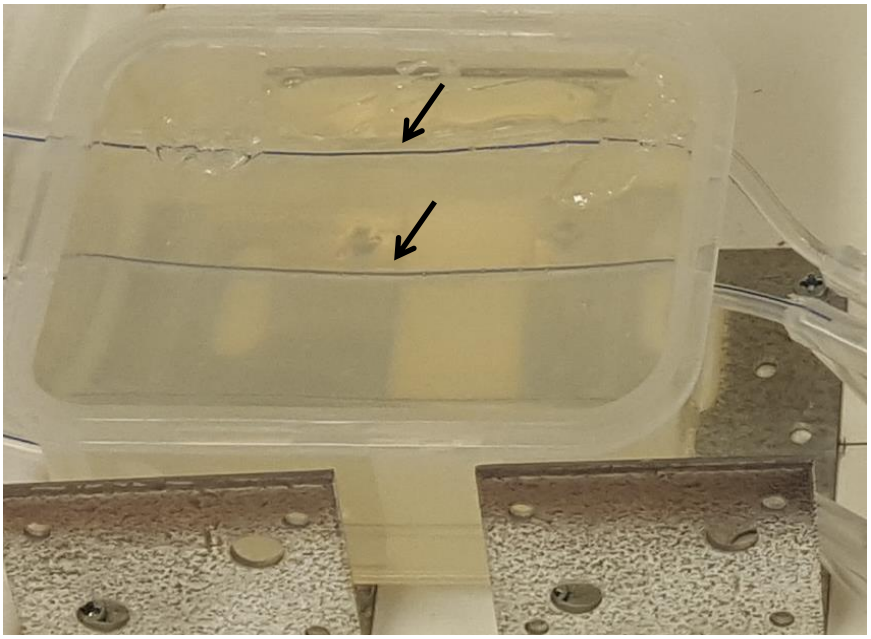

Figure 3.13 Clear flow phantom.

The completed flow phantom containing two Foley catheters (arrow) that are surrounded by clear PVCP.

Several tissue models with different catheter positions which were altered depending on the experimental setup were created. For preliminary experiments a model with one catheter tract was used initially. Two catheters inserted side by side were used to study the presence of a perfusion signal versus a control standard. To study the effect of tissue depth on perfusion signal strength, three catheters were inserted, one just below the surface and then at app. 2 cm depth and 4 cm depth.

All initial experiments were conducted with a clear PVCP mixture to measure non-concealed VM signal strength. To create a tissue model that closer resembles the colour of human livers, a brown mixture was created from black, brown, red and yellow colour additives. This colour was added to a tissue model which had two catheters side by side (Figure 3.14) (same as shown in Figure 3.13).

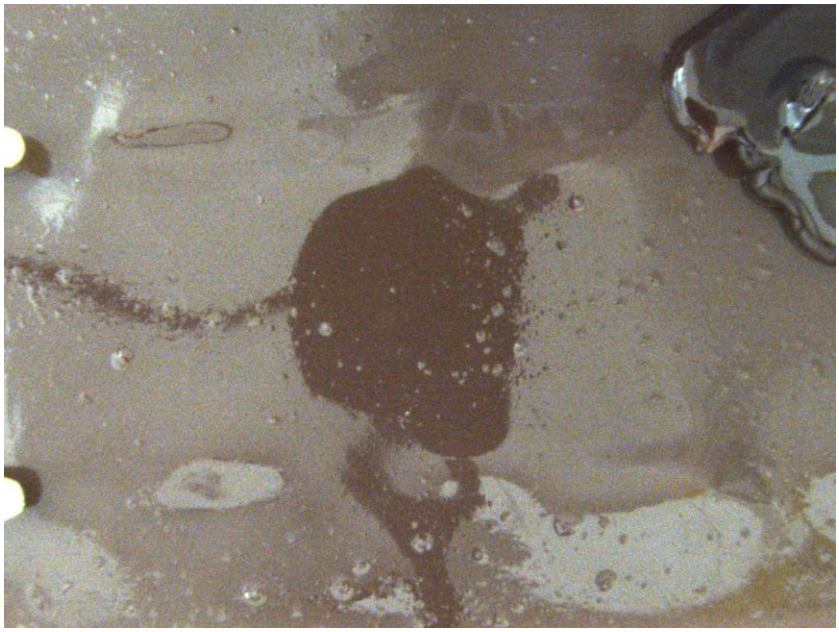

Figure 3.14 Brown flow phantom.

A brown coloured flow phantom was created to study how colour and opacity affects motion related VM signals. Because the flow channels are not visible, two yellow markers were placed at the left side of the screen to facilitate selection of the correct region of interest for statistical evaluation.

3.4.2.2 Perfusion circuit

Circulation of fluid was facilitated by a metering pump powered circuit that was constructed with the option to adjust flow rates and pressures. The basic principle was that fluid was taken from a container and propelled through this circuit by a pumping mechanism. The circuit was connected to the catheters which were embedded into the tissue model. Following perfusion through the catheters the fluid drained back into the container to be available for further re-circulation .

An electronic metering pump (LPJ7E2, E-Series, Pulsafeeder, Punta Gorda, FL, USA) was used to create flow within the circuit. The pump comes with adjustable stroke rate of 5-125 beats per minute (bpm) and output pressure of 1.1-5.5bar. Solenoid operated metering pumps create pulsatile flow with an inflow phase during which fluid is suctioned into the pump from a reservoir and an outflow phase during which the pressurised fluid is discharged through the efferent tubing. This characteristic makes metering pumps suitable to simulate flow conditions similar to that of the cardiac cycle with the inflow phase and outflow phase corresponding with the diastolic and systolic phase respectively. The advantage over roller pumps is that the stroke frequency and pressure can be adjusted to closely resemble physiological conditions (258). Connectors on the pump enable attachment to standard 3/8” tubing via plastic National Standard Pipe Thread (NPT- screw tightening) adapters.

The minimum pump output pressure of 1.1bar translates into approximately 825mmHg and therefore pressures needed to be reduced further to bring them into the physiological range between 50-250mmHg. This was facilitated by inter-positioning a pressure dampening fluid reservoir between metering pump and flow phantom. The reservoir was constructed from a 25ml serum pipette that was inserted into a T-piece connector that enabled connection to the rest of the flow circuit. A stopcock was fitted to the upper end of the pipette which made it possible to adjust the amount of fluid and air within the pipette. The ratio between air and fluid in the reservoir has an influence on circuit pressures. If the reservoir is devoid of fluid (i.e. filled with air), the amount of outflow pressure reduction is at its greatest. Pressure reduction moves inversely to the amount of fluid in the pipette. An additional effect is that the circuit pressure during the inflow phase drops off less quickly. So in essence the “systolic” or outflow pressure can be adjusted with the aid of the reservoir. The “diastolic” or inflow pressure can be adjusted with a pinch valve installed distally to the flow phantom (i.e. in the outflow limb). Increased pinch pressure reduces the outflow diameter and hence increases flow resistance according to the Hagen- Poiseuille law. Increased resistance affects the circuit by increasing pressure and flow velocity during the inflow phase. There is also an effect on circuit pressure during the outflow phase.

Pressures were measured continuously by connecting a pressure meter (Comark, Milford, MA, USA) to the circuit via a T-piece connector. Flow was measured when required with a Flowmeter (Transonic, Ithaca, NY, USA) that utilised ring-shaped Doppler probes that encircled the flow tubing. To establish how flow and pressure within the circuit were affected by pump and reservoir settings, calibration experiments were carried out initially. During these experiments a combination of different settings for pump pressure, pump stroke frequency, reservoir filling and outflow resistance were studied and the resulting flow rates and circuit pressures were recorded (Figure 3.15).

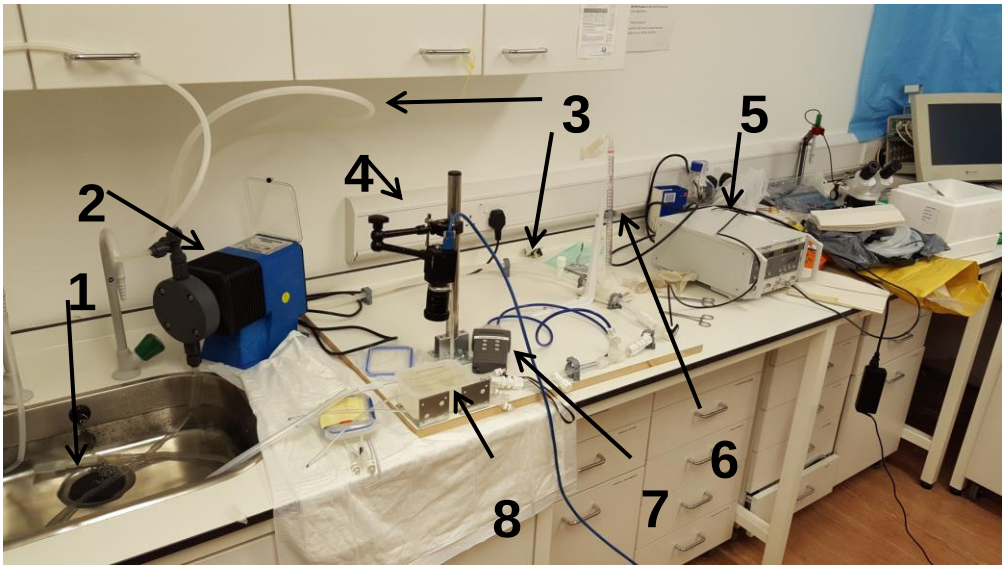

Figure 3.15 Complete flow phantom setup during experimentation.

1 – Fluid reservoir; 2 – Solenoid pump; 3 – Perfusion tubing; 4 – Camera on adjustable arm; 5 – Flow meter; 6 – Adjustable reservoir (pipette with stopcock); 7 – Pressure meter; 8 – Tissue phantom with flow channels

3.4.2.3 Camera setup

It was hypothesised that a maximum of image details in terms of resolution, contrast, motion and colours would result in richer video magnification signals. To enhance data extraction a research grade multi-pixel camera (Grasshopper GS3-U3-32S4C-C, FLIR Integrated Imaging Solutions Inc. – formerly Point Grey, Richmond, BC, Canada) with a high frame rate and image resolution was therefore chosen for flow phantom experiments. At maximum settings, a resolution of 2048x1536 pixels can be recorded at a rate of 121 frames per second (fps). The camera was connected to a standard windows computer via a USB3 port. Company issued software (Flycap2™) was used to record video sequences at maximum resolution and 30 fps. All sequences were recorded in the AVI file format at a running length of 7 seconds (s). This duration was chosen because the file size was limited to 2 gigabyte by the recording software which corresponded to a video duration of 7s at a desirable resolution and fps combination. In preliminary experiments no detrimental effect in VM signal quality was found in relation to video duration at lower video resolutions that enabled recording of longer periods.

3.4.3 Porcine study

3.4.3.1 Concept

The underlying hypothesis is that VM signal strength or quality would be influenced by the presence of circulation and associated blood vessel motion during pulsatile flow. An animal model was chosen to compare VM signals from a number of organs including the liver during presence of blood flow intraoperatively and the absence of flow following euthanasia.

3.4.3.2 Camera and recording

An experimental model of porcine laparoscopic liver resection was used to sequentially record data for CLE and VM experiments. For a description of the model please see above section on CLE imaging. VM data was recorded prior to CLE data. A stereo-laparoscope (Conmed – formerly Viking, Utica, NY, USA) was used for recording of sequences. Data from only one of the two laparoscope channels was processed for experiments. The channel with the best image quality (i.e. no smears or smoke causing visual occlusion) was chosen for processing. During recording the laparoscope was held in a stable position with both hands to reduce the amount of involuntary tremor that is common with laparoscopic videos. No mechanical laparoscope clamp was used. Sequences were recorded in H264 format at a resolution of 1920x1080 pixels and subsequently converted to MP4 format for further VM processing. File conversion was carried out using a non-commercial software programme (RipBot264, Freeware written by Atak Snajpera).

3.4.3.3 Impact of motion on VM signals

All sequences were recorded before and after euthanasia to evaluate if the cessation of circulation had a measurable impact on VM signal strength. It was anticipated that extraneous motion i.e. image tremor from holding the laparoscope and respiratory motion of the diaphragm would also influence VM signals. Therefore several sequences were recorded during brief apnoeic episodes of no more than 5s and then repeated during regular ventilation. The VM signals extracted from these sequences were then subsequently compared to each other.

Laparoscopic ultrasound doppler signals were recorded during some of the experiments to verify the presence of flow in the organ areas that were recorded for VM signal processing. Further doppler signals were recorded following euthanasia to verify the absence of blood flow.

3.4.3.4 Experimental design

To develop and test a quantification method for VM signals, a number of experiments were conducted that compared motion signals using the following experimental designs.

In flow phantom experiments, different areas in the same field of view (ROI's) were compared t each other. This was useful because perfusion and pulsation could be deliberately controlled. In the porcine experiment, two separate videos were recorded from a standardised scenario (e.g. laparoscopic view of the liver) during the presence or absence of perfusion (Figure 3.16).

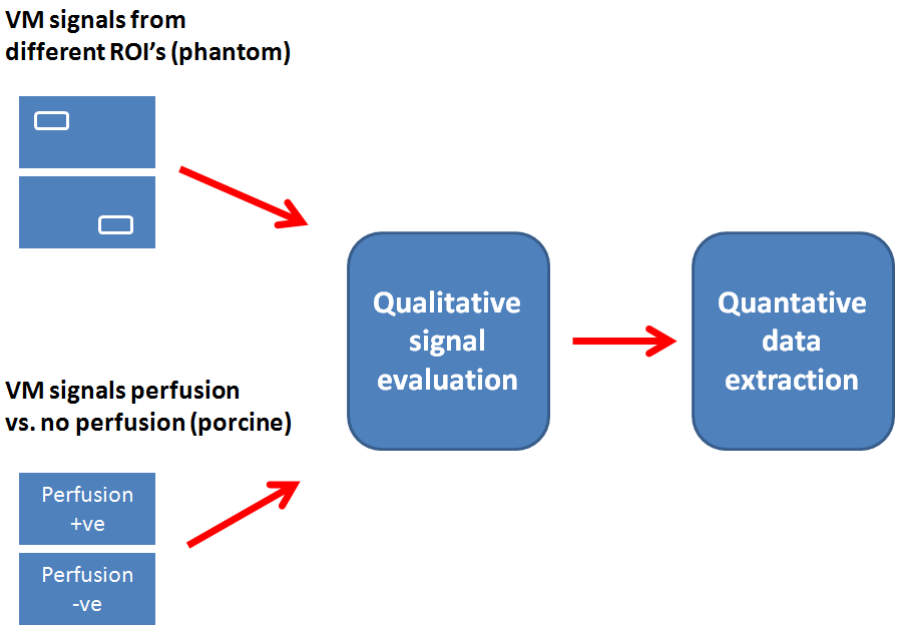

Figure 3.16 Experimental design structure for video magnification studies.

3.4.4 Use of the Gray level co-occurrence matrix for motion signal quantification

Quantification of motion signals could not be measured by simply plotting variations in pixel intensity as described previously (136) because the intensity of a pixel representing a moving object may or may not change with the extent of movement. Popular methods of estimating motion in video such as the use of a Kalman filter or Lucas-Kanade optical flow, work by tracking the change of object position over several video frames. Magnified motion signals however reveal themselves as a repetitive change in texture or outline of edges. Therefore applying the aforementioned methods to motion estimation in VM is problematic because there are no clearly identifiable objects that can be tracked. A more recently proposed method of motion estimation is based on the analysis of image texture through utilisation of the gray level co-occurrence matrix (GLCM). The GLCM can be regarded as a representation of the spatial relationship between pixels of an image that have been ordered into groups according to their grayscale intensity. The number of gray levels and spatial relationship to neighbouring pixels (e.g. horizontal direct neighbour or vertical 3 pixels distant neighbour) can be specified individually (Figure 3.17). It has been demonstrated previously (261) that temporal changes in the GLCM (i.e. image texture) can be used to estimate motion in video sequences. Statistics derived from a GLCM such as Energy, Homogeneity, Contrast and Correlation allow quantification of these temporal changes and these statistics will be employed in this work to measure and compare VM motion signals.

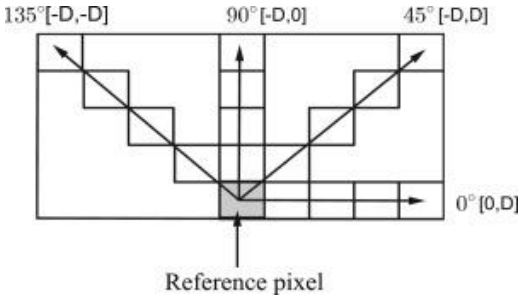

Figure 3.17 Example for variation in pixel offset for GLCM processing.

The pixel of interest may be compared to its direct neighbour or pixels that are further distant. The spatial relationship is further defined by neighbourship direction on a horizontal, vertical or diagonal plane (262)**. (reprinted with permission from Elsevier, copyright 2014)**

3.4.4.1 Selecting regions of interest

With a few exceptions, VM signals in a video sequence are not represented throughout the whole field of view. Therefore it is necessary to focus evaluation and quantification of signals on a defined region of interest (ROI) such as the liver surface on a laparoscopic video for example. To facilitate VM signal assessment in ROI's, a MATLAB function was created to define and retrieve image data (henceforth referred to as "grabbing") from a fixed region of a video sequence. In essence the retrieved data can be regarded as a cut-out "mini-video" that is part of the original video sequence (Figure 3.18). The colour and motion VM signals in the grabbed data were subsequently analysed using the methods outlined above. For standardisation purposes, fixed ROI dimensions were used for statistical comparison of signals from the same video or from the VM and control video as appropriate.

Figure 3.18 ROI marking in laparoscopic video

A ROI is marking a superficial liver tumour at the bottom edge of the liver. For subsequent image signal processing only signals from the ROI are processed.

3.4.4.2 Quantification of motion signals

The GLCM statistics were processed in the following manner. Initially two ROI's of identical dimensions were marked in regions were motion quantification was intended. Usually this involved one region with pulsatile motion and one region without, in flow phantom studies. In the porcine experiment identical ROI's from different videos were evaluated as described above. The video data from each ROI was stored separately and subsequently underwent transformation into 8bit grayscale format to enable GLCM processing. Consequently, the GLCM parameters: Energy, Correlation, Homogeneity and Contrast were extracted for each ROI. To facilitate comparison, GLCM statistical values were plotted against time in a 2D-coordinate system (Figure 3.19). In addition mean, median and standard deviation were calculated for the entire ROI window and visually compared using bar charts (Figure 3.20).

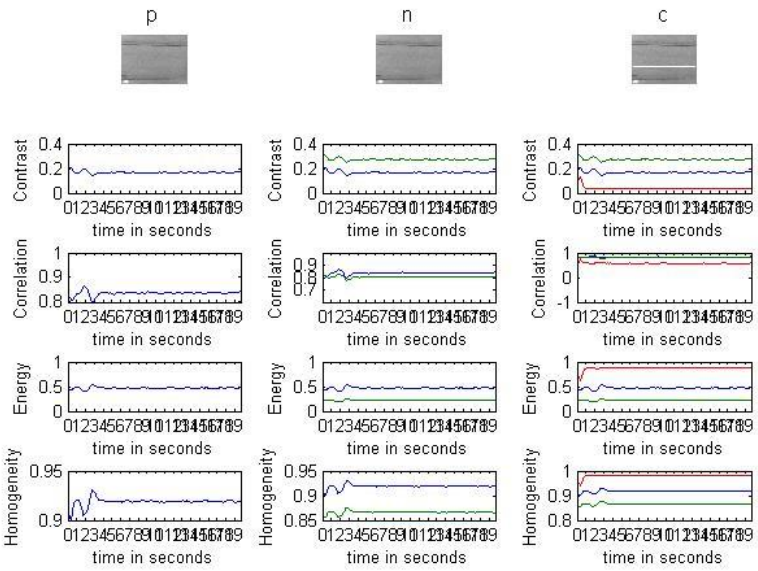

Figure 3.19 Plot of GLCM statistics.

GLCM statistics, measured on a perfused flow phantom, plotted over time. The top row shows the ROI's marked on the screen. In this experiment a third ROI was marked as control.

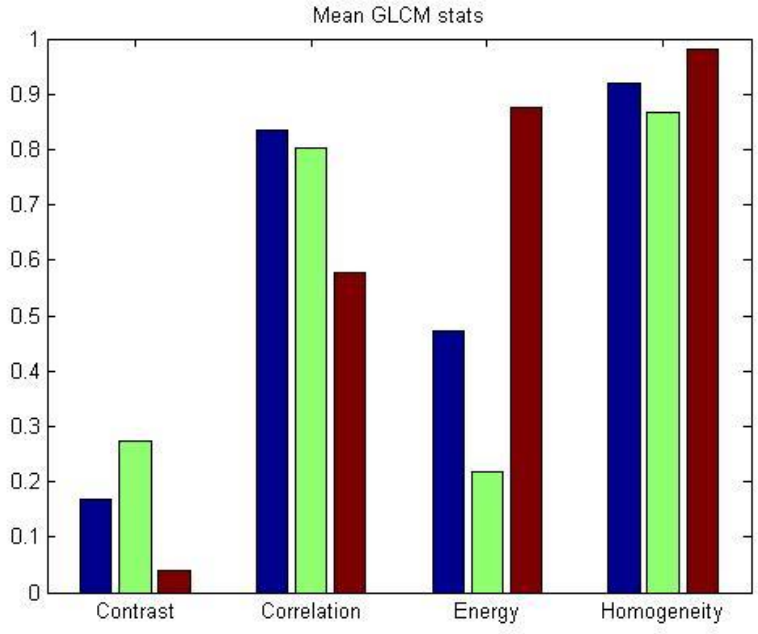

Figure 3.20 Mean GLCM statistics.

Mean GLCM statistics from the same experiment as figure 3.19 presented as bar charts of the mean values over the whole period.

3.4.4.3 Statistical analysis

Group values are stated as median ± IQR. The distribution for GLCM statistical values was evaluated with the Shapiro-Wilks test and found to be non-parametric. Therefore the Wilcoxon-sign or Kruskal Wallis tests were employed to compare groups as appropriate. Binominal regression analysis was used to elucidate if GLCM statistical values were independent predictors for the presence of motion. The variable selection method 'Enter' was used for the regressions analysis. Finally ROC analysis was carried out to determine the diagnostic accuracy of GLCM statistics for indicating presence of flow. As indicated below the GLCM statistics or their respective gain values are correlated with the presence of flow (perfused catheter vs. control catheter). Optimal sensitivity and specificity values were chosen arbitrarily, based on the highest combined values for sensitivity and specificity from an output table that summarises the relationship of these parameters as seen in the ROC curve. Depending on the scientific question a different cut-off point can be selected. For all tests, statistical significance was assumed at $p<0.05$. Statistical analysis was performed using SPSS™ Version 21 (IBM, Armonk, NY, USA).

The author helped with carrying out the surgery in the porcine laparoscopic model. All other experimental procedures were performed by the author himself.

3.5. Image guided surgery

Experiments related to the development of an image guidance system for laparoscopic liver surgery were carried out on the porcine model already described above (3.1.4.1). Once the system had matured sufficiently, it was evaluated in a clinical feasibility study, where its performance in terms of imaging accuracy in a real surgical setting could also be assessed.

3.5.1 General principle

Intraoperative image guidance facilitated by the use of an image guidance system (IGS) is a technology that is widely used in neuro- and spinal surgery and more recently has created considerable interest for laparoscopic applications (128,129,141,210). In essence an IGS allows the surgeon to view structures that can be seen on preoperative scans but that are not visible with a laparoscopic camera (128). This is highly desirable in LLR because it enables the surgeon to localise crucial subsurface structures such as tumours or blood vessels in real-time. This approach of combining virtual data in the form of a computer graphic with real life images from a video feed is also called augmented reality (AR).

The IGS consist of 3 key components or processes, namely: 1) 3D modelling and planning - to create a virtual representation of individual patient anatomy 2) registration and tracking - to align “virtual” and real anatomy and 3) Visualisation - to make the information interpretable to the surgeon. The individual processes are outlined in greater detail below.

3.5.2 IGS development and evaluation in a porcine model

The IGS (prototype named SmartLiver) used in these experiments was developed by a collaboration of clinicians and computer scientists at University College London. All IGS software component s with the exception of the 3D model creation process were developed de-novo by this team. In contrast to this the hardware components (e.g. laparoscopic camera, infrared tracked objects etc.) are all commercially available. The author of the thesis contributed significantly to this work at certain development stages, namely the preclinical (porcine experiments) and clinical stages, and will therefore present results from this collaboration within the relevant chapters. There was no author involvement in the technical development stage which included the creation and testing of an IGS hardware and software platform, but since the underlying concept is important to understand the experiments below, a brief summary of the technical phase will be provided here.

The SmartLiver software system has been assembled from a number of independently developed software components that each control individual tasks such as e.g. visualisation, tracking control or registration. To transform and integrate the single components into a working system the NifTK software platform was used (263). The advantage of the platform is that it excels in streaming stereoscopic video and tracking data simultaneously which means it is well placed to form the basis of a laparoscopic IGS. New software components were evaluated on a silicon liver imaging phantom (data not included in thesis as author did

not partake in these experiments) to ensure a robust and fluent performance before being transferred to *in*-vivo experiments (Figure 3.21).

Figure 3.21 Silicone liver phantom.

A liver phantom was created from silicone to emulate the subtle surface features of the human liver. The phantom was used to evaluate the SmartLiver in an *ex-vivo* setting.

One of the novel aspects of the IGS presented here is the use of stereoscopic surface reconstruction to automatically register 3D model and patient liver. Because processing speed for real time stereoscopic surface r is crucial, the first step was to create a computer algorithm that made use of fast parallel computing which is based on graphics processing units (GPU) that are commonly found in computer graphics card. The main advantage is that complex problems can be computed simultaneously as opposed to computer processor unit (CPU) based applications that use a sequential mode. To achieve this, the computer vision method of matching propagation was adapted to process multiple high resolution frames, an approach which overcomes essential restrictions on parallel data processing and therefore enabled a GPU implementation of the algorithm. The underlying work does not form part of this thesis and has been described in detail previously (264).

As an alternative to surface based reconstruction, a manual registration algorithm was also implemented into SmartLiver. Manual registration is based on moving a hand-held tracked object in which acts as a representative of the 3D liver model. Movement in the real world is translated into movement on the screen until a satisfactory position is achieved, which can

be locked and remain in place until the liver is manipulated which may require a further registration cycle. Although this approach proved useful in the preclinical phase it was complicated to use in the clinical study due to operating sterility issues. Therefore an additional option to carry out manual alignment with a graphic user interface (GUI) was implemented. At the later stages of the clinical study a GUI for SmartLiver was written which substituted system control via the NiftyK programme and made it amenable for use by non-technicians. The testing and integration of infrared tracking system, the stereo-laparoscope and the CT acquisition for the creation of 3D models is described in detail below.

3.5.2.1 Experimental workflow

A detailed description of the porcine model has been provided above (3.1.4.1). On the first day (OP1), ablation zones were created to simulate liver tumours. A CT scan was obtained while the pig remained under general anaesthetic and the data from this scan was transformed into a 3D model of the liver. Following the 7-10 day recovery period, the animal underwent a second laparoscopic operation that either was purely exploratory (i.e. no procedure was carried out) or that included a laparoscopic left hemi-hepatectomy as described above (OP2). During this 2nd operation the 3D model was registered to the porcine liver as seen on the laparoscopic screen which enabled the creation of an augmented reality environment. Data recorded during the 2nd procedure was subsequently analysed to study organ motion, deformation, overlay accuracy and to compare different methods of registration (manual vs. surface based registration). Following termination the pneumoperitoneum was maintained while a cone beam CT (GE healthcare, Chicago, IL, USA) of the porcine liver was obtained post-mortem to quantify postoperative liver deformation.

3.5.2.2 Intraoperative CT scans and 3D model creation

Prior to any abdominal surgery being carried out, central venous access was established to facilitate injection of intravenous contrast. This was achieved through a cut-down to the internal jugular vein and insertion of a 16G central venous line into the proximal portion of the internal jugular. The distal end of the vein was ligated immediately after insertion of the line. Contralateral internal jugular veins were used for access on OP1 and OP2. After removal of the line on OP1 the proximal end of the vessels was ligated as well.

A total of five CT scans were acquired for each animal. Two triple-phase CT's with intravenous contrast were taken on OP1 and OP2; one with a fully inflated pneumoperitoneum (10-12mmHg) and one with the pneumoperitoneum deflated (<5mmHg). These scans provided the basis for 3D liver models representing the organs shape with and without soft tissue deformation caused by increased intraabdominal pressure. Timing of scans was immediately after liver ablation on OP1 and after establishing the pneumoperitoneum on OP2. To facilitate imaging, laparoscopic ports were disconnected from the insufflators but kept close to maintain positive intraabdominal pressure. Animals remained under general anaesthetic and were then transported to a mobile CT scanner unit

(Name of company). Following CT scanning under insufflation, the laparoscopic ports were opened and a second CT scan was carried out in a deflated state. Triple phase CT's rendered arterial, venous and non-contrast liver image volumes at 2.5mm slice thickness. Following termination on OP2, a cone beam CT (company and parameters) without contrast was acquired post mortem to assess the amount of deformation caused by liver resection.

CT data was then submitted to the visible patient service provided by IRCAD™ (Strasbourg, France) (265) which created a 3D computer model depicting the livers vascular and biliary anatomy in relation to the ablation zones. The resulting computer model was loaded onto a custom made software platform (263) that was used as an experimental user interface for processing the image overlay and recording of resulting imaging and accuracy parameters.

3.5.2.3 Theatre layout

The surgeon was positioned on the right side of the operating table for most of the procedure. In addition to the laparoscopic monitor, two screens displaying to composite image overlay were positioned on either side of the operating table. The optical tracker was mounted onto a mobile, telescopic tripod system that could be adjusted in height to obtain a free line of sight of the tracking markers. In most instances an optimal position was achieved on the left top-end of the table. A wheeled stack containing a computer and video capture equipment was positioned on the left periphery of the operating theatre and connected to laparoscopy stack, additional screens and optical tracker via cables. The position of this stack was altered as required so as not to interfere with the surgical procedure.

3.5.3 Clinical evaluation

3.5.3.1 Description of the clinical image guidance system

3.5.3.1.1. Virtual 3D liver model

The 3D models used in this study (Figure 3.22) were reconstructed by Visible Patient™ (Strasbourg, France). In brief, the 3D models were produced from a contrast enhanced CT with a slice thickness of 0.5-3mm, which was carried out as part of routine clinical practice for staging of patients with suspected hepato-pancreato-biliary cancers. Patients were consented in outpatient clinic and their scans were retrieved from the hospitals imaging database. Subsequently images were transferred securely and anonymously to Visible Patient™. Maximal processing time for the 3D models was within a time frame of 5 working days.

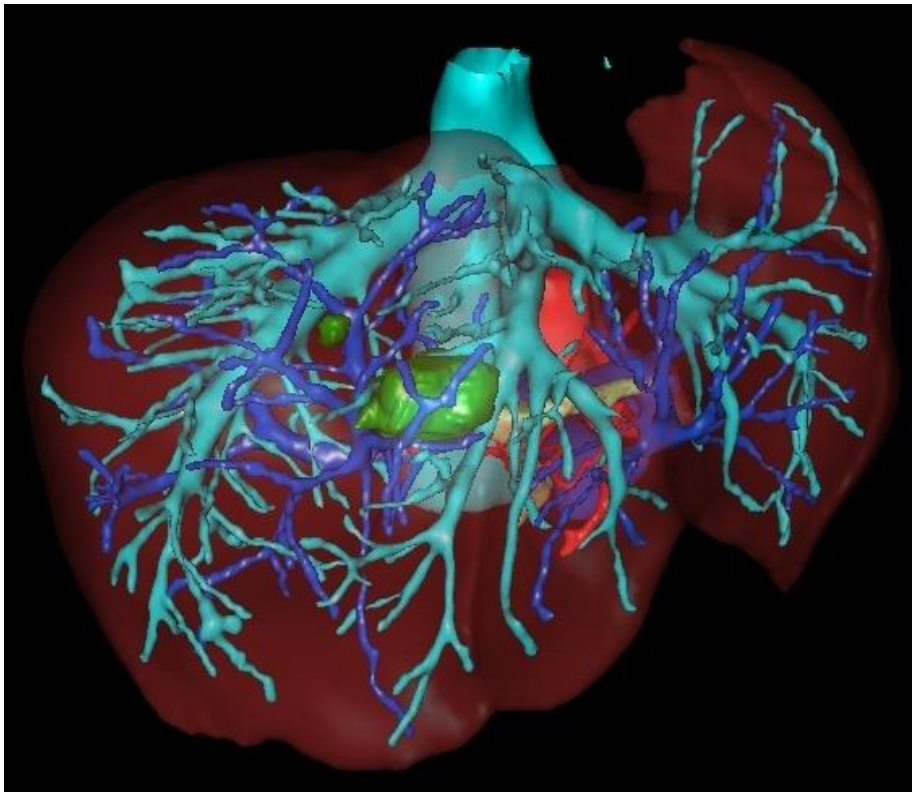

Figure 3.22 Example of a 3D liver model as used in the clinical study.

A 3D model showing the anatomical relationship of hepatic vasculature (hepatic veins, light blue - thick arrows, portal veins, dark blue – thin arrows; arteries, red - #) and liver tumours (green - *) is created in the first stage of the image guidance The semi-opaque brown volume delineates the outer margin of the liver parenchyma.

3.5.3.1.2. Tracking

Tracking was achieved by attaching passive infrared reflecting markers to the laparoscope prior to surgery (Figure 3.23). Intraoperatively, the position of these markers was then continuously recorded with a Polaris Spectra™ optical tracking camera (NDI Medical, Waterloo, Canada) which was positioned in the proximity of the operating table. Because SmartLiver provides AR visualisation (i.e. integration of real world video and virtual world 3D modelling), there is no need to track or calibrate surgical instruments as their positional relationship with the 3D model can be appreciated throughout the procedure.

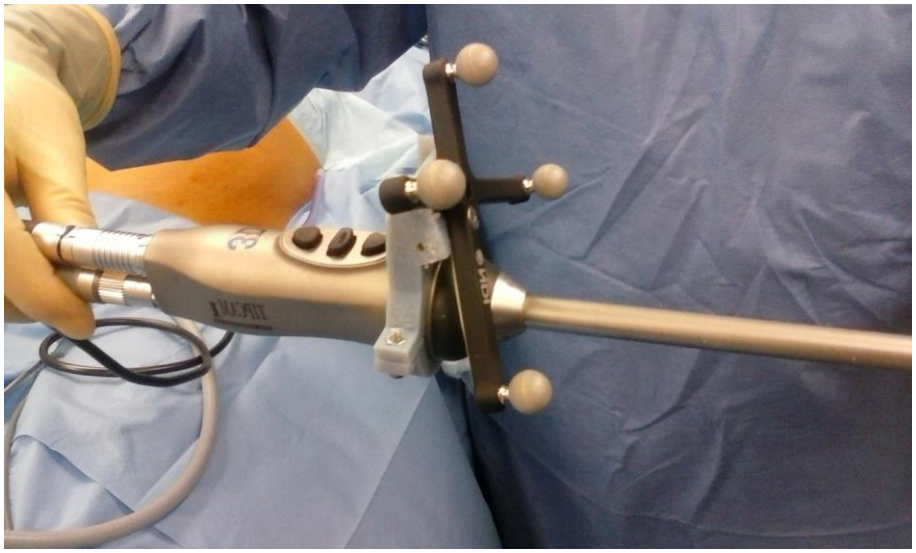

Figure 3.23 Position of tracking markers on the stereo-laparoscope.

Intraoperative configuration of passive reflective optical tracking markers installed onto a stereo-laparoscope.

3.5.3.1.3. Registration

SmartLiver was designed to enable either a manual or an automatic registration between the liver model produced from the pre-operative CT scan and the laparoscopic visualisation of the liver at surgery. Manual registration is facilitated by using the graphical user interface buttons on a touch screen monitor (Figure 3.24) to manipulate the 3D model into an anatomically appropriate position. The automatic registration mode utilises a computer vision technique called stereoscopic surface reconstruction (SSR) which recovers 3D geometry optically (208,264). In essence, the right and left channel of a 3D laparoscope (IMAGE 1S - TIPCAM, KARL STORZ, Tuttlingen, Germany) are used to triangulate the geometry of the visible liver surface. This geometric data is transformed into a cloud consisting of several hundred thousand points which represent the in-vivo liver surface shape Figure 3.25). Point clouds constructed from multiple views of the liver are composited using the tracking information from the Polaris tracking system. The point clouds are then resampled (i.e. points are combined to reduce their number) to several thousand points to make them computationally manageable. A corresponding point cloud is generated from the surface of the 3D liver model and subsequently both point clouds are computationally aligned with each other (i.e. registration process) using the iterative closest point (ICP) algorithm. Optimal alignment is calculated by minimising the residual error between 3D model and *in*-vivo liver surface. Our group has previously refined this registration method and demonstrated its feasibility in a porcine model of laparoscopic liver resection (172,264).

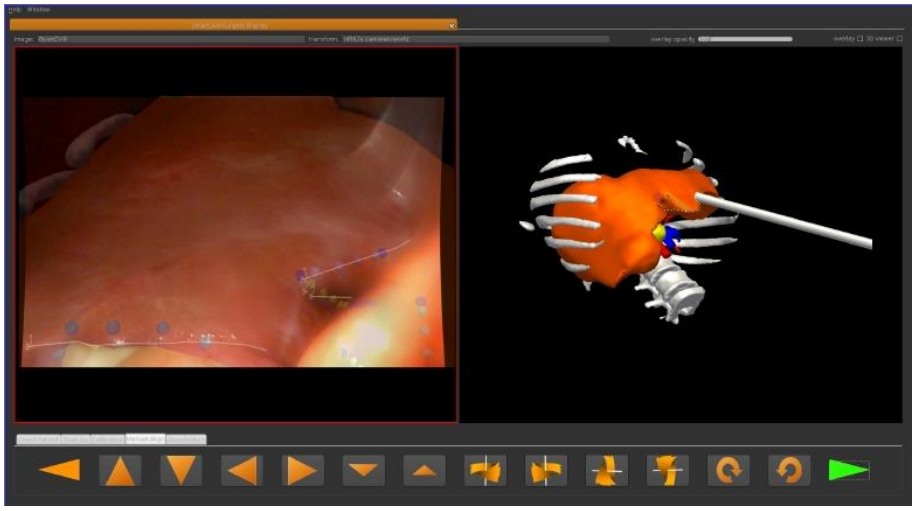

Figure 3.24 Touch screen control of the registration process.

The 3D model can be registered to the laparoscopic video stream via touch screen buttons.

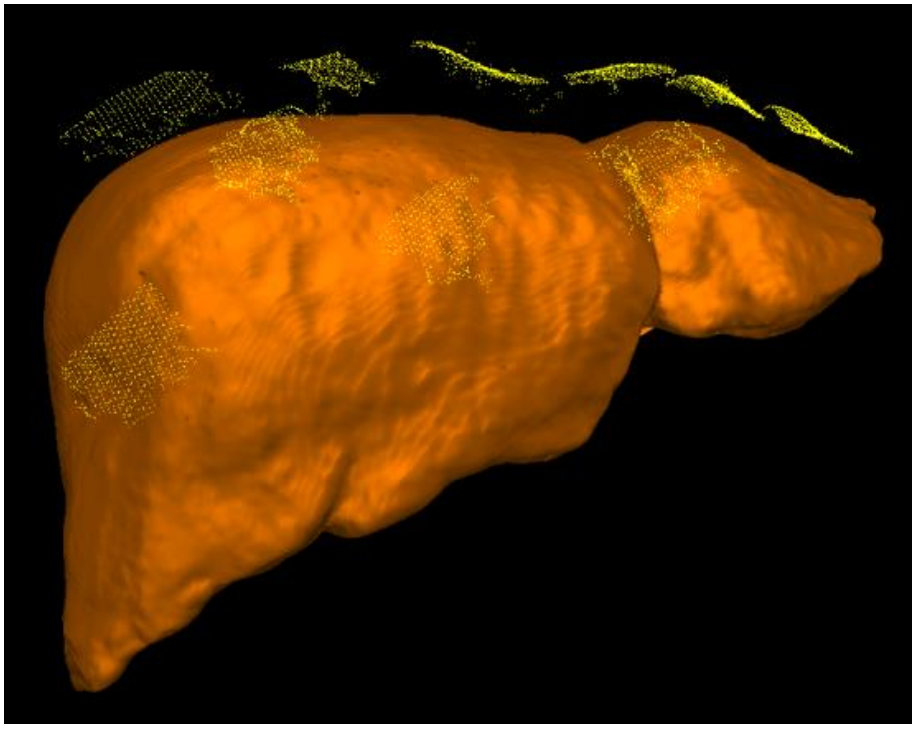

Figure 3.25 Point cloud used for ICP based registration.

The point cloud can be seen as yellow dots that outline a surface that is a close match to the 3D liver model outline.

3.5.3.1.4. Integration of the IGS into the operative workflow

The SmartLiver system consists of a mobile stack that contained all the required hardware and software components, a separate high definition (HD) screen and an additional flexible arm attachment for the positioning of the optical tracking camera (Figure 3.26). The 3D laparoscope system which has its own HD screen was kept on a separate factory-issue stack.

Figure 3.26 IGS setup in theatre.

The optical tracking camera attached to an adjustable arm can be seen on the right of the image. The laparoscopic screen showing a video feed without the 3D model overlay is further to the left.

In general, the setup process can be divided into a pre- and intraoperative phase. Prior to surgery both stacks were moved into the operating room and connected to each other using a DVI to SDI image splitter (ROI™ Mini-Converter, AJA, Grass Valley, USA). Subsequently, the SmartLiver system was initialised and the patient specific 3D model was loaded onto the platform. At completion of the anaesthetic induction the tracking camera was positioned at the head end of the operating table at approximately 160-190cm height to obtain an unobstructed line of sight of the laparoscopic camera with mounted trackers. Intraoperative setup commenced with the installation of the custom made collar bearing the tracking markers, onto the case of the laparoscopic camera. Tracking attachments were not sterilised and hence were covered with a sterile sheath to allow intraoperative handling. Subsequently a calibration procedure according to the Zhang (266) chequerboard method or in later cases according to our own “cross-hair” method (267) was carried out to adapt the system to the position of the tracking markers.. In practice the calibration involved filming of a standardised graphic figure from different angles. Once successful calibration was confirmed the recording of study data commenced.

3.5.3.2 Clinical study

The study was approved by the local research ethics committee (Reference: 14/LO/1264 & 10/HO720/87 and registered with ISRCTN (ID: 77923416). Patients who were 18 years or older undergoing staging laparoscopy or laparoscopic liver resection were eligible for inclusion in the study. Initially it was planned to only include patients undergoing LLR but because patients undergoing a staging laparoscopy offered the same potential for assessing SmartLiver, it was decided to include patients undergoing staging laparoscopy. Demographic patient information and perioperative data including operative time were recorded for all patients. In addition to these the conversion to open surgery rate, serious perioperative incidents, significant intraoperative blood loss, postoperative complications (Clavien-Dindo grade), resection margin status and length of hospital stay were also recorded for LLR patients. Significant intraoperative blood loss was defined as a requirement for intra- or postoperative blood transfusion or a reduction in postoperative haemoglobin level of ≥3g/dl compared to preoperative levels. Ethical approval allowed evaluation of the IGS, but surgeons were not permitted to use the displayed information to adjust intraoperative strategy.

3.5.3.3 Task description and endpoints of the clinical evaluation

The aim of the study was to assess the feasibility of using the SmartLiver system for intraoperative image guidance, to evaluate how accurately the 3D model represented *in-vivo* anatomy and to assess usability. The primary endpoint was defined as a successful registration resulting in an augmented reality display of 3D model and laparoscopic video feed. Secondary endpoints were the anatomical accuracy of the AR display, usability evaluation and the occurrence of critical incidences. Additionally, postoperative outcome data for patient that underwent LLR was also recorded.

The protocol for intraoperative data collection included the following steps. After the calibration was completed the laparoscope was inserted into the abdomen to record liver surface points individually from the anterior left and right hemi-liver. To prevent loss of surface data the laparoscope was moved at a slow and steady pace in an attempt to cover the entirety of each lobes anterior surface. To facilitate manual registration, the laparoscope was kept stationary focusing at anatomical landmarks of the right or left lobe such as the liver edge or the porta hepatis. While the surgeon handled the laparoscope one of the technical developers carried out the manual registration.

For the first patient registration was carried out intraoperatively to confirm the functionality of the system. The complete duration of the intraoperative data collection protocol was found to be in the range of 20-30 minutes. It was felt that this was too much time to add to a staging laparoscopy. To save time it was decided to focus solely on intraoperative data acquisition for the subsequent patients and to carry out the registration process after surgery. For standardisation purposes this approach was also maintained for LLR patients recruited to the study.

3.5.3.4 Clinical usability evaluation

A usability survey was drawn up by the research group with the aim of obtaining surgeon feedback on the systems usability. The questions were drawn up to guide the ongoing development of SmartLiver and to allow workflow adjustments if necessitated by clinical requirements. Following completion of each procedure, surgeons were asked to fill out the usability survey which was focused on system ergonomics and user friendliness. Seven standardised questions were scored on a Likert scale from 1-5. In addition there was space on the survey to provide suggestions for improvements.

3.5.3.5 Analysis of imaging accuracy

Due to the lack of any standardised methods for assessing the imaging accuracy of AR based IGS, our group has previously proposed a novel evaluation method which was also employed in this study (172). In summary the method utilises the 2D distances between corresponding anatomical landmarks on the laparoscopic video and the 3D model (Figure 3.27). Therefore the landmark position on the video can be regarded as the gold standard because it reflects the true position of liver anatomy as perceived by the surgeon. The accuracy for each relevant landmark is typically evaluated over multiple video frames to account for intra-patient variation. Finally the root mean square (RMS) value of all individual distance errors in millimetres is calculated to provide a meaningful estimate of the target registration error (TRE) for each patient.

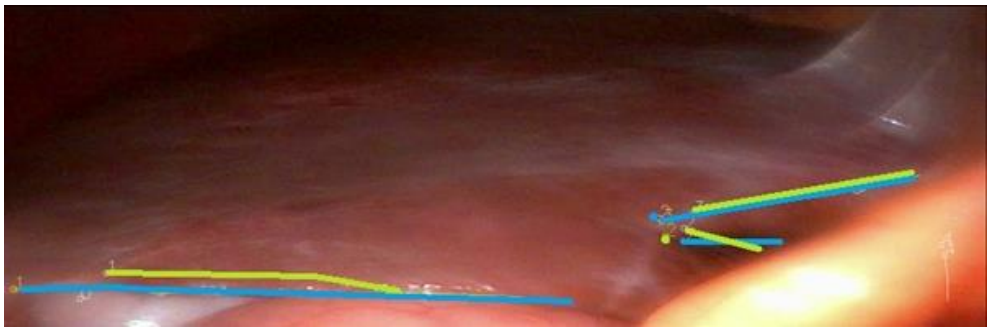

Figure 3.27 Anatomical landmark based accuracy estimation.

Distance between patient anatomy (blue landmarks) and 3D model anatomy (green landmarks) is measured to determine the registration error.

It is important to consider that due to current technological limitations, IGS depend on the static and rigid 3D models which do not change position or shape to reflect the physical forces exerted on the liver by respiratory motion, cardiac motion, increased intra-abdominal pressure or surgical manipulation. Therefore the TRE consists of three surgically relevant key components, namely the errors introduced by registration, motion and deformation. To provide an estimate of how much each of these components influences the final TRE, an assessment of motion error and deformation error is stated in addition to the overall TRE. The median and interquartile range of the motion error is stated in mm and was calculated

by plotting the maximum positional change of each video frame based landmark over time. Essentially it can be regarded as a measure of how much the liver moves in relation to the theatre environment. The deformation error in contrast to this measures how much the liver changes shape during surgery. It is calculated by observing to what extent the distances between different anatomical landmarks change over time. The landmark distances on the 3D model serve as a gold standard. In parallel with the TRE, overall deformation is expressed as root mean square in millimetres.

The author of this thesis was not involved in *ex-vivo* experiments on the silicon liver phantom. For the data acquisition during porcine experiments and clinical study he worked jointly as part of a research team. Analysis of the clinical data was carried out by the author with some assistance (provision of customised software modules) from the computer science members of the research team.

4. Identification of Liver Metastases with Probe-Based Confocal Laser Endomicroscopy at Two Excitation Wavelengths

4.1. Introduction

Colorectal cancer is one of the most common cancers globally, being the third most commonly diagnosed cancer in men and second most common in women (16)(268)(269)(270).

Surgical resection of solid tumour metastases is the preferred treatment for curative intent (271,272), resulting in 5-year survival rates approaching 60% (270). Incomplete tumour resection occur in up to 17% of cases and detrimentally affect patient survival (273,274). Macroscopically, colorectal cancer liver metastases (CRLM) usually exhibit a white appearance that makes larger nodules easy to distinguish from normal liver tissue, which appears brown.

Unfortunately, visual assessment is insufficient to confirm complete tumour excision. Although intraoperative ultrasonography (IOUS) and bi-manual palpation are frequently used to determine tumour location within the liver, this approach is not suitable to identify residual cancer following resection because it is mainly of a microscopic nature (275,276). Identification of residual disease using histopathology is not feasible during liver resection. An imaging modality that can confirm or refute the presence of malignancy within liver tissue at a microscopic level would therefore be helpful in ensuring complete resection, reducing the amount of liver tissue resected, or to avoid an unnecessary excision if cancer can be excluded (277).

Other imaging modalities such as cone beam CT, magnetic resonance imaging and near infrared fluoroscopy may be able to enhance imaging during liver surgery, but none of these modalities provides an image resolution that would enable identification of residual disease at a microscopic level (229,278,279).

Optical imaging modalities offer micrometer scale image resolution but at this stage only optical coherence tomography (OCT) and confocal laser endomicroscopy (CLE) are available in compact designs that make an intraoperative application feasible. Either imaging modality can visualise liver tissue ex-vivo, but only CLE has been extensively studied in an in-vivo setting (176,280–282). When employed in a compact design, CLE has a better lateral resolution than OCT at 1.4µm vs. 7µm (283). This is an important advantage of CLE which may allow imaging at subcellular level in greater detail. CLE can be performed with a bulkier rigid endomicroscope which contains the required optics in its tip (146) or with a thin, flexible fibre based endomicroscope that conducts the excitation laser and transmits signals to an external laser scanning unit (248,282). For the latter, a commercially available solution is the

Cellvizio™ system (Mauna Kea Technology, Paris) which can be used in conjunction with fibre-optic probes ranging from 0.3-4.5mm diameter.

Studies comparing confocal laser endomicroscopy (CLE) with standard histology in animal models, have proven its ability to visualise the cellular architecture of tissues, thereby providing a method of obtaining virtual, in vivo histology in real-time (281,284). In clinical practice, probe based confocal laser endomicroscopy (CLE) is licensed for the endoscopic diagnosis of gastrointestinal, bronchial and urinary malignancy and dysplasia. Depending on the tissue type, diagnostic accuracy is in the range of 86-91% (249,285–287). Recent reports suggest that CLE may also be a useful tool for the detection of breast and head and neck cancers (288,289)

4.1.1 Aims

The specific aims in this chapter are:

1) describe virtual histology of normal murine liver on CLE examination using fluorescein at 488nm and indocyanine green at 660nm illumination.
2) describe virtual histology of liver metastasis in this murine model and examine blood circulation characteristics in its tissue, using the same CLE imaging technique as in
3) assess the ability of CLE to predict the presence of normal vs. cancerous liver tissue based on fluorescence intensity variations.

4.2. Methods

General and specific methodology has already been described above (3.1.3). It was felt to be advantageous for ease of reading to avoid separating the methodology across chapters.

4.3. Results

4.3.1 Test sample size

The orthotopic CRLM model was established in 8 mice. One animal died before any CLE measurements could be carried out. The remaining 7 mice underwent CLE examination. In two animals the tumour burden relative to normal liver was too great to allow meaningful statistical comparison. Two animals died during image acquisition; one (ID6) before sufficient data at either wavelength could be collected and a further animal following completion of CLE imaging with fluorescein at 488nm (ID7). In summary 6 animals underwent consequential CLE imaging and of these, 4 (fluorescein / 488nm) and 3 (ICG / 660nm) experiments provided sufficient data for statistical analysis.

4.3.2 Evaluating normal liver at 488nm wavelength with fluorescein

Examples of CLE images and H&E histology for normal and CRLM tissue are shown below. Each example is from the same animal but due to the frequently small size of lesions, no attempt was made to spatially correlate CLE images with histological slides. Macroscopic lesion size was larger than the CLE field of view but otherwise variable between animals.

The smallest lesions were 1-2mm whereas in some animals the majority of the liver surface was covered by metastatic deposits.

Prior to administration of fluorescein no endogenous fluorescence was observed in normal or metastatic tissue. The initial period following fluorescein injection was termed the inflow phase. During this phase the fluorescein strongly accumulated within the vascular compartment and could be observed in hepatic sinusoids and interlobular vessels Figure 4.1). Occasionally, individual erythrocytes could be visualised moving through blood vessels or sinusoids. Because erythrocytes did not take up fluorescein they could be seen as small, dark, round or discoid shapes outlined against the bright contrast signal of the intravascular fluorophore (Figure 4.1). Generally, inflow phase images were dominated by a meshwork pattern of bright interlobular vessels criss-crossing dark areas which represented the parenchyma of liver lobules (Figure 4.1).

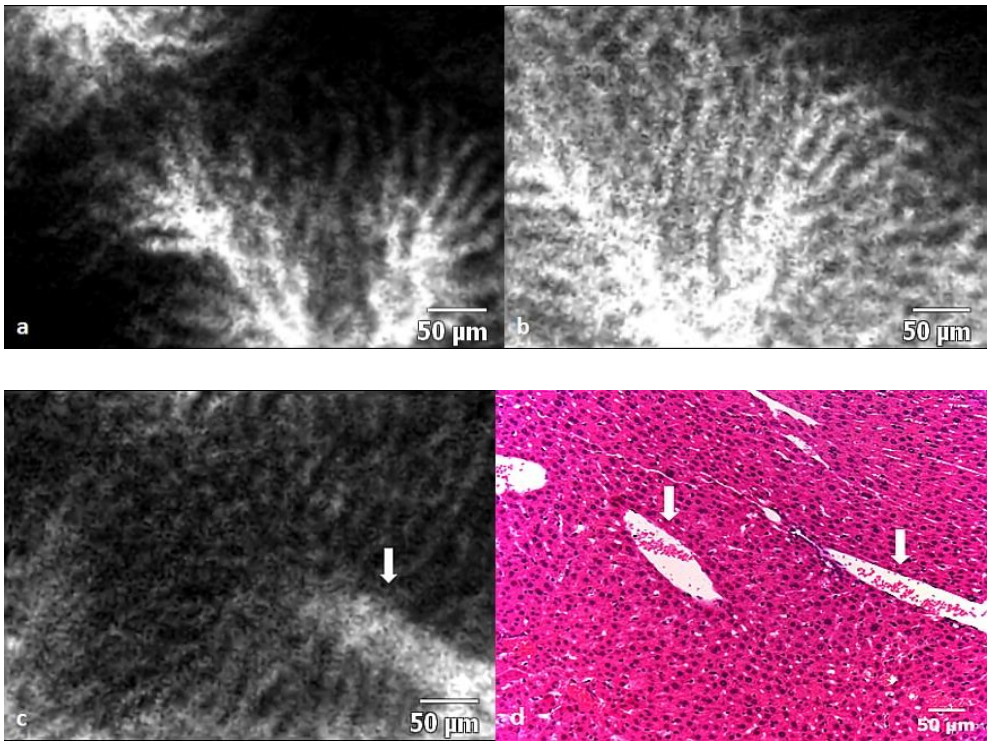

Figure 4.1 CLE of normal murine liver parenchym during the inflow phase at 488nm.

(a) A CLE image (488nm) showing fluorescein entering the intravascular space (bright areas) shortly after injection. (b) At completion of the inflow phase (>12 minutes after fluorophore injection), hepatocyte cords appear dark, whereas the intravascular space which includes sinusoids and larger lobular vessels is bright. (c) Erythrocytes can be seen as dark shapes within the bright intravascular space (arrow). The remainder of the image shows the typical pattern of normal liver parenchym consisting of a mixture of hepatocyte cords and sinusoids. (d) Histology of normal liver tissue with two blood vessels (arrows) containing erythrocytes.

Inflow phase duration varied between animals but was approximately 7-11 minutes. At the end of the inflow phase, the fluorophore shifted from the intravascular compartment to the liver parenchyma and connective tissue, which resulted in high signal intensity within liver lobules. This stage of the CLE examination, lasting throughout the remainder of observations, was termed the parenchymal phase. Throughout its duration, cords of hepatocytes and the sinusoid structure could frequently be observed (Figure 4.2). Sinusoids and other liver vessels appeared largely dark and devoid of fluorescence, and this phenomenon became more marked at the later stages of image acquisition.

Differentiation between types of vasculature (e.g. portal vs. central venous vessels) was challenging at either imaging phase but could sometimes be accomplished by interpreting the vessel's location and morphology. For example, a central vein (which drains towards hepatic vein) could be identified by its location and orientation within the middle of a liver lobule (Figure 4.2).

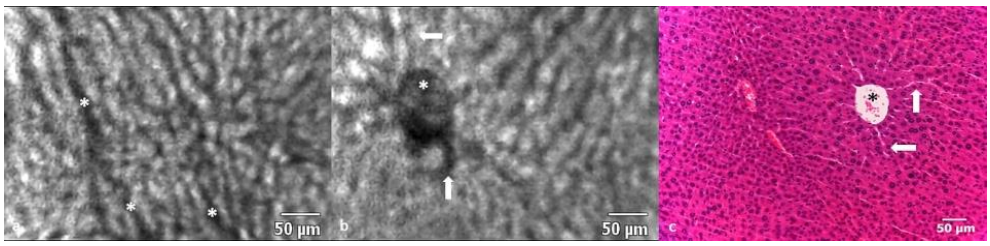

Figure 4.2 CLE of normal liver tissue in the parenchymal phase at 488nm.

(a**) In the parenchymal phase of fluorescein administration, hepatocytes appear bright in CLE images (488 nm) whereas the intravascular space (*) is dark due to extravasation of the fluorophore into the interstitium. (b and c) The central vein (*) can be visualised as a round area in the middle of the hepatic lobule with feeding sinusoid vessels (arrows) converging towards it. (c) Histology with a similar configuration to the CLE image in b.**

4.3.3 Evaluating liver metastases at 488nm wavelength with fluorescein

Areas of CRLM could be analysed in detail at 488nm wavelength using fluorescein. The majority of malignant tissue showed a pattern of dark patches criss-crossed by bright linear structures. The areas devoid of fluorescence represented malignant tissue which was interspersed by torturous, neoangiogenic vessels that traversed throughout the metastasis. Fluorescein appeared to be retained within tumour vessels for longer than in the healthy hepatic vasculature. This resulted in neoplastic vessels displaying high intensity fluorescence throughout most of the image acquisition. Infrequently, glandular structures typical of moderate to well differentiated colonic malignancy could be visualised (Figure 4.3).

Visible erythrocytes exhibited a mostly slow and erratic movement when compared to normal hepatic vessels (Fig. 3b & c). In two animals there was sufficient image data to estimate erythrocyte flow velocity in both tissue types. Median flow velocity in normal tissue

was 0.47±0.13mm/s and 0.52±0.31mm/s compared to 0.18±0.15mm/s and 0.15±0.1mm/s in CRLM tissue for animal ID1 and ID8 respectively. Subjective discrimination between normal and malignant tissue was feasible and a demarcation line could be visualised in all animals (Figure 4.3).

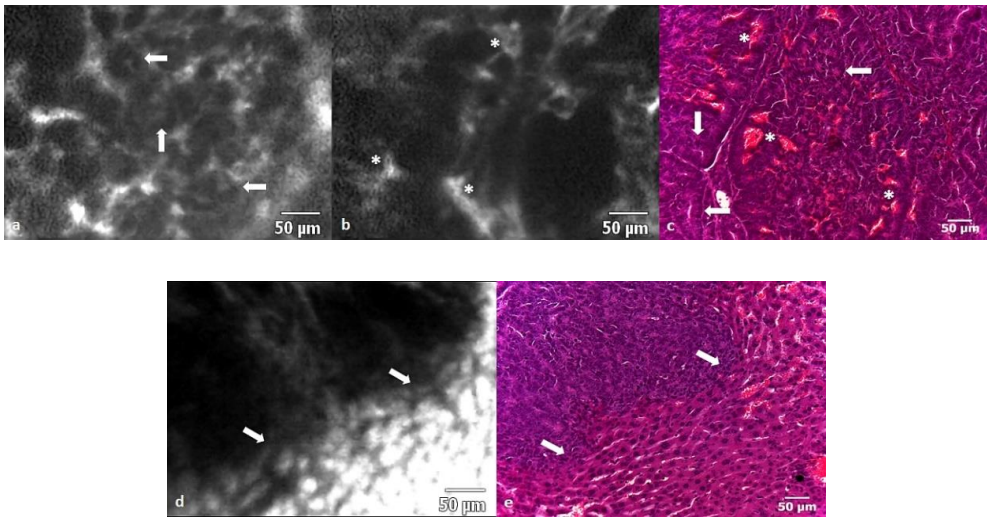

Figure 4.3 CLE of CRLM in the parenchymal phase at 488nm.

(a**) In the mouse model, fluorescein enhancement in CRLM tissue during the parenchymal phase was characterised in CLE images by dark, irregular, round structures that retain some of the original glandular architectural features that can also be seen on histology. The concentric arrangement of adenocarcinoma cells (arrows) results in the "bullseye" appearance of a dark ring around a bright centre on CLE and H&E histology. (b) Irregularly arranged vessels containing erythrocytes (*) can be seen throughout the tumour tissue. In contrast to normal liver tissue, the intravascular space within CRLM retained the circulating fluorophore throughout the entirety of the observation period. (c) The corresponding histology features showing concentrically arranged adenocarcinoma cells (arrows) and irregular vessels (*). (d) The border (arrows) between normal (bright) and cancerous tissue (dark) can be readily appreciated on CLE imaging. (e) Border between normal and cancerous tissue on H&E histology.**

4.3.4 Evaluating normal liver at 660nm wavelength with ICG

CLE examination at 660nm did not reveal any endogenous fluorescence in areas of normal liver or CRLM tissue prior to ICG injection. In contrast to CLE imaging at 488nm with fluorescein, no signal was detectable from blood vessels during the inflow phase following ICG administration, and erythrocyte movement could not be visualised. In the parenchymal phase however, structures with the configuration of central lobular veins could be identified (Figure 4.4). These had the typical appearance of round, irregularly outlined structures, situated in the centre of the lobule. During the parenchymal phase, ICG's high specificity for the cytoplasm of hepatocytes, resulted in good visualisation of sinusoidal structures and allowed distinction between hepatocytes and the surrounding vasculature (Figure 4.4).

In general, blood vessels were identified as linear or round structures that had a lower fluorescence signal, relative to the surrounding hepatocytes. Because of the prominent cytoplasmatic fluorescence, the nuclei of individual hepatocytes were identifiable as dark intracellular areas (Figure 4.4). Approximately 15 minutes after injection of ICG, bright regions of around 5-20µm diameter could be observed throughout the parenchyma. This phenomenon possibly represents areas of ICG accumulation (e.g. bile juice) (Figure 4.4).

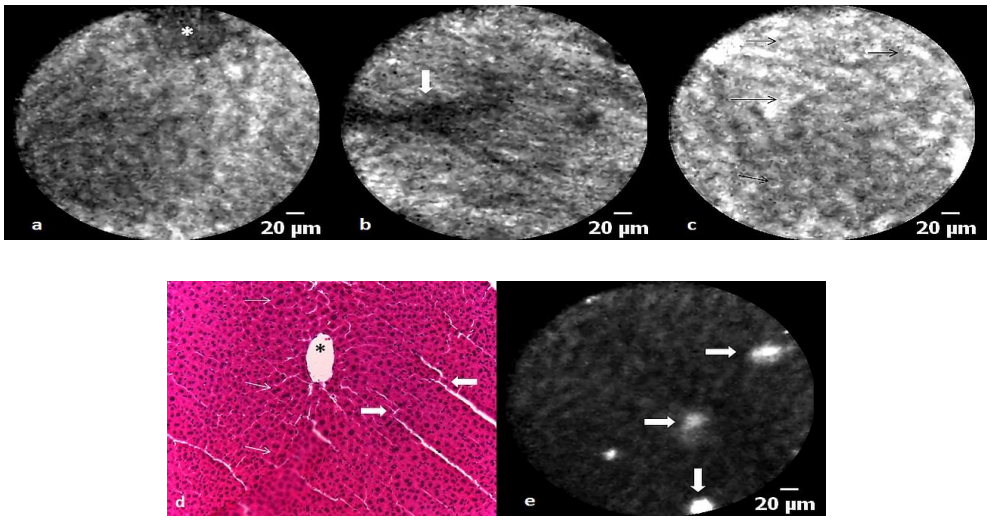

Figure 4.4 CLE of normal liver tissue at 660nm.

(a**) A central vein (*), acquired in vivo with CLE (660 nm), surrounded by normal parenchyma, acquired following ICG administration, which can also be seen in a corresponding H&E image. (b) The distribution pattern of ICG mediated fluorescence enables discrimination between sinusoids (thin arrows), larger blood vessels (wide arrow), and the hepatocytes, the latter of which make up most of the image. Vessels and their bifurcations are represented by dark linear structures (arrows). (c) Hepatocyte nuclei can be seen as small contrast sparing areas (thin arrows), surrounded by bright cytoplasm. (d) At the end of the parenchymal phase, hepatocytes have lost most of their fluorescence. Bright regions (arrows) spaced throughout the normal tissue likely presents areas where bile juice is concentrated (e.g. bile ducts). (e) Section of normal liver histology depicting a central vein (*), nuclei (thin arrows), and larger interlobular vessels (wide arrows).**

4.3.5 Evaluating liver metastases at 660nm wavelength with ICG

In contrast to CLE imaging of fluorescein at 488nm, areas of CRLM, as identified by visual inspection, did not emit any measurable fluorescence and therefore appeared as dark areas covering several fields of view (Figure 4.5). Although no specific tumour characteristics could be appreciated, it was possible to visualise the delineation between CRLM and normal hepatic tissue by observing a demarcation between high- and low intensity fluorescence areas (Figure 4.5).

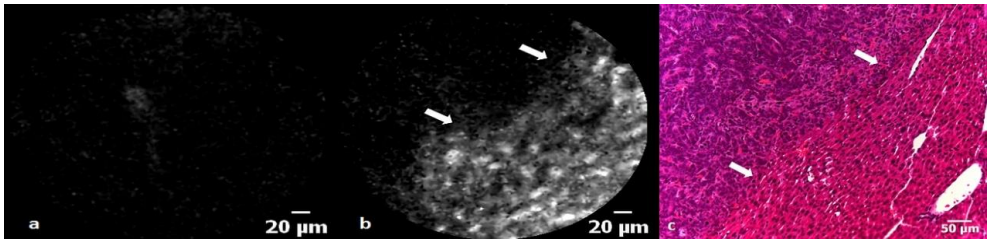

Figure 4.5 CLE of CRLM tissue at 660nm.

(a) A CLE image of a region of CRLM, which is devoid of any fluorescence following ICG administration. (b) An irregular transition (arrows) from low to high fluorescence represents the demarcation line between CRLM and normal tissue in a CLE image acquired at 660 nm. (c) The border between metastasis and normal liver tissue viewed on H&E histology.

4.3.6 Statistical analysis of fluorescence values

RFU values measured during the parenchymal phase in metastatic tissue were 53-94% lower for fluorescein/488nm and 65-100% lower for ICG/660nm when compared to normal liver tissue (Table 4.1 & Figure 4.6). GLIMMIX analysis showed that higher RFU values measured during the parenchymal phase were statistically significant predictors for the presence of normal liver tissue at either fluorophore and wavelength combination.

	488nm with fluorescein			660nm with ICG		
ID	normal (n=2195)	CRLM (n=1922)	RFU change (%)	normal (n=2681)	CRLM (n=2050)	RFU change (%)
1	3720 (2857)	226 (216)	94%	126 (53)	0 (0)	100%
2	2259 (760)	678 (308)	70%	462 (150)	0 (0)	100%
7	523 (164)	51 (128)	90%	*	*	*
8	2164 (1948)	1153 (1763)	53%	310 (43)	110 (113)	65%

Table 4.1 Relative fluorescence value changes at 488nm & 660nm.

Comparison of relative fluorescence units in normal liver and colorectal cancer liver metastasis. Median RFU values in normal and CRLM tissue during the parenchymal phase are shown for each animal with the interquartile range stated in brackets. Decrease of RFU from normal to CRLM tissue is shown in percent. Negative RFU values were thresholded to zero. * - no data collection as animal expired during experiment.

For the fluorescein / 488nm combination, a RFU value change from 37.8 to 38.8 increased the odds ratio of liver tissue being normal (e.g. non-metastatic) by 1.2 ($p<0.0001$, CI 1.21-1.24). This was also true for the ICG / 660nm combination where a RFU value change from 10.5 to 11.5 resulted in an odds ratio increase of 4.6 ($p<0.0001$, CI 3.8-5.7). The impact of treating individual animals as a random effect did significantly contribute to the fit of either model with a covariance parameter of 3.9±2.8 (SE, $p<0.001$) for fluorescein / 488nm and 43.0±35.8 (SE, $p<0.05$) for ICG / 660nm. The covariance parameter estimation indicates to what degree the random variable affects the fit of the mathematical model (e.g. aids in predicting outcome) and its associated standard error gives a measure of repeat sampling variability.

Subsequently, observations were randomised into a training- and validation set for each fluorophore and wavelength combination. GLIMMIX analysis of the training samples retained statistical significance with a RFU increase from 37.7 to 38.7 and 10.6 to 11.6 resulting in an odds ratio increase of 1.22 ($p<0.0001$, CI 1.20-1.24) and 5.08 ($p<0.0001$, CI 3.62-7.12) for the fluorescein / 488nm and ICG / 660nm combinations, respectively. Again the random effect from performing measurements in different animals did contribute to the fit of the model with a covariance parameter of 3.8±2.7 (SE, $p<0.001$) for fluorescein / 488nm and 49.2±42.0 (SE, $p>005$) for ICG / 660nm.

ROC analysis of the training set resulted in an area under the curve of 0.934±0.003 (CI 0.928-0.941) for fluorescein / 488nm and 0.994±0.001 (CI 0.992-0.997) for ICG / 660nm. A probability threshold value of 0.67 for fluorescein / 488nm and 0.69 for ICG / 660nm (representing a fixed RFU value and random animal effect) with a high corresponding sensitivity and specificity was chosen from the ROC curve coordinates. Based on these threshold values, the validation set observations were categorised into either normal or metastatic tissue which consequently enabled calculation of sensitivity and specificity for the proposed quantification method. For the fluorescein / 488nm combination, sensitivity and specificity was 82.9% (CI 81.1% - 84.6%) and 85.2% (CI 83.2% - 87.0%) respectively. For CLE imaging of ICG at 660nm wavelength the sensitivity and specificity was 97.9% (CI 97.0% - 98.6%) and 97.5% (CI 96.4% - 98.4%), respectively.

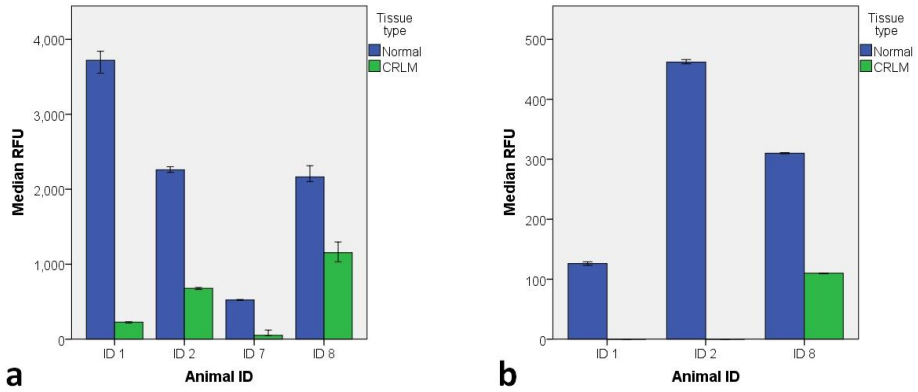

Figure 4.6 Relative fluorescence values normal tissue vs. CRLM.

(a) Median RFU values and 95%CI comparison between normal and CRLM tissue for each animal liver imaged at 488nm with fluorescein. (b) Median RFU values and 95%CI comparison between normal and CRLM tissue for each animal liver imaged at 660nm with ICG. Note that the median and 95%CI for CRLM tissue in animal ID 1 and ID2 is zero and is, therefore, not displaying on the bar chart.

4.4. Discussion

This article represents the first *in vivo* comparison of dual-wavelength CLE imaging in combination with two exogenous fluorescent probes as a method of differentiating liver metastases from normal liver parenchyma. The CLE system used in this study allows high-resolution (3.9 µm), imaging of fluorescence with a field of view of 424x302µm (488nm) or 323x323µm (660nm), thereby allowing *in-vivo* tissue structure and function evaluation in real time.

Two distinct phases of CLE liver imaging, based on fluorophore behaviour, have been described. The inflow phase lasted up to 11 minutes and was characterised by accumulation of fluorophore (and hence signal intensity) in the intravascular space. Following on seamlessly, and lasting for the remainder of the CLE examination, the parenchymal phase showed a signal intensity shift to the liver lobules. Images obtained in healthy liver tissue at 488nm wavelength with fluorescein provided good detail of the sinusoidal structure and hepatic vascular architecture. In contrast CRLM tissue showed a pattern of tumour cell agglomerations which were traversed by haphazardly-arranged blood vessels.

Quantitative estimation revealed that erythrocyte flow velocity in CRLM tissue was slower than in normal liver tissue. In contrast to healthy vessels that relatively quickly lost fluorescence during the inflow phase, the signal intensity in tumour vasculature remained high throughout the inflow and parenchymal phases of imaging. This was intriguing because, commonly, tumour vessels are reported as having increased permeability (290) which can lead to a rapid extravasation from the intra- to the extravascular compartment. This might have resulted in rapid transfer of fluorescence from the vasculature to the surrounding cancer tissue, whereas, In fact, the visualised cancer tissue was largely devoid of signal

which remains unexplained by our experiments. This finding could potentially be explained by a number of tumour specific or general factors such as local tissue necrosis, systemic hypoperfusion, arterio-venous shunts or the unique nature of the tumour cell line. Alternatively, tumour vasculature associated factors such as reduced permeability due to accelerated vessel maturation or volume expansion of the extravascular space causing dilution of fluorophore concentration could also be responsible for the observed lack of fluorescence intensity. Without further studies, it is difficult to put these findings into context because to the best of our knowledge, CLE imaging of a comparable small animal model has not been reported in the past.

Imaging at 660nm wavelength with ICG was dominated by the rapid uptake of ICG into the cytoplasm of normal hepatocytes. Visualising the whole field of view enabled sinusoid architecture to be identified, whereas on an intracellular level, hepatocyte nuclei could be observed as dark areas contrasted by the strong cytoplasmatic fluorescence signal. Localised regions of high intensity fluorescence that were seen at the later stage of imaging could not reliably be attributed to a specific feature of liver histology. Because ICG is known to be exclusively excreted by bile (291) it is possible that these regions were small bile ductules where the fluorophore accumulated before being transported to the larger bile ducts. During image acquisition, no vascular contrast could be observed but occasionally vessels could be identified as dark linear or circular structures outlined against the bright surrounding liver parenchyma.

Areas of CRLM were characterised by lack of ICG mediated fluorescence purportedly due to the lack of ICG uptake in the cancerous tissue. The absence of any relevant imaging signal prevented the characterisation of CRLM tissue with this wavelength and fluorophore combination. The general finding was that fluorescein in combination with CLE at 488nm was more suited to the imaging of the vasculature and for examining CRLM morphology, which was characterised by a mosaic of dark areas, irregular vasculature and, occasionally, glandular structures. In contrast, CLE imaging of ICG at 660nm appeared to be better suited to assess the structure of sinusoids and the surrounding hepatocytes

Although some reports on *in vivo* CLE examination of human liver disease have been published to date (178,282), no data exists describing the application of CLE in liver surgery for cancer. Several of the imaging features described in this animal model, indicate that they could be usefully translated to patients. For example the combination of glandular architecture and proliferation of irregular vasculature with abnormal flow characteristics, as observed on CLE examination of fluorescein at 488nm, is a common histological feature of human CRLM (292–295). A lack of ICG related fluorescence that was apparent at 660nm has previously been reported using camera based near-infrared imaging during liver resection for colorectal metastases (279).

The feasibility of using CLE intraoperatively to confirm complete removal of cancer in the resection of intracranial malignancy has been demonstrated previously (296). This approach could also be of benefit during resection of CRLM, where confirmation of malignancy at the borders of a resection may allow a more radical procedure to be performed with the intention of increasing cure rates. If presence of microscopic malignancy can be excluded on the other hand, it would allow surgeons to minimise the resected total liver volume which in turn can reduce the incidence of postoperative complications (297).

The same rationale can also be applied to ablation therapy of CRLM which is emerging as a feasible alternative or auxiliary treatment modality beside surgical resection. In liver ablation, cancerous tissue is destroyed by inducing coagulation necrosis through a variety of methods (e.g. radiofrequency, microwave ablation) (298). Because Cellvizio™ and other non-commercial CLE systems are not yet licensed for clinical use during surgery, it was crucial to investigate its potential benefit in an animal model before considering its clinical evaluation.

In the current study it was demonstrated that utilising a dual wavelength approach may be more advantageous than using single wavelength CLE (178,282), because two fluorophores and their respective imaging properties in tissue can be evaluated in short succession. Fluorescein and ICG CLE visualisation in hepatic tissue differs because the former has properties suited to the visualisation of vasculature (178) whereas the latter is exclusively cleared by the liver and therefore has a stronger affinity to hepatocytes and bile ducts (291).

Other groups have explored the potential of CLE imaging for identifying cancers and evaluated these in animal models (281,299,300). These, however, have been based on non-clinically approved CLE systems which would need further development before they can be used in a clinical context (284,299). The experiments outlined here were all performed with a CE marked device that has found widespread interest for the clinical diagnosis of malignancy (287,301–303) and it is hoped that the relatively widespread dissemination of this CLE imaging platform can help in facilitating the further clinical evaluation of the findings presented here.

Previous articles on CLE imaging of malignancy have been based on subjective, observer dependent image interpretation but have not identified quantifiable and reproducible parameters of malignancy (284,304). To establish such a quantifiable parameter that would allow discrimination between normal and malignant liver, a tissue evaluation centred on numerical fluorescence values was proposed. A GLIMMIX analysis revealed that normal liver tissue was more likely if high RFU values were recorded with either wavelength and fluorophore combination. Based on a random set of observations, a threshold probability value for distinguishing normal liver from CRLM tissue has been established for the measured CLE data. Subsequent validation on the remaining observations revealed a very good and excellent diagnostic accuracy of 83.9% and 97.8% for the fluorescein / 488nm and ICG / 660nm, combination, respectively. Based on the diagnostic results in the validation

datasets, CLE imaging of ICG at 660nm may be better suited for the use of fluorescence intensity to discriminate between normal and CRLM tissue. The superior performance when using CLE imaging of ICG at 660nm for this purpose probably reflects the more homogenous nature of CRLM tissue visualised with this CLE setting. As described above, an abundance of high intensity vascular structures seen with CLE imaging of fluorescein at 488nm causes a heterogeneous imaging pattern in areas of CRLM. Whether a combination of both fluorophore and wavelength combinations can enhance diagnostic accuracy, could not be shown in this study due to the inability of applying simultaneous dual waveband CLE imaging to exactly the same field of view. A new version of Cellvizio™ capable of simultaneous dual waveband imaging is now available but we did not have access to this system for application in this study.

Because probability values used for ROC analysis are based on a combination of a fixed (RFU) and a random effect (animal ID) it cannot be extrapolated into a specific RFU value for future studies. Before this can be considered, it is crucial to standardise RFU value calibration which could potentially result in reproducible and absolute fluorescence units that could be globally applied across different research groups.

Further limitations that have to be taken into account regarding the presented findings pertain to the animal model and the technical characteristics of confocal laser microscopy. The animal model of CRLM that was studied uses a human cancer cell line and a portal venous route of establishing liver metastasis which is the most common route of GI malignancy disseminating to the liver in humans (305). Despite these similarities, research on murine models of malignancy have well-described limitations when it comes to applying results to a clinical setting (306). A further issue is that experiments have focused on a single cell line of colorectal neoplasia. This cell line was chosen specifically because it exhibits a moderate- to well differentiated tumour histology that can display colonic glandular architecture (307) and therefore was felt to be more visually distinct on CLE imaging. It is however only representing a small spectrum of the histological characteristics that CRLM may exhibit on virtual histology and therefore further validation on different colorectal cancer cell lines may be necessary. No formal liver resection was carried out and therefore it is difficult to predict if cutting into CRLM tissue would lead to alteration of its fluorescence properties.

A clear trend for lower fluorescence intensity in CRLM compared to healthy liver tissue was especially prominent on CLE imaging of ICG fluorescence, probably because it has a strong affinity for hepatic tissue. Colorectal cancer liver metastasis is a common indication for surgical resection of liver malignancy in the western hemisphere and is generally regarded as the only curative treatment option for this disease (213,308). Some of these results may become relevant for this patient population in the future, but it is unlikely that these findings can be directly transferred to primary liver malignancy (e.g. hepatocellular carcinoma), because fluorophore behaviour probably depends on the organ of origin of the cancer. For

example, groups examining patients undergoing liver resection for either CRLM or hepatocellular carcinoma, found decreased or increased ICG related fluorescence within cancerous tissue, respectively (279,309).

Further restrictions that have to be accounted for are related to the technology behind CLE imaging. Optical imaging modalities including CLE can visualise details down to a sub-cellular level but at the cost of a limited imaging depth. The maximal imaging depth of the Cellvizio™ probes used by our group was 0-70µm depending on probe type, which means that only liver cell architecture that is either superficial or adjacent to the resection margin could be assessed. It has been shown that removal of tumour within an area of <1mm conveys a patient survival benefit in the resection of CRLM (310). Therefore a potential use of CLE would be to confirm that a resection margin is clear of cancer by probing the cut surface. Because of CLE's limited depth penetration it should not be considered as a potential substitute for intraoperative ultrasound imaging but more as a complementary modality that expands the borders of intraoperative imaging into the microscopic domain. The Cellvizio™ probes used in this study had a maximal field of view of 600µm^2 which may limit its applicability in the clinical examination of liver resection margins which are usually in the cm^2- range. It has previously been shown however that clinically relevant CLE imaging with a field of view of approximately 2mm^2 (282) is possible. Robotic control of CLE during laparoscopic liver surgery has been utilised to create even larger fields of view (150). If clinical translation for intraoperative use of CLE is considered, it would be crucial to encourage the development of probes that offer a field of view of ≥1mm^2, because this would greatly improve the integration of CLE imaging into the surgical workflow.

Currently, Cellvizio™ probes are only marketed for endoscopic applications and are not certified for intraoperative use. Some of the probes, however, can be fully sterilised and may potentially be used for imaging during laparoscopic liver resection. If a clinical benefit for the intraoperative usage of this system can be defined, sterility issues and clinical re-certification should not present a major obstacle.

4.5. Conclusion

In conclusion, a clinically licensed CLE system was used to provide a detailed description of discriminatory tissue characteristics in an orthotopic murine model of CRLM. A dual wavelength approach in conjunction with two fluorophores was found to be of benefit because CLE imaging of fluorescein at 488nm enabled better visualisation of metastatic tissue whereas quantification of ICG mediated fluorescence intensity demonstrated a better potential to objectively discriminate between normal liver and CRLM tissue at a cellular level. In the following chapter the findings relating to fluorescence intensity based tissue discrimination from the current chapter are applied to CLE imaging in a laparoscopic large animal model. Evaluation of simultaneous (i.e. non-sequential) dual waveband imaging and

standardisation of fluorescence values is the next crucial step to advance CLE imaging of liver malignancy.

In the next chapter CLE examination will be studied in a large animal model of laparoscopic liver surgery to assess the feasibility of using this imaging modality during laparoscopy to evaluate the adequacy of liver ablation.

5. Use of dual wavelength probe based confocal laser endomicroscopy to determine the adequacy of laparoscopic liver ablation

5.1. Introduction

Thermal ablation is a minimal invasive therapy which can be used for the treatment of primary or secondary liver malignancy (298,311). During the procedure an ablation probe is inserted into the liver lesion where it causes thermal-mediated denaturisation of proteins which results in the destruction of cancer cells. Most commonly, heat is created by radiofrequency or microwave energy, but laser or high intensity focused ultrasound induced heat can also be employed (311). The ablation probe can be applied by percutaneous, laparoscopic or open approaches. The laparoscopic approach allows easy access to tumours which are difficult to treat percutaneously such as those superficially in the liver or high under the diaphragm. It also permits use of laparoscopic ultrasound to localise the lesion and assess its relationship to local vital structures, hence reducing the incidence of collateral injuries (312).With small solitary liver cancers thermal ablation may produce comparable results to liver resection with a reduced morbidity and mortality (50).The main concern regarding thermal ablation is the high incidence of local recurrent disease and the main aim of ablation therapy is therefore to destroy not only the cancer harbouring tissue but also a 5-10mm safety margin to include any local satellite lesions. Ablated liver tissue changes in colour from brown to white (total coagulation effect) but the spatial dimension of cellular destruction and functional damage extends well beyond this phenomenon, therefore making ablation monitoring crucial and mandating development of a visual inspection or detection device to locate the real damage margins. Using ultrasound for monitoring is unreliable because ablation therapy generates gas bubbles within the hepatic tissue which subsequently creates an acoustic shadow effect, negating any diagnostic value to the images (313,314). Conventional computer tomography (CT) and magnetic resonance imaging (MRI) are commonly used for the postoperative assessment of ablation efficacy (315,316) only, whereas intraoperative cone beam CT and open MRI scanners may be used but technical restrictions such as incompatibility with metal instruments (MRI) (317) and limited imaging quality (cone beam CT), make them impractical for the intraoperative evaluation of ablation therapy.

During thermal ablation there is a significant change in tissue temperature which in itself can be regarded as a surrogate marker for cellular destruction (314). This relationship has been exploited for the purpose of non-invasive ablation monitoring, with MR- or CT thermography (317). In a more direct approach, tissue temperature can also be measured invasively by placing optical fibres under image guidance within liver tissue (313). This approach however confers the risk of needle tract seeding (318), i.e. the risk of displacing tumour cells with the needle, into normal tissue and therefore disseminating the malignancy unnecessarily.

Measuring changes in tissue elasticity by shear wave elastography has also been investigated for its utility in ablation monitoring (317,319). The modalities listed above measure surrogate markers for tissue necrosis but a method of directly imaging the changes in the ablation zone has yet to be identified.

Confocal laser endomicroscopy (CLE) is a novel optical imaging technology that enables accurate microscopic assessment of in-vivo histopathology. Its utilisation in a variety of experimental and clinical scenarios has been increasingly reported. CLE utilises a fibre optic element as its objective lens, allowing confocal microscopy with a micron-scale resolution that enables visualisation of sub-cellular details using endogenous or exogenous fluorescence. Exogenous fluorescence is provided by fluorescent dyes which can be applied in a systemic (e.g. intravenous) or topical fashion and are commonly referred to as fluorophores. They enhance CLE image contrast by absorbing and emitting light at wavelengths that are specific for each individual agent and circumstance (146,247).

CLE during laparoscopy or NOTES (Natural Orifice Transluminal Endoscopic Surgery) has been performed either with a rigid endomicroscope which contains the scanning optics in its tip (146) or with a slim, flexible optical fibre bundle which transmits light signals to laser scanning equipment situated at the far (e.g. extra-corporeal) end of the intrusive fibre (177,248). An example for a fibre based CLE system is Cellvizio™ (Mauna Kea Technologies, Paris, France) which is CE-marked for clinical use in luminal endoscopy and can be operated with probes that have a diameter range of 0.3-4.5mm. During endoscopy, Cellvizio™ can reveal histopathological cellular changes and has been shown to enhance accuracy in the diagnosis of malignancy and dysplasia (146,249).

Liver ablation has been visualised using a bench-top confocal laser microscope in a small animal model (320), but the diagnostic ability of a clinically approved CLE system to distinguish between healthy and necrotic liver tissue in a laparoscopic setting have yet to be tested. In these experiments, the aim was to evaluate if CLE imaging employing the Cellvizio™ system's can differentiate ablation induced tissue necrosis from normal liver tissue in an in-vivo porcine model of laparoscopic microwave liver ablation.

For establishment of the model, percutaneous microwave ablation was conducted under direct laparoscopic visualisation. As the CLE system used in this study has a limited imaging depth of <100µm, only superficial ablation zones were created and assessed. Optical scattering in hepatic tissue is very high and imaging depths are likely to be no better in any other optical technique. Imaging of subsurface ablation zones was not attempted. However, imaging of deeper ablated areas is of clinical relevance, and CLE via a placed optical fibre within the periphery of an ablation volume may be a potential approach to achieving this. Due to the small size of the probes, placement without significant damage to blood vessels or bile ducts should be feasible.

Previous groups evaluating laparoscopic CLE have used single fluorophores that are usually visible on CLE imaging within the blue-light or near-infrared spectrum (178,248,282). For the experiments presented here dual wavelength CLE imaging at 488nm (blue) and 660nm (red) wavelength was facilitated by the fluorophores fluorescein and indocyanine green (ICG). By evaluating liver tissue at two discreet wavelengths and dissimilarly partitioned fluorophores, we aimed to maximise imaging information and highlight any potential advantages or disadvantages between the wavelengths and their corresponding fluorophores. The image acquisition software (ImageCell™) supplied with Cellvizio™ can compute basic image values (mean, median, maximum, minimum intensities). As well as comparing images, basic image summary statistics have been analysed to establish if they can aid in defining the zone of tissue necrosis associated with microwave ablation.

5.1.1 Imaging of pathological tissue in a porcine model

In this chapter the focus is on the CLE examination of ablated liver tissue. For continuity and comparability, imaging of liver malignancy in a porcine model would have been preferable but this would have introduced a number of issues related to studying liver malignancy in large animal models. Although chemical induction of hepatocellular carcinoma in pigs has been reportedly successful, this approach is lengthy, costly and time consuming (253). The main obstacle to application of CLE in humans is technical handling and analysis of visual data. Both aspects can be studied without the presence of malignancy and hence it was felt that using the discrimination of ablated vs. non-ablated tissue would be a suitable substitute outcome to study the tissue visualisation characteristics of CLE.

5.1.2 Aims

In this chapter the aims are to:

1) describe virtual histology of normal porcine liver on CLE examination using fluorescein at 488nm and indocyanine green at 660nm illumination.
2) evaluate the technical feasibility and limitations of visualising virtual histology with CLE in a laparoscopic setting.
3) assess the ability of CLE to predict liver tissue necrosis induced by ablation therapy.

5.2. Methods

General and specific methodology has already been described above (3.1.4). It was felt to be advantageous for ease of reading to avoid separating the methodology across chapters in this case.

5.3. Results

5.3.1 General histology

The histological samples obtained within 7-10 days of microwave ablation showed different degrees of cellular injury in the ablated areas. Centrally, within the ablation zone, tissue

appeared macroscopically white and on histology, showed complete coagulation necrosis. Surrounding these areas was a rim of tissue that showed signs of sinusoidal obstruction, cell shrinkage and disruption of lobular architecture. On macroscopic inspection these areas were difficult to distinguish from the normal liver tissue in the periphery, validating the use of a sensitive imaging instrument for this purpose.

5.3.2 CLE evaluation of fluorescein at 488nm - normal liver

CLE images are shown adjacent to histology sections, obtained from normal porcine liver after conclusion of the experiments. To facilitate comparison, CLE images are shown in parallel to histology slides with comparable architectural features from the same animal.

When using 488nm CLE, no auto-fluorescence signals were recordable from the tissue before fluorescein administration. Intravenous fluorophore injection was followed by an “inflow phase” where the fluorophore is distributed and taken up by the liver parenchyma. This phase lasts for approximately 7-10 minutes after injection and is characterised by bright signals in blood vessels contrasting with dark lobule areas (Figure 5.1). Using CLE imaging of fluorescein at 488nm, individual erythrocytes flowing through blood vessels could be observed with greater regularity than was possible with CLE imaging of ICG at 660nm. Unfortunately the limited image resolution made a more detailed analysis of blood vessel flow difficult at either wavelength.

The inflow phase was followed by the “parenchymal phase” when the fluorescence pattern is reversed as the fluorophore has been redistributed from the vasculature into the liver parenchyma. During this phase, the vasculature is devoid of fluorescence signal and can be visualised as dark lines of increased contrast (i.e. absence of fluorescence) that surrounds the liver lobules which had by then become rich in fluorescein (Figure 5.1). CLE imaging of fluorescein at 488nm allowed sinusoid structure and individual hepatocyte cords visualisation (Figure 5.1). Usually a distinction between different types of vessels (arterial / venous) is not feasible, but in some instances the location and morphology of blood vessels can reveal its specific characteristics (Figure 5.1).

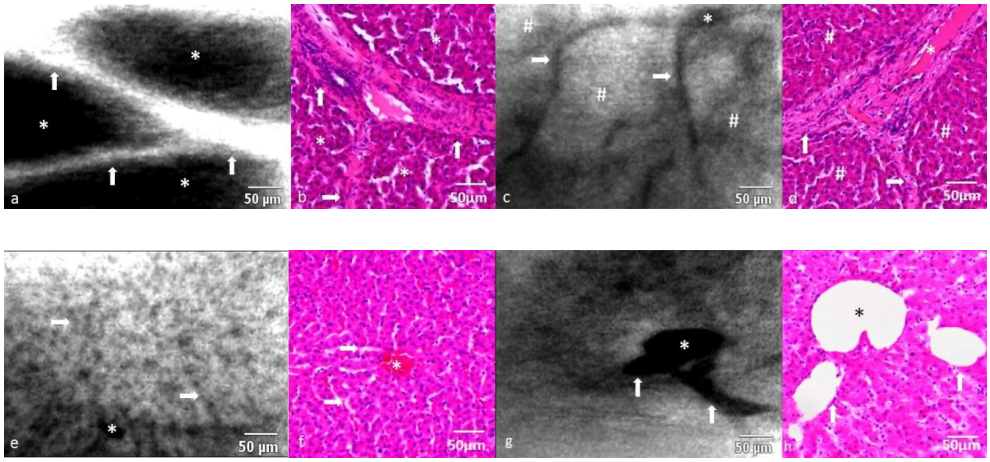

Figure 5.1 CLE of normal liver tissue at 488nm.

Comparison of CLE imaging with fluorescein/488nm and H&E liver histology. (a and b) Strong fluorescence signal in the intravascular compartment during the inflow phase. _Liver lobules; arrows, interlobular vessels. (c and d) Shift of fluorescence signal from the intravascular- to the intracellular compartment in the parenchymal phase. #Liver lobules; _vessel bifurcation; arrows, vessel branches. (e and f) Pattern of sinusoidal architecture. _Horizontal sinusoid; arrows, perpendicular sinusoid. (g and h) Vessel bifurcation of a centrilobular vein. _Vessel lumen; arrows, vessel branches.

5.3.3 CLE of ICG at 660nm - normal liver

Similar to the fluorescein system, 660nm CLE illumination of ICG, demonstrated no tissue auto-fluorescence and thus no imaging of liver architecture was possible prior to fluorophore administration.

In contrast to CLE of fluorescein under 488nm excitation, it was not possible to visualise any significant fluorescence within the intravascular compartment during the “inflow phase”. The combination of ICG and 660nm CLE however appeared to be better suited to imaging the sinusoid structure within liver lobules (Figure 5.2). Because ICG is rapidly taken up and cleared by the hepatocyte cytoplasm, the hepatocyte nuclei were seen outlined as dark spots within the liver cells (Figure 5.2). Central lobular veins that drain the blood towards the hepatic venous system could be seen as round dark structures within the centre of a lobule (Figure 5.2). Because the vasculature and connective tissues were both devoid of fluorescence signal in the parenchymal phase, blood vessels could not be distinguished from interlobular septations when using ICG as sole fluorophore (Figure 5.2). Within this limitation, the visualisation of fibrous tissue septations between lobules was readily reproducible with ICG CLE at this wavelength. Between 30-40 minutes after ICG infusion, bright spots were seen appearing throughout the liver parenchyma (Figure 5.3). This phenomenon possibly represents areas of ICG accumulation (e.g. bile juice).

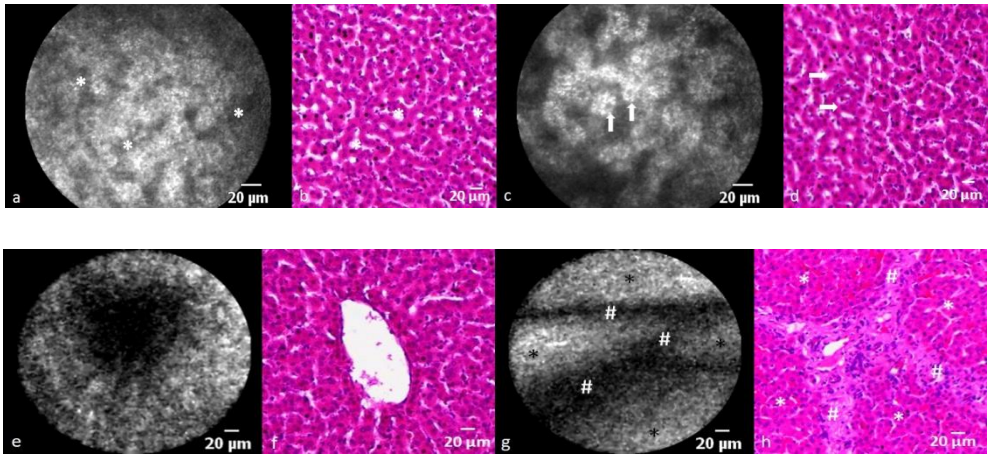

Figure 5.2 CLE of normal liver tissue at 660nm.

Comparison of CLE imaging with ICG/660nm and H&E liver histology. (a and b) Typical sinusoidal architecture of normal porcine liver. _Sinusoids. (c and d) Hepatocyte nuclei appear as intracellular contrast sparing. arrows, nuclei. (e and f) The dark central area represents a centrilobular vein. Note how the vessel lumen appears ragged because ICG does not accumulate in the vascular endothelial cells. (g and h) Interlobular septations appear as linear contrast sparing areas between liver lobules. #Septation; *liver lobule.

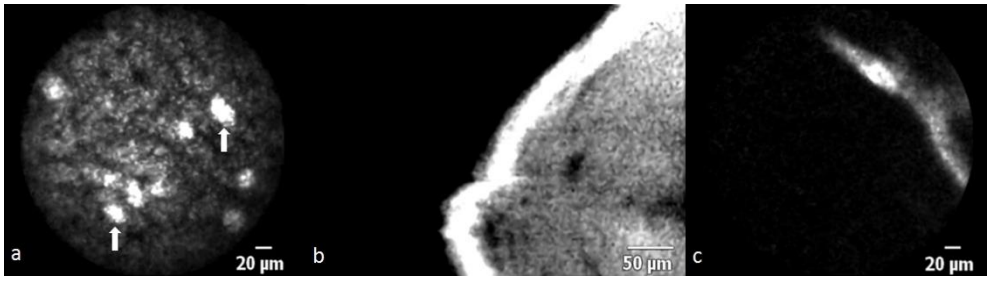

Figure 5.3 CLE of normal liver and resection surface at 488nm & 660nm.

(a) Bright foci of fluorescence (arrows) at the later stages of CLE imaging with ICG/660nm may correlate with areas where bile juice accumulates. The surface of the resected liver is mostly devoid of fluorescence but occasionally band-like fluorescence signals can be seen at 488nm (b) and 660nm (c) wavelength.

5.3.4 Probe manipulation, placement and image quality

As the CLE probe has no inherent navigability, the use of an intravascular catheter (Agilis™ St. Jude Medical, Saint Paul, MN, USA) afforded free rotation, flexion and retroflexion to 180 degrees. Familiarity with the steering system allowed instant successful use of the CLE instrument without additional prior expertise or training.

This degree of manoeuvrability allowed access to virtually any area on the liver surface (Figure 3.1). The main detractor to image quality was the respiratory movement of the liver. This made methodical and complete examination of liver tissue difficult because tissue

contact loss would frequently occur with each respiratory cycle. The problem of respiratory interference to CLE signal was greater on the anterior and superior surfaces of the liver and was compounded by pooling of fluids or blood on the liver surface which increased probe tip slipping. The size of the steerable access catheter allowed parallel insertion of two CLE probes, this method however made overall handling difficult and impaired image quality.

5.3.5 Evaluating ablation zones and liver resection surface

In ablated liver tissue, the characteristics of CLE images recorded with fluorescein and ICG were similar in all the animals studied. Whether the fluorophore was injected before or after ablation was carried out, did not affect visualisation of tissue characteristics. In the majority of the ablation zone no fluorescence was detectable which corresponded to zones of ablation induced injury on histology (Figure 5.4). When examining the border region between normal and ablated liver, the change from high to low fluorescence zone could often be observed in the same field of view (Figure 5.5). Because it was technically difficult to stabilise the probe over a very small area (<1mm), no differentiation between zones of cellular apoptosis and necrosis could be made. Similar to zones of ablated liver, the liver resection surface (divided using the ultrasonic scalpel) did not show any significant fluorescence signals. If signals were recorded on the resection surface they usually originated from linear structures of high signal intensity that potentially represent vessels (Figure 5.3) or zones of fluorophore extravasation following the destruction of fluorophore containing vessels.

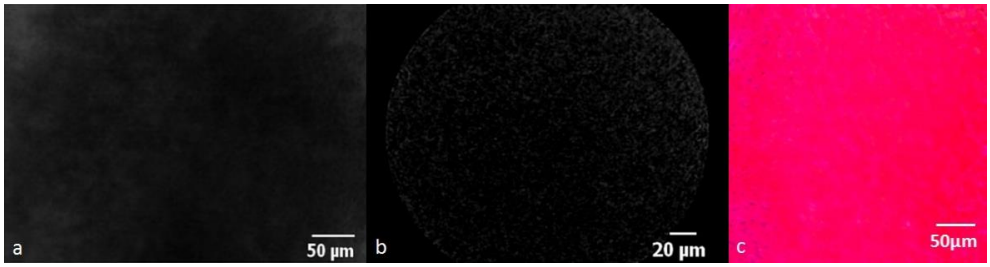

Figure 5.4 CLE images of liver necrosis at 488nm & 660nm.

Areas of complete necrosis with fluorescein/488nm (a) and ICG/660nm (b) show loss of fluorescence intensity which correlates with complete destruction of hepatic architecture on H&E histological analysis (c).

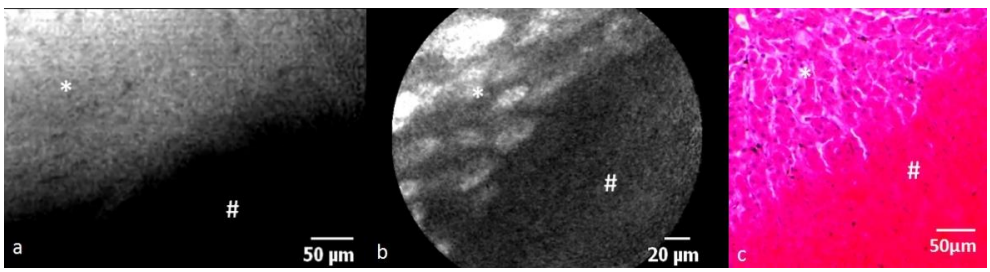

Figure 5.5 CLE images of liver necrosis and viable tissue at 488nm & 660nm.

The border between complete necrosis (#) and partial cellular injury (_) can be visualized with fluorescein/488nm (a) and ICG/660nm (b). The corresponding H&E histological appearance can be seen in (c).

5.3.6 Analysis of fluorescence values

Overall RFU values measured in non-ablated vs. ablated tissue decreased by 75-94% and 77-100% for CLE imaging with the fluorescein / 488nm system and the ICG / 660nm system respectively (Figure 5.6). In Table 5.1, median RFU values for each animal and tissue type are shown with ablated tissue further subdivided into individual lesions.

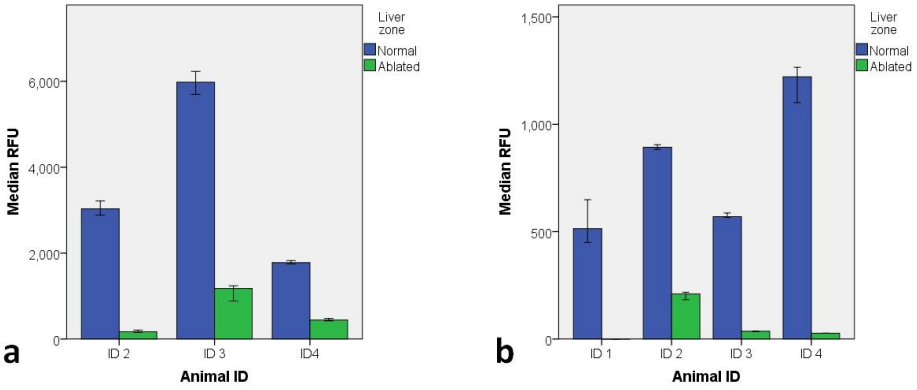

Figure 5.6 Relative fluorescence in normal vs. ablated liver tissue.

(a**) Median RFU values_95%CI for each animal liver studied with fluorescein/488 nm. (b) Median RFU values_95%CI for each animal liver studied with ICG/660 nm. The bar for ablated tissue in animal ID 1 is not visible because the median and 95%CI is zero.**

Animal ID.	Type of tissue	Fluorescein & 488nm	ICG & 660nm
1	Non-ablated	*	514(624)
	Ablated	*	0(20)
	RFU change in %		100%
	Lesion 1	*	20(18)
	Lesion 2	*	0(0)
2	Non-ablated	3030(1868)	893(240)
	Ablated (Lesion 1)	169(862)	210(123)
	RFU change in %	94%	77%
3	Non-ablated	5978(3782)	570(254)
	Ablated	1177(949)	37(29)
	RFU change in %	80%	94%
	Lesion 1	1177(949)	17(8)
	Lesion 2	*	63(106)
	Lesion 3	*	36(2)
4	Non-ablated	1778(846)	1221(532)
	Ablated	443(627)	27(3)
	RFU change in %	75%	98%
	Lesion 1	838(871)	24(3)
	Lesion 2	381(192)	20(16)
	Lesion 3	953(707)	27(1)

Table 5.1 Relative fluorescence value changes per ablated lesion for 488nm & 660nm.

The interquartile range is given in brackets. RFU change states the decrease of median RFU values in non-ablated (set as 100%) vs. ablated tissue. *No image acquisition for these lesion due to technical issues.

With CLE of fluorescein using 488nm excitation, a standardised RFU value change from 41 to 42 increased the odds ratio of liver parenchyma being normal (i.e. non-ablated) by 1.16 ($p<0.0001$; CI 1.15–1.17). At this fluorophore and wavelength combination the variation introduced by imaging individual animals and re-calibrating the Cellvizio™ system did not contribute to the fit of the model as a random effect with a covariance parameter of 1.66±1.66 (SEM, $p>0.05$). The covariance parameter estimation indicates to what degree the random variable affects the fit of the model (i.e. it aids in predicting outcome) of the model and its associated standard error gives a measure of repeat sampling variability. This means that the same RFU values could be applied across different animals in the study to predict the presence of healthy liver tissue. ROC analysis resulted in an area under the curve of 0.955±0.003 ($p<0.0001$, CI 0.95-0.96).

A standardised RFU value change from 17 to 18 with CLE imaging of ICG at 660nm increased the odds ratio of liver parenchyma being normal by 1.58 ($p<0.0001$, CI 1.54-1.63). Variation introduced by individual animals and re-calibration did significantly contribute to the fit of the model as a random effect with a covariance parameter estimation of 4.6±3.8 (SEM, $p<0.05$). This means that the predictive RFU values were not interchangeable for different animals in the study as each individual's fluorophore distribution pattern within the areas of interest, were unique to that animal. ROC analysis resulted in an area under the curve of 0.999±0 ($p<0.0001$, CI 0.998-1.0).

5.4. Discussion

This study has demonstrated that confocal laser endomicroscopy can be used in-vivo to distinguish thermally ablated liver, from healthy liver, during laparoscopic surgery. The main discriminating factor between healthy and ablated tissue was loss of fluorescence intensity as expressed by RFU. This phenomenon was independent from the time point of fluorophore injection which means that it is unlikely to be caused by the destruction of fluorophore carrying vasculature. It is proposed that the destruction of fluorophore containing cellular and intercellular structures that occurs during liver ablation is the most likely explanation for this finding.

Evaluation of ablated liver tissue is of relevance because similar to surgical excision of malignancy, a complete ablation margin around a treated lesion is necessary to optimise patient survival (321). An important limitation of thermal ablation is that it is relatively contraindicated when the tumour is close to vulnerable structures such as major bile duct and blood vessel structures (322). Proximity to large blood vessels also renders ablation less effective and predictable because of the "heat sink effect" (322). Although not demonstrated here, CLE probes could be deployed close to vulnerable structures to detect thermal injury and allow the progress of ablation to be monitored. Because the approach evaluated in this article enables direct visual tissue assessment in small and distinct areas of liver parenchyma, it may be advantageous compared to measuring surrogate markers of tissue necrosis such as temperature.

An analysis based on generalised linear mixed modelling has indicated that loss of fluorescence intensity can be used in vivo to identify ablated or non-vital liver tissue. This type of analysis was chosen over and above a more simplistic group-wise comparison because of the specific constraints that the collected data presented. Firstly we had to account for comparing two different types of tissues in the same animal (normal and ablated); secondly the tissue types were repeatedly measured to account for the inconsistency introduced by CLE probe movement and a small field of view; thirdly an incongruent number of mean RFU values in each group resulted from having a different number of frames available for analysis. Lastly the absolute values of the measured RFU

were not comparable between different experimental days because each new calibration of the Cellvizio™ altered the RFU value.

The general linear mixed model analysis allows for all these considerations and takes into account the correlation in measurements between different tissues in the same animal. It is also able to handle non-parametrically distributed data. A separate ROC analysis has been used to confirm the validity of the model. Before fluorescence values can be used to inform clinical decision making however, it is imperative that standardised, absolute fluorescence values are established. If an ablation dependent variability in absolute fluorescence can be validated in more extensive datasets, it has the potential to be transformed into a computational image recognition algorithm. This algorithm could then be integrated into a clinical imaging system with the ability to monitor and map liver ablation.

Each frame value was treated separately because unavoidable probe movement meant that some sections of tissue may just be represented by a single frame. Although a single image frame may not provide enough data for clinicians to evaluate tissue, it could provide sufficient data for an automatic tissue evaluation algorithm based on fluorescence intensity.

A description has been provided comparing key characteristics of liver tissue architecture as imaged on fluorescein and ICG facilitated CLE examination at 488nm and 660nm wavelength. To account for temporal variations in imaging characteristics following fluorophore injection, a categorisation into hepatic “inflow” and “parenchymal” phases has been proposed here. The inflow phase lasts approximately 7-10 minutes and takes place while the fluorophore is mainly concentrated in the hepatic vasculature. This blends over into the parenchymal phase when the bulk of fluorophore concentration has been re-distributed into the intracellular compartment. Although a number of articles have evaluated CLE of the liver for different indications in animals and humans, (148,177,178,248) no report to date has made a comparative description by employing a dual wavelength approach. Because fluorescein and indocyanine green have different distribution properties in tissues (282,291,323) they could be employed sequentially and within a time frame to allow examination of a particular area of interest. Overview images obtained during the inflow phase had different characteristics for both fluorophore and wavelength combinations. When focusing on blood flow evaluation in this phase, CLE examination of fluorescein with the blue-light system was advantageous because it enabled regular visualisation of erythrocyte movement within sinusoids and larger parenchymal vessels. Although ICG is similarly distributed through the vasculature, it was not possible to detect intravascular ICG mediated fluorescence in this study. A group investigating near-infrared CLE imaging of ICG in patients with liver disease were able to visualise blood flow in 8 out of 21 patients (282) possibly reflecting low / slow function of the hepatocytes in these particular 8 cases. No ICG related fluorescence was visualised within sinusoidal vessels which was also the case in our experiments. It is not possible to draw any conclusions from this because the employed CLE systems have different specifications and with only 4 subjects in our study, the inability to

visualise hepatic blood flow may have been accidental but it is tempting to ascribe it to good hepatocyte affinity for ICG in health, allowing a one-pass clearance effect.

In the parenchymal phase, CLE of the fluorescein /488nm system was better suited to imaging blood vessel morphology because low contrast areas correlated better with blood vessels, whereas these areas in the ICG/660nm system were consistent with both fibrous tissue septations and vasculature. A more homogenous and intense distribution of fluorescence throughout the liver tissue indicated that fluorescein accumulated in hepatocytes and other cells (e.g. fibrocytes and vascular endothelial cells). In comparison, ICG CLE at 660nm revealed a high affinity of ICG to hepatocytes with nuclear sparing, providing a strong contrast. Visualisation of interlobular septation architecture appeared to be better suited to the 660nm CLE system with ICG, which was able to clearly delineate liver lobules from surrounding fibrous tissue. At 30-40 minutes after ICG injection areas of 5-20μm^2 could be observed that accumulated high fluorescence intensity. Given that ICG is known to be rapidly excreted via bile (291) it is proposed that these signals may represent bile canaliculi, the smallest division of bile ducts . The fluorophore choice of fluorescein and ICG was guided by potential clinical applicability. There are many other potential fluorophores for 488 – 660nm CLE, but none are currently approved for clinical use or have the same low risk profile as fluorescein and ICG (291,323). The latter two fluorophores have been used in CLE studies of the human liver in the past (178,282) which could aid in the transferability of our findings to a clinical evaluation of CLE imaging in liver ablation.

Overall the detection sensitivity of ICG fluorescence intensity at 660nm was lower when compared to fluorescein at 488nm wavelength. This was likely due to the fact that the optical absorption maximum of ICG is 800nm (near-infrared spectrum) so our excitation efficiency was poorer at 660nm, and while not optimal, was adequately within the excitation range to excite fluorescence emissions for this fluorophore. This illumination wavelength is a manufacturer pre-set and cannot be altered. Near-infrared CLE imaging however is not available yet in a CE marked system and we felt that adequate signal was achieved in the system described, as the fluorophore has attractive properties relevant for clinical liver and bile duct imaging (291).

Although porcine models are frequently used to evaluate novel surgical technologies (324,325) the resulting findings have to be interpreted with caution. Firstly, porcine liver histology differs from humans with more pronounced interlobular septations. Despite these differences authors with extensive experience in CLE imaging of the liver state that data acquired from animal studies can be regarded as equivalent to human data (247). Secondly, we found during laparoscopy that the pig's distinctive multi-lobulated liver configuration altered the handling and manipulation of the liver considerably in comparison with the expected characteristics in humans. Although the number of animals tested was small, the extensive data acquisition was comparable to similar studies published by other groups (248,326). The acquired number of images was sufficient to describe dual wavelength CLE

imaging features and to evidence the feasibility of using fluorescence values to distinguish between vital and ablated liver parenchyma in an individual. Establishing large animal models of liver malignancy is expensive, time consuming and not routinely employed for research purposes (253). Therefore the pig model employed in this article solely focused on assessment of ablated tissue and did not account for the presence of malignant tissue with its commonly associated vascular disturbances, as would be encountered during clinical liver ablation procedures. The advantage of CLE imaging compared to a simpler fluorescence detection device is that it has the ability to demonstrate tissue architecture and thus discriminate between malignant and benign tissue (146), but due to the limitations of the porcine model this aspect could not be evaluated in this study. In addition the image quality alludes to fouling of the tip – a danger in single fibre spectrophotometry systems reporting no signal due to absence of fluorophore or a fouled tip?

The relation and distribution of fluorescence characteristics in healthy and ablated liver tissue demonstrated in this article indicate that CLE may well have utility in ablation monitoring but further research is required. Before absolute RFU values can be compared between different experiments or between research groups the Cellvizio™ platform or alternative CLE imaging systems would need to be adjusted and standardised to allow reproducible calibration of fluorescence intensity.

At this stage CLE imaging can offer micron level resolution in discriminating ablated from non-ablated liver tissue and may therefore be of interest as a novel imaging tool in liver ablation research. If clinical translation is considered in the future, technical limitations imposed by CLE imaging depth and probe vulnerability will have to be addressed.

The feasibility of utilising needle based, diffuse optical spectroscopy to evaluate liver malignancy (225,256) and steatosis (327) has been demonstrated in the past. A similar needle based approach could also be applied to increase the imaging depth of CLE which is currently restricted to <200µm. The smallest commercially available CLE probe has a diameter of 300µm which would enable insertion through the bore of a 24G needle which is smaller than liver core biopsy needles currently in routine use and therefore less likely to cause inadvertent injuries. Once placed within the bore of the needle, the CLE probe could be inserted into the liver parenchym under US guidance. Correlation of US and CLE images could then respectively provide anatomical and functional information about the adequacy of ablation therapy.

In the diagnosis and treatment of abdominal malignancy, there are a number of scenarios (e.g. transgastric fine needle aspiration of the pancreas, irreversible electroporation of the pancreas, liver biopsy) where a needle is intentionally inserted into malignant tissue. This is feasible because the risk of needle tract seeding is either small or outweighed by the clinical benefits of the procedure (328–330). To minimise the risk of needle tract seeding from needle based CLE, an ablation of the needle tract should be carried out which is advocated

by some authors as routine practice in any laparoscopic liver ablation (312). In addition, if the procedure is being conducted anyway, the obtaining of CLE data through the same needle track simply adds to the benefits side of the risk evaluation and offers the possibility of increased data yield from the same clinical exercise. Further testing and validation in an experimental setting will be required to elucidate if this solution is feasible. Until feasibility has been confirmed, experimental CLE ablation monitoring should be restricted to superficial liver tumours that do not require a needle based approach.

Another technical issue is the CLE probe's vulnerability to high temperatures. The Cellvizio™ probes are only licensed to work within the range of normal body temperature whereas liver ablation may generate temperatures in excess of 100˚C. This may prevent real time CLE monitoring within the centre of an ablation zone but the temperature in the periphery of an ablated region is generally lower than in the centre and rapidly deteriorates (331). Temperatures that are within the working range of a CLE probe can be expected within minutes of completing liver ablation therefore potentially allowing assessment during the same treatment session as near-real time monitoring.

5.5. Conclusion

In summary, this chapter has assessed dual-wavelength CLE for evaluating ablation therapy of focal liver lesions under laparoscopic guidance. Intraoperative CLE image acquisition during liver resection has been shown to be technically possible. In analogy to CLE studies conducted on murine CRLM in chapter 4, it was demonstrated that numerical analysis of fluorescence intensity can be employed to confirm the extent of liver ablation. Based on these findings, CLE may be of interest as a novel imaging modality in liver ablation research. Further investigation seems warranted to examine if technical limitations, that currently prevent a clinical translation of this approach, can be overcome.

In the following chapter normal and pathological liver tissue will be studied on a macroscopic scale with multispectral imaging.

6. Multispectral imaging

6.1. Introduction

The way that tissues interact with light is too a large extend determined by their chemical composition. As a generalisation it can be said that within the visible spectrum, tissues that appear bright reflect light (i.e. “throw” it back at the observer) whereas dark tissues mostly absorb light. Light absorption and reflection are inversely related to each other. This phenomenon also takes place outside the visible range e.g. in the infrared and ultraviolet spectrum. It has previously been established that as tissues undergo a pathological process they will often alter their absorption behaviour (and vice versa for reflection) within the visible and invisible spectra of light. The absorption characteristics of tissues and potential changes can be elucidated by obtaining a spectral response curve (SRC). These curves are created by plotting tissue absorption or reflection against light wavelengths. Many substances (e.g. lipids or water) have one or more absorption maxima (a wavelength where more light is absorbed than in the adjacent wavelengths) that is specific to them and that can be used to infer their respective presence and estimate their tissue concentration (224). The characteristics of SRC has been shown to reflect the tissue composition through further detailed analysis conclusions may be drawn as to the concentrations of a number of substances such as lipids, water or haemoglobin to name a few (163,224). This principle has found wide spread use in pulse oxymetry where the fractions of oxygenated vs. deoxygenated haemoglobin are measured with the aid of red and infrared light to allow the assessment of oxygen saturation.

Previously it was demonstrated that this technique can be transferred to laparoscopic surgery by fitting the laparoscope with a light filter that narrows the reflected (i.e. received by the laparoscope) light down to a certain spectral range (e.g. range of 20nm) by filtering out light received from tissue that is outside the desired range. This approach was facilitated by employing either an adjustable filtering process controlled by a liquid crystal tuneable filter (LCTF) (163)or by the use of a multiple bandpass filter that was used in conjunction with the RGB colour channels of the camera sensors (332). For example a multiple bandpass filter may allow transmission of light at 425-455nm, 500-535nm and 590-620nm. If an image is exclusively processed using the blue RGB channel then only light reflected at the range of 425-455 is recorded. The authors demonstrated that this method enabled laparoscopic evaluation of relative haemoglobin concentration (163) and an improved visibility of superficial vasculature (332). A different group that also utilised a LCTF showed that by focusing on determination of fat, water and haemoglobin contents, it was possible to clearly visualise the hepatic artery, portal vein and the common bile duct in a porcine model (155).

A more detailed analysis of tissue spectra can allow quantification of substance concentrations within tissue. One group has described the development of a needle-based probe device that can be used to perform diffuse optical spectroscopy by putting it into direct

contact with organic material. In one of their first publications they verified the devices capability to estimate concentrations of lipid and water in tissue phantoms and *ex*-vivo porcine liver samples (161,224). This approach has been further expanded to include the estimation of haemoglobin and bile content. By analysing various physiological and morphological parameters of spectral response characteristics of oxygenated haemoglobin, deoxygenated haemoglobin, water, bile and lipid, it was possible to fit a model representing the SRC of normal (i.e. non-pathological) liver tissue. This model was then subsequently utilised to distinguish between normal and malignant tissue in *ex*-vivo liver specimen that were resected from patients with CRLM. This technique has also been recently applied to an *in-vivo* model of primary liver cancer. Using probe-based diffuse optical spectroscopy, reduced fractions of lipids, blood and reduced tissue oxygenation were detected in areas of HCC in 5 woodchucks (257). Although these results are promising there are several disadvantages to employing a probe based design intraoperatively. Firstly, the tissue evaluation is limited to a small volume of tissue due to the small separation between the optical fibres delivering and receiving light (1.84 mm). This means it may take a long time to assess a clinically meaningful area. Secondly the tissue analysis depends on changes in the spectroscopic response curve which is not an intuitive or time efficient way to mentally integrate information during surgery.

Spectroscopic discrimination of tissue characteristics the nature of tissue has potential advantages for its application in laparoscopic surgery because it may replace in part the sense of touch that is lost in minimal invasive surgery, by displaying normally invisible tissue qualities to the surgeon. Tissues types of surgical relevance that have been successfully identified using either multispectral imaging (MSI) or diffuse optical spectroscopy include veins, arteries, bile ducts, steatotic liver and cancerous liver. To avoid the aforementioned disadvantages of diffuse optical spectroscopy however, it would be important to develop a no-touch method of spectroscopic assessment that does not require direct contact or the insertion of needles into tissue. It is hypothesised that a multispectral imaging system that can reproduce the tissue discrimination approach demonstrated for diffuse optical spectroscopy would be a potential solution to this problem.

The aim of this chapter is to formulate a technique and analysis method that enables intuitive, image based spectroscopic interpretation of liver tissue characteristics. The spectroscopic studies will be carried out on *ex-vivo* human liver tissue.

6.1.1 Aims

The specific in this chapter aims are to:

1) develop and test an imaging platform that enables spectroscopic tissue evaluation in a continuous wavelength range.
2) examine spectra of normal and pathological liver specimen and compare findings to data published in the literature.
3) perform statistical analysis of the predominant predictive components of the spectral response curve in liver tissue.

6.2. Methods

6.2.1 General setup

In this chapter spectroscopic response curves are recorded from liver tissue samples. This is achieved by illuminating tissue with an Optical Parameteric Oscillator, a wavelength-tuneable light source that can be finely tuned to wavelengths between 700-2000nm. The amount of light absorbed by tissues corresponds is inversely related to the amount of reflected light. Reduction of background illumination is achieved by conducting the recordings in a darkened room without additional light sources. A NIR camera with an InGaAs sensor is employed to record the reflected light which is measured as pixel intensity on a scale of 0-16.383. Generally it can be stated that higher pixel intensities correspond to higher tissue scattering and lower tissue absorption. The excitation wavelength is changed over time while images are recorded from the stationary liver specimen. As an analogy it can perhaps be compared to recording a video sequence where instead of moving objects, a change in light spectra is recorded. Tissues from the same source (e.g. patient) but different characteristics (e.g. healthy vs. pathological tissues) are always examined at the same time and within the same field of view. To reduce variability in illumination that is introduced by the synchronisation between OPO light pulse and camera recording, several frames (usually 20, if different number it is stated) are recorded at each wavelength. Approximately <1% of frames were grossly under-illuminated despite synchronisation. These were excluded from analysis using on an automatic outlier recognition algorithm that was based on the median absolute deviation method (333) that has been shown to be efficient in datasets with non-parametric distributions such as the spectroscopic data recorded for the experiments in this chapter. Simultaneous examination reduces experimental variables and ensures that most of the variability in the tissue spectra originates from differences in tissue composition. At the conclusion of the spectroscopic examination, specimen biopsies are taken for histological examination. Finally histological findings are correlated with spectroscopic response curves.

6.2.2 Comparison of spectral response curves

Initially results are analysed by observing the spectral response curves from whole tissue samples. For example in an experiment with three tissue sample, each sample is marked with a region of interest (ROI) and the mean pixel intensity (y-axis) from each ROI is subsequently plotted against the excitation wavelength (x-axis). This results in three separate spectral curves plotted on the same graph. Background noise is accounted for by subtracting the average value of non-illuminated frames that were recorded prior to each experiment. The characteristics of the spectral curves are compared against each other and in addition to spectroscopic tissue data from the literature.

6.2.3 Normalisation process

A limitation to statistical comparison across different experiments was that a number of factors such as illumination area, lens to specimen distance, specimen size and number varied between different experiments. To make the spectroscopic curves comparable, recorded data was normalised.

Normalisation was carried out by calculating the background noise subtracted mean intensity from all recorded tissue samples (including normal and pathological tissue) at individual wavelengths. The resulting mean intensity value for each wavelength was then set to a value of 1. The pixel intensities recorded at an experiment is subsequently expressed as a multiplicative term at each wavelength. If for example the intensity at 1200nm is 50% of the mean value across experiments, it is translated into a normalised value of 0.5. The equation for the normalisation process is shown in Equation 6.1.

$$I = \frac{I_o - I_b}{I_{\mathrm{M}}}$$

Equation 6.1 Equation used to normalise pixel intensities of MIS images. Pixel intensities inversely correlate with light absorption. I - normalised intensity; o - original intensity; b - background intensity; M – background subtracted mean intensity across all samples

This approach was chosen as initial attempts of utilising a white reflection standard (which can be seen in most images) were unsuccessful because there was too much of a discrepancy between the light absorption exhibited by liver samples and the reflection standard, respectively. As light absorption of the liver tissue was much higher, the illumination levels needed to produce a spectral response curve from tissue was at a level were at the majority of wavelengths, the reflectance standard was over-illuminated (i.e. at maximal intensity). A spectral response at maximal intensity, which was a limit set by the physical characteristics of the cameras sensor, translates into a flat line which cannot be used for data analyses purposes (Figure 6.1).

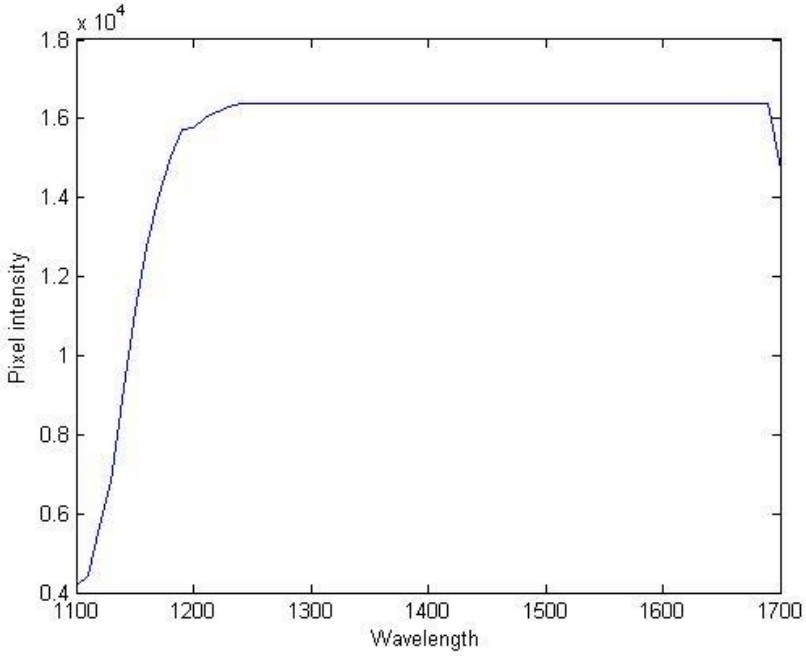

Figure 6.1 SRC of the white reflectance standard.

The spectroscopic response curve of the white reflection standard "flatlines" at most wavelengths at the illumination levels needed for producing spectroscopic response curves from liver tissue, due to detector saturation.

6.2.4 Statistical analysis

For statistical analysis single pixel values were compared rather than whole tissue samples. This method was chosen because images of cancer samples at certain wavelengths often appeared to be more heterogeneous than images from normal tissue. When taken the mean of a larger ROI however these variances would potentially cancel each other out. Normalised single pixel intensities were grouped according to tissue origin (normal tissue vs. cancer) and wavelengths (Cancer type distribution in results). Patient ID and cancer type (CRLM or HCC) were also recorded as covariates. At first it was investigated if any specific wavelengths would be particularly suitable to distinguish normal tissue from cancer. Bland-Altman plotting (334) was carried out initially to look at distribution differences between patients and subsequently to look at differences between wavelengths. In Bland-Altman plots the mean value of two tests, in this case pixel intensity for normal and cancer tissue, on the x-axis is plotted against the absolute difference between both tests on the y-axis. If both tests have congruent results the resulting plot follows a horizontal which is set at zero difference. Different test results diverge from this line. To carry out the analysis the BlandAltman function (©Ryan Kerner) that is available from MATLAB file exchange was used. Subsequently generalised linear mixed model analysis was carried out with two aims 1) to determine if normalised pixel intensities could independently predict the presence of cancer vs. normal tissue and 2) which particular wavelengths are most useful in

discriminating tissue. The analysis was conducted using SPSS™ Version 21 (IBM, Armonk, NY, USA). Intensity and wavelengths are used as fixed term whereas cancer type and patient ID (representing confounding factors between different experiments) are used as random terms for the analysis. For the analysis a multinominal distribution type was chosen combined with a logit link function.

6.3. Results

6.3.1 Assessment of feasibility and spatial resolution of the SCR

The first experiment was carried out to find the optimal setup configuration for and to evaluate image quality, to establish the spatial resolution of the spectroscopic data and to obtain preliminary data from spectral ranges that have been previously related to fat and water content. The setup configuration included lens to camera distance, upper illumination limit (i.e. maximum illumination without crossing the saturation limit of the camera sensor) as determined by use of optical filters and lens aperture. The preliminary experiments were conducted without synchronisation between camera and OPO laser source.

A low power output of the OPO at 900-1000nm meant that images recorded at this spectrum were hugely under-illuminated. It was possible to adjust for this by widening the lens aperture but this unfortunately meant that subsequent images at higher wavelengths were grossly over-illuminated and could therefore not be analysed. A decision was made at this point to limit MSI image acquisition to wavelengths > 1100nm (The OPO could not be tuned to wavelengths between 1000-1100nm).

For these experiments no synchronisation or automatic selection process was used, which means all frames regardless of illumination levels were recorded. A large number of frames were under-illuminated and hence a scatter plot representation was used to assess tissue SCR. A mean representation in the plot would have been heavily influenced by the under-illuminated frames.

Tissue used for this experiment were commercially purchased bovine liver and streaky bacon. The bacon was thought to be useful because of its contrast between lipid rich (fatty stripe) and water rich (red stripe) tissue. Bovine liver was used as a substitute to human liver samples. In addition a white reflectance standard was used to evaluate the consistency of the illumination. The reflection level is expected to be almost unchanged across wavelengths. Experiments were repeated three times, but at each repetition there was at least one wavelength for which no measurable illumination was recorded. These frames were depicted on the plots as circles lying directly on the x-axis which means that the corresponding mean ROI pixel intensity equalled zero or near zero. These values have been removed from the scatter plots to improve readability (Figure 6.2). The spectra with the lowest data loss are presented in the plots below, which compare SRC's at 1150-1250nm and 1400-1500nm from the same tissue area. These wavelength ranges were chosen

because the former contains the lipid absorption peak around 1200nm and the latter contains a water absorption peak which is broader at around 1450nm (224).

The ROI marked over the fatty region of the bacon slice exhibited the highest intensity (i.e. lowest absorption) of all the tested regions. Due to the lost data it is hard to interpret but it was felt that there is a suggestion of stronger absorption at 1200 & 1210nm (arrow). At 1400-1500nm the absorption was higher compared to 1150-1250nm (Figure 6.2). The ROI marked muscle tissue (red bacon stripe) was <1cm distant from the fatty area but did show a different spectral response. The absorption was stronger at both wavelength ranges compared to the lipid rich area (Figure 6.3). The absorption at 1400-1500nm was strongest for the liver tissue sample perhaps indication a greater water content (Figure 6.4). The spectral response of the white reflection standard, although exhibiting a slightly higher absorption at 1150-1250nm was generally constant (Figure 6.5).

Optimal camera lens to specimen distance was found to be 20-25cm which provided a good balance between a sharp image focus and a good illumination level. To prevent over-illumination, the lens aperture was kept very narrow and optical filters of 6 optical densities strength were used. Spatial resolution of the MSI imaging system was found to be in the range of app. 1mm meaning that tissues 1mm apart can display different absorption behaviour. Generally the absorption at 1400-1500nm was found to be higher for all tissues but the absorption for the liver sample was most pronounced. An absorption peak over the fatty tissue was recorded in two out of three experiments. In the 3rd experiment no usable image data was recorded at 1200nm and the adjacent wavelengths. It became apparent that a solution to prevent data loss in future experiments was required.

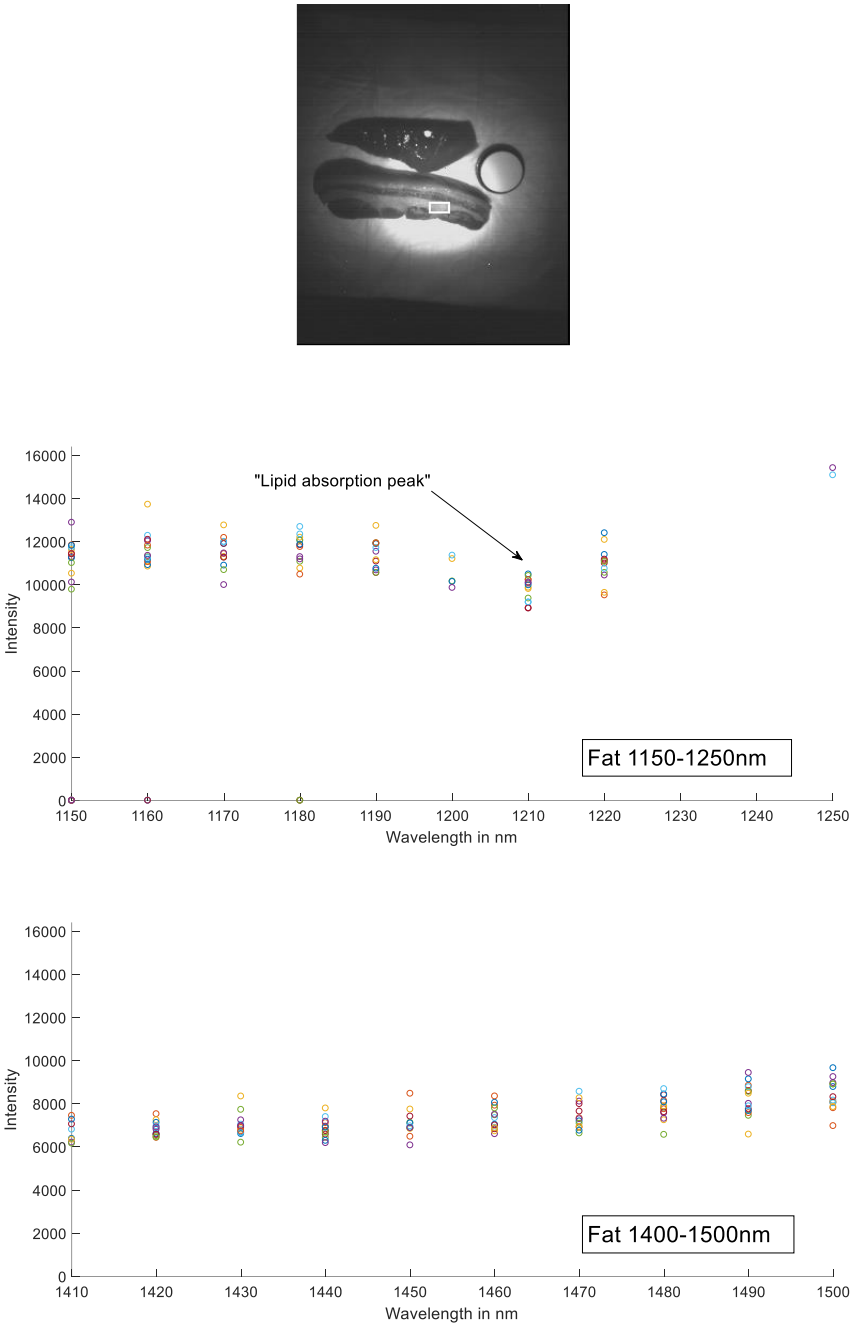

Figure 6.2 Scatter plot - SRC from lipid rich tissue.

Spectral response of fat tissue from a piece of bacon. Plotted is background noise subtracted pixel intensity on the y-axis and wavelength on the x-axis. Each circle represents one frame that was recorded at the respective wavelength. Top - ROI. Middle – spectrum of 1150-1250nm, The lipid absorption peak at 1210nm is annotated with an arrow. Bottom – spectrum of 1400-1500nm.

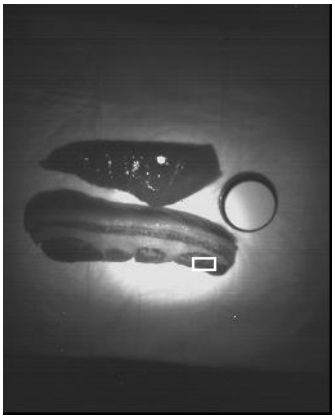

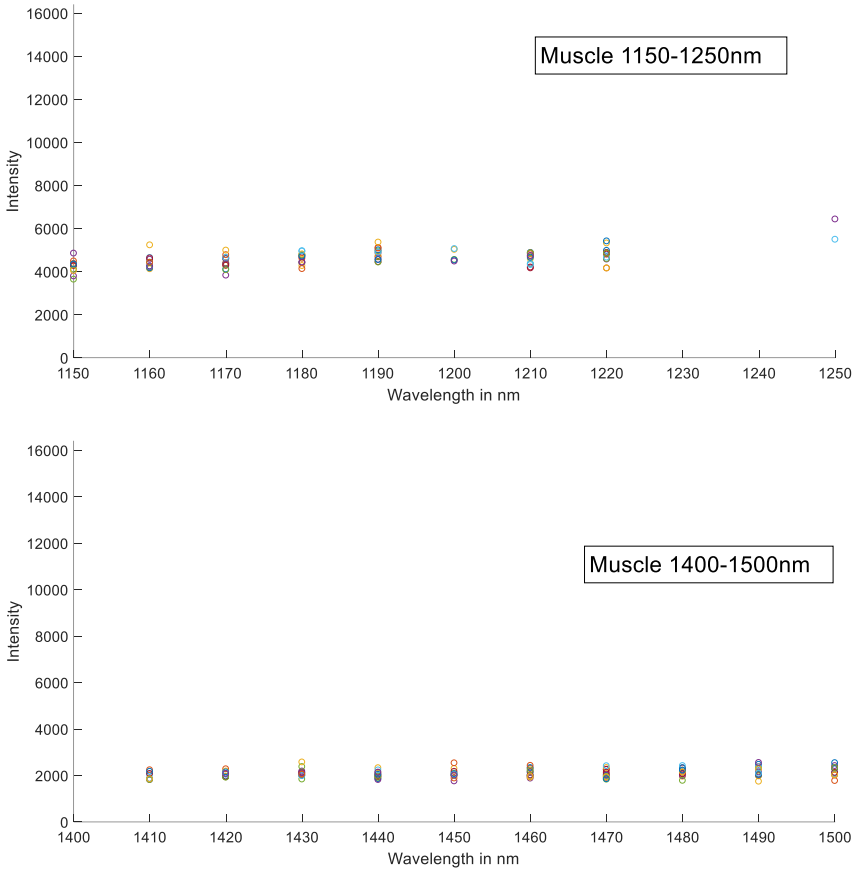

Figure 6.3 Scatter plot - SRC from muscle tissue.

Spectral response of muscle tissue from a piece of bacon. Plotted is background noise subtracted pixel intensity on the y-axis and wavelength on the x-axis. Top - ROI. Middle – spectrum of 1150-1250nm. Bottom – spectrum of 1400-1500nm.

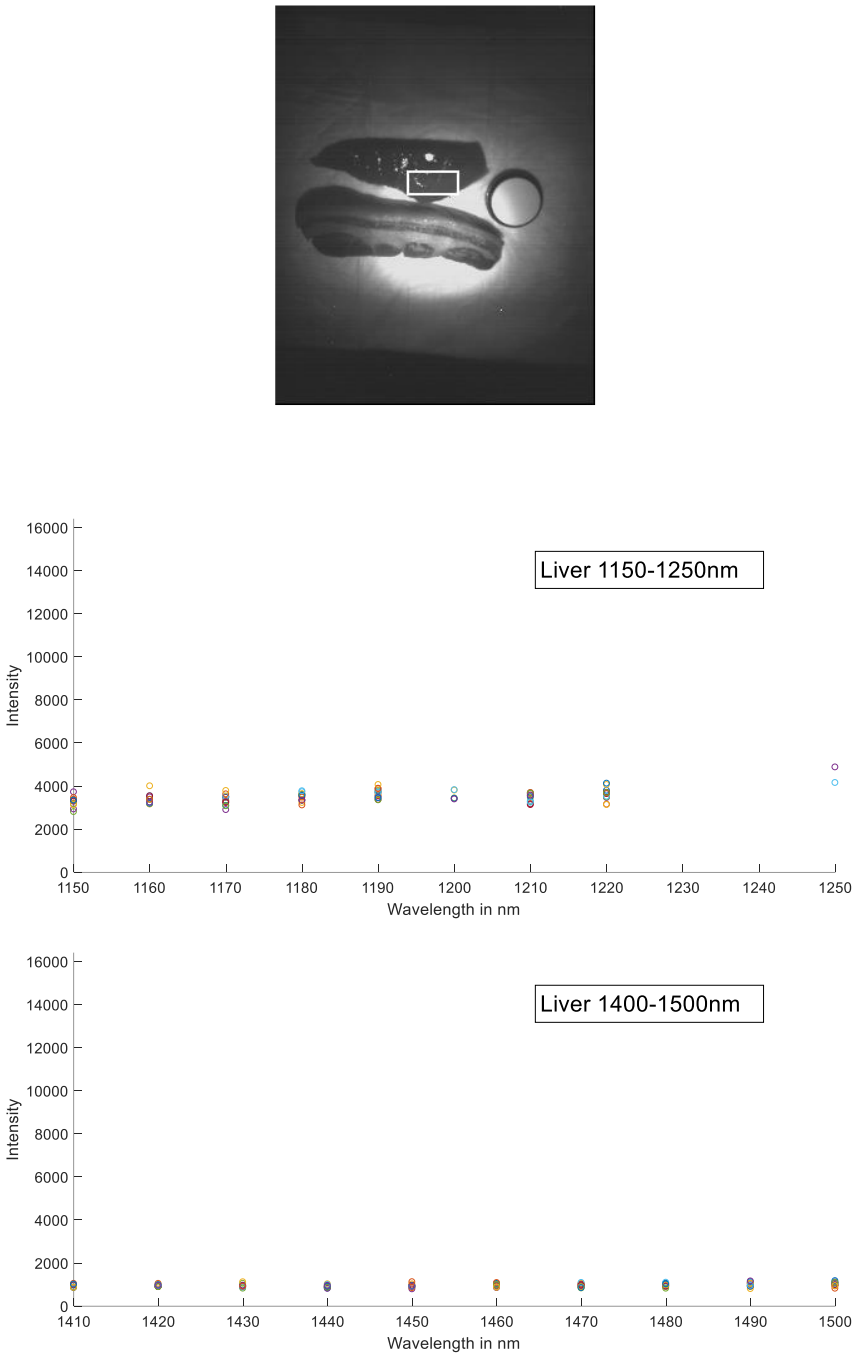

Figure 6.4 Scatter plot - SRC from liver tissue.

Spectral response of bovine liver tissue. Plotted is background noise subtracted pixel intensity on the y-axis and wavelength on the x-axis. Top - ROI. Middle – spectrum of 1150-1250nm. Bottom – spectrum of 1400-1500nm.

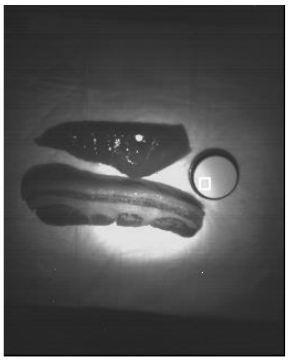

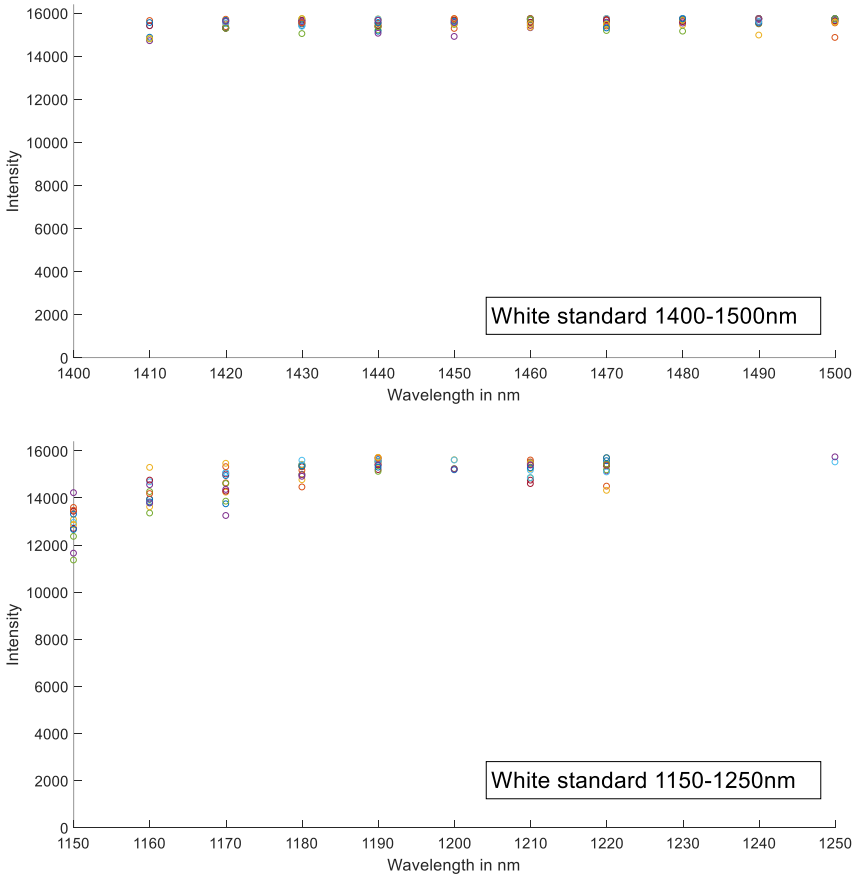

Figure 6.5 Scatter plot - SRC from a white reflectance standard.

Spectral response of the white reflection standard. Plotted is background noise subtracted pixel intensity on the y-axis and wavelength on the x-axis. Top - ROI. Middle – spectrum of 1150-1250nm. Bottom – spectrum of 1400-1500nm. A smaller area of the standard was marked because illumination did not reach the whole area of the standard

To improve data acquisition the Labview code was reprogrammed to ensure that at a minimum number of frames (usually 20) was obtained for each wavelength. Frames whose maximum intensity did not pass a certain threshold were automatically discarded. This new approach ensured that there were no further issues with “empty” wavelengths (Figure 6.6). An ongoing issue was however that some under-illuminated frames were still recorded because specular reflections did occasionally cross the required maximum intensity threshold.

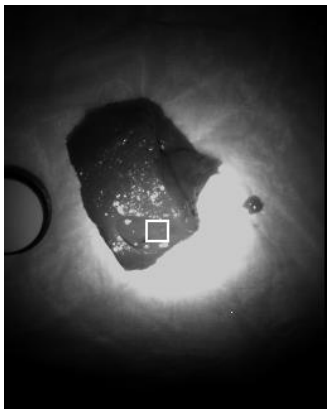

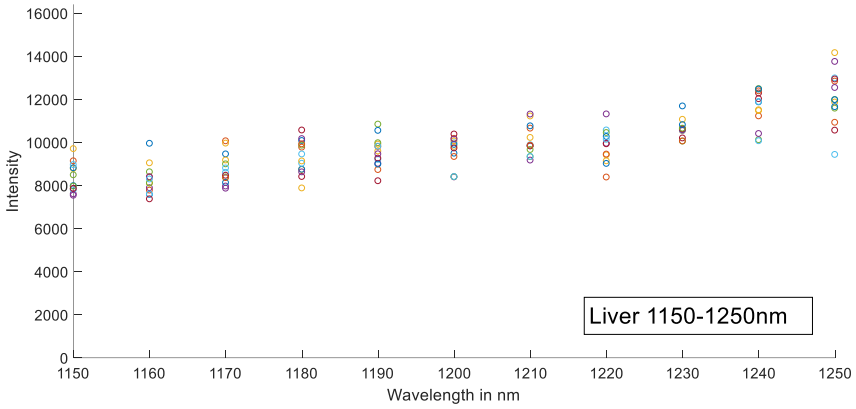

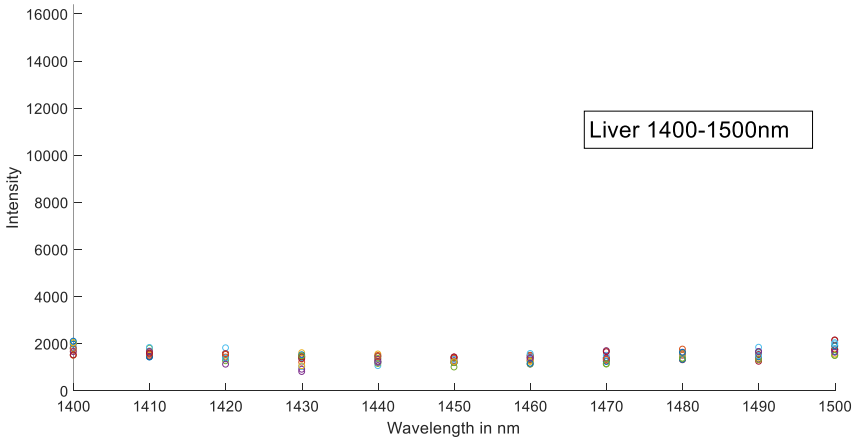

Figure 6.6 Scatter plot – SRC from liver tissue recorded with an improved image acquisition algorithm.

Automatic frame selection enabled continuous recording of SRC without "empty" wavelengths. Shown is a SRC from bovine liver tissue as a scatter plot.

6.3.2 Assessment of normal vs. steatotic liver

Before studies on steatotic liver tissue were conducted, an improved image acquisition algorithm was programmed. This minimised loss of data to <1% (Figure 6.7). A detailed description of the algorithm has been given in the General Methods section (3.3.3.3). Steatotic liver samples were retrieved from discarded donor livers. Non-steatotic liver samples were retrieved from liver resections carried out for cancer. The samples were taken from areas of the liver that did not show any cancer involvement. The tissue spectra were plotted and assessed for differences between steatotic and non-steatotic samples. A prominent absorption peak at 1210nm indicating a greater lipid content in the steatotic samples was observed Figure 6.8). The plotted intensity represents noise subtracted raw pixel intensity. No normalisation process was carried out due to the low number of tissue samples which made statistical analysis unfeasible. Therefore, absolute intensity differences could potentially be due to changes in illumination intensity, the shape of the spectra would however not be influenced by this. Presence of liver steatosis as indicated by vacuole formation was confirmed on H&E stain histology examination (Figure 6.9 & Figure 6.10). Vacuoles form at the location of adipocytes (fat cells) during the preparation process of histology slides (335).

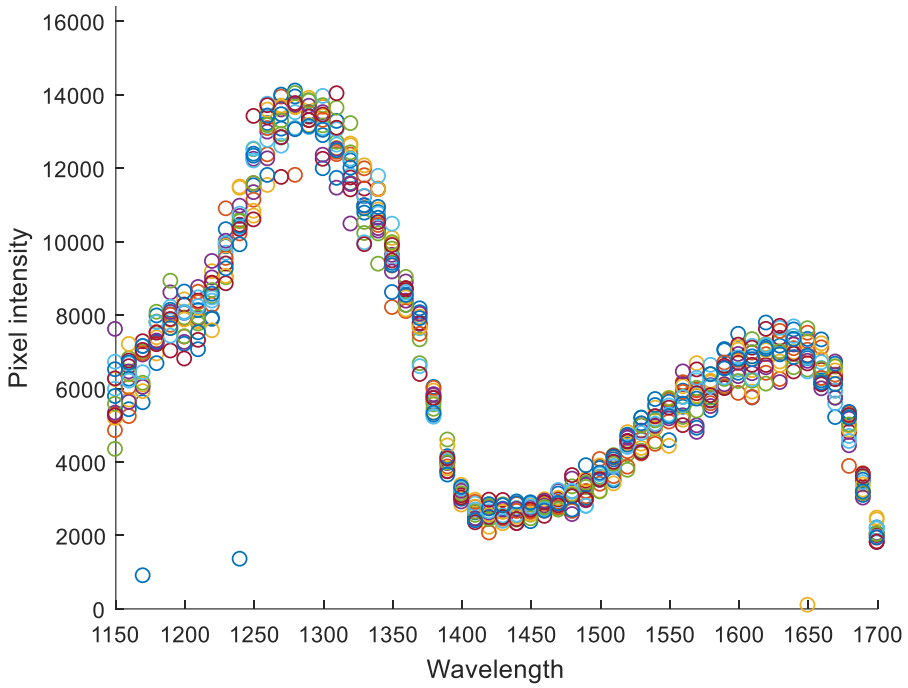

Figure 6.7 Scatter plot – SRC recorded using the final version of the MSI acquisition algorithm.

The improved MIS image acquisition improved data loss significantly. Each wavelength step has been measured with 15 repetitions. Out of a total of 56x15 frames, only 3 have been under-illuminated. These frames are excluded from further analysis by automatic outlier exclusion based on the median absolute deviation.

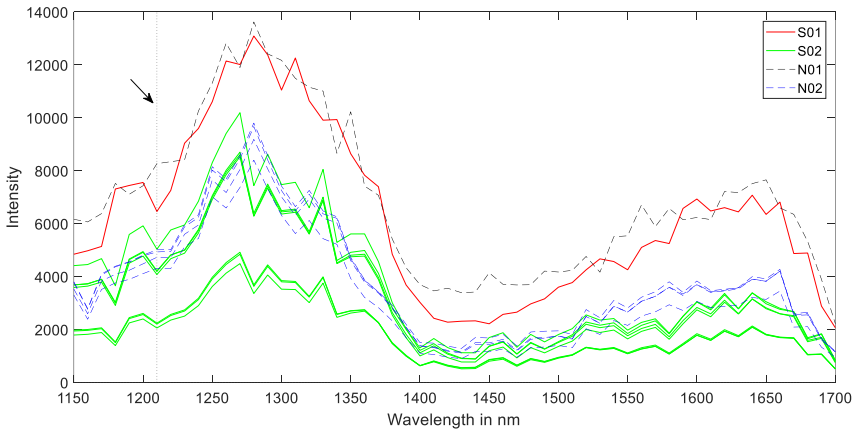

Figure 6.8 SRC from steatotic and non-steatotic liver specimen (n=2 each)

Tissue spectra from steatotic (S01 & S02 – solid lines) and non-steatotic (N01 & N02 – dashed lines) liver samples. The dotted vertical line (arrow) marks 1210nm where an increased absorption could be observed in steatotic liver tissue. Background noise has been subtracted from the plotted intensity.

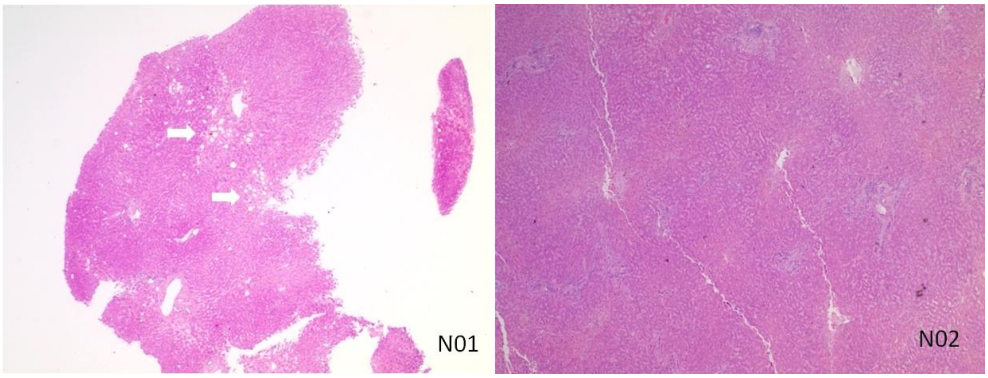

Figure 6.9 H&E histology from non-steatotic liver biopsies.

Histology H&E stains from non-steatotic livers. Vacuole formation indicating fat content (arrows) was only infrequently observed in one of the samples (N01). The other sample (N02) was virtually free of vacuole formation.

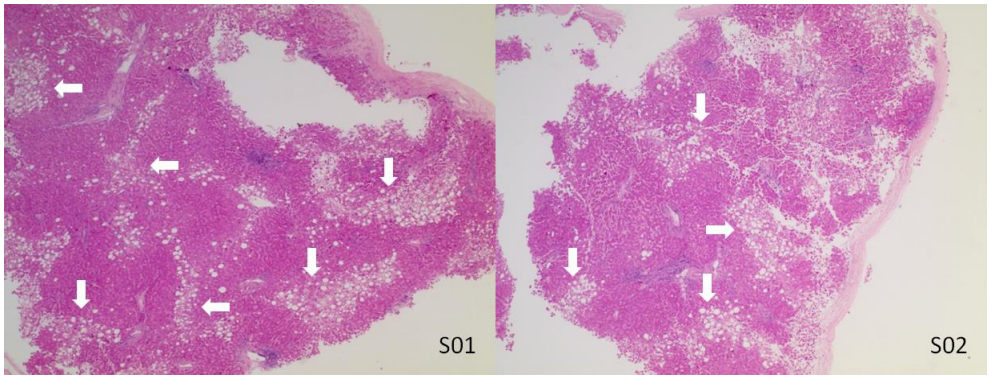

Figure 6.10 H&E histology from steatotic liver biopsies.

In steatotic liver tissue vacuole formation indicating fat content was frequently observed (arrows).

6.3.3 Qualitative assessment of cancer vs. normal liver

6.3.3.1 CRLM

Multi-spectral imaging was carried out on tissue samples from patients with CRLM (n=3). Images were analysed to create SRC from regions of interest that covered the whole tissue area. These were subsequently compared between normal and cancerous tissue (Figure 6.11). For patient ID's C02 and C03 one sample each was evaluated whereas for patient ID C03 one cancerous and 3 normal samples were evaluated. The number of samples was determined by the size and nature of the liver resection specimen. Samples for MSI experiments could only be obtained if the pathological resection margin would not be compromised. At the conclusion of experiments, tissue biopsies were taken for histological evaluation (Figure 6.12), which was used to confirm the nature of the tissue sample (i.e. normal vs. cancer). Analysis of the SRC did not reveal any obvious differences between cancerous and normal tissue. Samples taken from different patients did however exhibit different MSI characteristics, but this could not be clearly attributed to the absorption characteristics of a specific substance.

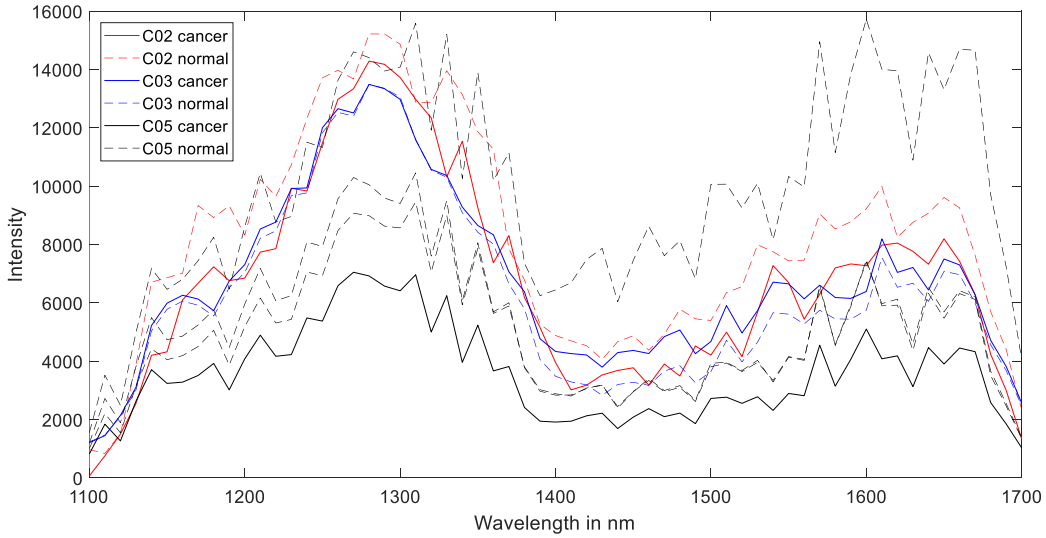

Figure 6.11 SRC of CRLM tissue vs. normal liver tissue.

Tissue absorption spectra of normal vs. CRLM tissue obtained from three different patients. Background noise has been subtracted from the plotted intensity.

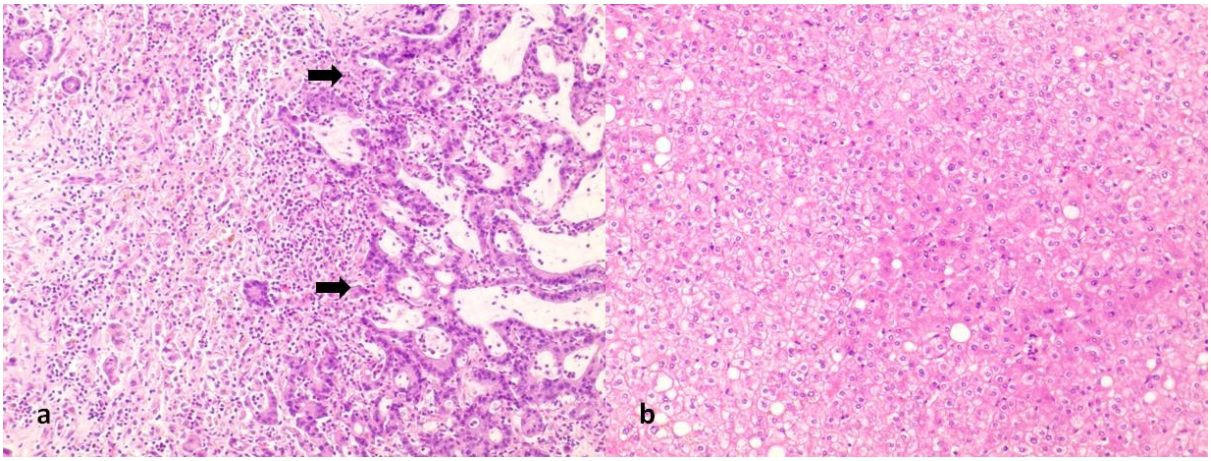

Figure 6.12 H&E histology from liver samples with CRLM.

H&E stained histology from a liver specimen containing CRLM. a) The arrows mark the border between normal tissue on the left and CRLM tissue on the right. b) Normal hepatocyte architecture with a few vacuoles on the left of the screen.

6.3.3.2 HCC

In analogy to MSI experiments on CRM tissue, data was obtained from HCC specimen using the same protocol. Tissue was obtained from two patients. For patient ID C01, two normal and one cancerous sample were available for examination, whereas for patient ID C04 two normal and three cancerous samples were available. Subjective analysis of the absorption spectra did not reveal any overt difference between normal and cancerous tissue. There were differences in the SRC characteristics between the two patients (Figure 6.13). It was also noted that C01 who had mild liver steatosis as marked on histological evaluation, exhibited a marked absorption peak at around 1210nm.Presence or absence of cancer was verified based on tissue histology (Figure 6.14).

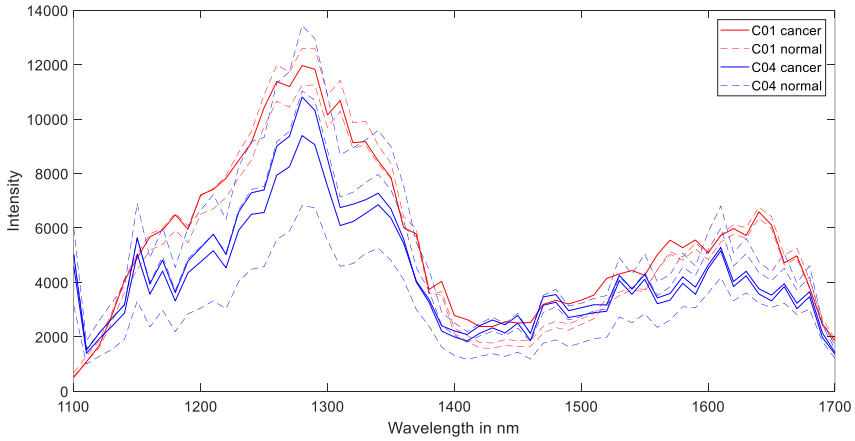

Figure 6.13 SCR of HCC vs. normal liver tissue.

Tissue absorption spectra of normal vs. HCC tissue obtained from two different patients. Background noise has been subtracted from the plotted intensity.

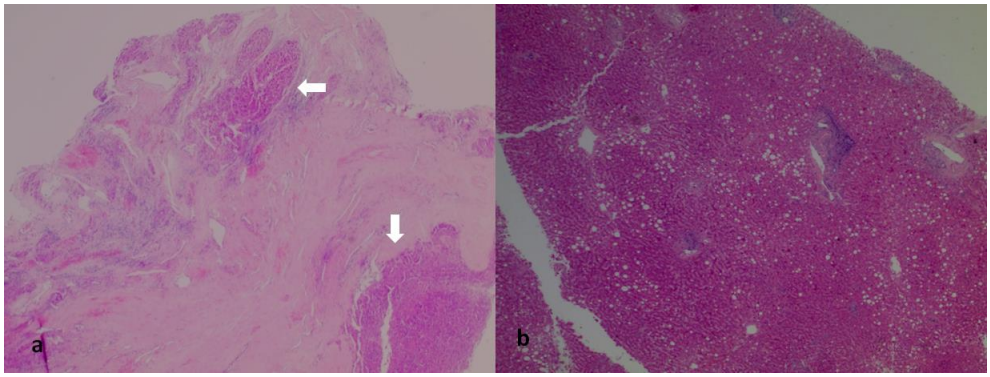

Figure 6.14 H&E histology from liver sample with HCC.

a) A accumulation of HCC cells (arrow) within fibrotic liver tissue. b) Tissue obtained from a normal section of tissue shows regular hepatocyte architecture with a slightly higher than normal amount of vacuoles.

6.3.4 Statistical analysis of cancer vs. normal liver

Because subjective evaluation of the tissue absorption spectra from cancer and normal tissue could not discern any defining characteristics it was decided to perform a statistical analysis on the available MSI data. It was noted that on visual inspection, liver tissue containing cancer often had a heterogeneous appearance. Therefore the main focus of the statistical analysis was on evaluating potential differences on a pixel by pixel basis. At first data from all samples was normalised as described above (6.2.3). The resulting normalised absorption spectra are shown below (Figure 6.15 & Figure 6.16).

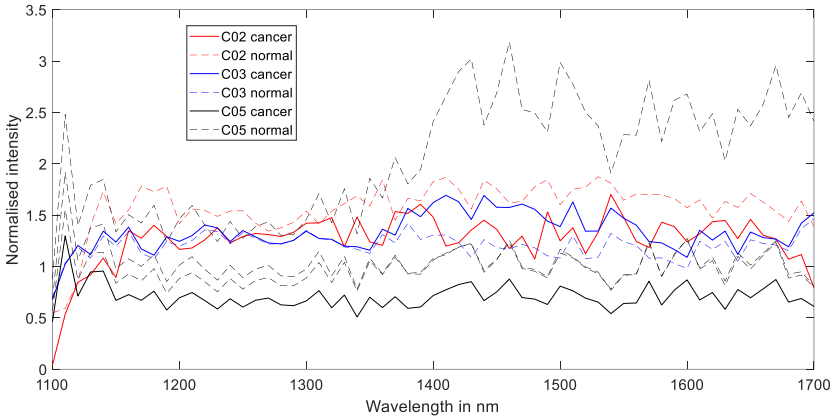

Figure 6.15 Normalised SRC of tissue from patients with CRLM.

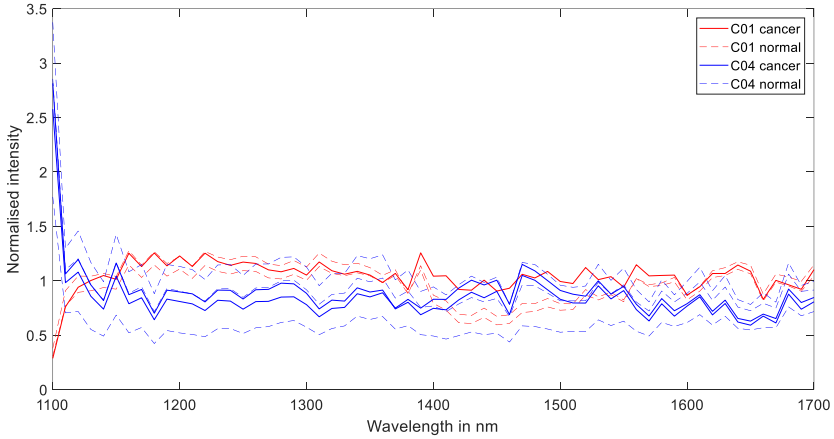

Figure 6.16 Normalised SRC of tissue from patients with HCC.

The next step was to analyse the data for differences between patients and between individual wavelengths using Bland-Altman plotting (BAP). For each patient ID, normalised intensity values were averaged for cancer and normal tissue to facilitate BAP. This was necessary because only two groups (i.e. normal & cancer) per patient ID can be analysed with BAP.

The resulting BAP initially grouped by patient ID (Figure 6.17) and then by wavelength (Figure 6.18) are depicted below. The aim was to identify any particular wavelengths that would be outside the expected distribution which is highlighted by the dashed horizontal lines which represent limits of agreement between cancer and normal tissue intensities. It was intended to include any wavelength that was repeatedly (i.e. across patient ID's) outside the agreement limit in a subsequent generalised linear mixed model analysis. Although several wavelengths were found to be outside this area this was not consistent across patients and was therefore more likely due to inter-individual differences.

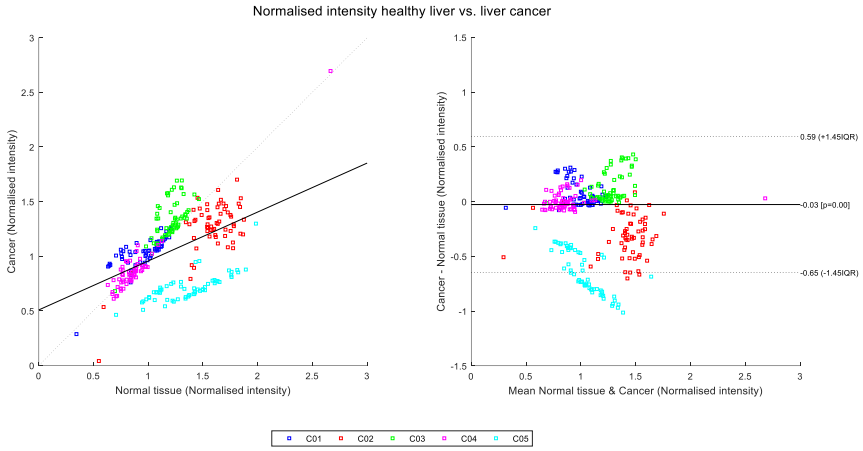

Figure 6.17 Bland-Altman Plot ordered according to patient ID's.

The left graph depicts cross-correlation between cancer and normal tissue values. The graph on the right is the actual Bland-Altman plot. It can be observed that normalised intensities for patient ID C05 and to a lesser extent C02 (both CRLM) are outside the limits of agreement.

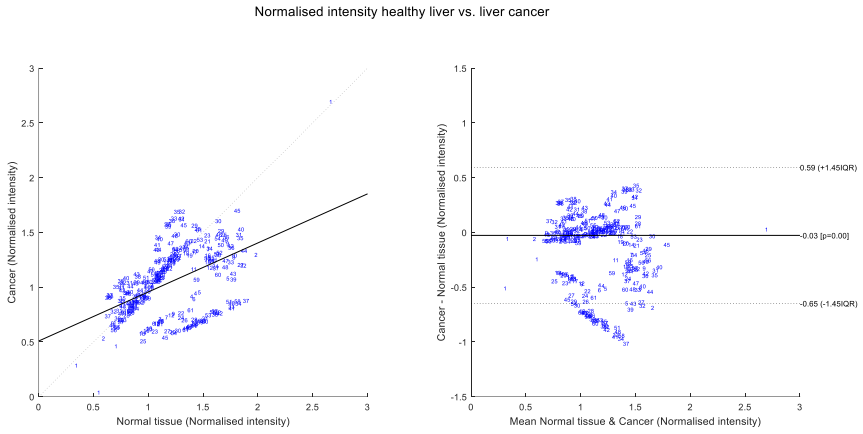

Figure 6.18 Bland-Altman plot ordered according to wavelengths.

The wavelengths outside the agreement limit were largely in the range of 1400-1600nm.

Because no particular wavelengths could be identified in the BAP, a generalised linear mixed model analysis was carried out including all wavelengths from 1100-1700nm. Essentially the pixels from all previously marked ROI's were combined and divided into two groups, cancer vs. normal, according to the tissue sample the ROI was taken from. The analysis included normalised intensity and wavelength as fixed terms whereas patient ID and cancer type were used as random terms. The tissue type cancer vs. normal tissue was used as dependent. A multinominal model with a logit link function was used. According to the analysis, the normalised pixel intensities measured at 14 out of 61 wavelengths (Table 6) were statistically significant as an independent predictor for the presence of normal vs. cancer tissue. The classification accuracy of the model was 69.1%.

Wavelength	Coefficient	95% lower	95% CI upper	p-value
1100	0.238	0.2	0.276	0
1110	0.125	0.087	0.162	0
1130	0.041	0.004	0.079	0
1180	-0.04	-0.078	-0.003	0.034
1190	-0.067	-0.105	-0.03	0
1220	-0.044	-0.082	-0.007	0.02
1320	-0.043	-0.08	-0.005	0.025
1430	0.038	0.001	0.075	0.047
1470	0.039	0.001	0.076	0.042
1480	0.061	0.023	0.098	0.001
1570	0.05	0.012	0.087	0.009
1600	0.047	0.01	0.084	0.014
1610	0.048	0.011	0.086	0.012
1660	0.042	0.005	0.079	0.028

Table 6.1 Results of the generalised linear mixed model analysis.

Wavelengths that were shown to be independent predictors for the presence of malignancy are shown in the table.

6.3.5 False colour visualisation

A 'false colour' image was created by combining data from several wavelengths in one image frame as described above (3.3.6). Image data obtained at wavelengths that were statistically significant with a positive coefficient on generalised linear mixed model analysis was averaged for each pixel. The resulting image is shown below (Figure 6.19).

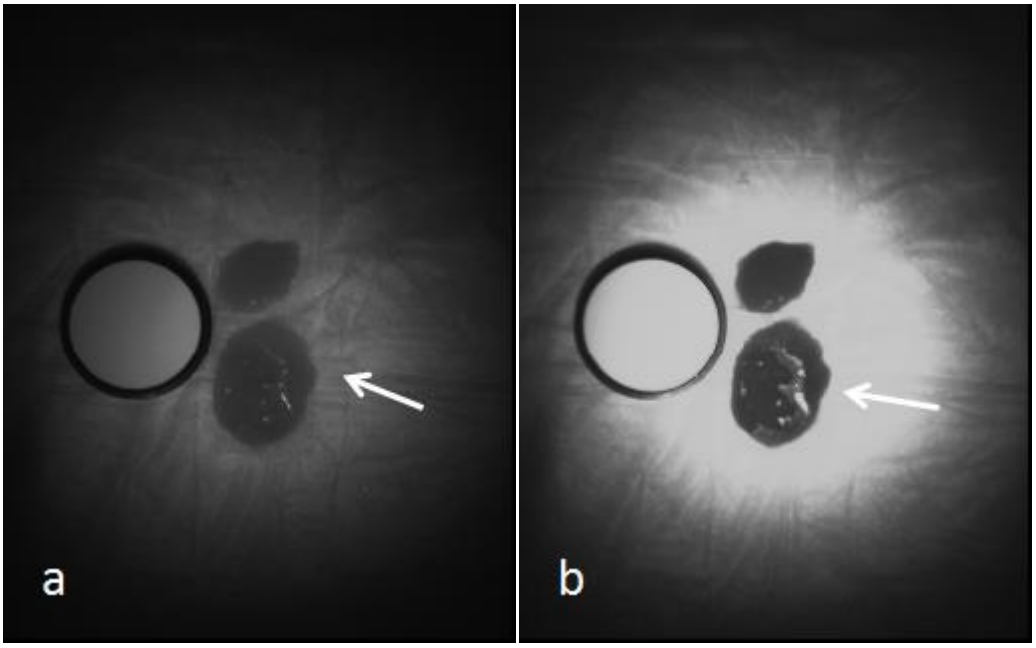

Figure 6.19 'False colour' representation of multiple wavelength spectra.

a) Image obtained at 1130nm. The sample containing CRLM is marked (arrow). b) False colour image combining the average for all wavelengths that were shown to be independent predictors for the presence of normal vs. CRLM tissue (arrow).

6.4. Discussion

In this chapter a system has been developed and tested to enable multispectral imaging of *ex-vivo* tissue samples. It was shown that depending on field of view MSI images enabled reconstruction of tissue absorption spectra at fine spatial resolution that could be interpreted based on individual pixels. Because a tuneable OPO was employed as excitation source, the spectral resolution was (i.e. distance between individual wavelengths) was in the range of 3-5nm. An additional advantage of this approach was that no direct contact with the tissue was required and the area of multispectral evaluation could be altered by changing the field of view.

Liver tissue specimen from normal and diseased tissue were qualitatively examined and the resulting SRC were compared to data from the existing literature. A prominent absorption peak at 1210nm was observed in steatotic liver samples which is congruent with previous reports (224,336). The steatosis in the specimen was not formally quantified because with tissue only being available from two patients an in depth quantitative analysis between fat content correlation and strength of the absorption peak would not have been feasible. Based on estimation however the steatosis involved <30% of the histological samples which means the steatosis was likely to be in the mild category (335). In preliminary experiments using bacon and bovine liver as *ex*-vivo tissue phantoms, the spectral range between 1400-1500nm which includes an absorption peak for water exhibited lower absorption in lipid rich

tissue. In the red meat part which was treated as a substitute for muscle tissue, the absorption at this range was stronger and in liver tissue it was the most prominent absorption out of all three examined tissues. It is hypothesised that this was due to greater water content in liver over muscle tissue but because a detailed tissue analysis was not performed this claim could not be verified.

The examination of liver specimen containing primary and secondary liver cancer did not show any obvious differences in the SRC characteristics of normal and cancerous liver tissue. There was however a difference when looking at tissue from different patients and between CRLM and HCC tissue. The generalised linear mixed model analysis indicated that a combination of absorption values taken at 14 different wavelengths could predict the presence of normal vs. cancerous liver tissue.

Having identified the most relevant wavelengths for the prediction of tissue quality, these were consequently incorporated into a false colour image processing algorithm. The aim of this approach was to enhance the visual perception of tissue quality in an intuitive and time efficient manner.

There were some limitations to the data presented in this chapter. The reported variations in the intensity values, normalised or otherwise could in part be explained by changes in experimental factors such as camera lens to specimen distance, which had to be altered to adjust the field, ensuring that specimen of different sizes were visible. Another factor with an impact on pixel intensity is the varying power output of the OPO laser source.

It is hypothesised however that impact of these two factors was attenuated because under-illuminated frames were automatically excluded during the image acquisition process. Using patient ID (tissue from different patients was examined on separate days) a random factor in the generalised mixed model accounts for variations in unknown parameters that could have changed between individual experiments. As is true for other optical imaging technologies, the imaging depth for MSI is limited. Penetration of light will vary slightly depending on wavelength but generally it has to be assumed that only tissue quality up to a maximal depth of ≈ 5mm can be assessed at present (144). There is some indication that stronger light sources may allow a deeper penetration within the region of >1cm depth (337) but if this is translatable to MSI remains to be seen. A further limitation is the small number of samples and the heterogeneous nature of the samples. The number of available cancer samples was limited due to practical issues. Tissue could only be obtained from one surgeons practice due to ethical considerations. The time frame in which tissue could be obtained was < 6 months because it took a substantial amount of time to build the MSI system and its accompanying software algorithm. In this context the process of synchronisation was especially time consuming. The samples themselves could only be obtained if a resection specimen was large enough to allow tissue harvest without compromising histopathological evaluation (i.e. to confirm that surgical excision of cancer was complete). The number of

liver specimen with steatosis underlay even greater restrictions because access depended on availability of discarded donor organs and sufficient staffing at the local tissue bank. A further limitation was that the effect of tissue perfusion could not be examined because all experiments were conducted on *ex*-vivo samples. Finally the breadth of the measured absorption spectra was limited by technical considerations. The InGaAs NIR camera used for recording the SRC had a wavelength range of 900-1700nm. The OPO laser source could be tuned to wavelengths between 700-1000 and 1100-2000nm.The power output and hence illumination intensity at 900-100nm was very low and hence it was decided to omit the range of 900-1000nm completely, because it would not have been possible to record a continuous spectrum. Evidence from the literature suggests that within the measured range of 1100-1700nm it is feasible to assess the absorption peaks of water and lipids because they have absorption peaks at around 1450nm and 1200nm respectively (224). Absorption peaks of other biologically relevant substances such as haemoglobin and bile lie within the range of 600-800nm.

The results from this chapter have highlighted the potential of MSI to remotely sense aspects of tissue composition that may reveal pathological changes. Further work is required before transferring this imaging modality into a clinical evaluation phase. Initially it would be useful to expand the width of the measured spectra to include biologically important substances such as bile and haemoglobin. This for example could be achieved by combining the existing system with an additional laser excitation source and sensing camera or a LCTF based system that can cover the range between 600-1100nm (155). It is also of crucial importance to expand the tissue data that was employed for building the predictive model. Because the nature, origin, biological behaviour and pathological composition of liver cancer types differs (20,23,338) it is proposed to evaluate tissue absorption spectra divided by cancer type. Once the spectral behaviour of different liver cancer types has been further evaluated the focus could be switched to developing a laparoscopic MSI system that can translate this methodology into clinical use. Although laparoscopic systems with MSI capabilities exist they are currently targeted at relatively narrow spectral range of a few hundred nanometres (155,195). It remains to be seen whether laser excitation, multi-bandwidth filtering or an alternative technique is the most useful method for MSI in laparoscopy. Based on the findings in this chapter a multi-bandwidth filter system appears to be the technically more feasible option because tuneable laser excitation sources are time consuming to use and comparably fragile. In terms of required timing for example, the InGaAs camera employed for the experiments in this chapter had a frame rate of 30fps, which translates to 30 individual wavelength spectra recorded per second. This frame rate was however limited by the OPO light emission frequency of 10Hz (i.e. 10fps). In contrast to this a bandwidth filter system would not have the same restriction.

6.4.1 Conclusion

In summary, the development of a broad spectrum remote multispectral imaging platform has been described. Its ability to record and visualise absorption spectra in liver tissue has been demonstrated and it was shown that variations in these spectra may allow prediction of pathological processes such as steatosis or malignancy. Statistical analysis of tissue spectra has led to the formulation of a predictive model that was consequently employed to develop an enhanced MSI based visualisation method for liver malignancy.

7. Video magnification

7.1. Introduction

In a previous chapter it was shown that CLE can visualise blood flow in small vessels and capillaries. Aside from tumour associated changes in microcirculation, the assessment of blood flow is of great importance during surgical procedures to evaluate the vitality of tissue and to guide surgical dissection. Failure to excise non-vital tissue, can result in ischaemic damage and this can activate inflammatory pathways and stress response (339).

Guidance is needed to make surgeons aware of blood vessel location which is important to avoid inadvertent injury that can lead to significant blood loss and associated morbidity. To achieve this form of guidance a technology that enables early detection of blood vessels and allows estimation of organ perfusion would be of benefit (67,141,265). Another scenario where visualisation of blood flow may be useful is during hepatectomy with hilar dissection (control of inflow vessels). When performing a traditional hepatectomy, the blood inflow to the liver is divided before liver tissue is transected. It can be difficult to appreciate which part of the liver is de-vascularised and hence decide on the optimal plane of transection. Visualisation of blood flow or segmental borders can be of benefit in this circumstance (159).

Because visual inspection to assess tissue perfusion is subjective and unreliable attempts have been made to develop an objective technique that can aid surgeons in this context. The approaches that have been proposed so far require the use of additional equipment and/or intravenous contrast agents which may increase procedure time or may have a negative impact on patient safety (184,340).

High resolution video that is routinely recorded during laparoscopic surgery contains potential physiological and anatomical information. However, surgeons cannot take advantage of this information because they are restricted by the limitations of the human visual system. A recent work on “Eularian Video Magnification” (136) has shown that physiological and anatomical information available due to variations in motion, colour and light can be brought to the attention of the observer by analysing space-time related variations of specific image regions in the video. Skin colour for example has been shown to fluctuate at the same rate as the heart frequency, which in turn can be translated into signals to record the pulse rate. Recording and analysis of vessel pulsation- and respiratory rate has also shown to be possible (136,341).

Despite these promising preliminary findings, major challenges have to be solved before real time VM can be used to assess tissue perfusion and detect hidden vasculature. One challenge for example is a standardised quantification or measurement method that enables researchers to directly compare different VM methods. Many improvements to the original work of Wu have been proposed (244,245,342). It is however difficult to decide without standardised metrics which of these methods is best suited to laparoscopic surgery. As part

of establishing quantifiable metrics, it would also be prudent to assess if the strength of the VM signal bears any correlation to the underlying physiological process e.g. when assessing blood vessels in the arm, would a higher blood pressure result in a stronger VM signal? Another challenge is to look at how VM processing is affected by different environments. Although pulsation of subsurface blood vessels (e.g. ulnar artery) have been made visible, it is not clear if this finding is transferable to the liver which has a much darker surface which absorbs more light. In this chapter video magnification is applied to experiments on imaging phantoms and a porcine laparoscopy model. Because it is a “wide field” method that encompasses the entire field of view it is more appealing for assessment of blood flow than a microscopic point based method such as CLE, where a vessel is only visualised when it is directly targeted. As a technology, VM could potentially be useful during laparoscopy by delineating perfused from non-perfused tissues and by localising non-visible blood vessels.

The texture of digital images can be analysed to extract features from a scene that enables an estimation of its content. This method has been popularised by some authors for the estimation of crowd density and crowd motion. The rationale behind this is that the texture becomes finer with an increasing crowd size because more persons on an image equate to a more detailed texture. These crowd and motion estimation algorithms are based on the Gray-level co-occurrence matrix (GLCM), a statistical texture representation method first described by Haralick (343). The GLCM methodology has been further described above (3.4.4.2). In this chapter the feasibility of employing GLCM analysis to estimate video magnification signals will be analysed. The proposed method will then be applied to the estimation of video magnification signals.

7.1.1 Aims

The aims in this chapter are to:

1) evaluate the feasibility of using texture based analysis to identify video magnification signals that originate from pulsatile motion.
2) elucidate if the analysis method from 1) enables quantification of pulsatile motion.
3) assess in how far the analysis method from 1) can be applied to pulsatile motion from structures that are concealed.

These objectives will be evaluated in a controlled laboratory setting first before being translated to an *in-vivo* model of laparoscopic liver resection.

7.2. Methods

7.2.1 Flow phantom experiments

In this section VM signals are evaluated on a pulsatile flow phantom. Tests in a controlled environment were a prerequisite to exploring this technology before evaluating VM signals in an *in-vivo* model. The first series of experiments was focused on determining the best combination of settings for 1) camera recording 2) VM processing 3) GLCM settings. The second series of experiments tested the ability of VM to enhance pulsatile motion (henceforth called 'VM signals') in a phantom with visible flow channels (henceforth called 'clear phantom'). The third series of phantom experiments repeated the same tests in a phantom with concealed flow channels (henceforth called 'brown phantom') which was created to better reflect the visual appearance of liver tissue.

All video sequences were processed and analysed using the same workflow. At first a video sequence is recorded. This is then processed with a VM algorithm to enhance motion. A region of interest (e.g. perfused catheter) is marked on the video to allow region specific processing of GLCM statistics. Finally the GLCM data is analysed for the presence of repetitive signals (e.g. pulsation) (Figure 7.1).

Figure 7.1 Steps involved in texture based VM signal analysis.

Flowchart showing the individual steps that are involved in analysing motion signals from VM enhanced videos.

7.2.1.1 Establishing the optimal evaluation setup

Before the evaluation of VM processing on the flow phantom could be carried out it was important to standardise three types of settings, namely 1) Camera recording settings 2) VM algorithm processing settings and 3) GLCM processing settings. Because all these settings have an impact on the characteristic of the resulting VM signal, it is crucial that the impact of different settings is well understood. Until now, the impact of video resolution, colour codec and recording speed on VM signals has not been evaluated.

7.2.1.2 Camera and video codec settings

In their first publication on VM processing Wu et al. (136) suggested that the field of view is centred on the object of interest and any additional objects should be avoided from this view. The field of view during experiments was therefore positioned to be completely occupied by the flow phantom. The camera was kept in a stationary position with the help of an adjustable camera arm which was fixed to a perpendicular pole (Figure 3.15). Lens- aperture and focus were set to provide a clear image avoiding formation of reflections and shadows

where possible. Video sequences were then recorded at different image resolutions; colour codecs (methods of compressing video data) and recording speeds (frame rates).

7.2.1.3 GLCM settings

The GLCM is processed based on the positional relationship of grayscale pixels in an image. Change in the statistical parameters of the GLCM reflect a change in image texture and as such can be utilised to estimate motion (261,344). The following set of parameters for the graycoprops MATLAB function determine the precise method of GLCM processing.

Offset: determines the position of the neighbouring pixel which can be found in any of 8 horizontal, vertical or diagonal directions (Figure 3.17).

Numlevels: Determines how many graylevels are used for processing. Default is 8, which means that all graylevel intensity values (e.g. 255 in an 8 bit image) are binned into 8 ordinal categories from low to high. If more levels are used then the bin categories shrink.

Graylimits: Sets the cut off points for the lowest and highest grayscale intensity. Any values below or above the threshold are binned into the next closest category.

7.2.1.4 Video magnification settings

As described above (3.4.1) video magnification settings determine how the original video data is processed.

In brief, a frequency range that includes the frequency of interest is selected (e.g. 60-100bpm for normal heart rhythm). The magnification factor ‘alpha’ determines the extent to which the signals are magnified. The spatial frequency ‘lambda’ is used to select the level of detail that is magnified with a high frequency chosen for finer details. Motions that fall below this level are filtered out. In general the amount of potential motion magnification is inversely related to image quality i.e. a strongly magnified video including many spatial and time frequencies results in a noisier image than videos that are weakly amplified. All sequences were processed using a temporal Butterworth filter, which is a filter setting targeted at enhancing motion (136).

7.2.1.5 Objective evaluation of motion signals

To enable objective decision making on optimal camera, VM and GLCM settings a quantifiable and reproducible evaluation method needed to be construed. The motion signals were analysed over time to evaluate if VM can elucidate frequency and flow pressure within the phantom at different depths. As described above (3.4.4.1) GLCM statistical values from a region of interest in the video are plotted over time. Subsequently they are processed using the MATLAB function ‘correlation’ that allows quantification of signal repeatability and an approximation of its frequency (i.e. number of pulsations over time). As a sensitivity analysis the signal frequency was additionally evaluated using Periodogram power spectral

density estimation employing the MATLAB function ‘periodogram’. Results from these calculations for all four GLCM statistical parameters energy, homogeneity, correlation and contrast were saved in a table format.

Signal processing methodology: At first two regions of interest are defined, one marking an area of pulsation and the other an area of exactly the same size and shape without pulsation. The mean value of the four GLCM stats is saved over time in a data matrix. Because of image noise the signal is often distorted by interference but can be improved by smoothing functions (described below at 7.3.1.2.1). At the beginning of each VM processed video there is a short time span of 1-2 seconds that is extremely noisy and therefore this is manually excluded from analysis. For normalisation purposes the smoothed signal is subtracted from its mean value before further processing (Figure 7.2).

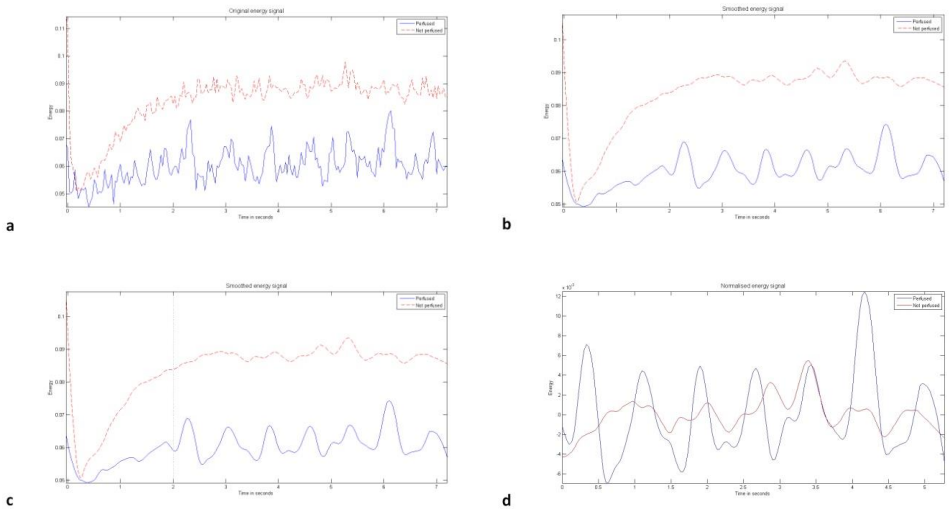

Figure 7.2 Processing steps of raw GLCM signal.

The raw signal (a) is smoothed using a loess filter (b). To avoid noise which frequently occurs at the start of the sequence, a starting point (dashed line in c) for data analysis is selected manually. Finally signals from both ROI’s are normalised by subtracting the mean over the whole sequence (d).

The signals from both ROI’s then undergo autocorrelation i.e. in simple terms the signal is phase shifted backwards and forwards over time to evaluate if there is some degree of matching between the signals curves (i.e. if the same pattern repeats itself in the signal). This phase shift is also called lag. For example every signal has maximal autocorrelation at zero lag. A completely homogeneously repetitive signal (e.g. sine curve) with a frequency of 1Hz would show a maximal correlation when phase shifted for a one second interval. The ‘coefficient’ option is chosen to normalise the signal meaning that at zero lag the autocorrelation is 1.0 (Figure 7.3). The resulting autocorrelation for each GLCM stat is then plotted and analysed using the ‘findpeak’ MATLAB function. This function essentially finds the position of a peak within a plot, peak being defined as a point on the x-axis where both

neighbouring points have lower values. The mean value of the distance between the peaks is then calculated. This reveals the average time passed between signals and hence the signal frequency.

Autocorrelation can be regarded as a measure for sameness and repeatability. For example a continuous sine wave signal at 1Hz does exhibit maximal autocorrelation values at 1s intervals corresponding with the signal interval.

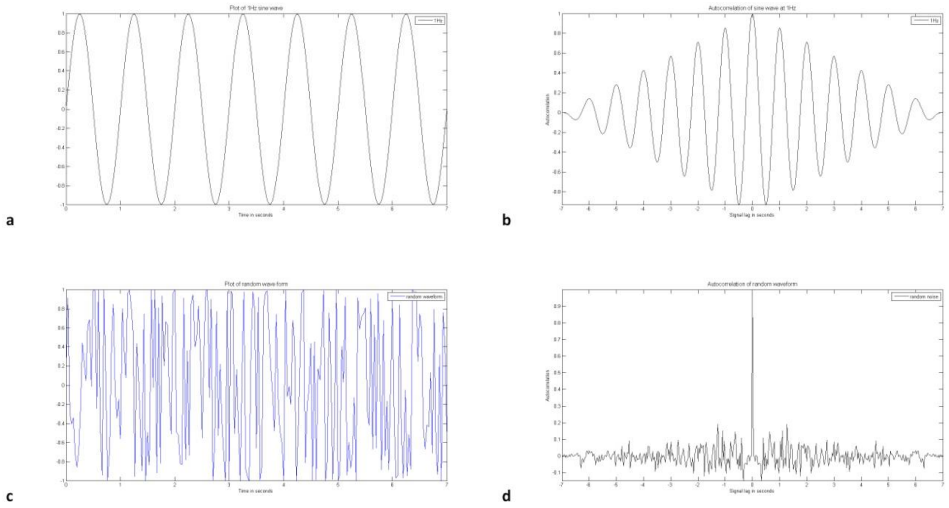

Figure 7.3 Example of autocorrelation analysis.

A sine wave of 1Hz (a) exhibits peaks of high autocorrelation values (b) at 1s intervals. A random waveform without regular components does not display any peak values other than at 0 lag when the signal is directly overlayed with a copy of itself.

Processing of autocorrelation gives us a measure of signal frequency and sameness. Another way of evaluating the signal characteristics is to compare it to a standardised signal with a known frequency. To achieve this, a sine-form signal was created with a frequency that corresponded to the pulse rate used in the perfusion phantom. This sine wave was used as the gold standard to which the signal from the VM sequence ROI was cross-correlated. The main difference between cross- and auto- correlation is that in the latter case the signal is compared to itself. The value of cross-correlation is again normalised with the coefficient option meaning that two identical signals would result in a value of 1.0 at a point other than zero lag.

As a sensitivity analysis, the signal was finally evaluated using the power spectral density estimation. This method uses a discrete fourier transform to represent the input signal as a frequency domain graph. The discrete fourier transform is useful because it reveals the periodicity of data as well as relative strengths of periodic components. The graphs x-axis represents the frequency spectrum (limited to 0-5Hz for relevance) and the y-axis indicating the power of the frequency. For example a sine wave signal of 1Hz would have a peak at

1Hz (Figure 7.4). Signals with multiple components do have several peaks, with the highest peak indicating the most dominant signal component (345).

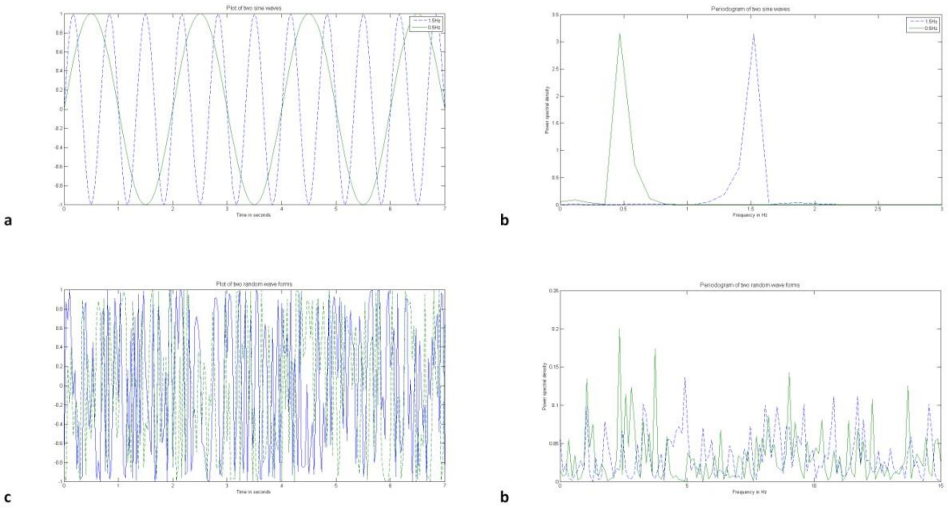

Figure 7.4 Example of periodogram analysis.

a) Two sine waves with distinct frequencies. b) Using periodogram analysis the two underlying frequencies can be identified at a point of maximal spectral density power. c) Two random waveforms. d) Periodogram analysis does not reveal a clear maximum of spectral density power because many frequencies are represented in the original waveforms.

As a measure of image quality the signal-to-noise ratio (SNR) for each VM sequence was processed (Equation 7.1). The SNR which frequently used in medical imaging is a value that describes the clarity of an image. A higher value results in more prominent and clear main signal (e.g. TV show). For example a standard definition video does have a lower SNR than a full high definition video.

$$SNR = \frac{P_S}{P_N}$$

Equation 7.1 SNR - signal to noise ratio; Ps – power signal; Pn – power noise

7.3. Results

7.3.1 Graylevel co-occurrence matrix statistics are representative of motion within a video area of interest

7.3.1.1 Workflow to determine the optimal parameters for VM signal evaluation

For every video there are a number of parameters for camera recording, VM- and GLCM processing. Taken together, all possible combination of parameters or settings result in an

unmanageable plethora of variations. Therefore it was initially important to elucidate the combination of parameters that would result in the optimal enhancement of pulsatile motion. To start with the optimal smoothing filter was tested. This was essential because without smoothing, signals were too noisy to be analysed with the methodology described above (7.2.1.5). Once the optimal filter was determined further tests focused on GLCM settings, VM processing parameters and camera recording settings in this order (Figure 7.5). It should be noted that the evaluation process was not conducted in a strictly linear fashion because occasionally new results led to a re-evaluation of earlier experiments. The video sequence used to test these settings was chosen because it subjectively showed a strong motion enhancement without suffering from excessive image noise (VM settings: magnification amplitude 100, spatial frequency 30, frequency bandwidth = 0.33 – 3.33Hz, chrominance = 0; GLCM settings: offset = [-1 1], symmetry = false, graylevel = 16, graylimit [] = no limit).

Figure 7.5 Stepwise approach to determining optimal VM processing parameters.

This flow diagram depicts the stepwise approach used to elucidate settings to enable the optimal enhancement of pulsatile motion in VM processed videos.

7.3.1.2 Testing settings for the processing of GLCM data

7.3.1.2.1. Data smoothing

First the issue of plot smoothing was addressed by testing different smoothing filter functions. Due to an abundance of image noise, non-smoothed GLCM data did not enable the extraction of any significant signals related to pulsation in the flow phantom (Figure 7.2). Smoothing filters create an approximating function from a given data set to enable the recognition of important patterns. During smoothing very high or low data points are approximated to neighbouring values to create a smoother curve that allows interpretation of slow change phenomena. The filters tested were the average-, loess-, robust- loess-, loew-, robust loew- and the Savitzky-Golay filter each at 4 different spans. A more detailed description of filtering can be found here (346). The filter span determines how many adjoining data points are used for filtering. Visual evaluation of the resulting plots was carried out to establish which filter function resulted in the best signal. While many filters resulted in a good representation of the expected pulse signal (e.g. 75 peaks per minute for a pump frequency of 75bpm), many did also show an extent of over-smoothing (flattening signal amplitude). Based on these tests and following visual assessment of the resulting plots, the loess filter with a span of 21 data points was selected (Figure 7.6).

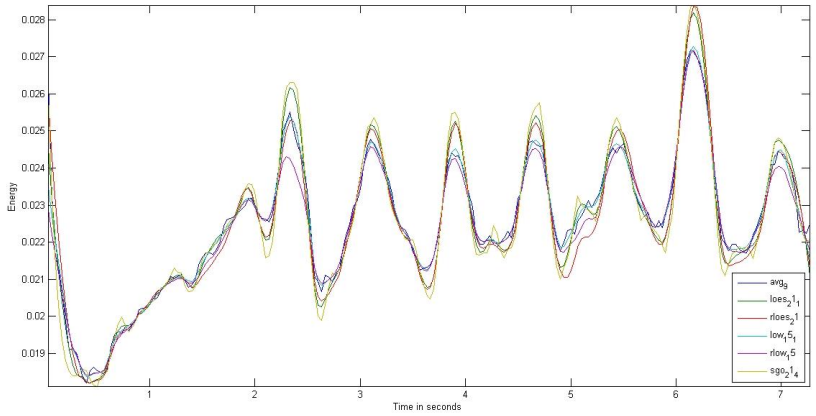

a

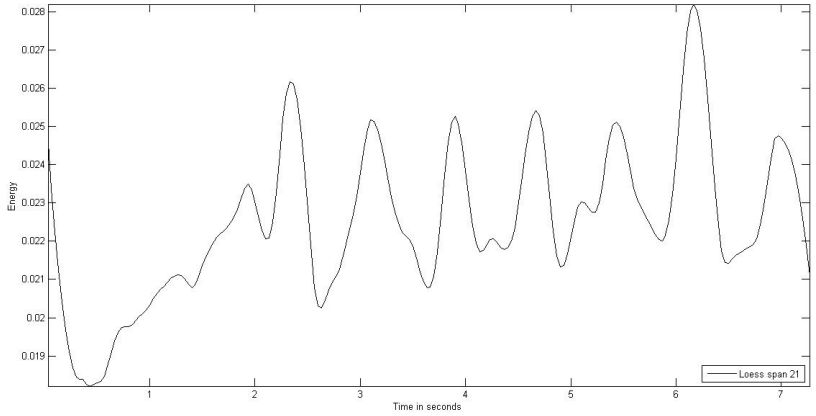

b

Figure 7.6 Comparison of smoothing filter functions.

a) Each smoothing filter was tested at different data point spans. This figure shows the best spans for each individual filter. b) From the selection in (a) the Loess filter at a span of 21 was selected because it displayed the best compromise between noise reduction and signal yield.

The next step involved a decision on the optimal GLCM settings. To this end a VM file was chosen as reference standard (Offset - [-1 0]; Numlevel - 32; Symmetry - off; Graylimit – no limitation) to which other processed files were compared. Each GLCM parameter was subsequently varied and tested against this reference file to compare resulting changes to signal strength. The settings with the strongest signal in all 4 GLCM statistical parameters were: Offset [0 1]; NumLevel 16 and Symmetry off. The offset [-1 1] was chosen over [0 1] because it resulted in an almost equally strong signal but had the theoretical advantage of assessing movement in two dimensions (up and down, left and right).

7.3.1.2.2. Selection of optimal GLCM stats processing

For the tested data set, the Loess filter method with a span of 21 data points showed a good balance between signal amplitude and noise suppression. For GLCM processing the settings chosen for all future experiments were: Numlevel =16; Offset = [-1 1] without any restrictions on Graylimit.

7.3.1.3 Video magnification settings

7.3.1.3.1. Amplitude and spatial frequency

A video file was recorded at a resolution of 800x600 in an analogy to the original work of Wu et al (136). This file was VM processed with a combination of different amplitude factors - alpha signified by “A” (25A, 50A, 100A and 200A) and spatial frequencies –lambda signified by “L” (20L, 30L, 40L, 60L, 80L and 100L). The resulting signal strengths were analysed and compared to elucidate the combination that resulted in the best signal. Additionally it was assessed how well the known pulse frequency of 75 could be identified with the ‘findpeak’ and ‘periodogram’ methods (henceforth called frequency discrimination). The combinations 40L & 50A; 30L & 100A; 60L & 100A and 80L& 100A produced the best signal. On visual assessment a pulsation in the perfused section of the phantom was clearly visible for all tested combinations. With the exception of videos processed at 20L who had a very poor SNR (i.e. high image noise), no obvious difference was found with regards to image noise between the other combinations as is evidenced by comparable SNR values (SNR 9.4 – 10.1).

7.3.1.3.2. Frequency range

The signal strength in terms of autocorrelation and gold standard signal cross-correlation was best for a range of 1Hz (1.83Hz- 0.83Hz) and 3Hz (3.3Hz – 0.3Hz). During this stage it was not clear which frequency range would result in optimal VM signals and hence it was decided to carry out flow phantom experiments using a 1Hz and 3Hz range.

7.3.1.3.3. Chrominance

Chrominance was evaluated at a setting of 0.25, 0.5, 0.75 and 1.0. The impact of chrominance on signal strength and SNR was minimal hence a setting of zero was chosen for future experiments.

7.3.1.3.4. Selection of optimal VM processing settings

Based on the experiments above, camera settings were evaluated with the following spatial frequency and amplification settings: 30L/100A, 40L/50A, 60L/100A and 80L/100A. Each of these settings was evaluated at 1Hz and 3Hz frequency range. Chrominance was kept at zero.

7.3.1.4 Camera settings

7.3.1.4.1. Resolution

The three magnification and spatial frequency combinations with the best signal strength (40L & 50A; 60L & 100A, 80L& 100A and 30L & 100A) were further evaluated at different video resolutions. The aim was to establish if there was a relationship between video resolution and VM signal characteristic. In their original work Wu et al. recommended use of non-HD video (around 800x600) for VM processing. Hypothetically however a higher resolution could result in a less noisy video and a better pick up rate for subtle signals. The resolutions tested in addition to the reference file were 640x480, 1024x786 and the maximal camera resolution of 2048x1536. Processing the video sequence at the highest resolution of 2048x1536 resulted in the best VM signal and frequency discrimination.

7.3.1.4.2. Colour codec

Video sequences recorded at maximal resolution and processed at 30L/100A were processed at two different colour codecs to evaluate any differences in the resulting VM signals. From the 5 available codecs three (Directional, Rigorous and Integrated Performance Primitives codec) were excluded because they required extensive processing speed that was beyond the processing power of the laptop used for these experiments. The two remaining codecs namely ‘Edge Sensing’ and ‘Multithread’ were evaluated. No difference was found in the signal strength, frequency discrimination or image noise between the two colour codecs. The ‘Multithread’ codec was chosen for future experiments because it performed more stable (i.e. less software crashes).

7.3.1.4.3. Frame rate

Video sequences were recorded at 90fps at a resolution of 800x600. Although a higher frequency is supported by the camera, the processing speed of the laptop used did not allow recording at speeds beyond 90fps. No improvement in the VM signal or frequency discrimination was found at the highest feasible frame rate of 90fps. The SNR (9.6) was the same at 30fps and 90fps.

7.3.1.4.4. Selection of optimal camera recording settings

With the exception of 640x480 it was possible to extract good VM signals and to discriminate pulsation frequencies from all tested resolutions. The best mixture of signal strength, frequency discrimination and image noise however was elucidated at the maximal resolution of 2048x1536. The impact of frame rate and colour codec choice on signal strength was minimal and hence the standard settings used at the outset were maintained in future experiments.

7.3.1.5 Preliminary pressure and frequency evaluation

Using the previously determined settings for camera recording, GLCM stats and VM processing two further sequences were recorded at a 100bpm and pressures of

250/30mmHg and 140/20mmHg respectively. Each sequence was processed at two different frequency ranges of 1.17Hz – 2.17Hz (1Hz range) and 0.67Hz – 3.67Hz (3Hz range). At 140/20mmHg only the 3Hz range produced a signal that was stronger over the perfused channel. Frequency recognition was not functional as the same frequency was attributed to the perfused and non-perfused catheters. The periodogram sensitivity analysis did however yield valid frequency results. At pressures of 250/30mmHg use of either frequency range did result in a strong signal and good frequency discrimination. At 1Hz range signal strength was better compared to the 3Hz range Table 7.1.

Pressure (mm/Hg)	Range (Hz)	Auto-correlation	Cross-correlation	Findpeak (Hz)	Periodo-gram (Hz)	mean SNR
130/70	1	0.39 vs. 0.06	0.35 vs. 0.15	1.33	1.29	9.1
	3	0.39 vs. 0.12	0.36 vs. 0.16	1.30	1.29	8.7
140/20	1	0.16 vs. 0.17	0.14 vs. 0.07	1.68	0.97	10.0
	3	0.2 vs. 0.1	0.19 vs. 0.03	1.64	1.64*	8.5
250/30	1	0.55 vs. 0.11	0.33 vs. 0.03	1.64	1.64	9.8
	3	0.44 vs. 0.09	0.28 vs. 0.06	1.63	1.64	8.4

Table 7.1 VM signal strength based on GLCM Energy stats.

The strongest signal based on autocorrelation is recorded at 250/30mmHg whereas the strongest cross-correlation signal is found at 130/70mmHg. Frequency discrimination is most accurate at 130/70mmHg. * - frequency discrimination same over perfused and non-perfused catheter.

7.3.2 Correlation of perfusion pressure and location with the VM signal

7.3.2.1 Experimental design and perfusion settings

A flow phantom containing three flow channels, respectively embedded just below the surface and at app. 2 cm and 4 cm depth was created using clear PVCP as described above (3.4.2). The construction required a plastic container of greater depth and width than the container used for the flow phantom that contained two catheters at equal depth. There were no other substantial differences between the perfusion phantoms.

Each catheter was perfused at three different pressures, namely 90/40mmHg, 120/80mmHg and 200/100mmHg at a stroke frequency of 75bpm (1.25Hz) and 100bpm (1.67Hz) while

video sequences were recorded. Solenoid pump power was adjusted to achieve the required perfusion pressures which were constantly measured throughout the experiment. Because the catheters were at different depths and hence were exposed to different external pressure from the PVCP material, the pump power varied according to the catheter position. This was also reflected by the variation in perfusion flow which was constantly measured using a flowmeter. Video recording for each pressure and frequency combination was recorded at least twice using the settings established in (7.3.1). Each video sequences was processed at two frequency ranges of 1Hz and 3 Hz respectively (i.e. at 100bpm:1.17Hz - 2.17Hx and 0.67Hz-3.67Hz; at 75bpm 0.83-1.83 and 0.33Hz – 3.33Hz). Subsequently signals were analysed as described above (3.4.4.3). Experiments were conducted on three separate days. As a control two sequences were recorded without any flow being present on each day.

7.3.2.2 VM signals do not reflect perfusion depth in the clear perfusion phantom

On subjective evaluation, catheter motion was not clearly visible in any of the tested perfusion pressure and frequency settings. In some sequences it appeared that the whole phantom as opposed to individual catheters was in pulsatile motion. All comparison and statistical tests were carried out separately for sequences processed at 1Hz and 3Hz frequency range. In the main data was of a non-parametric distribution type. Median values at different pressures and depths are shown in Table 7.2 and Table 7.3.

Paired Wilcoxon signed rank test was performed for all 4 GLCM values. No statistical significant difference ($p>0.05$) between values obtained during pulsatile perfusion (PP group) and without perfusion (NP group).

Pressure	Position	Energy	Correlation	Contrast	Homog.
90/40 (n=6)	bottom PP	0.129 (0.051)	0.145 (0.167)	0.109 (0.070)	0.108 (0.076)
	bottom NP	0.106 (0.052)	0.083 (0.114)	0.100 (0.084)	0.100 (0.062)
	middle PP	0.141 (0.113)	0.122 (0.092)	0.207 (0.108)	0.206 (0.105)
	middle NP	0.146 (0.071)	0.179 (0.129)	0.145 (0.159)	0.195 (0.185)
	top PP	0.127 (0.104)	0.167 (0.090)	0.116 (0.053)	0.116 (0.058)
	top NP	0.141 (0.146)	0.189 (0.064)	0.190 (0.132)	0.219 (0.138)
120/80 (n=4)	bottom PP	0.162 (0.174)	0.105 (0.076)	0.120 (0.101)	0.122 (0.083)
	bottom NP	0.160 (0.168)	0.090 (0.062)	0.108 (0.097)	0.108 (0.097)
	middle PP	0.086 (0.143)	0.121 (0.194)	0.068 (0.201)	0.073 (0.178)
	middle NP	0.152 (0.072)	0.123 (0.187)	0.199 (0.206)	0.197 (0.211)
	top PP	0.197 (0.048)	0.154 (0.090)	0.137 (0.142)	0.136 (0.142)
	top NP	0.095 (0.086)	0.101 (0.080)	0.188 (0.710)	0.185 (0.259)
200/100 (n=6)	bottom PP	0.129 (0.062)	0.130 (0.097)	0.122 (0.071)	0.129 (0.047)
	bottom NP	0.138 (0.050)	0.155 (0.097)	0.131 (0.124)	0.146 (0.124)
	middle PP	0.109 (0.080)	0.176 (0.114)	0.135 (0.139)	0.141 (0.150)
	middle NP	0.141 (0.086)	0.149 (0.133)	0.168 (0.068)	0.163 (0.066)
	top PP	0.138 (0.088)	0.166 (0.017)	0.097 (0.038)	0.094 (0.040)
	top NP	0.110 (0.012)	0.112 (0.091)	0.136 (0.062)	0.136 (0.076)

Table 7.2 Median values and (IQR) of GLCM autocorrelation stats at 1Hz

Pressure	Position	Energy	Correlation	Contrast	Homog.
90/40 (n=6)	bottom PP	0.095 (0.067)	0.083 (0.085)	0.1 (0.157)	0.107 (0.181)
	bottom NP	0.134 (0.165)	0.124 (0.181)	0.139 (0.103)	0.143 (0.135)
	middle PP	0.122 (0.154)	0.148 (0.222)	0.185 (0.142)	0.169 (0.123)
	middle NP	0.155 (0.146)	0.164 (0.395)	0.159 (0.226)	0.207 (0.3)
	top PP	0.149 (0.093)	0.188 (0.105)	0.132 (0.089)	0.119 (0.079)
	top NP	0.121 (0.078)	0.168 (0.2)	0.106 (0.015)	0.111 (0.025)
120/80 (n=4)	bottom PP	0.126 (0.1)	0.152 (0.118)	0.092 (0.078)	0.095 (0.08)
	bottom NP	0.119 (0.033)	0.107 (0.054)	0.07 (0.032)	0.071 (0.05)
	middle PP	0.13 (0.12)	0.216 (0.278)	0.165 (0.104)	0.149 (0.1)
	middle NP	0.132 (0.085)	0.186 (0.678)	0.131 (0.226)	0.13 (0.21)
	top PP	0.204 (0.17)	0.183 (0.666)	0.207 (0.246)	0.206 (0.247)
	top NP	0.094 (0.069)	0.319 (0.794)	0.246 (0.736)	0.24 (0.746)
200/100 (n=6)	bottom PP	0.113 (0.066)	0.093 (0.11)	0.117 (0.044)	0.113 (0.052)
	bottom NP	0.102 (0.053)	0.207 (0.178)	0.097 (0.077)	0.121 (0.084)
	middle PP	0.116 (0.21)	0.162 (0.014)	0.123 (0.066)	0.125 (0.083)
	middle NP	0.117 (0.143)	0.191 (0.111)	0.12 (0.092)	0.131 (0.071)
	top PP	0.164 (0.124)	0.146 (0.159)	0.161 (0.135)	0.172 (0.125)
	top NP	0.083 (0.064)	0.175 (0.198)	0.104 (0.072)	0.113 (0.07)

Table 7.3 Median values and (IQR) of GLCM autocorrelation stats at 3Hz

Looking exclusively at absolute GLCM values obtained during perfusion (PP group), there was no obvious relation to perfusion -pressure or -depth. To get a better understanding of relative changes in GLCM values they were standardised with the aid of the control signal from the NP group. Mean values obtained from the ROI's overlying the perfused and non-perfused catheter were expressed as percentage change using the formula below (Equation 7.2**Error! Reference source not found.**). Simplified this means that the ROI (either PP or NP) with the stronger signal has a value of >100%.

$$G = 100 \times (\frac{(x_P - x_N)}{|x_N|})$$

Equation 7.2 Calculation of fractional change in GLCM values expressed as percentage.

For the calculation of the non-perfused Gain, xP and xN are reversed. G – Gain; xP – perfused GLCM value; xN – non-perfused GLCM value.

The gain values (Figure 7.7) were subsequently compared across individual depths and perfusion pressures (e.g. 90/40mmHg vs. 120/80mmHg vs. 200/100mmHg at middle depth or bottom vs. middle vs. top catheter at 90/40mmHg) using the Kruskal-Wallis test. At 1Hz range there were two statistical significant differences found. First there was a difference in median Energy gain when comparing individual depths (-15.7% -bottom vs. -45.1% - middle vs. 127.4% - top; $p < 0.05$). For the catheter closest to the surface (top) differences in Energy gain (0.1% – 90/40mm/Hg vs. 127.4% - 120/80mmHg vs. 16.5% - 200/100mm/Hg; $p<0.05$) and Correlation gain (-27.7% - 90/40mmHg vs. 75.9% - 120/80mmHg vs. 41.7% - 200/100mm/Hg; $p<0.02$) were found. No statistically significant differences were elucidated at 3Hz range.

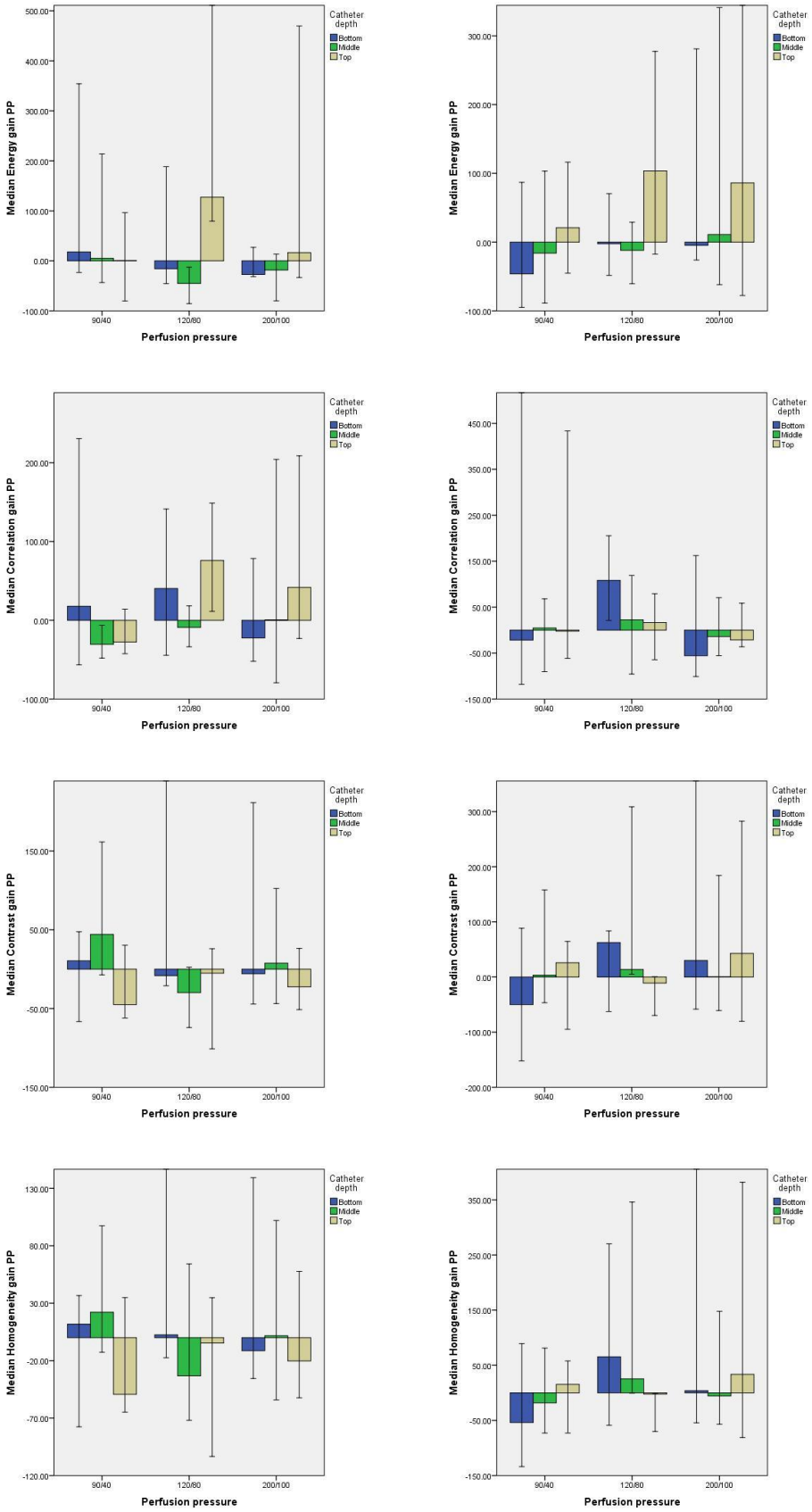

Figure 7.7 Median GLCM stat gains at 1Hz (left) and 3Hz (right).

Error bars indicate 95% CI. Y-axis dimension has been limited to improve visibility of bar the graphs.

To assess if Gain is an independent predictor of flow in an examined ROI, a binominal regression analysis was carried with presence of flow as the dependent and Gain, perfusion pressure, depth and perfusion rate as covariates. To improve the fit o the model any variable except Gain could be removed. None of the covariates was found to be an independent predictor for this model ($p>0.05$). To assess if despite these negative findings GLCM gain could be used as a test for predicting VM enhanced motion a ROC analysis was carried out for the original GLCM values and the processed gain values. None of the GLCM stats or their respective gains had an AUROC of>0.65 and statistical significance was not reached for any of them ($p>0.05$).

7.3.2.2.1. Utilisation of cross-correlation and sinus wave controls to assess presence of flow

In the paragraph above, GLCM auto-correlation values and their respective gain values were analysed. The same analysis approach was then applied to cross-correlation values which were obtained by comparing GLCM signal changes to a sinus wave which functioned as a gold-standard signal (i.e. perfect pulsatile signal). The median cross-correlation values are shown in Table 7.4 and Table 7.5.

Pressure	Position	Energy	Correlation	Contrast	Homog.
90/40 (n=6)	bottom PP	0.104 (0.049)	0.107 (0.055)	0.101 (0.053)	0.096 (0.05)
	bottom NP	0.081 (0.053)	0.094 (0.074)	0.097 (0.062)	0.097 (0.059)
	middle PP	0.135 (0.15)	0.103 (0.067)	0.101 (0.06)	0.098 (0.058)
	middle NP	0.085 (0.05)	0.105 (0.042)	0.104 (0.055)	0.095 (0.043)
	top PP	0.083 (0.131)	0.107 (0.088)	0.084 (0.087)	0.086 (0.083)
	top NP	0.097 (0.128)	0.077 (0.089)	0.096 (0.104)	0.095 (0.09)
120/80 (n=4)	bottom PP	0.146 (0.082)	0.102 (0.056)	0.111 (0.039)	0.109 (0.04)
	bottom NP	0.123 (0.088)	0.081 (0.092)	0.118 (0.065)	0.108 (0.059)
	middle PP	0.086 (0.059)	0.065 (0.04)	0.089 (0.039)	0.081 (0.046)
	middle NP	0.121 (0.072)	0.07 (0.041)	0.061 (0.091)	0.062 (0.07)
	top PP	0.111 (0.063)	0.104 (0.062)	0.125 (0.072)	0.12 (0.062)
	top NP	0.115 (0.04)	0.083 (0.071)	0.096 (0.042)	0.094 (0.041)
200/100 (n=6)	bottom PP	0.101 (0.077)	0.081 (0.043)	0.108 (0.061)	0.115 (0.054)
	bottom NP	0.124 (0.09)	0.079 (0.021)	0.104 (0.052)	0.108 (0.053)
	middle PP	0.08 (0.134)	0.079 (0.041)	0.097 (0.045)	0.09 (0.053)
	middle NP	0.102 (0.078)	0.067 (0.075)	0.082 (0.076)	0.074 (0.073)
	top PP	0.105 (0.175)	0.087 (0.077)	0.135 (0.063)	0.118 (0.066)
	top NP	0.111 (0.042)	0.072 (0.037)	0.087 (0.052)	0.08 (0.045)

Table 7.4 Median values and (IQR) of GLCM cross-correlation stats at 1Hz

Pressure	Position	Energy	Correlation	Contrast	Homog.
90/40 (n=6)	bottom PP	0.094 (0.039)	0.062 (0.058)	0.076 (0.044)	0.071 (0.034)
	bottom NP	0.071 (0.021)	0.098 (0.066)	0.081 (0.039)	0.077 (0.034)
	middle PP	0.086 (0.051)	0.077 (0.053)	0.081 (0.081)	0.076 (0.068)
	middle NP	0.084 (0.085)	0.09 (0.04)	0.088 (0.034)	0.083 (0.029)
	top PP	0.088 (0.06)	0.105 (0.087)	0.09 (0.087)	0.091 (0.082)
	top NP	0.163 (0.07)	0.072 (0.085)	0.111 (0.113)	0.114 (0.113)
120/80 (n=4)	bottom PP	0.119 (0.069)	0.091 (0.033)	0.107 (0.058)	0.108 (0.056)
	bottom NP	0.113 (0.09)	0.099 (0.062)	0.088 (0.079)	0.093 (0.079)
	middle PP	0.107 (0.105)	0.065 (0.042)	0.085 (0.043)	0.081 (0.035)
	middle NP	0.079 (0.092)	0.048 (0.068)	0.047 (0.086)	0.047 (0.074)
	top PP	0.105 (0.112)	0.086 (0.033)	0.079 (0.1)	0.076 (0.1)
	top NP	0.099 (0.077)	0.077 (0.053)	0.095 (0.044)	0.09 (0.049)
200/100 (n=6)	bottom PP	0.114 (0.06)	0.077 (0.051)	0.09 (0.044)	0.084 (0.049)
	bottom NP	0.09 (0.047)	0.075 (0.046)	0.096 (0.056)	0.093 (0.045)
	middle PP	0.073 (0.038)	0.066 (0.033)	0.067 (0.025)	0.072 (0.028)
	middle NP	0.095 (0.091)	0.064 (0.034)	0.09 (0.04)	0.084 (0.055)
	top PP	0.1 (0.064)	0.085 (0.084)	0.089 (0.047)	0.073 (0.04)
	top NP	0.089 (0.045)	0.062 (0.03)	0.061 (0.03)	0.063 (0.025)

Table 7.5 Median values and (IQR) of GLCM cross-correlation stats at 3Hz

Paired testing of the PP vs. NP group (Figure 7.8) values did not show any statistically significant difference. Testing across different catheter depths revealed a statistically significant difference for Correlation gain at 90/40mmHg perfusion pressure (6.95% - bottom vs. -4.30% - middle vs. 5.03% - top; $p<0.03$). No such difference was found when comparing different perfusion pressures. Regression analysis results indicated that at 1Hz Correlation gain ($p<0.07$; CI 1.01-1.03), Contrast gain ($p<0.04$; CI 1.00-1.02) and Homogeneity gain ($p<0.05$; CI 1.00-1.02) were all independent predictors for the presence of flow. At 3Hz range only Correlation gain ($p<0.07$; CI 1.00-1.02) was found to be an independent predictor. ROC analysis yielded statistically significant results for Correlation gain with an Area under the Curve (AUC) of 61% ($p<0.05$) at 1Hz and an AUC of 64% ($p<0.02$) at 3Hz. Sensitivity and specificity were 57% and 55% at 1Hz and 68% and 52% at 3Hz.

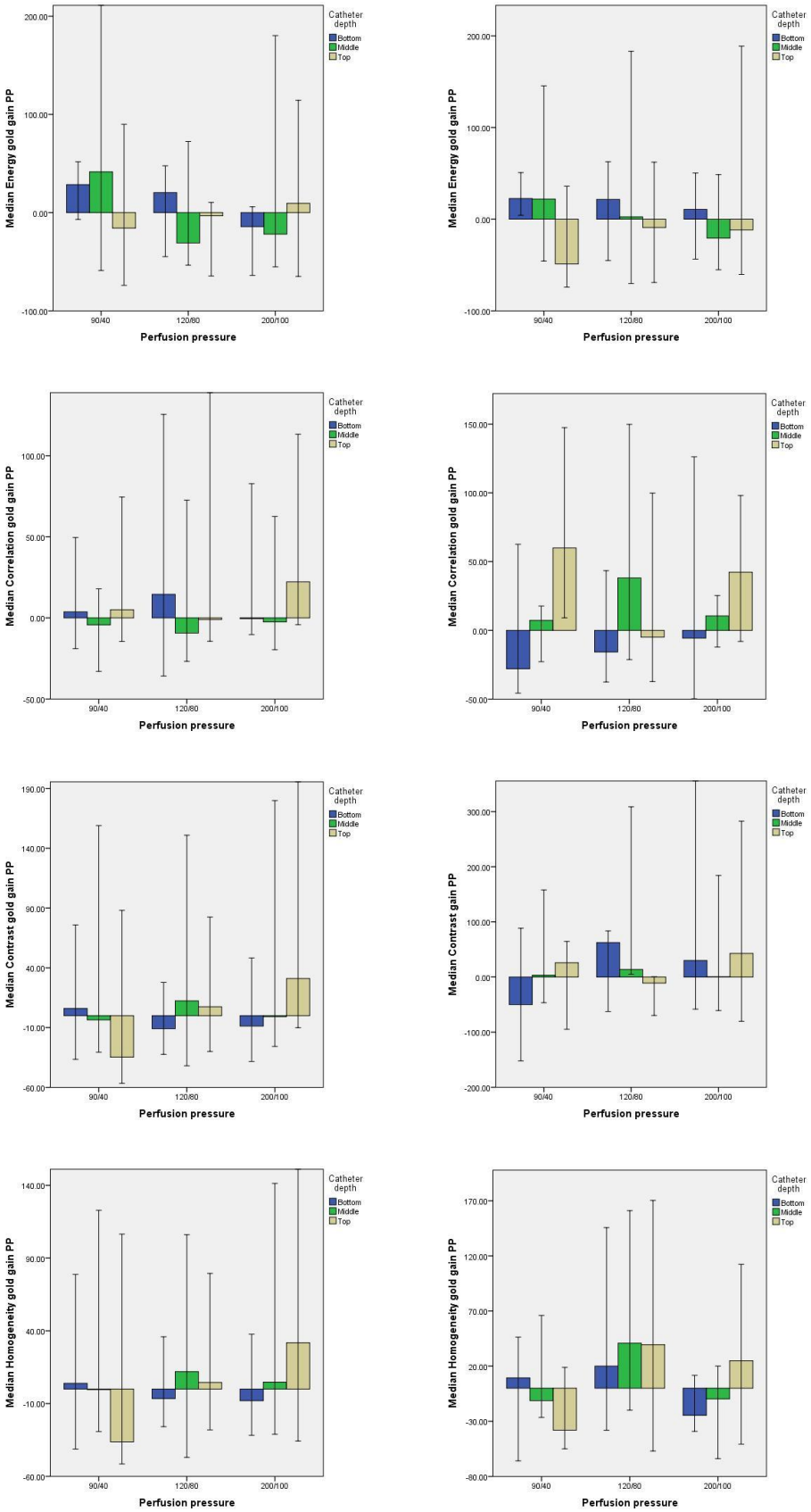

Figure 7.8 Median GLCM cross-correlation stat gains at 1Hz (left) and 3Hz (right).

Error bars indicate 95% CI. Y-axis dimension has been limited to improve visibility of bar the graphs.

The recorded GLCM signals were examined using the findpeak function (Table 7.6) and periodogram function (Table 7.7) as described above (7.3.1.3.1). Frequency discrimination was deemed to be successful if the estimated frequency was within a ±20% range of the actual perfusion rate. At 75bpm (=1.25Hz) the frequency range where a result was counted as positive was at 1-1.5Hz whereas at 100bpm (=1.67Hz) the range was 1.3-2Hz. Positive frequency discrimination also occurred in the NP group in some cases even if this was not the case in the PP group. Frequency discrimination with the findpeak method was best for Energy at 1Hz but even here only 50% of cases had the correct frequency. The majority of these cases did also exhibit positive frequency discrimination at the corresponding NP signal. Frequency discrimination using the periodogram method was overall poor with only a few positive measurements. Anecdotally a peak was often observed at the correct frequency but this was only rarely the maximal peak and hence could not be counted. During initial experiments (7.3.1.3) one or two dominant peaks was found in most cases whereas the periodograms for the experiments in this section exhibited several peaks which indicates that many different frequencies were present at once.

Frequency range	Group	Energy	Correlation	Contrast	Homogeneity
1Hz n=56	PP	28	12	23	21
	NP	28	14	20	20
3Hz n=56	PP	24	11	13	14
	NP	23	5	16	17

Table 7.6 Frequency discrimination using the findpeak method.

Frequency range	Group	Energy	Correlation	Contrast	Homogeneity
1Hz n=56	PP	5	0	1	1
	NP	7	0	3	3
3Hz n=56	PP	0	0	0	0
	NP	0	0	0	0

Table 7.7 Frequency discrimination using the periodogram method.

7.3.3 Enhancing motion of concealed structures

7.3.3.1 Experimental design and perfusion settings

Using brown dye a fully opaque perfusion phantom containing two catheters both at approximately 0.5cm depth was created. With the exception of PVCP colour the phantom construction was the same as the 2-catheter phantom used in 7.3.1.3. The same perfusion pressures and pulsatile frequencies were used as for the 3-catheter phantom. For each setting at least two recordings were acquired. As control two sequences were recorded without any flow being present (Table 7.8 & Table 7.9).

Pressure	Perfusion	Energy	Correlation	Contrast	Homog.
90/40 (n=11)	PP	0.156 (0.103)	0.189 (0.383)	0.127 (0.072)	0.129 (0.076)
	NP	0.142 (0.076)	0.181 (0.102)	0.133 (0.078)	0.125 (0.058)
120/80 (n=10)	PP	0.163 (0.142)	0.133 (0.077)	0.178 (0.105)	0.172 (0.108)
	NP	0.114 (0.113)	0.183 (0.143)	0.151 (0.066)	0.144 (0.069)
200/100 (n=13)	PP	0.123 (0.076)	0.138 (0.154)	0.149 (0.209)	0.151 (0.211)
	NP	0.118 (0.058)	0.137 (0.099)	0.11 (0.107)	0.14 (0.13)
Max. pres (n=9)	PP	0.159 (0.156)	0.22 (0.22)	0.173 (0.18)	0.166 (0.165)
	NP	0.114 (0.075)	0.15 (0.131)	0.144 (0.157)	0.145 (0.16)

Table 7.8 Median values and (IQR) of GLCM stats at 1Hz

Pressure	Perfusion	Energy	Correlation	Contrast	Homog.
90/40 (n=11)	PP	0.191 (0.134)	0.196 (0.196)	0.083 (0.058)	0.143 (0.166)
	NP	0.097 (0.074)	0.183 (0.248)	0.068 (0.146)	0.12 (0.141)
120/80 (n=10)	PP	0.094 (0.123)	0.138 (0.118)	0.07 (0.123)	0.107 (0.043)
	NP	0.109 (0.062)	0.159 (0.133)	0.072 (0.082)	0.113 (0.105)
200/100 (n=13)	PP	0.116 (0.114)	0.126 (0.256)	0.081 (0.204)	0.182 (0.208)
	NP	0.092 (0.09)	0.098 (0.084)	0.081 (0.116)	0.106 (0.196)
Max. pres (n=9)	PP	0.072 (0.074)	0.18 (0.266)	0.071 (0.067)	0.09 (0.128)
	NP	0.067 (0.032)	0.153 (0.125)	0.07 (0.052)	0.104 (0.094)

Table 7.9 Median values and (IQR) of GLCM stats at 3Hz

7.3.3.2 Pulsatile motion of concealed structures in a perfusion phantom is enhanced by VM processing

Original GLCM values were compared between the PP and NP group using the paired Wilcoxon sign test. At 1Hz range a statistical significant difference was found for Contrast ($p < 0.02$) and Homogeneity ($p<0.01$), whereas differences between groups at3Hz range were found to be non significant. Gain values for different perfusion pressures are shown in Figure 7.9. On statistical analysis of GLCM gain differences between perfusion pressures, a statistical significant difference was found for Correlation at 3Hz range ($p=0.05$).

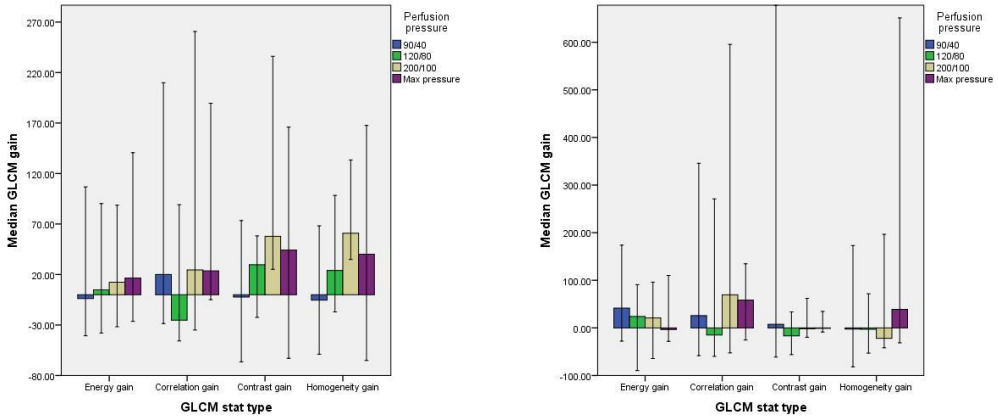

Figure 7.9 Median GLCM stat gains at 1Hz (left) and 3Hz (right).

Error bars indicate 95% CI. Y-axis dimension has been limited to improve visibility of the bar graphs.

Binominal regression analysis was carried out for each raw and gain GLCM value to assess if they were independent predictors for the presence of flow in the phantom. Contrast ($p=0.055$,OR CI 0.91-14461.49), Contrast gain ($p=0.077$, OR CI 1.00-1.01) and Homogeneity gain ($p=0.074$, OR CI 0.79 - 14388.69) came close to reaching statistical significance. Reviewing the graphical representation of this data revealed a very wide 95% confidence interval for values recorded at 90/40mmHg pressure. Exclusion of these values did have a substantial impact on the results of the binominal regression analysis with Contrast ($p<0.05$, CI 1.32- 83470.08), Contrast gain ($p<0.02$, OR CI 1.00-1.02) and Homogeneity gain ($p<0.04$, CI 1.00-1.01) becoming statistically significant independent predictors for the presence of flow.

To evaluate if GLCM stats could be useful in determining the presence of flow in VM processed videos, a ROC analysis was carried out for raw GLCM and gain GLCM values, individually at 1Hz and 3Hz range respectively A number of these showed statistically significant results with an AUC of <0.65. The best ROC performance however was identified for Contrast gain (AUC = 0.70, $p<0.005$, CI 0.58-0.81) and Energy gain (AUC = 0.71,

p<0.005, CI 0.59-0.82) at 1Hz. Sensitivity and specificity were 74% and 65% for Contrast gain and 81% and 60% for energy gain, respectively (Figure 7.10).

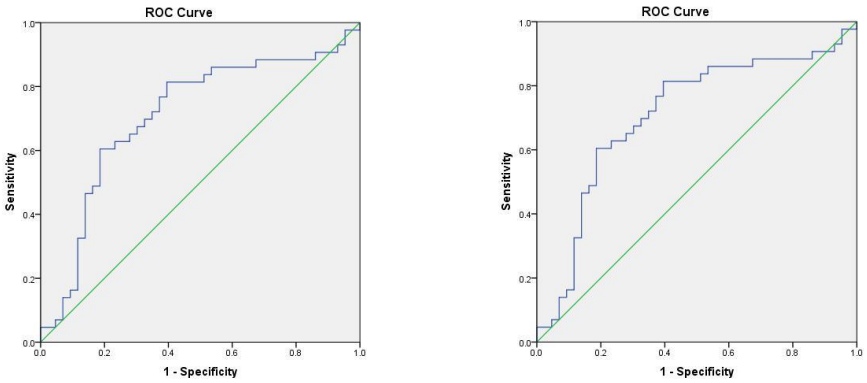

Figure 7.10 ROC curve for Energy gain (left) and Contrast gain (right) both at a range of 1Hz.

7.3.3.2.1. Utilisation of cross-correlation and sinus wave controls to assess presence of flow in concealed structures

Auto-correlation values for VM sequences recorded on the brown flow phantom are shown in Table 7.10 and Table 7.11. Paired Wilcoxon-matched pair-signed rank testing did not reveal any statistical significant differences between GLCM cross-correlation values in the PP and NP group. GLCM gain values (Figure 7.11) were tested across different perfusion pressures using the Kruskal-Wallis test which showed a statistical significant difference between pressures Figure 7.11) at 1Hz for Correlation gain (p<0.03) and at 3Hz for Contrast gain (p<0.05) and Homogeneity gain (p<0.003).

Pressure	Perfusion	Energy	Correlation	Contrast	Homog.
90/40 (n=11)	PP	0.118 (0.062)	0.067 (0.124)	0.117 (0.08)	0.113 (0.081)
	NP	0.063 (0.097)	0.064 (0.07)	0.107 (0.041)	0.1 (0.031)
120/80 (n=10)	PP	0.109 (0.073)	0.087 (0.034)	0.125 (0.072)	0.119 (0.083)
	NP	0.07 (0.083)	0.075 (0.05)	0.108 (0.066)	0.109 (0.066)
200/100 (n=13)	PP	0.085 (0.06)	0.075 (0.069)	0.091 (0.104)	0.078 (0.106)
	NP	0.088 (0.052)	0.077 (0.094)	0.08 (0.084)	0.061 (0.087)
Max. pres (n=9)	PP	0.147 (0.168)	0.108 (0.283)	0.244 (0.283)	0.242 (0.239)
	NP	0.137 (0.073)	0.114 (0.07)	0.133 (0.128)	0.126 (0.135)

Table 7.10 Median cross-correlation values and (IQR) of GLCM stats at 1Hz

Pressure	Perfusion	Energy	Correlation	Contrast	Homog.
90/40 (n=11)	PP	0.065 (0.07)	0.06 (0.096)	0.079 (0.015)	0.068 (0.044)
	NP	0.076 (0.065)	0.063 (0.038)	0.074 (0.021)	0.07 (0.042)
120/80 (n=10)	PP	0.086 (0.062)	0.088 (0.062)	0.091 (0.036)	0.082 (0.038)
	NP	0.084 (0.063)	0.087 (0.069)	0.099 (0.028)	0.087 (0.042)
200/100 (n=13)	PP	0.071 (0.058)	0.069 (0.07)	0.075 (0.021)	0.052 (0.036)
	NP	0.078 (0.064)	0.074 (0.068)	0.076 (0.025)	0.071 (0.047)
Max. pres (n=9)	PP	0.102 (0.101)	0.124 (0.312)	0.087 (0.105)	0.096 (0.212)
	NP	0.093 (0.025)	0.111 (0.074)	0.085 (0.048)	0.08 (0.04)

Table 7.11 Median cross-correlation values and (IQR) of GLCM stats at 3Hz

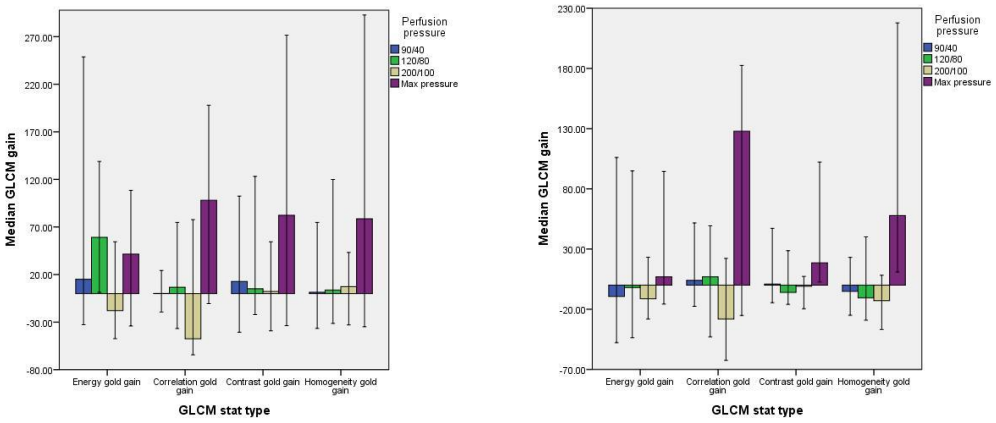

Figure 7.11 Median GLCM stat cross-correlation gains at 1Hz (left) and 3Hz (right). Error bars indicate 95% CI.

Binominal regression analysis found that Contrast ($p<0.02$, CI 6.3- 88157175.9) and Homogeneity ($p<0.03$, CI 4.5 - 52670673.02) as well as Energy gain ($p<0.02$, CI 1.00-1.02), Contrast gain ($p<0.02$, 1.00-1.02) and Homogeneity gain ($p<0.02$, CI 1.00-1.02) were all statistically significant independent predictors for the presence of flow at 1Hz range, in the brown flow phantom. At 3Hz only Correlation gain ($p<0.05$, CI 1.00-1.02) was found to be a statistically significant independent predictor. ROC analysis found that Energy gain (AUC=66%, $p<0.02$), Contrast gain (AUC=65%, $p<0.02$) and Homogeneity gain (AUC=65%, $p<0.02$) –values crossed the threshold of statistical significance for the prediction of flow presence.

Frequency discrimination utilising the findpeak method was best for Homogeneity at 1Hz with 21/43 positive results (Table 7.12). Again virtually the same numbers of positive results were obtained for the PP and NP group (21 vs. 19). When using periodogram based frequency discrimination, optimal results were obtained for Energy at 1Hz (22/43). In contrast to previous results there were virtually no positive results found for the NP group at this setting Table 7.13).

Taken together with the results from the clear phantom it is suggestive that Energy at 1Hz range may be the GLCM statistic best suited to determine the frequency of a signal in a VM processed video.

Frequency range	Group	Energy	Correlation	Contrast	Homogeneity
1Hz n=43	PP	18	13	21	21
	NP	14	8	18	19
3Hz n=43	PP	13	13	10	10
	NP	10	10	12	10

Table 7.12 Frequency discrimination using the findpeak method.

Frequency range	Group	Energy	Correlation	Contrast	Homogeneity
1Hz n=43	PP	22	5	6	6
	NP	2	2	6	4
3Hz n=43	PP	10	5	1	3
	NP	0	2	1	2

Table 7.13 Frequency discrimination using the periodogram method.

7.3.4 Assessment of VM motion signals in an *in-vivo* setting

7.3.4.1 Setup for signal recording

The premise of the following experiments was to transfer the GLCM stats based motion signal methodology to an *in-vivo* model of laparoscopic surgery. To this end the porcine model of laparoscopic surgery that has already been described in the General methods section (3.4.3) was used. Image sequences of abdominal organs with and without the presence of pulsatile blood flow were recorded with a laparoscopic camera. While the animal was alive (PP group) videos were recorded with the hand held laparoscope in a stationary position. To reduce respiratory motion, ventilation was stopped during sequence recording. Each organ/area was recorded with the laparoscope very close to its surface and then again with the laparoscopic tip further away so that adjacent areas or organs could be viewed as well.

Following euthanasia, another video which served as the control (NP group) was recorded from the same organ area, again from up close and at a greater distance. The absence of blood flow was confirmed by monitoring the ECG trace and performing ultrasound duplex imaging of the organ area in question.

Original videos were stereoscopic (i.e. 3D video) and required transformation into monocular sequences before VM processing could be carried out. Results from the flow phantom indicated a frequency range of 1Hz appeared to be superior to a 3Hz range in terms of retrieval of GLCM motion signals. Also it was felt that a wider range may lead to inclusion of non-pulsatile repetitive signals such as respiratory motion. Therefore VM processing was

only carried out with a 1Hz range. Because the pulse rate of the animal fluctuated wildly between 70-120bpm, an average pulse rate of 100bpm (1.32 Hz) was utilised as the gold standard and control. All other VM processing settings including magnification factor, chrominance and spatial frequency were used at identical settings to the flow phantom experiments above (7.3.1.3).

To compare GLCM signals between the PP and NP group, ROI's of equal dimensions and shape were marked on the pre- and post mortem recorded video sequences. IN contrast to the flow phantom experiments however the ROI position had to be altered because it was not possible to record each organ area from exactly the same camera position and distance. The GLCM signals retrieved from these ROI's were subsequently processed and analysed in exactly the same manner as described above.

7.3.4.2 Respiratory motion impairs the interpretation of VM signals during laparoscopy

Video sequences were recorded from the liver, small bowel, colon and stomach. Subjectively there was strong respiratory motion visible in the VM processed videos that were obtained pre euthanasia. Although mechanical ventilation was held during recording, the animals started to breathe spontaneously hence causing a motion signal. Comparison of GLCM signals in the PP and NP group only rarely showed stronger autocorrelation or cross-correlation in the PP group. When a positive gain (i.e. stronger signal pre-mortem) was present, this was usually at a frequency that correlated with respiratory motion (around 0.3Hz). As evidenced by duplex scanning, flow was absent in the NP group. Despite the lack of perfusion, low amplitude GLCM signals were present (Figure 7.12, Figure 7.13). Frequency discrimination was not successful for any of the examined organs. Due to the lack of viable VM signals and the comparably small number of VM processed videos, no attempt at statistical analysis was made.

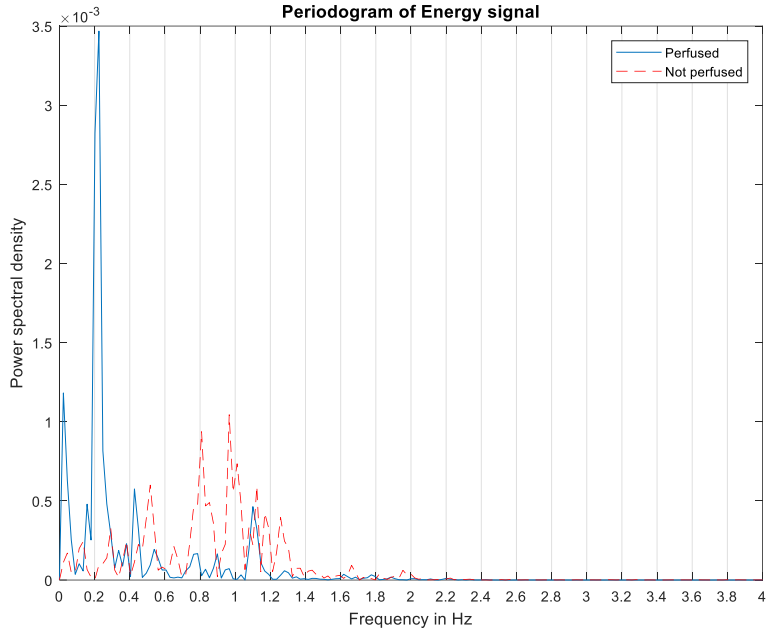

Figure 7.12 Periodogram of VM signals recorded over porcine liver (blue pre-mortem; red post-mortem).

The dominant frequency is around 0.2Hz which falls within the respiratory rate observed during surgery of app. 10-18 breaths per minute.

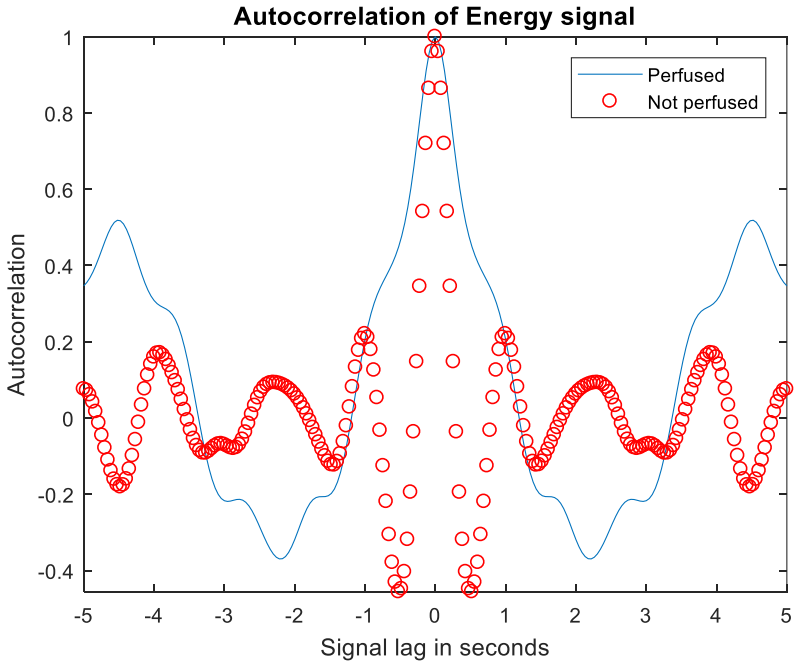

Figure 7.13 Autocorrelation of the same VM signal as in Fig. 7.12.

The VM signal recorded pre-mortem exhibits a maximal autocorrelation at app. 4.5s lag which corresponds well with the periodogram analysis in Fig. 7.12.

7.4. Discussion

In this chapter it was shown that the utilisation of texture analysis, specifically the time based plotting of the Gray-level co-occurrence matrix (GLCM) allows an objective assessment of VM signals and can provide metrics for subsequent statistical analysis. The repeatability of these methods has been verified as it has produced constant results in 12 different video sequences, using a variety of image resolutions and colour codecs and having been recorded over the space of a day. Based on these metrics a number of VM processing settings and camera recording options were established based on their utility for recording sequences in the environment used for subsequent flow phantom experiments. It was also established that higher image resolution enhances the quality of the VM signal to a certain extent. GLCM analysis has previously been used to assess the flow of crowds on CCTV cameras (261,344) but this approach has not been used previously to assess VM signals. It is purported that it is advantageous to use texture based motion analysis over more conventional approached such as the Lucas-Kanade method for the estimation of optical flow (347) because it does not rely on specific markers or objects to motion. It is very difficult to use foreign objects in a surgical site for the sole purpose of research. Although this has been successfully employed in open surgery by some groups for the purpose of intraoperative image guidance (348), it is exponentially more complicated to replicate this method in laparoscopic surgery as objects would have to be placed and retrieved via narrow laparoscopic ports. To circumvent this limitation one group has utilised tattooing of the liver to facilitate landmark recognition during surgery organs to create a tractable objects (349). This latter approach, has the disadvantage of requiring the use of additional procedures and substances and hence there are some additional ethical and workflow considerations that have to be taken into account.

A number of flow phantoms were produced to facilitate testing of VM signals in a controlled environment. These phantoms were integrated into a solenoid pump powered person circuit. The circuit‘s settings were adjustable via a number of adapters and connectors which made it possible to fine tune a variety of pressure and perfusion rate combinations. The perfusion circuit’s pressure and flow rate was closely monitored and hence the creation of a consistent experimental environment was made possible. These circuit design was previously proven to provide a close approximation of the systolic and diastolic phase found in human blood circulation (258).

The hypothesis that the strength of the VM signal can allow conclusions about the strength or location of the underlying motion process could not be verified. The flow phantom has been recorded under a multitude of perfusion settings including different perfusion –pressures, rates and –depths. Although a statistical significant difference of GLCM stats was found between different pressures and perfusion depths in some experiments, these differences were not expressed in any coherent pattern. For example, frequently the highest perfusion pressure exhibited lower GLCM stat values than lower pressures and perfusion at

the shallowest depth did not usually produce stronger VM signals as would have been expected.

Although no direct correlation between VM signal and signal source strength was found, statistical test indicated that the difference between perfused and non-perfused regions as expressed as percentage gain could be useful in determining the presence or absence of motion. Using cross-correlation and comparison to a gold-standard sine wave signal, binominal logistic regression analysis revealed that increased gain for Correlation, Contrast and Homogeneity was an independent predictor for the presence of flow. The ROC analysis using gain values resulted in AUC levels that indicated a poor accuracy (<0.7) for the prediction of flow. The same analysis using auto-correlation based analysis did not yield any significant results.

In parallel to the clear phantom experiments, no correlation between perfusion pressure and VM signal strength was found in the brown flow phantom where flow tubes were concealed. Binominal regression analysis however indicated that gain for Contrast and Homogeneity was an independent predictor of flow presence using the auto-correlation. In contrast to results from the clear phantom the raw Contrast values also reached statistical significance. ROC analysis showed that Energy gain and Contrast gain exhibited a fair accuracy (both > 0.7) for the prediction of flow presence.

Cross-correlation based evaluation indicated that Contrast, Homogeneity, Energy gain, Contrast gain and Homogeneity gain were all independent predictors for the presence of flow. Perhaps somewhat surprisingly, ROC analysis using these GLCM stats did not result in an accuracy > 0.65. Because no correlation between perfusion depth and VM signal strength was found in the clear phantom, no attempt was made to replicate this experiment with concealed perfusion catheters in the brown phantom.

Frequency discrimination using either the findpeak- or the periodogram method was poor for either phantom type. This is a striking difference to initial experiments conducted to evaluate optimal settings. Based on the experiments on both phantoms, it is purported that a frequency range of approximately 1Hz centred around the expected frequency of a physiological signal is better suited for VM analysis than a frequency range of 3Hz.

It was not possible to demonstrate an implementation of statistical VM signal analysis in the *in-vivo* model. The overpowering motion signal during all sequences was at around 0.2-0.4Hz and hence most likely originated from diaphragmatic motion. It is also possible that a tremor originating from the surgeon's hand holding the laparoscope added further motion noise (350) to some extent. Attempts were made to minimise respiratory motion by executing a "breath hold" (i.e. stopping mechanical ventilation. This was however futile because the animal would start to breath spontaneously almost immediately. In a surgical

setting this would probably not be a problem because patients receive muscle relaxants. The use of muscle relaxants was not included in the ethical approval for these experiments.

It is clear that respiratory motion from the diaphragm and perhaps to some extent cardiac motion will pose one of the biggest limitations to implementing VM processing in laparoscopic surgery. Interestingly this was not an issue that was highlighted by other groups who published their experience on VM in laparoscopic surgery. One group developed and utilised a new algorithm in robotic nephrectomy to detect vessels that were obscured by retroperitoneal fat (351). Although the kidney is also in close proximity to the diaphragm, it is less affected by respiratory motion because it lies in the retroperitoneal space and as such is in a more fixed position than the liver (352). The same can be said for the prostate. A different group used a similar approach in robotic prostatectomy (245) and again no issues with respiratory motion were reported.

Further limitations in the experiments described here is that it was not possible to control the presence of shadows in the recorded video sequences because the configuration of the laboratory and the use of regular ceiling lighting made this difficult. Attempts were made to minimise these effects by positioning light blocking screens at certain positions in the lab. Regarding the construction of the flow phantom it may be that the consistency of the flow catheter wall which was stiffer than that of a human blood vessel had some impact on the flow characteristics. The use of wall-less flow phantoms which avoid this limitation has been reported previously (353). It could however be argued that human blood vessels do have a wall that regularly is of a different consistency to surrounding tissues. Subjectively it was striking that the VM motion signals were very strong during the initial experiments that were conducted to establish optimal settings. Out of 12 sequences only one sequence which was recorded at a low resolution (640x480) did not show a clear and unequivocally perceptible motion signal. This was however not true for videos recorded for experiments on the clear (three catheters) and the brown phantom during subsequent experiments. Although the same setup was used, motion signals were only visible in a minority of video sequences. In some sequences the entire background was moving which perhaps indicates that the kinetic energy from the perfusion circuit was transferred onto the plastic case that envelops the flow phantom. This may also explain why rate discrimination was often equally positive for the ROI in the PP and the NP group. The difficulties encountered in the visual interpretation of VM signals does highlight the importance of having a reproducible quantification method. Instead of relying on observer interpretation for example it would potentially be feasible to extract statistical values from ROI's in VM processed video sequences and then base the discrimination of motion signals on this data. If shown to be feasible in future experiments, this approach may improve the interpretation of VM videos that have been recorded under less than ideal conditions. If taken further this approach may allow to leave the analysis of VM signals entirely to a computer algorithm based on GLCM stats. It would then be possible to extract the location of VM signals on the screen and overlay it on the regular video feed.

The advantage would be that the surgeon would still benefit from the motion enhancing abilities of VM but would no longer be distracted by the often rather noisy original VM video.

In summary it was shown that quantification of VM signals using a texture based approach is feasible. Pulsatile flow in concealed structures was shown to be independently predicted by analysing GLCM based stats. It could not be established if VM signal strength correlates with the strength of the underlying signal. It is hypothesised that this may have been due to poor recording quality of the video sequences examined. Analysis of perfusion based VM signals in an *in-vivo* setting was prevented by strong respiratory motion. Future efforts in VM for laparoscopic use should focus on enabling perfusion signal extraction in the presence of added motion noise (e.g. respiratory, cardiac, hand tremor). Another important factor is processing speed which will need to be improved significantly to allow analysis of high definition video feeds (136).

8. Image guided surgery

8.1. Introduction

Laparoscopic liver resection (LLR) has been shown to benefit patients by improving short term outcomes such as pain control, length of hospital stay and rate of complications while offering comparable oncological long term outcomes to open liver resection (74,98,102,122). Most HPB units are carrying out some liver resections laparoscopically. However major procedures are being carried out routinely in only a small number of centres because of the technical challenges of major laparoscopic liver resection. A very small number of centres have championed increasingly complex and technically challenging laparoscopic techniques such as the Glissonian-, trans-diaphragmatic- and single port approaches to LLR (354–356).

Concomitant with these novel surgical techniques, the potential indications for LLR have been expanded from minor segmental-, sectional and non-anatomical liver resections to major hepatectomies, superior-posterior segmentectomies and donor hepatectomies (73,74,357). Although uptake has been generally slow (122,123), the laparoscopic approach for liver resection is becoming increasingly popular with a recent world wide review reporting on over 9000 cases that have been published in the literature so far (102). A 2014 consensus conference found that minor LLR (≤2 liver segments) have now progressed to stage 3 of the Balliol IDEAL framework and can therefore be regarded as standard practice (74). In contrast to this, the technically more challenging complex and major LLR are mainly carried out in highly specialised centres with doubts remaining about external reproducibility (123). A major contributor to the technical complexity of LLR is the intraoperative loss of anatomical orientation which is caused by the lack of depth perception, tactile feedback and a reduced field of view, factors which are further exacerbated by the liver's intricate vascular anatomy (127,141). These issues have led to concerns about the technical difficulty, haemorrhage control and oncological radicality of LLR. Many authors perceive these concerns as one of the major obstacles to the wide spread dissemination of LLR (94,102,122–124,358).

Although routine use of laparoscopic ultrasound during laparoscopic liver surgery is recommended (74), its utility is limited by its two-dimensionality and because some lesions may be difficult to identify as they have a tissue density similar to liver. The latter is especially true for, lesions in steatotic livers, livers with chemotherapy associated changes, cirrhotic livers and with small or vanishing (shrinking tumour size following neoadjuvant chemotherapy) lesions (141,142,218). Further issues are related to the practicalities of using laparoscopic ultrasound during surgery because it is difficult to use once parenchymal transection has started (141,143,144) and visualisation of ultrasound images on a separate screen is not intuitive (210).

The development and implementation of novel technologies in laparoscopic liver surgery has been driven by an effort to lessen its complexity, to make it simpler and quicker to perform, and to increase safety through identification of key structures during resection. It may also improve the learning curve for surgeons training in advanced laparoscopic liver surgery. Some examples for technologies that have been proposed as surgical aids in LLR are: near-infrared laparoscopy, parenchymal transection with energy devices or the use of preoperative surgical simulation (74,133).

Intraoperative image guidance facilitated by the use of an image guidance system (IGS) is a technology that is widely used in neuro- and spinal surgery and more recently has created considerable interest for laparoscopic applications (128,129,141,210). In essence an IGS allows the surgeon to view structures that can be seen on preoperative scans but that are not visible with a laparoscopic camera (128). This is highly desirable for LLR as it enables to surgeon to localise crucial sub-surface structures such as tumours or blood vessels in real-time. Two IGS licensed for open hepatic resection have been shown to facilitate anatomical orientation and the detection of vulnerable structures (66,359). Their integration into the surgical workflow involves several steps. Liver structures are visualised with the aid of a 3D liver model which is constructed from a preoperative CT or MRI scan. During surgery the position of the *in-vivo* liver is recorded with a probe and these location coordinates are subsequently used to align the 3D model with the intraoperative site. This process, called “registration” is the technically most complex step in an image guidance procedure. The positional relationship of the probe, liver, patient and surgical instruments is continuously determined with the aid of optical tracking markers which are attached to the instruments and probe.

These licensed devices have also been adapted and applied to laparoscopic and robotic liver resection (141,143) with one study demonstrating comparable image guidance accuracy in laparoscopic and open surgery (141). Both IGS do however have significant limitations that have prevented their widespread uptake by the surgical community. Firstly, the visual interpretation of image guidance data is rendered somewhat counter-intuitive due to the utilisation of a parallel screen configuration where the 3D model is shown on a screen next to a regular laparoscopic screen. This approach is cumbersome because it requires additional mental integration by the surgeon to analyse the provided image guidance information analogous to the simultaneous viewing of laparoscopic video and laparoscopic ultrasound images. Another design issue of these systems that has a negative impact on workflow and registration error is the probe based registration method which due to its user dependency, is a potential source of errors and time delay.

8.1.1 Aims

The specific aims in this chapter were:

1) To assess the feasibility of using the proposed IGS during laparoscopy
2) To determine the systems performance with regards to accuracy and usability
3) To evaluate manual and automatic registration methods for aligning 3D liver model and patient *in-situ* anatomy

The initial IGS development carried out on a porcine model is described before the clinical study to better illustrate the concept of the systems concept.

8.2. Results

8.2.1 Preclinical evaluation

Automatic registration and real time AR visualisation during surgery was attempted in 5 animals. Due to issues with excessive organ deformation following the ablation procedure, registration was possible in 3/5 of cases. The ablation caused adhesions between thin porcine liver lobes and the diaphragm which resulted in overt kinking of the liver lobe and a grossly deformed surface area of the whole liver. The extent of the deformation was so great that the similarity between intraoperative liver and 3D liver model shape was insufficient to perform a successful registration. In the remaining animals an automatic registration was carried out and its accuracy calculated as described above (3.5.3.5). The resulting accuracy is compared to 2 best case scenarios. The first called best single deformation uses a one-off deformation (i.e. as opposed to continuous) to adjust the preoperative 3D liver models shape so that it closer matches that of the intraoperative liver. This registration mode relies on data from the intraoperative CT scans that were taken during the first surgical procedure. The best rigid registration registers the liver based on the postoperative accuracy analysis. Corresponding landmarks on 3D model and intraoperative liver are registered to each other to achieve an alignment with minimal residual distances between corresponding landmarks. Both registration modes are based on data that is not usually available during routinely performed laparoscopic procedures. The final registration method which is intended to form the principle registration mode for SmartLiver is based on stereoscopic surface reconstruction (SSR) and an ICP matching process as described above (3.5.3.1.3). As opposed to single deformation and best rigid registration it is functional without requiring additional pre- or post-operative data. Due to these restrictions, the single deformation and best static registrations were carried out postoperatively only. Real-time registration during attempted laparoscopic liver resection was only carried out using the SSR based registration method. All three methods yielded TRE's <10mm RMS. The resulting accuracies from carrying out the three different registration methods (172) are shown in the table below (Table 8.1).

Animal ID	Single deformation	Best rigid	SSR	No. of frames	No. of landmarks
1	5.1 (20.7)	7.3 (20.2)	8.6 (18.2)	476	4
2	6.1 (26.0)	8.2 (33.4)	10.7 (25.6)	234	6
3	6.5 (46.7)	6.9 (48.7)	9.0 (43.3)	483	6

Table 8.1 The TRE in mm RMS (max) for three different registration methods and each study animal.

The number of frames and landmarks used for accuracy calculation is also given.

8.2.1.1 Patient characteristics and registration outcome

In total 12 patients were recruited for the study, of which 5 were scheduled for LLR and 7 for staging laparoscopy (SL). The gender ratio was 7 women to 5 men and the mean age was 59 years at time of surgery (range 38-77). Three of the 12 patients had to be excluded prior to data processing, two due to a fault with the laparoscopic camera and one patient due to a technical failure to establish a pneumoperitoneum secondary to extensive previous surgery. In the remaining 9 patients data acquisition was successful however in one patient a registration was not possible due to a calibration error. Hence, a successful registration could be carried out in 8 cases. No critical intraoperative incidents occurred in the study population. All patients undergoing staging laparoscopy were discharged on the same day with the exception of one patient who stayed overnight due to urinary retention. Patient characteristics for LLR patients are summarised in Table 8.2.Total operative time for LLR patients was 210-360 minutes. All patients had clear resection margins (R0) on histopathological evaluation. Two patients had to be converted to open surgery, one for failure to establish pneumoperitoneum secondary to extensive adhesions (LR03) and the other patient required a more extensive hepatic resection than pre-operatively anticipated (LR04) and therefore was converted for safety reasons. There was only one postoperative complication (Clavien-Dindo grade 4) in a patient who required re-intubation on postoperative day 2 for type 1 respiratory failure and hospital acquired pneumonia. Median length of hospital stay was 7 days (range 3-14).

Patient ID	Indication	Op time	Blood loss	Conversion	Liver segment affected	Lesion size (in mm)	LOS
LR01	Adenoma	210	y	n	5&6	60mm	6
LR02	CRLM	240	n	n	5&6	25mm	3
LR03	CCA	275	y	y	2&3	35mm	7
LR04	CRLM	360	y	y	3&4	84mm	8
LR05	HCC	240	y	n	4 a&b	60mm	14

Table 8.2 Characteristics of laparoscopic liver resections.

CCA – cholangio carcinoma; CRLM – colorectal cancer liver metastasis; HCC – hepatocellular carcinoma; LOS – length of hospital stay

8.2.1.2 Assessment of intraoperative workflow and usability feedback

Preoperative setup took 20-35 minutes and because it was carried out before or during anaesthetic induction it did not impact on the operating time. In contrast to this the intraoperative setup added approximately 10-20 minutes to the operating time. Setup time did not include the time needed for manual or automatic registration, which was carried out postoperatively in all but one case. Following the introduction of the “crosshair calibration” method (267) it was found that intraoperative setup time decreased by approximately 5 minutes.

Feedback forms were completed fully for 8 cases. The surgeon survey was largely positive about handling of the altered laparoscope, visual profile and the positioning of the SmartLiver equipment stack. Negative feedback largely centred on the difficulty of the intraoperative setup (collar installation, calibration) and the associated delay it caused in the surgical workflow (Table 8.3). Comments for improvement suggested a more convenient way of fixing the tracking collar and a desire for a smaller footprint of the SmartLiver stack.

Question	Mean	Median
Did the system impair handling of the laparoscopic camera? 1 (no impairment) – 5 (substantial impairment)	2.4	2
Did the system impair handling of the laparoscopic instruments? 1 (no impairment) – 5 (substantial impairment)	1.6	1
How easy was the system to setup? 1 (very easy) – 5 (very difficult)	3.2	3
Did you feel that the equipment setup caused delay in completing the surgical procedure? 1 (no delay) – 5 (substantial delay)	3	3
Did the system setup impair your line of view of the	1.2	1

patient? 1 (no impairment) – 5 (substantial impairment)		
Did the system setup impair your line of view of the laparoscopic monitor? 1 (no impairment) - 5 (substantial impairment)	1.2	1
Were you overall satisfied with the positioning of the system within the theatre environment? 1 (very satisfied) – 5 (very unsatisfied)	1.7	2

Table 8.3 Summary of surgeon feedback (n=8) on a Likert scale of 1-5.

8.2.1.3 Manual vs. automatic registration

Manual registration was successfully performed in two patients intraoperatively (Figure 8.1) and in 7 patients postoperatively. Initially it proved to be impossible to carry out an automatic registration for any of the cases. This was surprising as pre-clinical studies from our group on a porcine liver resection model had indicated that automatic registration should be possible in at least a third to a half of the cases. An error analysis revealed that the acquisition of surface points worked well but the computer algorithm was unable to discriminate between surface points from the liver and other surrounding structures (e.g. stomach, diaphragm). This issue rendered it impossible to match the corresponding point clouds to each other, resulting in a failure of the automatic registration. To confirm our hypothesis, the video data of one patient was visually analysed and the liver surface was manually marked out in several hundred video frames. In essence, this pre-processing of video data enabled the computer algorithm to now discriminate between liver and non-liver surfaces. Subsequently automatic registration was successfully carried out on this data set.

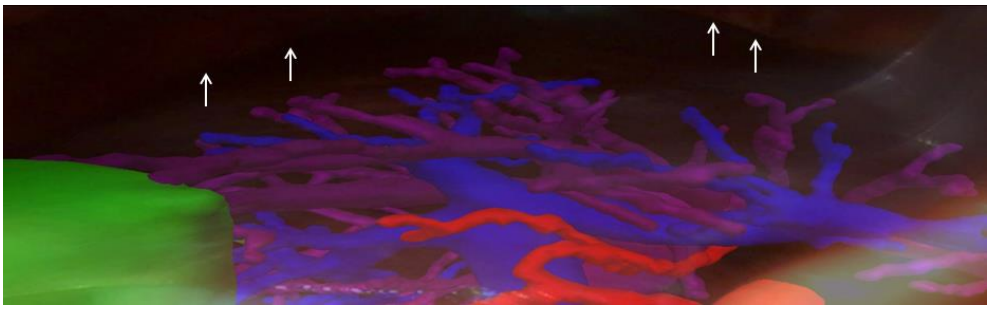

Figure 8.1 Real time AR display of a patient with hepatic adenoma in segment 5/6.

The liver surface is not displayed to allow a clear view of the vasculature. AR visualised structures: green – adenoma; blue – portal veins; cyan – hepatic veins; red – hepatic artery; arrows liver edge.

8.2.1.4 Anatomical accuracy

The target registration error (TRE) as a measure of anatomical accuracy was calculated as described above (Table 8.4). Usually several video sequences were recorded for each patient. Separate registrations for anatomical left lobe (i.e. segment 2&3), anatomical right lobe and the area between lobes were carried out and analysed individually. The number of video frames and landmarks used for TRE evaluation are also given in the table. The best possible TRE's were <10 mm RMS in one patient, ≈10mm RMS in two patients, ≈ 15mm RMS in three patients and 20-25mm RMS in two patients. A TRE >30mm occurred in 3 patients and 5 separately recorded sequences and was considered as a failure of registration because on visual inspection the resulting AR images looked anatomically grossly inaccurate. There was no statistically significant correlation found between organ deformation and TRE (Pearson correlation coefficient = 0.3; $p>0.05$). In fact soft tissue deformation of the liver was in the main consistent around ≈10mm RMS in patients with low and high TRE's which may indicate that this factor has a constant impact on accuracy. In contrast to this, liver motion was greatly variable between patients and a statistically significant correlation with the TRE was found in this study population (Pearson correlation coefficient = 0.53; $p<0.05$). (Table 8.5).

Patient ID	Liver lobe	No of frames	No. landmarks	Best TRE (RMS mm -range)
LR01	RL	75	13	17.7 (0.3-47.8)
	LL	22	4	15.4
LR02	RL	n.a.	n.a.	n.a.
	LL	146	7	22.7 (0.4-44.6)
LR05 manual	RL	n.a.	n.a.	n.a.
	LL	34	6	9.4 (0.6-44.7)
LR05 - automatic	RL	n.a.	n.a.	n.a.
	LL	39	6	8.5 (0.3-17)
LS03	RL	64	6	24.6 (0.3-87.5)
	LL	n.a.	n.a.	n.a.
LS04	RL*	42	7	5.9 (0.2-12.2)
	LL	102	8	5.9 (0.1-26.6)
LR04	RL	35	4	14.5 (0.2-28.6)
	LL	68	4	83.7 (3.6 142.7) -fail
LS06	RL*	23	11	18.9 (0.1-27.5)
	LL*	162	12	16.1 (0.2-59.1)

LS07	RL	28	4	10.0 (0.6-19.2)
	LL	4	8	10.7 (1.1-24.9)

Table 8.4 Listed is the best possible TRE for each liver lobe and all sequences combined.

***RL and LL combined in sequence. In LR02, LR05 and LR04 only one liver lobe was available for analysis.**

Patient ID	Liver lobe	Deformation in mm RMS	Motion in mm ± SD (IQR)
LR01	RL	7.5	22.9±18.6 (0.9-34.7)
	LL	5.1	8.5±3.8 (5.8-11.8)
LR02	RL	8.7	15.3±4.9 (1.3-46.5)
	LL	8.8	23.5±19.3 (9.1-80.7)
LR05 manual	RL	na	na
	LL	11.3	18.5±27.6 (3.6-43.3)
LR05 auto	RL	na	na
	LL	9.3	18.6±19.8 (5.7-55.7)
LS03	RL	9.8	14.2±22.3 (2.4-34.4)
	LL	21	25.8±27 (18-55.2)
LS04	RL	10.7	15.6±18.5 (3.8 66.6)
	LL	36.2	17.8±38.7 (12-63.6)
LR04	RL	7.9	28.7 18.9 (12.5 39.0)
	LL	19.8	32.6 50.7 (1.1 95.2)
LS06	RL	13.6	13.7 18.7 (1.5 - 46.7)
	LL	15.1	12.5 21.7 (3.2 - 58.7)
LS07	RL	12.1	18.9 41.4 (0.7 48.8)
	LL	5.7	16.2 23.3 (1.2 41.6)

Table 8.5 Shown are measures of soft tissue deformation and liver motion.

8.3. Discussion

This study has demonstrated that SmartLiver is capable of providing augmented reality based intraoperative image guidance for use in laparoscopic liver surgery. Applied for the first time in patients, a computer vision technique called stereoscopic surface reconstruction was used to automatically register a 3D model which had been created pre-operatively to an individual patient's anatomy. All components required to perform image guidance were used intraoperatively without any incidents or safety concerns and the perioperative patient outcomes for patients undergoing LLR were similar to previous reports on minor LLR (102,360,361).

Image guidance systems (IGS) have been used in neurological surgery for decades before this concept was transferred to intraabdominal surgery (226). In open liver resection and ablation, IGS have demonstrated their ability to improve intraoperative orientation and precisely indicate the location of blood vessels and tumours (66,218,359). There is ongoing interest in exploiting the benefits of IGS for laparoscopic procedures other than liver resection. In a recent example a group has presented its experience with using a side-by-side display IGS with manual alignment in 23 patients undergoing laparoscopic gastrectomy (131). With a mean TRE of 14mm the system was found to be a useful tool for identifying the correct blood vessels prior to division.

As with open liver resections, the precise knowledge of tumour location and its relationship to major vascular structures is crucial to prevent incomplete resection and uncontrolled haemorrhage in LLR. Because it is technically more challenging than open surgery, the benefit gained from use of IGS in LLR is hypothetically greater than for open liver resections. Previously a group reported on the advantage of producing an individualised "stand alone" 3D liver model without image guidance components, for improving anatomical orientation during LLR. The authors stated that a non-registered 3D model displayed alongside the laparoscopic screen was found to improve the safety and accuracy of hepatic resection in the cases studied (362).

An accurate spatial correlation between the 3D model and patient anatomy is likely to yield greater benefits, but to maximise the potential of IGS in LLR it is important to make it easy to use and to enable a smooth integration into the operative workflow. The main benefit of an AR display is to facilitate the intuitive use of image guidance information by obviating the need for mental image integration that is required when using two separate screens and therefore reducing the potential for associated errors (210). Employing user independent automatic registration to align the 3D model will likely confer further benefits in terms of eliminating operator bias while at the same time being more user friendly.

An alternative approach to image guided surgery is the use of intraoperative cone beam CT to identify anatomical landmarks on the liver and subsequently register them with a preoperative 3D model. Compared to manual alignment of 3D models, this method has the

advantage of smaller registration errors but this comes at the cost of exposing the patient to ionising radiation, workflow interruptions to facilitate repeat CT acquisition and the lack of real time spatial correlation between surgical instrument and anatomical site (229). Another limitation of this approach is that it can only be performed in specially designed operating theatres with an integrated cone beam CT system, a requirement which confers significant cost implications.

Instead of recovering camera movement from optical tracking the “Simultaneous Localisation and Mapping” method (SLAM) utilises vision to estimate the trajectory and speed of camera motion (363). In a recent publication the feasibility of using SLAM to determine the laparoscope position during experimental liver surgery was demonstrated (129). The advantage of this method is that there is no requirement for a direct line of sight between optical tracking camera and laparoscope. Indeed no additional tracking equipment is needed. At the current development stage however SLAM based tracking in liver surgery is associated with higher tracking inaccuracies when compared with optical tracking (129).

Laparoscopic ultrasound (LUS) is currently the gold standard for anatomical orientation during LLR. Its limitations derive from the fact that it is a two dimensional imaging modality and as such it contributes little to the understanding of complex 3D liver anatomy (142). In addition, laparoscopic ultrasound is impractical to use while simultaneously carrying out transection of hepatic parenchyma. In large animal studies, our group has previously demonstrated the feasibility of visually combining laparoscopic US images with a 3D liver model (236). This approach enables surgeons to record US images at the start of surgery and subsequently recall and display them within seconds in the anatomically correct position on the 3D model, without having to redeploy the laparoscopic US probe(236).

Utilising SSR registration in porcine laparoscopy, the TRE’s where in the range of 9-10mm RMS. Analysis of the TRE’s resulting from single deformation- and best rigid- registration methods, revealed some important information about factors that contribute towards the accuracy of AR guided surgery. In single deformation registration the 3D model is deformed to create an optimal match with the intraoperative liver shape, hence the majority of the TRE will be caused by dynamic organ motion (e.g. ventilation and heart beat). In best rigid registration additional error is introduced by subjective picking of anatomical landmarks and the rigidity of the 3D model. For both cases a triangulation error caused by use of a stereo-laparoscope is also present. The triangulation error may lead to imprecision when picking anatomical landmarks on the video-laparoscopic stream Based on an analysis of these factors it is estimated that the optimal TRE for a rigid 3D model is ≈ 8mm RMS, for single deformation ≈ 5mm RMS and for dynamic real time deformation ≈ 3mm RMS. An improvement of accuracy beyond this limit would require better tracking technology and can therefore not be addressed by optimising registration (172).

With the exception of one outlier that was considered as a failed registration, the TRE in the patients studied varied in the range of 5.9-24.6 mm RMS. To the best of our knowledge, this is the first report on registration errors in an IGS that offers real-time AR visualisation. Anatomical accuracy in parallel screen based systems has been evaluated before in open hepatic surgery but these TRE values are not directly comparable to an AR environment because there is no real gold standard that can be used as reference. The accuracy evaluation method used in this study is based on anatomical landmarks located on the visible surface of the liver that are directly compared to their counterparts on the 3D model. On a parallel screen display the 3D model and intraoperative site are not integrated on the same screen and therefore the error calculation is based on landmark features that are located with a tracked stylus. Because the liver anatomy outside these landmark features is not perceivable, the resulting registration errors are perhaps more representative of local liver deformation as opposed to a global evaluation of anatomical accuracy.

Our group has previously studied a number of factors that affect alignment errors in SmartLiver. The 3D tracking system has an innate albeit small error in determining the position of tracking markers. This error is magnified by the long distance between the collar, which is the reference point for tracking, and the laparoscope tip, which is the point of interest. For better understanding this phenomenon could perhaps be described as an “optical tracking lever effect”. If a manual alignment is performed, this may become erroneous by the user failing to sufficiently match visible landmarks on the in-situ liver and 3D model. Automatic registration on the other hand can occasionally confuse different regions on the liver surface with each other because they consist of structurally similar point cloud configurations. This is a particular weakness of using stereoscopic surface reconstruction on smooth and relatively featureless surfaces such as the liver. As was demonstrated in this study, SSR of the human liver may be feasible if areas of an image which represent the liver surface are pre-selected. Although promising, this process is very time intensive and it is therefore not suited for real time intraoperative image guidance. With recent advances in machine learning however it may be possible to teach SmartLiver to independently discriminate between the liver surface and adjacent structures. Using Caffe, a deep learning framework (364), our group has recently reported promising results with this approach (365) and it is intended to integrate and evaluate this method within an upgraded version of SmartLiver.

In our previous work it was estimated that even if all the above mentioned sources for registration errors could be rectified, a residual TRE of app. 7.5mm RMS would remain due to the liver motion and deformation (172) which are caused by a number of intraoperative factors including cardiac motion, ventilation, pneumoperitoneum and surgical manipulation (174,216). Because currently used 3D models are non-deformable and fixed in space this baseline TRE must be regarded as the optimal reference standard that IGS should currently be measured against. Therefore it is important to address technical components of the IGS

to improve anatomical accuracy but a residual error will remain until a feasible solution for modelling intraoperative soft tissue deformation has been found.

The research community has attempted to predict liver deformation by developing computer algorithms that can alter the shape and position of 3D models to reflect intraoperative conditions. Despite recent advances, (219,366) this technology has not yet matured enough to be employed in a clinical environment because the modelling of soft tissue deformation is exceedingly complex and computationally expensive. A positive correlation between organ motion and TRE was found in our study population and therefore we hypothesise that compared to deformation, organ motion has a more pronounced impact on the registration error in IGS that use a rigid 3D organ model. The significance of this assumption is that in contrast to liver deformation, it is technically less challenging to model repetitive liver motion from ventilation and cardiac movement. If this can be confirmed in future studies it may re-direct research efforts towards liver motion which potentially has a greater translatable value.

Although the results from this study have demonstrated the feasibility of using SmartLiver as a image guidance tool in LLR, there are some limitations that have to be taken into account. In two patients SmartLiver setup, registration and AR visualisation has been performed in real time. For the remainder of the study however, data was collected at surgery but the registration and overlay was performed later to reduce the time during surgery, particularly for patients who underwent staging laparoscopies which are relatively short procedures. By choosing a retrospective approach for this study it was possible to maximise data acquisition in a relatively limited time frame and therefore accelerate the development of SmartLiver. Once the overlay procedure can be done more quickly overlays will be carried out during surgery.

The average intraoperative setup time of up to 20 minutes was longer than reported for parallel screen display IGS used in open hepatic resections (359). This is likely due to the fact that the latter do not require a laparoscopic camera calibration. The calibration time however was improved by approximately 5 minutes in the later stages of the study by implementing the cross-hair calibration method (30). Another time intensive step in the intraoperative setup was the installation of the tracking collar which had to be manually tightened with small screws. Alternative methods for the fixation of tracked objects onto the laparoscope have been explored for future studies and it is expected that this will further reduce setup times.

Based on the surgeon survey, the procedural delay caused by the intraoperative setup time was felt to be the most negative aspect of SmartLiver. However this represents only a small fraction of the time taken to perform a laparoscopic liver resection. In addition to making improvements to laparoscope calibration and tracking collar fixation, our group is also working on a graphic user interface which will allow non-technical users to setup SmartLiver

independently, a feature which hypothetically could further decrease the required setup time. A further concern raised in the survey was that the 30 degree laparoscope angle movement of the IMAGE 1S – TIPCAM is restricted. This is a limitation of 3D laparoscopy caused by fixed spatial relationship of the two video channels and is not a specific for SmartLiver. Furthermore 3D laparoscopes have been demonstrated to be a safe tool in complex LLR (202,203).

Intraoperative use of SmartLiver does not require tracking of surgical instruments. Although instrument tracking has advantages such as allowing point based registration and interaction with the 3D model during surgery (67,367), it does also has disadvantages because 1) each additional instruments has to be calibrated which increases setup time and 2) overall accuracy may deteriorate because further tracking errors are introduced for each additional instrument used.

In summary, this paper has described a novel augmented reality image guidance system for LLR and in addition reported crucial anatomical accuracy metrics that can be utilised as benchmarks for future development work in this field. It was demonstrated that the system is able to operate in real time during surgery. Stereoscopic surface reconstruction was shown to be a feasible approach to user independent registration with a comparable target registration error to manual alignment. Future research efforts in our group are dedicated to improving SmartLiver's setup speed, user friendliness and the target registration error. The latter may potentially be achieved by refining the stereoscopic surface reconstruction algorithm with the aim of enabling it to independently discriminate between the liver and adjacent organs.

9. General discussion and conclusions

9.1. Summary of results

In this doctoral research project, the aim was to investigate the hypothesis that optical imaging and computer vision technologies have the ability to extract sensory information from the liver that is useful for guiding laparoscopic liver surgery.

The results shown here provide evidence that optical imaging technology can be employed to characterise liver tissue to an extent that is not possible with the naked eye. Computer vision was shown to enable creation of an augmented reality environment to facilitate intraoperative guidance for laparoscopic liver surgery. During laparoscopic surgery the sense of touch is lost which deprives surgeons of an important sense that in the main is used to assess the firmness of tissue which is increased in disease processes such as liver cirrhosis or malignancy. While the imaging modalities tested within the framework of this thesis cannot completely replace the sense of touch, they may provide a lot of information usually provided by touch, for example, whether the tissue is normal liver tissue or cancer, or the position of blood vessels in the operating site. Therefore, they can enhance and extend surgical vision and therefore, can substitute and in some cases, may even provide additional information that is not available from touch.

The first two results chapters (chapter 4 & 5) of this thesis focused on utilising confocal laser endomicroscopy to image minute details of liver tissue at the microscopic level. In chapter 4 one objective was to describe normal and cancerous liver histology using a dual wavelength method in a mouse model of colorectal cancer liver metastasis. It was demonstrated that using CLE imaging, typical features of normal and cancerous virtual liver histology could be described which correlated with tissue H&E histology examination from liver biopsies. It was found that evaluation at two different wavelengths, within the visible spectrum, was complementary and improved the quality of tissue characterisation. This was likely made possible by exploiting differences in the behaviour of the exogenous fluorophores fluorescein and indocyanine green. In addition, erythrocyte flow velocities could be estimated using this technology. Another objective in this chapter was to evaluate if fluorescence intensity could indicate the nature (i.e. normal vs. cancer) of examined tissues. Statistical analysis found that the relative fluorescence in tissue could be employed as an independent predictor for the presence of normal vs. cancerous tissue. An increase in relative fluorescence unit raised the odds ratio for the presence of normal liver tissue by 1.2 and 4.6, for CLE imaging at 488nm and 660nm, respectively. These findings indicate that virtual histology images can be obtained with probe-based CLE. Whether fluorescence intensity can indicate the presence of liver malignancy in patients cannot be commented on until this imaging modality is evaluated in a clinical setting.

Once it had been established that CLE imaging enables discrimination between normal and pathological liver tissue, the next question was if this could be applied during laparoscopic surgery. The objective in the subsequent chapter (chapter 5) was to test the feasibility of employing CLE during laparoscopic surgery in a porcine model and to evaluate if a visualisation of virtual liver histology can be achieved in analogy to the preceding chapter. It was shown that virtual liver histology can be visualised but that it is more problematic due to the technical difficulties of controlling the imaging probe. In parallel to chapter 4, fluorescence intensity was shown to be an independent predictor for the presence of normal vs. ablated liver tissue. Statistical analysis indicated that an increase in one relative fluorescence unit raised the odds ratio for the presence of normal liver tissue by 1.2 and 1.6 for CLE imaging at 488nm and 660nm, respectively. The results in this chapter indicate that laparoscopic CLE is feasible but would require an additional laparoscopic port and a steerable catheter. To determine if discrimination between normal and ablated liver tissue is feasible in humans, would require a clinical study for further evaluation.

In the chapters 4 and 5 it was shown that optical imaging can be utilised to sense pathological (malignant) or therapeutically induced (tissue necrosis secondary to thermal ablation) changes in liver tissue. As a microscopic imaging modality, CLE has limited use in sensing tissue on a larger macroscopic level (i.e. > 1-2cm^2). In other words, it is impractical to apply CLE to sensing a wider field of view. The aim of the subsequent chapter (chapter 6) was therefore to evaluate an optical imaging modality, called multispectral imaging, that could provide optical sensing on a wider field of view. The first objective in chapter 6 was to develop and test an imaging platform that enables spectroscopic tissue evaluation in a continuous wavelength range. Development and testing of a multispectral imaging platform consisting of an OPO light source and a NIR camera was outlined and the platforms ability to reliably obtain multispectral images was confirmed. The next objective was to acquire images from pathological *ex*-vivo liver tissue and compare it to tissue spectra that were previously published in the literature. This was only partially successful as no clear delineation between normal and malignant liver tissue spectra could be observed. It was however possible to record increased light absorption at 1210nm which corresponded with a well documented spectral feature which is associated with an increase in tissue lipid concentration. The presence of steatosis and malignancy was confirmed on H&E histology examination. The last objective in chapter 6 was to identify any particular wavelengths in the tissue spectra that are predictive for the presence of liver malignancy (HCC or CRLM). A generalised linear mixed model analysis carried out on the recorded multispectral data revealed a number of wavelengths that were statistically significant independent predictors for the presence of normal vs. cancerous tissue. The classification accuracy of the resulting model was relatively poor at 69.1%.

The concept of the multispectral imaging platform used in chapter 6 was based on equipment that allows a detailed spectroscopic examination but that due to limitations with

regards to laser safety and robustness (i.e. ability to withstand positioning in theatre) may not be ideally suited for laparoscopic use. Suggestions for the future development of a MSI system more suitable for laparoscopy were made (6.4.). The appeal of such a system is that it could potentially be incorporated into a laparoscope without requiring additional instruments or probes. Computer vision technology is similar in this aspect because it utilises video data as its main sensory input and therefore it can be applied to laparoscopy without requiring additional probes. To further investigate this avenue, the next chapters (chapter 7) aimed to investigate to what extent Eulerian video magnification could provide visual sensing during laparoscopic liver surgery.

The first objective in the chapter was to develop and test a texture based analysis method to quantify VM signals that were derived from motion. The proposed analysis method correctly and repeatedly identified the presence of VM signals in 12 different video sequences obtained from observations of a flow phantom. In some sequences the VM enhanced pulsatile motion was not clearly visible but a variation in GLCM statistics enabled identification despite this. It is therefore postulated that this approach to VM signal analysis may be useful in scenarios were enhanced motion is not clearly visible to the observer. The second objective in this chapter was to establish if the texture analysis method could be employed to quantify the extent of pulsatile motion. The series of experiments did not verify this hypothesis. The third objective in chapter 7 was to apply texture based VM signal identification to concealed flow channels in an opaque flow phantom. It was demonstrated that VM signals could be correctly identified in a majority of occasions. On ROC analysis, the diagnostic test accuracy was found to be fair (>0.7) for two out of four GLCM statistical values (Energy and Correlation). It was therefore concluded that identification of VM signals in concealed structures is feasible using the proposed method. Finally an attempt was made to utilise the texture based analysis method in an *in-vivo* setting. Video recorded during laparoscopy in a porcine model was processed and subsequently analysed. No VM signals related to pulsatile motion were discernible and it is purported that this was due to extraneous respiratory motion. This result suggests that VM processing algorithms require further refinement in order to allow filtering of undesired motion signals.

A shared limitation of the imaging modalities tested in chapters 4-7 is that they have a limited penetration depth and are therefore not capable of sensing deep lying structures within the liver. In chapter 8 an image guidance system (IGS) was evaluated as an example of a computer vision technology that can overcome this restriction. By using stereoscopic surface reconstruction to register detailed 3D liver model to the liver surface, the system exemplifies how the precision of computer vision technology can be amalgamated with the detailed volumetric data from a preoperative CT scan. The data in this chapter has been obtained as part of a clinical feasibility study. Before any of the objectives are addressed, a description is given of how the system was developed and how it performed in the pre-clinical phase. The first objective in this chapter was to assess the feasibility of using the IGS

during laparoscopy. In 9 out of 12 recruited patients, the IGS was functional and no incidents were recorded. As two out of the three failures to function were secondary to a technical fault of the laparoscope with no malfunction recorded in any of the IGS components, it was concluded intraoperative use is feasible. In the next step, accuracy and usability were assessed. The target registration error was in the region of 14mm RMS. Based on the user survey the main issue regarding usability was the additional time required for the setup of the IGS. The last objective was to compare manual and automatic registration. Manual registration was always possible but occasionally yielded high registration errors. Although it was fully functional during preclinical evaluation, automatic registration was hampered by the systems inability to distinguish liver tissue from other surrounding tissues in humans. With the aid of manual delineation of the liver surface (manual segmentation), automatic registration at a TRE of <6mm RMS, was successfully demonstrated in one patient. This approach however is very time intensive and hence would not be an option during surgery. It was therefore concluded that manual registration is fully functional, whereas automatic registration required further refinement before meaningful clinical evaluation of its performance could be continued. Suggestions of how to implement a machine learning algorithm that can aid in liver segmentation, has been made (8.3) and its feasibility of use has been demonstrated elsewhere (365).

Development and clinical evaluation of an augmented reality based image guidance system in chapter 8, investigated the ability of computer vision techniques to enhance imaging on a centimetre (i.e. macroscopic) level. The current accuracy of the system was shown to be in the region of 10-20mm which was sufficient to improve anatomical orientation during laparoscopic surgery. A positive correlation between organ motion and imaging accuracy was elucidated and it is hypothesised that accuracy may be improved by implementing adjusting factors for organ motion into the registration process.

9.2. Potential clinical application

Intraoperative ultrasound is an essential tool for the visualisation of functional liver anatomy and has therefore to be regarded as the gold standard for imaging in laparoscopic liver resection (73–77,368). Its advantages are a good spatial- and temporal resolution which is combined with an excellent depth penetration (232,352). Its use in LLR does however have some limitations such as operator dependence and decreased diagnostic accuracy for small lesions especially if found on the background of liver cirrhosis or steatosis. Furthermore it is a 2D imaging modality and hence does not offer much orientation in space (141–144,233). In this section potential clinical applications for the imaging modalities explored in this thesis are described. An attempt is also made to highlight how alternative experimental imaging technologies could be used in this context. Because LUS has already found widespread use in LLR and is clinically established (74), it will not be elaborated on any further in this section. The potential clinical applications of novel imaging technologies are focused on areas where LUS has limitations (e.g. 3D imaging, small lesions).

None of the tested imaging modalities in this thesis are at a technical maturity level where they could be applied in clinical studies to inform a change in surgical strategy. Confocal laser endomicroscopy and SmartLiver have been demonstrated to be safe in a laparoscopic environment (150). It is however crucial to determine the optimal way of utilising the provided image data to guide surgical therapy before potential benefits for patient care can be evaluated. Multispectral imaging and video magnification are perhaps even further away from being evaluated clinically but the underlying technology behind these systems can be integrated into existing laparoscopic equipment without having to overcome great technical hurdles. In the case of video magnification the main requirement on hardware would be the use of a high definition laparoscope. From a software point of view it would be crucial to increase the processing speed of existing algorithms to enable the real time implementation for high definition video (136). Multispectral imaging has already been used in laparoscopic surgery and threre are even commercially available systems (103,108). To truly evaluate and unlock the potential of this modality it would however be pertinent to develop a device that can examine a wide range of spectra including the wavelengths from 600-1500nm and perhaps even beyond. Outlined below are some ideas and visions of how to apply optics and computer vision in a clinical context. To relate directly to clinical translation, potential forms of applying enhanced visualisation are divided according to clinical need.

9.2.1 Intraoperative histology

With the exception of the primary tumour in case of liver metastasis, the majority of liver resections are only beneficial if there is no extrahepatic spread. If tissue is suspicious for malignancy it is often excised and sent for histological evaluation. This however is time consuming and has a comparatively low accuracy. An imaging method such as CLE may enable the examination of suspicious tissue at a microscopic level and in future studies this may be shown to be beneficial. One group is currently exploring the feasibility of sending the image information obtained via CLE through a video conference to a histopathologist for real-time evaluation (150). The increasing role for parenchyma sparing liver resection for HCC and CRLM has already been discussed above (1.1.5). An intraoperative microscopic imaging modality could be a useful adjunct if unexpected disease (e.g. HCC nodules and regenerative nodules) is found outside the planned resection area (369).

The safety and feasibility of using CLE during laparoscopic surgery has been demonstrated almost a decade ago (178). Based on the results of this thesis, the main hurdle to the use of CLE in LLR is that the fine control of the CLE probe tip is not sufficiently accurate yet. Suggestions of how address this issue in the future have been outlined below (9.4.1).

9.2.2 Verifying clear oncological margins

The complete removal of malignancy is an important factor in improving long term survival rates. Indeed if based on preoperative imaging a complete removal is not feasible then alternative techniques of cancer treatment need to be considered (55,370). Enhanced intraoperative orientation such as can be provided by image guided surgery (chapter 8) may

improve chances of locating cancer lesions. Before utilisation of IGS for precise intraoperative guidance can be advocated though, it is crucial to improve accuracy to a degree where surgeons can be confident that the position of lesions displayed within an AR environment are correct. In addition it needs to be ensured that an IGS can provide excellent accuracy on a consistent level. Suggestions on how this could be achieved with future research efforts are stated below (9.4.4).

A different approach to ensuring that cancer has been cleared completely in the immediate vicinity of the operating site (i.e. avoiding R1 resections) is to develop a method of checking the resection margin of the liver for any residual disease. Within this context MSI could be utilised to directly examine the margins of the liver remnant. If future studies confirm that detection of malignancy by MSI is reliable, than a routine examination of resection margins could reveal if any disease is left behind. Narrow band spectral imaging is already clinically licensed, therefore the main obstacle to clinical implementation of 'broad band' spectral imaging or in other words MSI, is to find a technical solution to expanding the wavelength range of existing systems (195). A complementary approach to this would be the ICG mediated visualisation of NIR fluorescence. Based on previous reports an increased fluorescence in contrast to surrounding liver parenchyma may be present in the rim of CRLM lesions or throughout the whole of a HCC lesion (189). Fluorescence ICG imaging can be described as MSI in conjunction with an exogenous fluorophore, because existing MSI systems would be able to visualise ICG mediated fluorescence in addition to the previously described tissue spectra (6.3.3). Therefore it is proposed that both imaging approaches could be utilised in a complementary fashion. Theories on how to take MSI based imaging forward and mature it to a stage where it can be studied clinically are given below (9.4.2).

9.2.3 Assessing the vitality of tissue

Assessment of liver vitality and perfusion is useful to guide parenchymal transection of the liver. A popular technique for carrying out major liver resections involves the ligation and division of blood vessels that carry blood into the liver. Once blood flow is cut off, the affected portion of the liver changes its colour. The border between changed and unchanged liver is used as orientation for the parenchymal transection line. It may however be difficult to appreciate this line in some circumstances and here is where an evaluation of tissue vitality and perfusion may be helpful. A number of the evaluated imaging modalities could be used in this context. The use of CLE may highlight absence of fluorophore inflow in the non-perfused part of the liver. Imaging via MSI may reveal a reduction in oxygenated haemoglobin (aspect not tested in this thesis) whereas video magnification could be used to enhance an imperceptible change in colour. Restrictions to the clinical translation of CLE and MSI have already been discussed above (9.2.1, 9.2.2). An important limitation of VM to its application in LLR is liver motion secondary to respiration, a finding of this work which has been described above (7.3.4.2). Potential solutions to overcome this issue are stated below (9.4.3).

9.2.4 Haemorrhage preventive techniques

Major haemorrhage from the liver can lead to a blood loss of several litres within minutes. It is difficult to control laparoscopically and is one of the leading causes for converting to open surgery (358). For this reason, prevention of haemorrhage is paramount in laparoscopic liver resection and for this to be effective, it is important to appreciate the vascular anatomy and location of individual blood vessels. Providing a registered and accurate 3D liver model during surgery as has been outlined in chapter 8 is likely to be of value in enhancing the surgeons understanding of the livers vascular anatomy and its use may prevent inadvertent injury to vascular structures. Multispectral imaging has been shown to enable visualisation of extrahepatic blood vessels that were obscured by fat (155). If it is possible to extend this application to intrahepatic vessels, even if only at 1-2mm imaging depth then it may be another tool useful for the prevention of haemorrhage. The limitations that prevent a clinical translation of IGS and MIS for laparoscopic liver surgery have been outlined above (9.2.2) and potential solutions are proposed below (9.4).

9.2.5 Identification of hilar structures

A standard approach to major hepatic resection is to identify and control the blood vessels that carry blood into the liver (hepatic artery and portal vein). If a blood vessel is identified wrongly and consequently divided, it can have fatal consequences for the patient. In this scenario a number of imaging modalities may be helpful. Successful discrimination between hepatic artery, portal vein and common bile duct in a porcine model has been reported by a group that used a LCTF based MSI laparoscope (155). Video magnification could be used to highlight pulsation in the hepatic artery and interpretation of hilar anatomy may be facilitated by comparing it with a registered 3D liver model as can be provided by an image guidance system. Obstacles to the clinical translation of MSI, VM and IGS have already been described in this section and potential solutions are outlined below (9.4).

9.2.6 Assessing the future liver remnant

A crucial paradigm in liver surgery is that the volume and function of the liver remaining after resection must be sufficient to prevent postoperative liver failure (371). Generally liver function is difficult to assess, it is well documented though that patients with cirrhotic or fatty livers are more prone to develop postoperative liver failure. Hence the use of MSI to quantify liver steatosis in such patients may theoretically be of benefit. One group reported on the successful use of spectroscopic fibre based analysis in the evaluation of liver cirrhosis. Although this has not been translated into a remote image based approach yet, this is certainly an enticing prospect. In this context the assessment of liver fibrosis and cirrhosis utilising CLE via a mini-laparoscopic approach has previously been demonstrated in 47 patients (147,178). This method of assessing tissue quality could potentially be combined with a 3D liver model based estimation of residual liver volume. Segmental vascular anatomy and precise volumetric assessment of the liver is an inherent part of the 3D liver model. It is relatively straight forward to visualise this data and it could also be employed to

simulate a liver resection and assess the functional residual volume (371,372). The limitations of CLE, MSI and image guided surgery have already been discussed in this section and potential solutions to facilitate a future clinical translation are outlined below. (9.4)

9.2.7 Alternative imaging modalities

There are several alternative experimental imaging technologies that could be applied to the clinical situations that have been described above.

Optical coherence tomography is an alternative microscopic optical imaging modality and as such it could potentially be used to assess virtual *in-vivo* histology (9.2.1) and be used to evaluate the quality of liver tissue in the future liver remnant (9.2.6). It has a similar limitation in terms of depth penetration to CLE but a further disadvantage is that it has an inferior lateral resolution at (7µm vs. 1.4µm) compared to CLE. This means optical coherence tomography is less suited to visualising subcellular details in liver architecture (283,373). Also its ability to image liver tissue *in-vivo* has not been evaluated yet (374).

Photoacoustic imaging is a hybrid imaging technology that combines optical and ultrasound technology (232). The majority of photoacoustic research is focused on macroscopic imaging but a number of systems have been developed that enable imaging on a microscopic scale which potentially could be applied to obtaining virtual *in*-vivo histology (9.2.1). The design of microscopic photoacoustic systems is however very complex and at this stage a miniaturisation for laparoscopic use has not been reported yet to the best of my knowledge (375). More commonly photoacoustic imaging is evaluated for macroscopic imaging (i.e. millimetre scale). It has been shown to have the potential to enable highly specific imaging of oxyhaemoglobin, deoxyhaemoglobin and bilirubin in a mouse model (240). If this can be replicated in a clinical setting, this modality could become a useful aid for the identification of structures in the liver hilum (9.2.5). Visualisation of oxygenated and deoxygenated haemoglobin could also enable photoacoustic imaging based evaluation of liver tissue vitality (9.2.3). Hypothetically, decreased vitality would be associated with a decrease in oxygen content. The design of a laparoscopic probe that is capable of visualising haemoglobin has previously been described (242). In this report though the probe was only studied *ex-vivo* and to the best of my knowledge, a laparoscopic application has not been reported.

The majority of preoperative liver diagnostic for surgical planning and surveillance is conducted with CT and MRI. They can also be utilised intraoperatively in the form of cone beam CT (CBCT) and open plane MRI. Excellent accuracy for of CBCT used in LLR has been demonstrated by one group (229) and in addition depth penetration is not an issue with this modality or with open plane MRI. Intraoperative imaging to facilitate: verification of clear oncological resection margins (9.2.2), prevention of haemorrhage (9.2.4), identification of hilar structures (9.2.5) and for the volumetric assessment of the future liver remnant (9.2.6)

should all be potentially possible. There are however many disadvantages to utilising CBCT for image guidance in LLR including a low resolution, ionising radiation, high costs, lack of portability and an inability to allow spatial correlation between instruments and 3D model in real time (228,229). With the exception of ionising radiation and low resolution, open MRI based image guidance has the same limitations. MRI also has a slower image acquisition time than CBCT but the most significant obstacle to utilising it for image guidance during laparoscopy is its incompatibility with metallic equipment. This restriction makes the use of custom built metal free surgical equipment mandatory (230,231).

Finally 3D ultrasound could enable the volumetric assessment of the future liver remnant (9.2.6). One group reported on the reconstruction of liver volumes in *ex-vivo* porcine tissue (376). If this can be replicated *in-vivo*, then it could provide a useful tool for assessing the volume of the future liver remnant. Disadvantages of 3D ultrasound are comparable to its 2D variant perhaps with the exception of providing a better spatial orientation within the imaged volume (9.2).

9.3. Limitations of the current work

The experimental results presented as part of this thesis have several limitations. The mouse model used for CLE assessment has been widely reported on and has been shown to be a reliable and reproducible model in the study of metastatic liver disease (250).

It is however only representative for colorectal cancer liver metastasis and hence findings cannot be transferred to other types of liver cancer. Furthermore this animal model is created with one specific colorectal cancer cell line. This line was chosen because it is known to stem from a well differentiated cancer that was more likely to have typical imaging characteristics that would set it apart from hepatic cells. It is however important to verify the applicability of CLE imaging for identification of metastatic disease on a variety of cancer cell population because this is more reflective of the clinical setting.

The ability to sequentially record CLE images and combine them to form a larger image or so called mosaic has been demonstrated previously (149). This may be of value because it allows the assessment of larger and clinically more meaningful tissue areas. The commercial software package that can facilitate this recording mode was however not accessible for experimental use. The importance of standardising the fluorescence values that have been used in the statistical analysis of CLE image data has already been stressed above (4.4).

A major issue during laparoscopic CLE imaging in the porcine model was the stabilisation of the CLE probe. Stability of images was hugely dependent on the area of the liver being visualised which meant that some liver regions may have been over-represented. Occasionally more pressure had to be exerted to obtain images and this may have influenced the local tissue perfusion and hence distribution of fluorophores. A change in this

distribution pattern may have influenced the quality of images. In both animal models, porcine and murine, normal tissue was compared to pathological tissue (ablated or cancer tissue) from the same animal. It could be argued that a comparison to control animals may have been preferable. The rationale behind comparing tissues in the same animal was that this approach is more relevant in a clinical context where it is important to delineate areas of diseased form non-diseased tissue (134).

A clinical evaluation of CLE imaging of liver pathology and an attempt to verify the predictive algorithm developed for the murine and porcine model in this context would have been desirable. It was however not possible to obtain ethical approval in the required time frame. Furthermore it was felt that more data was needed on different forms of cancer and that in addition a better stabilisation method for laparoscopic CLE imaging was required to make a clinical evaluation beneficial. More recent CLE platforms enable simultaneous dual wavelength visualisation. If this technology would have been available for experiments, a better direct correlation between CLE images in the red and blue light spectrum could have been achieved.

Studies into multispectral imaging were only conducted on *ex-vivo* liver tissue. Examination of *in-vivo* tissue may have provided a better estimate of the impact of perfusion and bile content on tissue spectra. On the other hand, the range of the spectral imaging was 1100-1700nm which does not include absorption peaks that are relevant for haemoglobin or bilirubin (256). This means that theoretically only the water content could have been different in an *in-vivo* experiment as the content of fat is unlikely to be influenced by blood flow. Naturally it would have been preferable to conduct MSI employing a wider spectral range, perhaps between 600-1700nm (155,240). This was however not possible due to the technical restrictions of the excitation laser source and the InGaAs NIR camera.

The number of studied animals and *ex-vivo* specimen was small across studies, but comparable to previous reports from other groups (225,241,248,336,377). In the murine model some animals were lost before they could be studied and for some of the studied animals data was insufficient to allow comparison between healthy and cancerous liver (4.3.1).

In the porcine model the main issues were the high costs for each experiment and the fact that several different imaging modalities were tested on each animal which meant that the time that could be spared for each modality was limited. The findings from murine and porcine experiments however were sufficiently congruent (i.e. decreased fluorescence form pathological areas) to support the intended analysis strategies. The main restrictions of obtaining more *ex-vivo* tissue for MSI experiments on liver steatosis were related to the difficulty in obtaining discarded donor livers. A larger number of live cancer specimen could not be obtained because no tissue could be taken from the vicinity of the resection margin because this would have impacted negatively on the clinical decision making process.

During histopathological evaluation it is crucial to ensure that the resection margin is clear from cancer. This would potentially be compromised if tissue for experiments were to be taken from this margin. This essentially means that only very large resection specimen that had cancer lesions distant from the resection margin could be used. Given this limitation it was fortunate that tissue from two different patients with HCC could be retrieved because, HCC is a rare indication for surgical excision in the UK (378). The time frame in which specimen could be retrieved was also limited (<8 months) because it took a significant amount of time to develop and test the MSI platform used for experiments in this thesis.

During analysis of video magnification experiments, a striking discrepancy between initial results and results form later experiments was found (7.4). This difference related to visibly less enhanced pulsation in the latter experiments which correlated with a decrease in the measured VM signal strength as expressed by GLCM stats. It is unclear whether this discrepancy was due to a variation in the perfusion circuit itself i.e. related to pressure and flow although this was monitored continuously. It is also possible that the change was related to the use of a different flow phantom construction, because initial experiments used a clear phantom with two perfusion catheters whereas later recordings were made employing a clear phantom with three perfusion catheters and a brown phantom with two perfusion catheters. More concerning than this discrepancy however was the inability to replicate the enhancement of vessel pulsation in laparoscopic video that was reported by other authors (244,245). A potential explanation could be that other groups preferred the use of video sequences recorded with a surgical robot whereas the video material in this thesis was derived from laparoscopic video. The significance of this is that robotically recorded video is not influenced by hand tremor which would usually affect laparoscopic video recordings (350).

It is however more likely that hand tremor played a minor role. The dominant VM signals observed in the laparoscopic video had a similar frequency to the respiratory motion. It is therefore hypothesised that respiratory motion of the liver prevented acquisition of more subtle pulsatile motion signals (7.4). Another possible problem with the video sequences recorded for VM processing may be related to ambient light conditions. These were not controlled for and hence differing amounts of light and shade were present in some of the sequences. Standard ceiling lighting was used for illumination and as the flow phantom was placed in the same position on the lab table, this factor should not have varied to a great extent. Because of the negative results from the porcine laparoscopy no attempts were made to study laparoscopic video data from patients.

Due to time constraints during surgery, intraoperative registration was only carried out in two out of 9 patients who underwent image guided surgery. As highlighted above it was not justifiable to significantly prolong surgical procedures to optimise the accuracy of registration. A retrospective registration was carried out for the remaining patients. This mode of evaluation was not originally intended but it nevertheless provided valuable data

and helped in making improvements to the SmartLiver IGS. The accuracy of the system was objectively assessed with a validation method that has been previously verified in a porcine model (172). The validation method utilises visual assessment of anatomical landmarks as gold standard but it could perhaps be argued that an additional marker of registration accuracy would have been desirable. One alternative method of assessing accuracy is (141) to measure the distance of cancer lesions to the resection margin based on IGS data and then to compare this metric with a distance measurement taken from the pathological resection specimen. The disadvantage of this method though is that it relies solely on one measured dimension whereas the method used in this thesis combines metrics form two dimensions. In addition tumour growth in the period between preoperative image acquisition and time of surgery may decrease the distance between lesion and resection margin on histopathological evaluation. There is some indication that electromagnetic tracking of the laparoscope may be advantageous to optical tracking (267) and it would have been useful to elucidate this in a clinical setting. It was not possible to test this though because no safe means of integrating the electromagnetic tracker into the laparoscope could be established. Because of this shortcoming no attempt was made to gain ethical permission for the clinical use of an electromagnetic tracker. Finally the use of retrospective registration meant that any potential clinical impact of using an IGS could not be assessed. This however was not intended in the original study protocol as the main objective was to assess performance metrics (e.g. accuracy) and device safety.

9.4. Areas of future work

9.4.1 Microscopy

As a microscopic imaging modality, the main advantage of CLE, its detailed view of cellular architecture could perhaps also be regarded as its Achilles heel, because by focusing on a small field of view it is difficult to put images into a larger and clinically meaningful context. An important step would therefore be to enhance the field of view so that an area >1 cm^2 can be viewed. The capability of combining several smaller fields of view together has already been implemented by one commercial system (149). A crucial hurdle for making this 'mosaicing' approach viable during laparoscopy, is the need for a stable point of view. To provide this sort of stability it is essential to have the ability to control the position of a CLE probe with millimetre precision. The ability to achieve this is no trivial matter because the probe motion needs to be coordinated with the respiratory motion of the liver. It has previously proposed to use a robotic arm for this purpose and this method has been evaluated via a natural orifice transluminal endoscopic surgery and a standard laparoscopic approach in a porcine model (149,150). This group's proposed methodology addresses the issue of precise control but it does not allow adaptation to organ motion and furthermore robotic liver resection is not practiced widely at present (118).

The liver largely consists of smooth and featureless surfaces on the outside. Theoretically a frame attached to several suction cups or fine atraumatic graspers could be applied to the liver surface. This frame could provide a steady point of reference. A motorised device attached to this frame could then be used to move the CLE probe smoothly across the underlying liver surface while ensuring that the surface is covered in its entirety. The fine control for this motorised movement could either be carried out manually or automatically. To create such a device it is proposed to aim for a spider or crab- like design with several arms centrally arranged around the motorised manipulator of the CLE probe in the middle. Such a device however would have to overcome many hurdles with the biggest probably being the issue of miniaturising it to such a degree where its introduction through a 12mm laparoscopic port is possible. If such an undertaking is considered, it is suggested to design it for open surgery first and then expand on this design later to apply it to minimal invasive surgery.

A more sophisticated and practical solution would perhaps be a combination of CLE, robotic (379) and image guided surgery. In essence the robotic control provides precise manoeuvring of the CLE probe whereas the IGS is used to guide the robotic movements (221). Should future IGS gain the ability to adjust for liver deformation and motion then it would be possible to alter the movement of robotic arms accordingly. Combination of these technologies would potentially permit precise mosaicing of large patches of liver surface. As an added bonus the recorded CLE images could be integrated into the 3D liver model and hence be viewed within the correct macroscopic context (Figure 9.1).

A further aid in providing visualisation of greater surface areas would be a CLE probe that is customised to the specific requirements of laparoscopy. The CLE device tested in this thesis is licensed for use in luminal endoscopy and hence has been miniaturised to fit through an endoscopic working channel of <3mm. During laparoscopy however it would be feasible to used devices with a diameter of up to 12mm. Greater circumferential size would not only aid in covering a greater surface area but it would also likely have a positive impact on image quality (380).

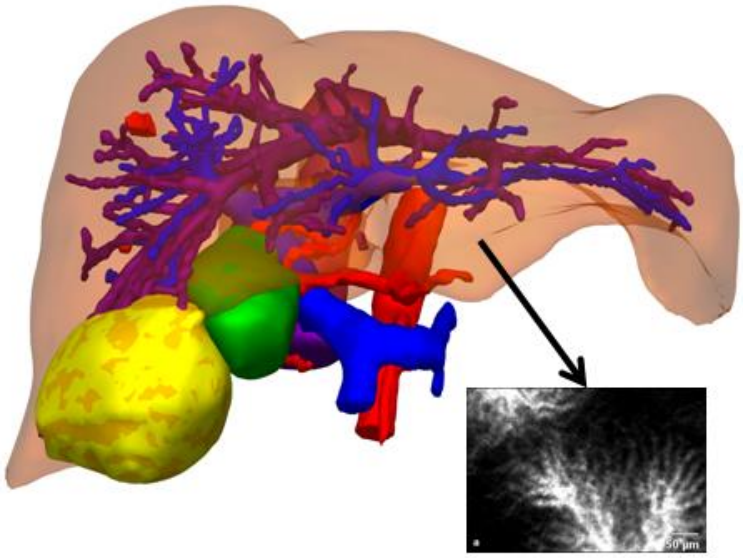

Figure 9.1 Integration of CLE images into a 3D liver model.

It was demonstrated in this thesis that the relative fluorescence values (RFU) measured with CLE can be used to predict the presence of malignancy in a mouse model and of ablated tissue in a porcine model. Due to the nature of the underlying methodology no fluorescence threshold values that are indicative of pathological liver tissue states could be determined. To create a predictive clinical tool based on this method though, comparable threshold values are required. Creation of a system with such capabilities would require a novel and reproducible method of using a reference standard to calibrate the optical fibres within a CLE probe (299). It is proposed that a light source that emits light at a constant power through a narrow band filter could be used to calibrate such a system. The consistency of the calibration signal could be verified with the aid of a spectrometer and a photometer. The system used in this thesis utilises a chemical calibration standard that undergoes degradation over time and therefore it is unlikely to form a useful basis for producing calibration norms that are comparable between different users.

9.4.2 Multispectral imaging

Tissue evaluation with MIS depends on the interpretation of absorption characteristics that are inherent to different biological substances. Some substances such as lipids have more than one absorption peak at different wavelengths (app. 900nm and 1200nm) whereas others such as oxygenated haemoglobin possess only one absorption peak (256). To extract a maximum of spectral data from tissue it is therefore essential to cover a broad wavelength range. Based on previous *in-vivo* studies into MSI of the liver, it is purported that a desirable range would include wavelengths from 600-1700nm hence covering absorption peaks for bile at the lower end and water and collagen at the upper end (240,256). No single system capable of covering this spectral range in its entirety has been described in the literature so far. It is believed that it should be feasible to combine existing systems to cover the desired spectrum. The construction of such a broad spectrum MSI system would be the first important hurdle towards the accelerating clinical translation of MSI of the liver.

Once the foundation is formed to interrogate liver tissue at the most relevant wavelengths the following step should be the formation of an extensive database, correlating spectral response curves (SRC) with pathological and healthy liver tissue. It is presently unclear how *ex-vivo* and *in-vivo* analysis will compare but it is hypothesised that the main differences will be related to the absorption characteristics of haemoglobin and perhaps to a lesser extent water. The rationale behind this theory is that blood perfusion present in *in-vivo* studies will likely have an impact on the concentration of the main components of blood namely haemoglobin (163) and possibly also on water. Nevertheless studies from *ex-vivo* human liver specimen have the advantage of mirroring the histological composition of clinical disease (e.g. cancer) more closely than would be the case for animal disease models. The latter model however would provide a valuable insight into how blood flow will affect the spectral signature of disease. An integral approach to analysing findings from both experimental models in context will likely yield a close approximation of what can be expected from intraoperative MSI of the liver.

To facilitate clinical studies, it will likely be most efficient to focus on spectral responses in certain narrowly defined wavebands as opposed to requiring a full acquisition of SRC in small wavelength steps (381), because this is heavily time and resource dependent. Once the relevant spectral ranges have been established from a SRC database, it should be possible to fit a spectral response curve to normal liver tissue and a variety of liver pathologies, respectively (161,256). Instead of measuring a full spectral response in clinical studies, MSI could focus on obtaining spectra from specific wavebands only and this data could then be processed to compare its fit to the pre-established pathological and healthy “signature” spectra. If this approach is shown to be feasible it would mean that technical solutions to laparoscopic MSI could be based on multiple bandpass filters instead of tuneable laser excitation. The former approach would be much less complicated as it avoids concerns about laser safety, costs and theatre space (382).

A recently established method of MSI completely dispenses with the need for interrogating tissue at specific wavelengths. In parallel to video magnification this methodology has the advantage that no specific hardware adaptations are required. The authors describe how they employ radiometric colour calibration of the endoscopic camera's sensor in conjunction with a Bayesian framework to analyse blood volume and oxygen saturation in the observed tissues (383).

9.4.3 Video magnification

Experiments into video magnification in this thesis have corroborated findings from other groups which found that imperceptible motion can be enhanced and made visible in a variety of settings (136,244,245). A major drawback of Eulerian video magnification however is an increase in image background noise which correlates with the magnitude of the magnification factor and the quality of the original video (7.3.1.4.1). For this reason much of the future work into this computer vision modality will likely be directed at improving image noise (244,342,384,385). Although primarily investigated as a method to improve laparoscopic vision, VM has also been applied to standard video cameras utilised for a number of clinical diagnostics. One group has proposed VM as a method of monitoring viability of skin flaps after reconstructive surgery (386). Other authors have suggested to utilise VM for the diagnosis of fasciculation in patients with amyotrophic lateral sclerosis. The fact that VM technology can be utilised in conjunction with standard video cameras that are nowadays ubiquitously available is one of its main advantages. A further step towards implementing VM as a methodology for the remote monitoring of vital signs in a large number of subjects has been its incorporation into mobile app technology (341). In addition to using standard RGB video signals as input for VM, thermal video data has also been successfully utilised to assess microvascular health in diabetic feet.

Based on the reports from a number of authors groups it is clear that utilisation of VM in laparoscopic surgery has led to some promising results (244,245,385). Despite this there is a significant requirement for further improvements and clinical evaluation before this computer vision modality can be employed to enhance surgical sensing of physiological motion. Based on the results in this thesis it is purported that considerable efforts should go into standardising the evaluation of VM processed video scenes. Extraneous motion such as respiratory and cardiac motion, may also prove an important obstacle to the implementation of VM in laparoscopy. A potential solution that has not been evaluated here may be to track a region of interest on the liver surface and transform it into a virtual "still image" to facilitate consequent VM processing without the interference of extraneous motion.

9.4.4 Image guided surgery

The results from the SmartLiver clinical feasibility study presented in this thesis indicate that two key areas requiring more development work in image guided surgery are accuracy and usability. Quite simply an improved accuracy will increase surgical confidence in the reliability of the displayed augmented reality environment. Accuracy as reflected by target registration errors (TRE) in the range of 5-20mm RMS did vary significantly between cases and at this stage it is justifiable to regard the system as an aid to intraoperative orientation. To achieve the sub-centimetre accuracy required to carry out precise intraoperative navigation more improvements are required.

Most efforts of improving accuracy are directed towards creation of a deformable 3D liver model that can simulate changes in liver shape in real time. Many groups are working towards this goal but due to the scientific complexity and immense computational demands the realisation of a real-time deformable liver model remains elusive so far (174,228,348,387). It was highlighted in chapter 8 (8.3) that a rigid 3D model that adjusts for liver motion would be less complex and hence may be a more realistic short to medium-term solution. Refinement of the 3D liver model is not the only area where accuracy may be enhanced. Based on preclinical experiments with the SmartLiver system it was estimated that a TRE of 1-2mm RMS is caused by inaccuracies of the optical tracking method. Utilising electromagnetic tracking instead of optical tracking was consequently shown to convey an improved accuracy (267). An entirely novel approach to tracking has been proposed by a group that employs stereoscopic surface reconstruction to estimate the laparoscopic pose. Initial results were promising although the best accuracy was achieved when combining the stereoscopic surface reconstruction method with conventional optical tracking (129).

The second key component of IGS is usability and integration within the surgical workflow. This is dependent on performance of different technical aspects such as time needed for registration and calibration (66,67) but also on the human-to-machine interface ergonomics of operating the system. At the later development stages of the SmartLiver system a graphic user interface that is controllable via a touch screen display was implemented. Subjectively this was felt to be a palpable improvement over the mouse and keyboard directed controls in the earlier development stages of the system. A novel way of addressing IGS control during surgery is the utilisation of natural user interfaces, namely gesture control sensors in the form of wristbands and voice control. This method circumvents sterility issues that are encountered during surgery. A reported disadvantage is that one hand needs to be freed up for performing gestures, but this is also true for any other form of interacting with machines, systems and the surgical environment in general (388).

9.5. Conclusion

The major conclusions drawn from this study with regards to the stated objectives were:

1) Confocal laser endomicroscopy can be utilised to discriminate between normal and pathological liver tissue in experimental mouse and porcine models. Reduction of fluorescence intensity increases the likelihood for the presence of colorectal cancer liver metastasis or ablated liver tissue.
2) Characteristics of liver tissue absorption spectra reconstructed from multispectral images, are related to the nature of the underlying tissue composition. Within the limitations of the available data, there is some indication that tissue absorption at particular wavelengths may independently predict the presence of malignant tissue.
3) Texture based analysis of video magnification signals can be used to verify the presence of subtle signals. This analysis method however does not enable a quantification of the underlying signal strength.
4) The feasibility of using an augmented reality based image guidance system for laparoscopic liver surgery has been demonstrated. The average accuracy of the system suggests that it will be useful in enhancing intraoperative orientation.

The above conclusions support the hypothesis of this thesis that optical imaging and computer vision technologies have the ability to extract sensory information from the liver that is useful for guiding laparoscopic liver surgery.

References

1. Sherlock S, Dooley J. Diseases of the liver and biliary system. 2008.

2. Rouiller C. The liver : morphology, biochemistry, physiology. Volume II. 674 p.

3. Jarido V, Kennedy L, Hargrove L, Demieville J, Thomson J, Stephenson K, et al. The emerging role of mast cells in liver disease. Am J Physiol - Gastrointest Liver Physiol. 2017 Aug 1;313(2):G89–101.

4. Brandl K, Kumar V, Eckmann L. Gut-liver axis at the frontier of host-microbial interactions. Am J Physiol - Gastrointest Liver Physiol. 2017 May 1;312(5):G413–9.

5. Aspinall R, Taylor-Robinson S. Mosby's color atlas and text of gastroenterology and liver disease. 2002;

6. Blumgart L. Surgery of the liver, biliary tract, and pancreas. 2007.

7. Couinaud C. Le foie: études anatomiques et chirurgicales. Masson & Cie; 1957.

8. Clavien PA, Strasberg SM. Terminology of liver anatomy and resections: The Brisbane 2000 terminology. Atlas Up Gastrointest Hepato-Pancreato-Biliary Surg. Elsevier Masson SAS; 2007;2(3):313–7.

9. Glenn F. Biliary tract disease since antiquity. Bull N Y Acad Med. New York Academy of Medicine; 1971 Apr;47(4):329–50.

10. Hand BH. An anatomical study of the choledochoduodenal area. Br J Surg. John Wiley & Sons, Ltd.; 1963 Mar 1;50(223):486–94.

11. Wolff H. Geschichte der hepatobiliären Tumorchirurgie. In: Hepatobiliäre und Pankreastumoren. Berlin, Heidelberg: Springer Berlin Heidelberg; 2010. p. 108–15.

12. Bryan PJ, Martin Dinn W, Grossman ZD, Wistow BW, McAfee JG, Kieffer SA. Correlation of Computed Tomography, Gray Scale Ultrasonography, and Radionuclide Imaging of the Liver in Detecting Space-Occupying Processes. Radiology. 1977 Aug;124(2):387–93.

13. Damadian R. Tumor detection by nuclear magnetic resonance. Science. 1971 Mar 19;171(3976):1151–3.

14. Allison DJ, Modlin IM, Jenkins WJ. Treatment of carcinoid liver metastases by hepatic-artery embolisation. Lancet (London, England). 2(8052–8053):1323–5.

15. Elliot JW. IV. Surgical Treatment of Tumor of the Liver, with the Report of a Case. Ann Surg. Lippincott, Williams, and Wilkins; 1897 Jul;26(1):83–95.

16. Ferlay J, Soerjomataram I, Dikshit R, Eser S, Mathers C, Rebelo M, et al. Cancer incidence and mortality worldwide : Sources , methods and major patterns in GLOBOCAN 2012. 2015;386.

17. El-Serag HB. Epidemiology of viral hepatitis and hepatocellular carcinoma. Gastroenterology. 2012 May;142(6):1264–1273.e1.

18. Mazzaferro V, Regalia E, Doci R, Andreola S, Pulvirenti A, Bozzetti F, et al. Liver Transplantation for the Treatment of Small Hepatocellular Carcinomas in Patients with Cirrhosis. N Engl J Med. Massachusetts Medical Society ; 1996 Mar 14;334(11):693–700.

19. Rizvi S, Gores GJ. Pathogenesis, diagnosis, and management of cholangiocarcinoma. Gastroenterology. 2013 Dec;145(6):1215–29.

20. Khan SA, Davidson BR, Goldin RD, Heaton N, Karani J, Pereira SP, et al. Guidelines for the diagnosis and treatment of cholangiocarcinoma: an update. Gut. 2012 Dec 1;61(12):1657–69.

21. Poston GJ. Surgical strategies for colorectal liver metastases. Surg Oncol. 2004;13(2–3):125–36.

22. Manfredi S, Lepage C, Hatem C, Coatmeur O, Faivre J, Bouvier A-M. Epidemiology and management of liver metastases from colorectal cancer. Ann Surg. Lippincott, Williams, and Wilkins; 2006 Aug;244(2):254–9.

23. Jones RP, Kokudo N, Folprecht G, Mise Y, Unno M, Malik HZ, et al. Colorectal Liver Metastases: A Critical Review of State of the Art. Liver cancer. Karger Publishers; 2016 Nov;6(1):66–71.

24. Abdalla EK, Adam R, Bilchik AJ, Jaeck D, Vauthey J-N, Mahvi D. Improving Resectability of Hepatic Colorectal Metastases: Expert Consensus Statement. Ann Surg Oncol. 2006 Oct 6;13(10):1271–80.

25. Van Cutsem E, Nordlinger B, Adam R, Köhne C-H, Pozzo C, Poston G, et al. Towards a pan-European consensus on the treatment of patients with colorectal liver metastases. Eur J Cancer. 2006 Sep;42(14):2212–21.

26. Ziff O, Rajput I, Adair R, Toogood GJ, Prasad KR, Lodge JPA. Repeat liver resection after a hepatic or extended hepatic trisectionectomy for colorectal liver metastasis. HPB. 2014 Mar;16(3):212–9.

27. Yao KA, Talamonti MS, Nemcek A, Angelos P, Chrisman H, Skarda J, et al. Indications and results of liver resection and hepatic chemoembolization for metastatic gastrointestinal neuroendocrine tumors. Surgery. 2001 Oct;130(4):677–

85.

28. Madoff DC, Gupta S, Ahrar K, Murthy R, Yao JC. Update on the management of neuroendocrine hepatic metastases. J Vasc Interv Radiol. 2006 Aug;17(8):1235–49; quiz 1250.

29. Naik R, Nordin A, Cross PA, Hemming D, de Barros Lopes A, Monaghan JM. Optimal Cytoreductive Surgery Is an Independent Prognostic Indicator in Stage IV Epithelial Ovarian Cancer with Hepatic Metastases. Gynecol Oncol. 2000 Aug;78(2):171–5.

30. Takemura N, Saiura A. Role of surgical resection for non-colorectal non-neuroendocrine liver metastases. World J Hepatol. Baishideng Publishing Group Inc; 2017 Feb 18;9(5):242–51.

31. Belghiti J, Cauchy F, Paradis V, Vilgrain V. Diagnosis and management of solid benign liver lesions. Nat Rev Gastroenterol Hepatol. Nature Publishing Group; 2014 Dec 2;11(12):737–49.

32. Foster JH. Survival after liver resection for cancer. Cancer. Wiley Subscription Services, Inc., A Wiley Company; 1970 Sep 1;26(3):493–502.

33. Frankel TL, D'Angelica MI. Hepatic resection for colorectal metastases. J Surg Oncol. 2014;109(1):2–7.

34. Rahbari NN, Mehrabi A, Mollberg NM, Müller S a, Koch M, Büchler MW, et al. Hepatocellular carcinoma: current management and perspectives for the future. Ann Surg. 2011;253(3):453–69.

35. Lin TY. A simplified technique for hepatic resection: the crush method. Ann Surg. Lippincott, Williams, and Wilkins; 1974 Sep;180(3):285–90.

36. Schwarz C, Klaus DA, Tudor B, Fleischmann E, Wekerle T, Roth G, et al. Transection Speed and Impact on Perioperative Inflammatory Response - A Randomized Controlled Trial Comparing Stapler Hepatectomy and CUSA Resection. PLoS One. Public Library of Science; 2015;10(10):e0140314.

37. Fritzmann J, Kirchberg J, Sturm D, Ulrich AB, Knebel P, Mehrabi A, et al. Randomized clinical trial of stapler hepatectomy versus LigaSure™ transection in elective hepatic resection. Br J Surg. 2018;105(9):1119–27.

38. Moggia E, Rouse B, Simillis C, Li T, Vaughan J, Davidson BR, et al. Methods to decrease blood loss during liver resection: a network meta-analysis. Cochrane Database Syst Rev. John Wiley & Sons, Ltd; 2016 Oct 31;(10).

39. Chen JM, Geng W, Zhang S, Liu FB, Zhao HC, Zhao YJ, et al. Randomized clinical trial of BiClamp forceps versus clamp-crushing technique in open liver resection. J Hepatobiliary Pancreat Sci. 2017;24(3):137–42.

40. Chang C-M, Yin W-Y, Wei C-K, Lee C-H, Lee C-C. The combined effects of hospital and surgeon volume on short-term survival after hepatic resection in a population-based study. PLoS One. Public Library of Science; 2014;9(1):e86444.

41. Chapman BC, Paniccia A, Hosokawa PW, Henderson WG, Overbey DM, Messersmith W, et al. Impact of Facility Type and Surgical Volume on 10-Year Survival in Patients Undergoing Hepatic Resection for Hepatocellular Carcinoma. J Am Coll Surg. American College of Surgeons; 2017;224(3):362–72.

42. Moggia E, Rouse B, Simillis C, Li T, Vaughan J, Davidson BR, et al. Methods to decrease blood loss during liver resection: a network meta-analysis. In: Gurusamy KS, editor. Cochrane Database of Systematic Reviews. Chichester, UK: John Wiley & Sons, Ltd; 2016. p. CD010683.

43. Lochan R, Ansari I, Coates R, Robinson SM, White SA. Methods of Haemostasis During Liver Resection - A UK National Survey. Dig Surg. 2013;30(4–6):375–82.

44. Huang G, Chen X, Lau WY, Shen F, Wang RY, Yuan SX, et al. Quality of life after surgical resection compared with radiofrequency ablation for small hepatocellular carcinomas. Br J Surg. 2014;101(8):1006–15.

45. Abdalla EK, Vauthey J-N, Ellis LM, Ellis V, Pollock R, Broglio KR, et al. Recurrence and outcomes following hepatic resection, radiofrequency ablation, and combined resection/ablation for colorectal liver metastases. Ann Surg. 2004 Jun;239(6):818-25; discussion 825-7.

46. Velez E, Goldberg SN, Kumar G, Wang Y, Gourevitch S, Sosna J, et al. Hepatic Thermal Ablation: Effect of Device and Heating Parameters on Local Tissue Reactions and Distant Tumor Growth. Radiology. Radiological Society of North America; 2016 Dec;281(3):782–92.

47. Frühling P, Nilsson A, Duraj F, Haglund U, Norén A. Single-center nonrandomized clinical trial to assess the safety and efficacy of irreversible electroporation (IRE) ablation of liver tumors in humans: Short to mid-term results. Eur J Surg Oncol. 2017;43(4):751–7.

48. Mauer K, O'Kelley R, Podda N, Flanagan S, Gadani S. New Treatment Modalities for Hepatocellular Cancer. Curr Gastroenterol Rep. 2015;17(5).

49. Vroomen LGPH, Petre EN, Cornelis FH, Solomon SB, Srimathveeravalli G.

Irreversible electroporation and thermal ablation of tumors in the liver, lung, kidney and bone: What are the differences? Diagn Interv Imaging. Editions françaises de radiologie; 2017;98(9):609–17.

50. Chen M-S, Li J-Q, Zheng Y, Guo R-P, Liang H-H, Zhang Y-Q, et al. A prospective randomized trial comparing percutaneous local ablative therapy and partial hepatectomy for small hepatocellular carcinoma. Ann Surg. 2006 Mar;243(3):321–8.

51. Kinoshita H, Sakai K, Hirohashi K, Igawa S, Yamasaki O, Kubo S. Preoperative portal vein embolization for hepatocellular carcinoma. World J Surg. 1986 Oct;10(5):803–8.

52. Pandanaboyana S, Bell R, Hidalgo E, Toogood G, Prasad KR, Bartlett A, et al. A systematic review and meta-analysis of portal vein ligation versus portal vein embolization for elective liver resection. Surgery. 2015 Apr;157(4):690–8.

53. Jaeck D, Oussoultzoglou E, Rosso E, Greget M, Weber J-C, Bachellier P. A two-stage hepatectomy procedure combined with portal vein embolization to achieve curative resection for initially unresectable multiple and bilobar colorectal liver metastases. Ann Surg. Lippincott, Williams, and Wilkins; 2004 Dec;240(6):1037-49; discussion 1049-51.

54. Schadde E, Ardiles V, Robles-Campos R, Malago M, Machado M, Hernandez-Alejandro R, et al. Early Survival and Safety of ALPPS. Ann Surg. 2014;260(5):829–38.

55. Schnitzbauer AA, Lang SA, Goessmann H, Nadalin S, Baumgart J, Farkas SA, et al. Right Portal Vein Ligation Combined With In Situ Splitting Induces Rapid Left Lateral Liver Lobe Hypertrophy Enabling 2-Staged Extended Right Hepatic Resection in Small-for-Size Settings. Ann Surg. 2012 Mar;255(3):405–14.

56. Peng SY, Wang XA, Huang CY, Zhang YY, Li JT, Hong DF, et al. Evolution of associating liver partition and portal vein ligation for staged hepatectomy: Simpler, safer and equally effective methods. World J Gastroenterol. 2017;23(23):4140–5.

57. de Santibañes E, Alvarez FA, Ardiles V, Pekolj J, de Santibañes M. Inverting the ALPPS paradigm by minimizing first stage impact: the Mini-ALPPS technique. Langenbeck's Arch Surg. Langenbeck's Archives of Surgery; 2016;401(4):557–63.

58. Pichlmayr R, Grosse H, Hauss J, Gubernatis G, Lamesch P, Bretschneider HJ. Technique and preliminary results of extracorporeal liver surgery (bench procedure) and of surgery on the in situ perfused liver. Br J Surg. 1990;77(1):21–6.

59. Lodge JP, Ammori BJ, Prasad KR, Bellamy MC. Ex vivo and in situ resection of

inferior vena cava with hepatectomy for colorectal metastases. Ann Surg. Lippincott, Williams, and Wilkins; 2000 Apr;231(4):471–9.

60. Azoulay D, Lim C, Salloum C, Andreani P, Maggi U, Bartelmaos T, et al. Complex Liver Resection Using Standard Total Vascular Exclusion, Venovenous Bypass, and In Situ Hypothermic Portal Perfusion. Ann Surg. 2015;262(1):93–104.

61. Hasegawa K, Kokudo N, Imamura H, Matsuyama Y, Aoki T, Minagawa M, et al. Prognostic impact of anatomic resection for hepatocellular carcinoma. Ann Surg. Lippincott, Williams, and Wilkins; 2005 Aug;242(2):252–9.

62. Gold JS, Are C, Kornprat P, Jarnagin WR, Gonen M, Fong Y, et al. Increased use of parenchymal-sparing surgery for bilateral liver metastases from colorectal cancer is associated with improved mortality without change in oncologic outcome: trends in treatment over time in 440 patients. Ann Surg. 2007/12/25. 2008;247(1):109–17.

63. Torzilli G, Montorsi M, Donadon M, Palmisano A, Del Fabbro D, Gambetti A, et al. “Radical but conservative” is the main goal for ultrasonography-guided liver resection: Prospective validation of this approach. J Am Coll Surg. 2005;201(4):517–28.

64. Donadon M, Torzilli G. Intraoperative Ultrasound in Patients with Hepatocellular Carcinoma: From Daily Practice to Future Trends. Liver Cancer. 2013/10/26. 2013;2(1):16–24.

65. Gotra A, Sivakumaran L, Chartrand G, Vu K-N, Vandenbroucke-Menu F, Kauffmann C, et al. Liver segmentation: indications, techniques and future directions. Insights Imaging. Springer; 2017 Aug;8(4):377–92.

66. Cash DM, Miga MI, Glasgow SC, Dawant BM, Clements LW, Cao Z, et al. Concepts and preliminary data toward the realization of image-guided liver surgery. J Gastrointest Surg. 2007 Jul;11(7):844–59.

67. Peterhans M, Vom Berg A, Dagon B, Inderbitzin D, Baur C, Candinas D, et al. A navigation system for open liver surgery: Design, workflow and first clinical applications. Int J Med Robot Comput Assist Surg. 2011 Mar;7(1):7–16.

68. Zaraca F, Catarci M, Gossetti F, Carboni M. Senior versus proctored young and resident surgeons’ experience in laparoscopic cholecystectomy: is there any need of previous exposure to open biliary surgery? J Laparoendosc Surg. 1995 Oct;5(5):303–7.

69. Sussenbach SP, Silva EN, Pufal MA, Casagrande DS, Padoin AV, Mottin CC. Systematic review of economic evaluation of laparotomy versus laparoscopy for

patients submitted to Roux-en-Y gastric bypass. PLoS One. Public Library of Science; 2014;9(6):e99976.

70. Suh S-W, Lee K-W, Lee J-M, Choi Y, Yi N-J, Suh K-S. Clinical outcomes of and patient satisfaction with different incision methods for donor hepatectomy in living donor liver transplantation. Liver Transpl. 2015 Jan;21(1):72–8.

71. Costa SRP, Araújo SLM, Teixeira OA, Pereira AC. Setorectomia posterior direita laparoscópica no tratamento dos tumores hepáticos. ABCD Arq Bras Cir Dig (São Paulo). Colégio Brasileiro de Cirurgia Digestiva - CBCD; 2010 Dec;23(4):275–9.

72. Zand B, T. P. Robotic Surgery in Gynecologic Oncology. In: Advanced Gynecologic Endoscopy. InTech; 2011.

73. Ishizawa T, Gumbs AA, Kokudo N, Gayet B. Laparoscopic segmentectomy of the liver: from segment I to VIII. Ann Surg. 2012 Dec;256(6):959–64.

74. Wakabayashi G, Cherqui D, Geller D a., Buell JF, Kaneko H, Han HS, et al. Recommendations for Laparoscopic Liver Resection. Ann Surg. 2015;261(4):619–29.

75. Topal B, Fieuws S, Aerts R, Vandeweyer H, Penninckx F. Laparoscopic versus open liver resection of hepatic neoplasms: comparative analysis of short-term results. Surg Endosc. 2008;22(10):2208–13.

76. Koffron AJ, Auffenberg G, Kung R, Abecassis M. Evaluation of 300 minimally invasive liver resections at a single institution: less is more. Ann Surg. Lippincott, Williams, and Wilkins; 2007 Sep;246(3):385-92; discussion 392-4.

77. Hasegawa Y, Nitta H, Takahara T, Katagiri H, Baba S, Takeda D, et al. Safely extending the indications of laparoscopic liver resection: When should we start laparoscopic major hepatectomy? Surg Endosc Other Interv Tech. Springer US; 2017;31(1):309–16.

78. Mühe E. Long-Term Follow-Up after Laparoscopic Cholecystectomy. Endoscopy. © Georg Thieme Verlag KG Stuttgart · New York; 1992 Nov 17;24(09):754–8.

79. Dubois F, Berthelot G, Levard H. [Cholecystectomy by coelioscopy]. Presse Med. 1989 May 13;18(19):980–2.

80. Gagner M. Laparoscopic partial hepatectomy for liver tumor. Surg Endosc. 1992;

81. Wayand W, Woisetschläger R. [Laparoscopic resection of liver metastasis]. Chirurg. 1993 Mar;64(3):195–7.

82. Croce E, Azzola M, Russo R, Golia M, Angelini S, Olmi S. Laparoscopic liver tumour resection with the argon beam. Endosc Surg Allied Technol. 1994;2(3–4):186–8.

83. Hüscher CG, Lirici MM, Chiodini S, Recher A. Current position of advanced laparoscopic surgery of the liver. J R Coll Surg Edinb. 1997 Aug;42(4):219–25.

84. Yamanaka N, Tanaka T, Tanaka W, Yamanaka J, Yasui C, Ando T, et al. Laparoscopic partial hepatectomy. Hepatogastroenterology. 1998;45(19):29–33.

85. Katkhouda N, Hurwitz M, Gugenheim J, Mavor E, Mason RJ, Waldrep DJ, et al. Laparoscopic management of benign solid and cystic lesions of the liver. Ann Surg. Lippincott, Williams, and Wilkins; 1999 Apr;229(4):460–6.

86. Huscher CG, Lirici MM, Chiodini S. Laparoscopic liver resections. Semin Laparosc Surg. 1998;5(3):204–10.

87. Rau HG, Meyer G, Cohnert TU, Schardey HM, Jauch K, Schildberg FW. Laparoscopic liver resection with the water-jet dissector. Surg Endosc. 1995;9(9):1009–12.

88. Ker CG, Chen HY, Juan CC, Chang WS, Tsai CY, Lo HW, et al. Laparoscopic subsegmentectomy for hepatocellular carcinoma with cirrhosis. Hepatogastroenterology. 47(35):1260–3.

89. Dagher I, O'Rourke N, Geller DA, Cherqui D, Belli G, Gamblin TC, et al. Laparoscopic major hepatectomy: an evolution in standard of care. Ann Surg. 2009/10/07. 2009;250(5):856–60.

90. Rehman S, John SKP, French JJ, Manas DM, White SA. A single centre experience of first "one hundred laparoscopic liver resections". HPB Surg. 2014 Jan;2014:930953.

91. Dulucq J-L, Wintringer P, Stabilini C, Mahajna A. Isolated laparoscopic resection of the hepatic caudate lobe: surgical technique and a report of 2 cases. Surg Laparosc Endosc Percutan Tech. 2006;16(1):32–5.

92. Yoon Y-S, Han H-S, Choi YS, Jang J-Y, Suh K-S, Kim S-W, et al. Total Laparoscopic Right Posterior Sectionectomy for Hepatocellular Carcinoma. J Laparoendosc Adv Surg Tech. 2006 Jun;16(3):274–7.

93. Soubrane O, Cherqui D, Scatton O, Stenard F, Bernard D, Branchereau S, et al. Laparoscopic left lateral sectionectomy in living donors: safety and reproducibility of the technique in a single center. Ann Surg. Lippincott, Williams, and Wilkins; 2006 Nov;244(5):815–20.

94. Buell JF, Cherqui D, Geller D a, O'Rourke N, Iannitti D, Dagher I, et al. The international position on laparoscopic liver surgery: The Louisville Statement, 2008. Ann Surg. 2009;250(5):825–30.

95. Topal H, Tiek J, Aerts R, Topal B. Outcome of laparoscopic major liver resection for colorectal metastases. Surg Endosc. 2012;26(9):2451–5.

96. Nguyen KT, Gamblin TC, Geller DA. World review of laparoscopic liver resection-2,804 patients. Ann Surg. 2009/10/06. 2009 Nov;250(5):831–41.

97. Troisi R, Montalti R, Smeets P, Van Huysse J, Van Vlierberghe H, Colle I, et al. The value of laparoscopic liver surgery for solid benign hepatic tumors. Surg Endosc Other Interv Tech. 2008;22(1):38–44.

98. Fuks D, Cauchy F, Ftériche S, Nomi T, Schwarz L, Dokmak S, et al. Laparoscopy Decreases Pulmonary Complications in Patients Undergoing Major Liver Resection. Ann Surg. 2015;00(00):1.

99. Cipriani F, Rawashdeh M, Stanton L, Armstrong T, Takhar A, Pearce NW, et al. Propensity score-based analysis of outcomes of laparoscopic versus open liver resection for colorectal metastases. Br J Surg. 2016;103(11):1504–12.

100. Vibert E, Perniceni T, Levard H, Denet C, Shahri NK, Gayet B. Laparoscopic liver resection. Br J Surg. 2006;93(1):67–72.

101. Gigot J-F, Glineur D, Santiago Azagra J, Goergen M, Ceuterick M, Morino M, et al. Laparoscopic liver resection for malignant liver tumors: preliminary results of a multicenter European study. Ann Surg. 2002;236(1):90–7.

102. Ciria R, Cherqui D, Geller D a., Briceno J, Wakabayashi G. Comparative Short-term Benefits of Laparoscopic Liver Resection. Ann Surg. 2015 Apr;XX(X):1.

103. Yu H, Wu SD, Chen DX, Zhu G. Laparoscopic resection of bismuth type I and II hilar cholangiocarcinoma: An audit of 14 cases from two institutions. Dig Surg. 2011;28(1):44–9.

104. Aoki T, Murakami M, Fujimori A, Koizumi T, Enami Y, Kusano T, et al. Routes for virtually guided endoscopic liver resection of subdiaphragmatic liver tumors. Langenbeck's Arch Surg. 2016;263–73.

105. Aoki T, Murakami M, Koizumi T, Fujimori A, Gareer H, Enami Y, et al. Three-Dimensional Virtual Endoscopy for Laparoscopic and Thoracoscopic Liver Resection. J Am Coll Surg. United States: American College of Surgeons; 2015 Aug;221(2):e21–6.

106. MacHado M a., Surjan RC, Makdissi FF. Intrahepatic Glissonian approach for pure laparoscopic right hemihepatectomy. Surg Endosc Other Interv Tech. 2011;25:3930–3.

107. Soubrane O, Perdigao Cotta F, Scatton O. Pure laparoscopic right hepatectomy in a living donor. Am J Transplant. 2013;13(9):2467–71.

108. Wong-Lun-Hing EM, van Dam RM, van Breukelen GJP, Tanis PJ, Ratti F, van Hillegersberg R, et al. Randomized clinical trial of open *versus* laparoscopic left lateral hepatic sectionectomy within an enhanced recovery after surgery programme (ORANGE II study). Br J Surg. 2017;104(5):525–35.

109. Fretland ÅA, Dagenborg VJ, Bjørnelv GMW, Kazaryan AM, Kristiansen R, Fagerland MW, et al. Laparoscopic Versus Open Resection for Colorectal Liver Metastases. Ann Surg. 2017;XX(Xx):1.

110. Lewin JW, O'Rourke NA, Chiow AKH, Bryant R, Martin I, Nathanson LK, et al. Long-term survival in laparoscopic vs open resection for colorectal liver metastases: inverse probability of treatment weighting using propensity scores. HPB (Oxford). Elsevier; 2016 Feb;18(2):183–91.

111. Montalti R, Berardi G, Laurent S, Sebastiani S, Ferdinande L, Libbrecht LJ, et al. Laparoscopic liver resection compared to open approach in patients with colorectal liver metastases improves further resectability: Oncological outcomes of a case-control matched-pairs analysis. Eur J Surg Oncol. Elsevier Ltd; 2014;40(5):536–44.

112. Himpens J, Leman G, Cadiere GB. Telesurgical laparoscopic cholecystectomy. Surg Endosc. 1998 Aug;12(8):1091.

113. Kitisin K, Packiam V, Bartlett DL, Tsung A. A current update on the evolution of robotic liver surgery. Minerva Chir. 2011 Aug;66(4):281–93.

114. Ho CM, Wakabayashi G, Nitta H, Ito N, Hasegawa Y, Takahara T. Systematic review of robotic liver resection. Surg Endosc Other Interv Tech. Germany: Springer; 2013 Mar;27(3):732–9.

115. Antoniou SA, Antoniou GA, Koch OO, Pointner R, Granderath FA. Robot-assisted laparoscopic surgery of the colon and rectum. Surg Endosc. 2012 Jan 20;26(1):1–11.

116. Brody F, Richards NG. Review of robotic versus conventional laparoscopic surgery. Surg Endosc. 2014 May 20;28(5):1413–24.

117. Huang X, Wang L, Zheng X, Wang X. Comparison of perioperative, functional, and oncologic outcomes between standard laparoscopic and robotic-assisted radical prostatectomy: a systemic review and meta-analysis. Surg Endosc. 2017 Mar 21;31(3):1045–60.

118. Spampinato MG, Coratti A, Bianco L, Caniglia F, Laurenzi A, Puleo F, et al. Perioperative outcomes of laparoscopic and robot-assisted major hepatectomies: an

Italian multi-institutional comparative study. Surg Endosc Other Interv Tech. Germany; 2014 Oct;28(10):2973–9.

119. Tsung A, Geller D a, Sukato DC, Sabbaghian S, Tohme S, Steel J, et al. Robotic versus laparoscopic hepatectomy: a matched comparison. Ann Surg. United States; 2014 Mar;259(3):549–55.

120. Wu YM, Hu RH, Lai HS, Lee PH. Robotic-assisted minimally invasive liver resection. Asian J Surg. China; 2014 Apr;37(2):53–7.

121. Montalti R, Berardi G, Patriti A, Vivarelli M, Troisi RI. Outcomes of robotic vs laparoscopic hepatectomy: A systematic review and meta-analysis. World J Gastroenterol. United States; 2015 Jul;21(27):8441–51.

122. Kirchberg J, Reißfelder C, Weitz J, Koch M. Laparoscopic surgery of liver tumors. Langenbecks Arch Surg. 2013;398:931–8.

123. Nomi T, Fuks D, Kawaguchi Y, Mal F, Nakajima Y, Gayet B. Learning curve for laparoscopic major hepatectomy. Br J Surg. 2015 Jun;102(7):796–804.

124. Cai X, Li Z, Zhang Y, Yu H, Liang X, Jin R, et al. Laparoscopic liver resection and the learning curve: a 14-year, single-center experience. Surg Endosc. 2014;1–8.

125. Vigano L, Laurent A, Tayar C, Tomatis M, Ponti A, Cherqui D. The learning curve in laparoscopic liver resection: improved feasibility and reproducibility. Ann Surg. 2009 Nov;250(5):772–82.

126. Robinson SM, Hui KY, Amer A, Manas DM, White SA. Laparoscopic liver resection: is there a learning curve? Dig Surg. 2012 Jan;29(1):62–9.

127. Fusaglia M, Hess H, Schwalbe M, Peterhans M, Tinguely P, Weber S, et al. A clinically applicable laser-based image-guided system for laparoscopic liver procedures. Int J Comput Assist Radiol Surg. 2015 Oct;

128. Nicolau S, Soler L, Mutter D, Marescaux J. Augmented reality in laparoscopic surgical oncology. Surg Oncol. Elsevier Ltd; 2011;20(3):189–201.

129. Reichard D, Bodenstedt S, Suwelack S, Mayer B, Preukschas A, Wagner M, et al. Intraoperative on-the-fly organ-mosaicking for laparoscopic surgery. J Med Imaging. 2015 Oct 10;2(4):045001.

130. Wagner OJ, Hagen M, Kurmann A, Horgan S, Candinas D, Vorburger SA. Three-dimensional vision enhances task performance independently of the surgical method. Surg Endosc. 2012 Oct;26(10):2961–8.

131. Hayashi Y, Misawa K, Oda M, Hawkes DJ, Mori K. Clinical application of a surgical

navigation system based on virtual laparoscopy in laparoscopic gastrectomy for gastric cancer. Int J Comput Assist Radiol Surg. 2015 Oct 1;

132. Alleblas CCJ, Vleugels MPH, Coppus SFPJ, Nieboer TE. The effects of laparoscopic graspers with enhanced haptic feedback on applied forces: a randomized comparison with conventional graspers. Surg Endosc Other Interv Tech. Springer US; 2017;(791):1–7.

133. Kawaguchi Y, Nagai M, Nomura Y, Kokudo N, Tanaka N. Usefulness of indocyanine green-fluorescence imaging during laparoscopic hepatectomy to visualize subcapsular hard-to-identify hepatic malignancy. J Surg Oncol. United States; 2015 Oct;112(5):514–6.

134. Vigano L, Ferrero A, Amisano M, Russolillo N, Capussotti L. Comparison of laparoscopic and open intraoperative ultrasonography for staging liver tumours. Br J Surg. 2013/01/23. 2013;100(4):535–42.

135. Stoyanov D. Surgical vision. Ann Biomed Eng. 2012 Feb;40(2):332–45.

136. Wu H-Y, Rubinstein M, Shih E, Guttag J, Durand F, Freeman W. Eulerian video magnification for revealing subtle changes in the world. ACM Trans Graph. 2012;31:1–8.

137. Maier-Hein L, Mountney P, Bartoli a., Elhawary H, Elson D, Groch a., et al. Optical techniques for 3D surface reconstruction in computer-assisted laparoscopic surgery. Med Image Anal. Elsevier B.V.; 2013;17(8):974–96.

138. Goetz M, Deris I, Vieth M, Delaney PM, Murr ER, Galle PR, et al. Near infrared confocal imaging of the human liver during ongoing mini-laparoscopy: A newly developed rigid endomicroscope with increased imaging plane depth. Gastrointest Endosc (conference DDW). 2009;69(5):AB373-.

139. Ishizawa T, Gumbs A a., Kokudo N, Gayet B. Laparoscopic segmentectomy of the liver: from segment I to VIII. Ann Surg. 2012 Dec;256(6):959–64.

140. Abu Hilal M, Di Fabio F, Abu Salameh M, Pearce NW. Oncological efficiency analysis of laparoscopic liver resection for primary and metastatic cancer: a single-center UK experience. Arch Surg. 2012 Jan;147(1):42–8.

141. Kingham TP, Jayaraman S, Clements LW, Scherer MA, Stefansic JD, Jarnagin WR, et al. Evolution of image-guided liver surgery: transition from open to laparoscopic procedures. J Gastrointest Surg. United States; 2013 Jul;17(7):1274–82.

142. Kingham TP, Scherer MA, Neese BW, Clements LW, Stefansic JD, Jarnagin WR. Image-guided liver surgery: intraoperative projection of computed tomography

images utilizing tracked ultrasound. HPB (Oxford). 2012 Sep;14(9):594–603.

143. Buchs NC, Volonte F, Pugin F, Toso C, Fusaglia M, Gavaghan K, et al. Augmented environments for the targeting of hepatic lesions during image-guided robotic liver surgery. J Surg Res. United States; 2013 Oct;184(2):825–31.

144. Tummers QRJG, Verbeek FPR, Prevoo H a JM, Braat AE, Baeten CIM, Frangioni J V, et al. First Experience on Laparoscopic Near-Infrared Fluorescence Imaging of Hepatic Uveal Melanoma Metastases Using Indocyanine Green. Surg Innov. United States; 2014 Feb;22(1):20–5.

145. Schols RM, Bouvy ND, Van Dam RM, Stassen LPS. Advanced intraoperative imaging methods for laparoscopic anatomy navigation: An overview. Surg Endosc Other Interv Tech. 2013;27(6):1851–9.

146. Goetz M, Kiesslich R. Advances of endomicroscopy for gastrointestinal physiology and diseases. Am J Physiol Gastrointest Liver Physiol. 2010/02/27. 2010;298(6):G797-806.

147. Goetz M, Deris I, Vieth M, Murr E, Hoffman A, Delaney P, et al. Near-infrared confocal imaging during mini-laparoscopy: A novel rigid endomicroscope with increased imaging plane depth. J Hepatol. England; 2010 Jul;53(1):84–90.

148. Becker V, Wallace MB, Fockens P, von Delius S, Woodward TA, Raimondo M, et al. Needle-based confocal endomicroscopy for in vivo histology of intra-abdominal organs: first results in a porcine model (with videos). Gastrointest Endosc. 2010/04/28. United States; 2010 Jun;71(7):1260–6.

149. Newton RC, Noonan DP, Vitiello V, Clark J, Payne CJ, Shang J, et al. Robot-assisted transvaginal peritoneoscopy using confocal endomicroscopy: a feasibility study in a porcine model. Surg Endosc. 2012 Sep;26(9):2532–40.

150. Gayet B, Validire P, Pierangelo A, Benali A, Fuks D, Takahashi H, et al. Technical feasibility of confocal laser endomicroscopy in laparoscopic surgery: The persee project. Gastroenterol (conference Abstr. AGA Institute; 2015;148(4):S-1160.

151. Holzinger F, Krähenbühl L, Schteingart CD, Ton-Nu HT, Hofmann AF, Demling L. Use of a fluorescent bile acid to enhance visualization of the biliary tract and bile leaks during laparoscopic surgery in rabbits. Surg Endosc. 2001;15(2):209–12.

152. Kudo H, Ishizawa T, Tani K, Harada N, Ichida A, Shimizu A, et al. Visualization of subcapsular hepatic malignancy by indocyanine-green fluorescence imaging during laparoscopic hepatectomy. Surg Endosc Other Interv Tech. Germany; 2014 Aug;28(8):2504–8.

153. Nambu M, Namihisa T. Hepatic transport of serum bilirubin, bromsulfophthalein, and indocyanine green in patients with congenital non-hemolytic hyperbilirubinemia and patients with constitutional indocyanine green excretory defect. J Gastroenterol. 1996 Apr;31(2):228–36.

154. Matsui A, Tanaka E, Choi HS, Winer JH, Kianzad V, Gioux S, et al. Real-time intra-operative near-infrared fluorescence identification of the extrahepatic bile ducts using clinically available contrast agents. Surgery. United States; 2010 Jul;148(1):87–95.

155. Zuzak KJ, Naik SC, Alexandrakis G, Hawkins D, Behbehani K, Livingston E. Intraoperative bile duct visualization using near-infrared hyperspectral video imaging. Am J Surg. 2008;195(4):491–7.

156. Minagawa M, Kurosaki I, Ogawa H, Hatakeyama K. Navigation surgery with autofluorescence imaging for small hepatocellular carcinomas invisible to ultrasonography. Surgery. 2011;149(6):848–50.

157. Guyon L, Lesage JC, Mordon S, Betrouni N, Mordon S, Claude Lesage J, et al. Development of a new illumination procedure for photodynamic therapy of the abdominal cavity. J Biomed Opt. United States; 2012 Mar;17(3):038001.

158. Yserbyt J, Dooms C, Decramer M, Verleden GM, Thiberville L, Salaün M, et al. Probe-based confocal laser endomicroscopy of the respiratory tract: A data consistency analysis. Respir Med. Elsevier; 2013 Aug;107(8):1234–40.

159. Ishizawa T, Zucker NB, Kokudo N, Gayet B. Positive and Negative Staining of Hepatic Segments By Use of Fluorescent Imaging Techniques During Laparoscopic Hepatectomy. Arch Surg. United States; 2012 Apr;147(4):393–4.

160. Fabila D, de la Rosa JM, Stolik S, Moreno E, Su??rez-??lvarez K, L??pez-Navarrete G, et al. In vivo assessment of liver fibrosis using diffuse reflectance and fluorescence spectroscopy: A proof of concept. Photodiagnosis Photodyn Ther. Netherlands; 2012 Dec;9(4):376–82.

161. Nachabé R, Hendriks BHW, Desjardins AE, van der Voort M, van der Mark MB, Sterenborg HJCM. Estimation of lipid and water concentrations in scattering media with diffuse optical spectroscopy from 900 to 1,600 nm. J Biomed Opt. 2010/07/10. 2010;15(3):37015.

162. Evers DJ, Nachabé R, Hompes D, van Coevorden F, Lucassen GW, Hendriks BHW, et al. Optical sensing for tumor detection in the liver. Eur J Surg Oncol. 2013 Jan;39(1):68–75.

163. Clancy NT, Stoyanov D, James DRC, Di Marco A, Sauvage V, Clark J, et al.

Multispectral image alignment using a three channel endoscope in vivo during minimally invasive surgery. Biomed Opt Express. 2012 Oct 1;3(10):2567–78.

164. Feng C, Rozenblit JW, Hamilton AJ. A computerized assessment to compare the impact of standard, stereoscopic, and high-definition laparoscopic monitor displays on surgical technique. Surg Endosc. 2010 Nov;24(11):2743–8.

165. Kobayashi E, Sakuma I, Konishi K, Hashizume M, Dohi T. A robotic wide-angle view endoscope using wedge prisms. Surg Endosc Other Interv Tech. Germany; 2004 Sep;18(9):1396–8.

166. Terry BS, Ruppert AD, Steinhaus KR, Schoen JA, Rentschler ME. An integrated port camera and display system for laparoscopy. IEEE Trans Biomed Eng. United States; 2010 May;57(5):1191–7.

167. Sahu D, Mathew MJ, Reddy PK. 3D Laparoscopy - Help or Hype; Initial Experience of A Tertiary Health Centre. J Clin Diagn Res. 2014 Jul;8(7):NC01-3.

168. Smith R, Day A, Rockall T, Ballard K, Bailey M, Jourdan I. Advanced stereoscopic projection technology significantly improves novice performance of minimally invasive surgical skills. Surg Endosc. 2012 Jun;26(6):1522–7.

169. Buchs NC, Volonte F, Pugin F, Toso C, Morel P. Three-dimensional laparoscopy: A step toward advanced surgical navigation. Surg Endosc Other Interv Tech. 2013;27(2):692–3.

170. Azagury DE, Dua MM, Barrese JC, Henderson JM, Buchs NC, Ris F, et al. Image-guided Surgery. Curr Probl Surg. 2015;52:476–520.

171. Fusaglia M, Peterhans M, Wallach D, Beldi G, Candinas D, Weber S. Validation of image overlay accuracy in a instrument guidance system for laparoscopic liver surgery. Hpb (IHPBA 2012). 2012;14:520.

172. Thompson S, Totz J, Song Y, Johnsen S, Stoyanov D, Gurusamy K, et al. Accuracy Validation of an Image Guided Laparoscopy System for Liver Resection. SPIE Proc. 2015;9415(7).

173. Okamoto T, Onda S, Yanaga K, Suzuki N, Hattori A. Clinical application of navigation surgery using augmented reality in hepatobiliary pancreatic surgery. Surg Today. 2015;45(4):397–406.

174. Plantefève R, Peterlik I, Haouchine N, Cotin S. Patient-Specific Biomechanical Modeling for Guidance During Minimally-Invasive Hepatic Surgery. Ann Biomed Eng. United States; 2016 Jan 22;44(1):139–53.

175. Newton RC, Noonan DP, Vitiello V, Clark J, Payne CJ, Shang J, et al. Robot-assisted transvaginal peritoneoscopy using confocal endomicroscopy: A feasibility study in a porcine model. Surg Endosc Other Interv Tech. Germany; 2012 Sep;26(9):2532–40.

176. Goetz M, Ansems J V, Galle PR, Schuchmann M, Kiesslich R. In vivo real-time imaging of the liver with confocal endomicroscopy permits visualization of the temporospatial patterns of hepatocyte apoptosis. Am J Physiol Gastrointest Liver Physiol. 2011/07/23. 2011;301(5):G764-72.

177. Goetz M, Deris I, Vieth M, Murr E, Hoffman A, Delaney P, et al. Near-infrared confocal imaging during mini-laparoscopy: a novel rigid endomicroscope with increased imaging plane depth. J Hepatol. European Association for the Study of the Liver; 2010 Jul;53(1):84–90.

178. Goetz M, Kiesslich R, Dienes H-PP, Drebber U, Murr E, Hoffman A, et al. In vivo confocal laser endomicroscopy of the human liver: a novel method for assessing liver microarchitecture in real time. Endoscopy. 2008/07/09. Germany; 2008 Jul;40(7):554–62.

179. Meining A, Shah RJ, Slivka A, Pleskow D, Chuttani R, Stevens PD, et al. Classification of probe-based confocal laser endomicroscopy findings in pancreaticobiliary strictures. Endoscopy. © Georg Thieme Verlag KG; 2012 Mar 19;44(3):251–7.

180. Pierangelo A, Fuks D, Validire P, Benali A, Gayet B. Diagnostic accuracy of confocal laser endomicroscopy for the characterization of liver nodules. Eur J Gastroenterol Hepatol. 2017;29(1):42–7.

181. Gayet B, Pierangelo A, Fuks D, Validire P, Benali A, B. G, et al. Accuracy of confocal laser endomicroscopy for the characterization of peritoneal carcinosis and liver nodules. In: Gastroenterology. AGA Institute; 2016. p. S1199.

182. Latt WT, Newton RC, Visentini-Scarzanella M, Payne CJ, Noonan DP, Shang J, et al. A hand-held instrument to maintain steady tissue contact during probe-based confocal laser endomicroscopy. IEEE Trans Biomed Eng. 2011;58(9):2694–703.

183. Pierangelo A, Fuks D, Benali A, Validire P, Gayet B. Role of intraoperative confocal endomicroscopy for the realtime characterization of tissues during laparoscopic procedures. Surg Endosc (016 Sci Sess Soc Am Gastrointest Endosc Surg (SAGES), Boston, Massachusetts, USA, 16-19 March 2016). 2016;30:S431.

184. Ashitate Y, Stockdale A, Choi HS, Laurence RG, Frangioni J V. Real-time simultaneous near-infrared fluorescence imaging of bile duct and arterial anatomy. J Surg Res. United States; 2012 Jul;176(1):7–13.

185. European Association For The Study Of The Liver EOFRATOC. EASL-EORTC clinical practice guidelines: management of hepatocellular carcinoma. J Hepatol. 2012 Apr;56(4):908–43.

186. Sakoda M, Ueno S, Iino S, Hiwatashi K, Minami K, Kawasaki Y, et al. Anatomical Laparoscopic Hepatectomy for Hepatocellular Carcinoma Using Indocyanine Green Fluorescence Imaging. J Laparoendosc Adv Surg Tech A. 2014 Dec;24(12):878–82.

187. Kawaguchi Y, Nomi T, Fuks D, Kokudo N, Gayet B. Visualization of the biliary ducts and anatomical segments using indocyanine green-fluorescence imaging. Surg Endosc Other Interv Tech. 2015;29:279 (supplement).

188. Ishizawa T, Masuda K, Urano Y, Kawaguchi Y, Satou S, Kaneko J, et al. Mechanistic background and clinical applications of indocyanine green fluorescence imaging of hepatocellular carcinoma. Ann Surg Oncol. 2014;21(2):440–8.

189. Ishizawa T, Fukushima N, Shibahara J, Masuda K, Tamura S, Aoki T, et al. Real-time identification of liver cancers by using indocyanine green fluorescent imaging. Cancer. 2009;115(11):2491–504.

190. Boogerd L, Handgraaf H, Lam H, Van De Velde C, Braat A, Vahrmeijer A. Fluorescence-guided laparoscopic hepatectomies. HPB Conf 12th World Congr Int Hepato-Pancreato-Biliary Assoc Sao Paulo Brazil. 2016;18:e124.

191. Kawaguchi Y, Velayutham V, Fuks D, Christidis C, Kokudo N, Gayet B. Usefulness of Indocyanine Green-Fluorescence Imaging for Visualization of the Bile Duct during Laparoscopic Liver Resection. J Am Coll Surg. United States; 2015 Dec;221(6):e113–7.

192. Fan YF, Xiang F, Cai W, Yang J, Xiang N, Zeng N, et al. [Analysis of intrahepatic Glisson's sheath vascular disconnection approach for anatomical hepatectomy by three-dimensional laparoscope]. Zhonghua Wai Ke Za Zhi. China; 2016 Mar;54(3):191–5.

193. Tanaka M, Inoue Y, Mise Y, Ishizawa T, Arita J, Takahashi Y, et al. Laparoscopic deroofing for polycystic liver disease using laparoscopic fusion indocyanine green fluorescence imaging. Surg Endosc. Germany; 2016 Jun;30(6):2620–3.

194. Kitajima T, Fujimoto Y, Hatano E, Mitsunori Y, Tomiyama K, Taura K, et al. Intraoperative fluorescent cholangiography using indocyanine green for laparoscopic fenestration of nonparasitic huge liver cysts. Asian J Endosc Surg. Japan; 2015 Feb;8(1):71–4.

195. Diana M, Usmaan H, Legner A, Yu-Yin L, D'Urso A, Halvax P, et al. Novel

laparoscopic narrow band imaging for real-time detection of bile leak during hepatectomy: proof of the concept in a porcine model. Surg Endosc. Germany; 2016 Jul;30(7):3128–32.

196. Iida H, Kaibori Kwon M, Ishizaki M, Matsui K, Kaibori Kwon M, Kudo M. Intraoperative navigation by ICG fluorescence imaging in patients with laparoscopic hepatic resection. Liver Cancer. 2015;(Apple):1–257.

197. Otsuka Y, Katagiri T, Kubota Y, Maeda T, Ishii J, Tsuchiya M, et al. Usefulness of ICG fluorescence imaging system in laparoscopic liver resection for liver tumors. HPB. 2016;18:e275.

198. Diana M, Liu Y, Pop R, Kong S, Legner A, Beaujeux R, et al. Super-selective intra-arterial indocyanine green injection for positive fluorescence image guided hepatic segments staining: Proof of the concept in the porcine model. Surg Endosc. 2016;30:325–500.

199. Aoki T, Murakami M, Fujimori A, Kusano T, Matsuda K, Yamada K, et al. Laparoscopic image-guided liver surgery with a color near-infrared light overlay of imaging system. J Am Coll Surg Laparosc image-guided liver Surg with a Color near-infrared Light overlay imaging Syst. 2015;4(Supplement 1):221.

200. Zuzak KJ, Naik SC, Alexandrakis G, Hawkins D, Behbehani K, Livingston E. Intraoperative bile duct visualization using near-infrared hyperspectral video imaging. Am J Surg. 2008 Apr;195(4):491–7.

201. Starkov Y, Dzhantukhanova S, Vyborniy M. 3D laparoscopic liver cyst surgery. Surg Endosc (EAES suppl). 2016;27:1–52.

202. Suh K-S, Hong SK, Yi N-J, Lee K-W, Kim H-S, Yoon KC, et al. Pure 3D Laparoscopic Extended Right Hepatectomy in a Living Donor. Liver Transpl. 2016 Jun;

203. Velayutham V, Fuks D, Nomi T, Kawaguchi Y, Gayet B, V. V, et al. 3D visualization reduces operating time when compared to high-definition 2D in laparoscopic liver resection: a case-matched study. Surg Endosc Other Interv Tech. V. Velayutham, Department of Digestive Diseases, Institut Mutualiste Montsouris, 42 Boulevard Jourdan, Paris 75014, France. E-mail: drvimmi@gmail.com, Germany: Springer New York LLC; 2016 Jan;30(1):147–53.

204. Nakamura Y, Hayashibe M. Laser-Pointing Endoscope System for Intra-Operative. Stud Health Technol Inform. Netherlands; 2001;81:1543–8.

205. Hayashibe M, Suzuki N, Nakamura Y, Hattori A. Real-time 3D deformation imaging of abdominal organs in laparoscopy. Stud Health Technol Inform. Netherlands;

2003;94:117–23.

206. Hayashibe M, Suzuki N, Nakamura Y. Laser-scan endoscope system for intraoperative geometry acquisition and surgical robot safety management. Med Image Anal. Netherlands; 2006 Aug;10(4):509–19.

207. Yi B, Wang G, Li J, Jiang J, Son Z, Su H, et al. The first clinical use of domestically produced Chinese minimally invasive surgical robot system “Micro Hand S”. Surg Endosc. Germany; 2016 Jun;30(6):2649–55.

208. Stoyanov D, Scarzanella MV, Pratt P, Yang G-Z. Real-time stereo reconstruction in robotically assisted minimally invasive surgery. Med Image Comput Comput Assist Interv. 2010 Jan;13(Pt 1):275–82.

209. Haouchine N, Dequidt J, Berger MO, Cotin S. Deformation-based augmented reality for hepatic surgery. Stud Health Technol Inform. 2013 Jan;184:182–8.

210. Kang X, Azizian M, Wilson E, Wu K, Martin AD, Kane TD, et al. Stereoscopic augmented reality for laparoscopic surgery. Surg Endosc. Germany; 2014 Jul;28(7):2227–35.

211. López-Mir F, Naranjo V, Fuertes JJ, Alcañiz M, Bueno J, Pareja E. Design and validation of an augmented reality system for laparoscopic surgery in a real environment. Biomed Res Int. 2013;2013.

212. Satou S, Mitsui T, Ninomiya R, Komagome M, Akamatsu N, Ozawa F, et al. Image overlay navigation of laparoscopic liver resection. Hepatol Int. 2014;8:1–405.

213. Mbah NA, Scoggins C, McMasters K, Martin R. Impact of hepatectomy margin on survival following resection of colorectal metastasis: the role of adjuvant therapy and its effects. Eur J Surg Oncol. 2013/10/03. 2013;39(12):1394–9.

214. Are C, Gonen M, Zazzali K, Dematteo RP, Jarnagin WR, Fong Y, et al. The impact of margins on outcome after hepatic resection for colorectal metastasis. Ann Surg. 2007/08/02. 2007;246(2):295–300.

215. Peterhans M, Oliveira T, Banz V, Candinas D, Weber S. Computer-assisted liver surgery: clinical applications and technological trends. Crit Rev Biomed Eng. 2012;40(3):199–220.

216. Haouchine N, Cotin S, Peterlik I, Dequidt J, Kerrien E, Berger M, et al. Impact of Soft Tissue Heterogeneity on Augmented Reality for Liver Surgery. IEEE Trans Vis Comput Graph. 2015 May 1;21(5):584–97.

217. Pua EC, Light ED, Wolf PD, Smith SW, Von Allmen D. 3-D ultrasound guidance of

surgical robotics: A feasibility study. Proc - IEEE Ultrason Symp. United States; 2006 Nov;1(11):993–6.

218. Hammill CW, Clements LW, Stefansic JD, Wolf RF, Hansen PD, Gerber DA. Evaluation of a minimally invasive image-guided surgery system for hepatic ablation procedures. Surg Innov. United States; 2014 Aug;21(4):419–26.

219. Suwelack S, Röhl S, Bodenstedt S, Reichard D, Dillmann R, dos Santos T, et al. Physics-based shape matching for intraoperative image guidance. Med Phys. American Association of Physicists in Medicine; 2014 Nov 8;41(11):111901.

220. Schneider C, Thompson S, Song Y, Totz J, Desjardins A, Gurusamy K, et al. Preliminary results from a clinical study evaluating a novel image guidance system for laparoscopic liver surgery. HPB. Elsevier; 2017 Jun 7;18(Conference Publication):e99.

221. Pessaux P, Diana M, Soler L, Piardi T, Mutter D, Marescaux J. Towards cybernetic surgery: robotic and augmented reality-assisted liver segmentectomy. Langenbeck's Arch Surg. Germany; 2014 Apr;400(3):381–5.

222. Huber T, Baumgart J, Peterhans M, Weber S, Heinrich S, Lang H, et al. [Computer-assisted 3D-navigated laparoscopic resection of a vanished colorectal liver metastasis after chemotherapy]. Zeitschrift für Gastroenterol. Germany; 2016 Jan;54(1):40–3.

223. Volonté F, Pugin F, Bucher P, Sugimoto M, Ratib O, Morel P. Augmented reality and image overlay navigation with OsiriX in laparoscopic and robotic surgery: Not only a matter of fashion. J Hepatobiliary Pancreat Sci. Japan; 2011 Jul;18(4):506–9.

224. Nachabe R, Hendriks BH, van der Voort M, Desjardins AE, Sterenborg HJ. Estimation of biological chromophores using diffuse optical spectroscopy: benefit of extending the UV-VIS wavelength range to include 1000 to 1600 nm. Biomed Opt Express. 2011/01/25. 2010;1(5):1432–42.

225. Nachabé R, Hendriks BHW, Schierling R, Hales J, Racadio JM, Rottenberg S, et al. Real-Time In Vivo Characterization of Primary Liver Tumors With Diffuse Optical Spectroscopy During Percutaneous Needle Interventions: Feasibility Study in Woodchucks. Invest Radiol. 2015 Mar 16;

226. Clements LW, Dumpuri P, Chapman WC, Dawant BM, Galloway RL, Miga MI. Organ surface deformation measurement and analysis in open hepatic surgery: method and preliminary results from 12 clinical cases. IEEE Trans Biomed Eng. 2011 Aug;58(8).

227. Schneider C, Thompson S, Clarkson MJ, Hawkes DJ, Davidson BR. A novel

approach to image guidance in laparoscopic liver surgery. Surg Endosc. 2015;20 Suppl 1.

228. Zijlmans M, Langø T, Hofstad EF, Van Swol CFP, Rethy A. Navigated laparoscopy – liver shift and deformation due to pneumoperitoneum in an animal model. Minim Invasive Ther Allied Technol. England; 2012 May;21(3):241–8.

229. Kenngott HG, Wagner M, Gondan M, Nickel F, Nolden M, Fetzer A, et al. Real-time image guidance in laparoscopic liver surgery: first clinical experience with a guidance system based on intraoperative CT imaging. Surg Endosc. Germany; 2014 Mar;28(3):933–40.

230. Chopra SS, Schmidt SC, Eisele R, Teichgräber U, Van Der Voort I, Seebauer C, et al. Initial results of MR-guided liver resection in a high-field open MRI. Surg Endosc Other Interv Tech. Germany; 2010 Oct;24(10):2506–12.

231. Yasunaga T, Konishi K, Yamaguchi S, Okazaki K, Hong JS, Ieiri S, et al. MR-compatible laparoscope with a distally mounted CCD for MR image-guided surgery. Int J Comput Assist Radiol Surg. 2007;2(1):11–8.

232. Beard P. Biomedical photoacoustic imaging. Interface Focus. 2012/08/07. 2011;1(4):602–31.

233. Solberg O V, Langø T, Tangen G a, Mårvik R, Ystgaard B, Rethy a, et al. Navigated ultrasound in laparoscopic surgery. Minim Invasive Ther Allied Technol. 2009;18(1):36–53.

234. Konishi K, Nakamoto M, Kakeji Y, Tanoue K, Kawanaka H, Yamaguchi S, et al. A real-time navigation system for laparoscopic surgery based on three-dimensional ultrasound using magneto-optic hybrid tracking configuration. Int J Comput Assist Radiol Surg. 2007;2(1):1–10.

235. Hildebrand P, Schlichting S, Martens V, Besirevic A, Kleemann M, Roblick U, et al. Prototype of an intraoperative navigation and documentation system for laparoscopic radiofrequency ablation: First experiences. Eur J Surg Oncol. England; 2008 Apr;34(4):418–21.

236. Song Y, Totz J, Thompson S, Johnsen S, Barratt D, Schneider C, et al. Locally rigid, vessel-based registration for laparoscopic liver surgery. Int J Comput Assist Radiol Surg. Germany; 2015 Dec;10(12):1951–61.

237. Tao K, Liu X, Deng M, Shi W, Gao J. Three-Dimensional Against 2-Dimensional Laparoscopic Colectomy for Right-sided Colon Cancer. Surg Laparosc Endosc Percutan Tech. 2016 Aug;26(4):324–7.

238. Fanfani F, Rossitto C, Restaino S, Ercoli A, Chiantera V, Monterossi G, et al. How Technology Can Impact Surgeon Performance: A Randomized Trial Comparing 3-Dimensional versus 2-Dimensional Laparoscopy in Gynecology Oncology. J Minim Invasive Gynecol. 23(5):810–7.

239. Aykan S, Singhal P, Nguyen DP, Yigit A, Tuken M, Yakut E, et al. Perioperative, pathologic, and early continence outcomes comparing three-dimensional and two-dimensional display systems for laparoscopic radical prostatectomy--a retrospective, single-surgeon study. J Endourol. 2014 May;28(5):539–43.

240. Xu G, Meng Z-X, Lin J-D, Deng CX, Carson PL, Fowlkes JB, et al. High resolution Physio-chemical Tissue Analysis: Towards Non-invasive In Vivo Biopsy. Sci Rep. 2016;6:16937.

241. Miyata A, Ishizawa T, Kamiya M, Shimizu A, Kaneko J, Ijichi H, et al. Photoacoustic tomography of human hepatic malignancies using Intraoperative indocyanine green fluorescence imaging. PLoS One. 2014;9(11).

242. Hill ER, Xia W, Nikitichev DI, Gurusamy K, Beard PC, Hawkes DJ, et al. Interventional multi-spectral photoacoustic imaging in laparoscopic surgery. Proc SPIE. 2016;9708:97080B.

243. Rubins U, Spigulis J, Miscuks A. Application of Colour Magnification Technique for Revealing Skin Microcirculation Changes under Regional Anaesthetic Input. Spigulis J, Kuzmina I, editors. International Society for Optics and Photonics; 2013 Nov 18;9032:2–6.

244. Amir-Khalili A, Hamarneh G, Peyrat J-M, Abinahed J, Al-Alao O, Al-Ansari A, et al. Automatic Segmentation of Occluded Vasculature via Pulsatile Motion Analysis in Endoscopic Robot-Assisted Partial Nephrectomy Video. Med Image Anal. Elsevier Ltd.; 2015;25(1):103–10.

245. McLeod a. J, Baxter JSH, de Ribaupierre S, Peters TM. Motion magnification for endoscopic surgery. Yaniv ZR, Holmes DR, editors. SPIE Proc. 2014 Mar 12;9036(1):90360C.

246. Jones G, Clancy NT, Arridge S, Elson DS, Stoyanov D. Inference of Tissue Haemoglobin Concentration from Stereo RGB. Springer International Publishing; 2016;1:50–8.

247. Becker V, van den Broek FJ, Buchner AM, Dekker E, Wallace MB, von Delius S, et al. Optimal fluorescein dose for intravenous application in miniprobe-based confocal laser scanning microscopy in pigs. J Biophotonics. 2011 Jan;4(1–2):108–13.

248. von Delius S, Feussner H, Wilhelm D, Karagianni A, Henke J, Schmid RM, et al. Transgastric in vivo histology in the peritoneal cavity using miniprobe-based confocal fluorescence microscopy in an acute porcine model. Endoscopy. 2007/05/23. 2007;39(5):407–11.

249. Giovannini M, Bories E, Monges G, Pesenti C, Caillol F, Delpero JR. Results of a phase I-II study on intraductal confocal microscopy (IDCM) in patients with common bile duct (CBD) stenosis. Surg Endosc. 2011 Jul;25(7):2247–53.

250. Rajkumar V, Goh V, Siddique M, Robson M, Boxer G, Pedley RB, et al. Texture analysis of (125)I-A5B7 anti-CEA antibody SPECT differentiates metastatic colorectal cancer model phenotypes and anti-vascular therapy response. Br J Cancer. 2015 Jun 9;112(12):1882–7.

251. Le Goualher G, Perchant A, Genet M, Cave C, Viellerobe B, Berier R, et al. Towards optical biopsies with an integrated fibered confocal fluorescence microscope. Lect-Notes-Comput-Sci. 2004;3217:761–8.

252. Lewandowski D, Barroca V, Ducongé F, Bayer J, Van Nhieu JT, Pestourie C, et al. In vivo cellular imaging pinpoints the role of reactive oxygen species in the early steps of adult hematopoietic reconstitution. Blood. American Society of Hematology; 2010 Jan 21;115(3):443–52.

253. Li X, Zhou X, Guan Y, Wang Y-XJ, Scutt D, Gong Q-Y. N-nitrosodiethylamine-induced pig liver hepatocellular carcinoma model: radiological and histopathological studies. Cardiovasc Intervent Radiol. 2006;29(3):420–8.

254. Schneider C, Desjardins AE, Gurusamy K, Hawkes DJ, Davidson BR. Laparoscopic manipulation of a probe-based confocal laser endomicroscope using a steerable intravascular catheter. Surg Laparosc Endosc Percutan Tech. United States; 2015 Apr;25(2):e83-5.

255. Jahne B. Digital Image Processing. Berlin/Heidelberg: Springer-Verlag; 2005.

256. Nachabé R, Evers DJ, Hendriks BHW, Lucassen GW, van der Voort M, Wesseling J, et al. Effect of bile absorption coefficients on the estimation of liver tissue optical properties and related implications in discriminating healthy and tumorous samples. Biomed Opt Express. 2011 Jan;2(3):600–14.

257. Nachabé R, Hendriks BHW, Schierling R, Hales J, Racadio JM, Rottenberg S, et al. Real-Time In Vivo Characterization of Primary Liver Tumors With Diffuse Optical Spectroscopy During Percutaneous Needle Interventions Feasibility Study in Woodchucks. 2015;00(00):1–6.

258. Greaby R, Zderic V, Vaezy S, Manuscript A. Pulsatile flow phantom for ultrasound image-guided HIFU treatment of vascular injuries. Ultrasound Med Biol. 2007 Aug;33(8):1269–76.

259. Hoskins PR. Simulation and Validation of Arterial Ultrasound Imaging and Blood Flow. Ultrasound Med Biol. 2008;34(5):693–717.

260. Nikitichev DI, Barburas A, McPherson K, Mari J-M, West SJ, Desjardins AE. Construction of 3-Dimensional Printed Ultrasound Phantoms With Wall-less Vessels. J Ultrasound Med. 2016;35(6):1333–9.

261. Srivastava S, Ng KK, Delp EJ. Crowd flow estimation using multiple visual features for scenes with changing crowd densities. 2011 8th IEEE Int Conf Adv Video Signal Based Surveill. IEEE; 2011 Aug;60–5.

262. Beura S, Majhi B, Dash R. Mammogram classification using two dimensional discrete wavelet transform and gray-level co-occurrence matrix for detection of breast cancer. Neurocomputing. Elsevier; 2015;154:1–14.

263. Clarkson MJ, Zombori G, Thompson S, Totz J, Song Y, Espak M, et al. The NifTK software platform for image-guided interventions: platform overview and NiftyLink messaging. Int J Comput Assist Radiol Surg. 2015 Mar;10(3):301–16.

264. Totz J, Thompson S, Stoyanov D, Gurusamy K, Davidson BR, Hawkes DJ, et al. Fast Semi-dense Surface Reconstruction from Stereoscopic Video in Laparoscopic Surgery. 5th Int Conf IPCAI 2014. 2014;8498:206–15.

265. Soler L, Nicolau S, Pessaux P, Mutter D, Marescaux J. Real-time 3D image reconstruction guidance in liver resection surgery. Hepatobiliary Surg Nutr. 2014 Apr;3(2):73–81.

266. Zhang Z. A flexible new technique for camera calibration. IEEE Trans Pattern Anal Mach Intell. 2000;22(11):1330–4.

267. Thompson S, Stoyanov D, Schneider C, Gurusamy K, Ourselin S, Davidson B, et al. Hand–eye calibration for rigid laparoscopes using an invariant point. Int J Comput Assist Radiol Surg. Germany; 2016 Jun;11(6):1–10.

268. Van Cutsem E, Nordlinger B, Cervantes A. Advanced colorectal cancer: ESMO Clinical Practice Guidelines for treatment. Ann Oncol. 2010 May;21 Suppl 5:v93-7.

269. Helling TS, Martin M. Cause of death from liver metastases in colorectal cancer. Ann Surg Oncol. 2014 Feb;21(2):501–6.

270. Page AJ, Cosgrove DC, Herman JM, Pawlik TM. Advances in understanding of

colorectal liver metastasis and implications for the clinic. Expert Rev Gastroenterol Hepatol. 2015;9(2):245–59.

271. Pawlik TM, Schulick RD, Choti MA. Expanding criteria for resectability of colorectal liver metastases. Oncologist. 2008 Jan;13(1):51–64.

272. Antoniou A, Lovegrove RE, Tilney HS, Heriot AG, John TG, Rees M, et al. Meta-analysis of clinical outcome after first and second liver resection for colorectal metastases. Surgery. 2006/12/26. 2007;141(1):9–18.

273. de Jong MC, Pulitano C, Ribero D, Strub J, Mentha G, Schulick RD, et al. Rates and patterns of recurrence following curative intent surgery for colorectal liver metastasis: an international multi-institutional analysis of 1669 patients. Ann Surg. 2009 Sep;250(3):440–8.

274. Welsh FK, Tekkis PP, O'Rourke T, John TG, Rees M. Quantification of risk of a positive (R1) resection margin following hepatic resection for metastatic colorectal cancer: an aid to clinical decision-making. Surg Oncol. 2008/01/29. 2008;17(1):3–13.

275. Torzilli G, Del Fabbro D, Palmisano A, Donadon M, Bianchi P, Roncalli M, et al. Contrast-enhanced intraoperative ultrasonography during hepatectomies for colorectal cancer liver metastases. J Gastrointest Surg. 2005 Nov;9(8):1148-53; discussion 1153-4.

276. Conlon R, Jacobs M, Dasgupta D, Lodge JPA. The value of intraoperative ultrasound during hepatic resection compared with improved preoperative magnetic resonance imaging. Eur J Ultrasound. 2003 Feb;16(3):211–6.

277. Kishi Y, Abdalla EK, Chun YS, Zorzi D, Madoff DC, Wallace MJ, et al. Three hundred and one consecutive extended right hepatectomies: evaluation of outcome based on systematic liver volumetry. Ann Surg. 2009/09/05. 2009;250(4):540–8.

278. Chopra SS, Schmidt SC, Eisele R, Teichgräber U, Van Der Voort I, Seebauer C, et al. Initial results of MR-guided liver resection in a high-field open MRI. Surg Endosc Other Interv Tech. 2010;24(10):2506–12.

279. Peloso A, Franchi E, Canepa MC, Barbieri L, Briani L, Ferrario J, et al. Combined use of intraoperative ultrasound and indocyanine green fluorescence imaging to detect liver metastases from colorectal cancer. HPB. 2013/03/06. 2013;15(12):928–34.

280. Zhu Y, Gao W, Zhou Y, Guo Y, Guo F, He Y. Rapid and high-resolution imaging of human liver specimens by full-field optical coherence tomography. J Biomed Opt. 2015;20(11):116010.

281. Goetz M, Fottner C, Schirrmacher E, Delaney P, Gregor S, Schneider C, et al. In-vivo confocal real-time mini-microscopy in animal models of human inflammatory and neoplastic diseases. Endoscopy. 2007/04/12. © Georg Thieme Verlag KG Stuttgart · New York; 2007 Apr;39(4):350–6.

282. Goetz M, Deris I, Vieth M, Murr E, Hoffman A, Delaney P, et al. Near-infrared confocal imaging during mini-laparoscopy: a novel rigid endomicroscope with increased imaging plane depth. J Hepatol. 2010/05/11. 2010;53(1):84–90.

283. Leggett CL, Gorospe EC, Chan DK, Muppa P, Owens V, Smyrk TC, et al. Comparative diagnostic performance of volumetric laser endomicroscopy and confocal laser endomicroscopy in the detection of dysplasia associated with Barrett's esophagus. Gastrointest Endosc. 2016 May;83(5):880–888.e2.

284. Goetz M, Hoetker MS, Diken M, Galle PR, Kiesslich R. In vivo molecular imaging with cetuximab, an anti-EGFR antibody, for prediction of response in xenograft models of human colorectal cancer. Endoscopy. 2013 Jun;45(6):469–77.

285. Bok GH, Jeon SR, Cho JY, Cho JH, Lee WC, Jin SY, et al. The accuracy of probe-based confocal endomicroscopy versus conventional endoscopic biopsies for the diagnosis of superficial gastric neoplasia (with videos). Gastrointest Endosc. 2013/03/12. 2013;77(6):899–908.

286. Chang TC, Liu JJ, Liao JC. Probe-based confocal laser endomicroscopy of the urinary tract: the technique. J Vis Exp. 2013/01/29. 2013;(71):e4409.

287. Fuchs FS, Zirlik S, Hildner K, Schubert J, Vieth M, Neurath MF. Confocal laser endomicroscopy for diagnosing lung cancer in vivo. Eur Respir J. 2012/09/22. 2013;41(6):1401–8.

288. De Palma GD, Esposito D, Luglio G, Limite G, Accurso A, Sollazzo V, et al. Confocal laser endomicroscopy in breast surgery: a pilot study. BMC Cancer. 2015 Jan;15:252.

289. Nathan C-AO, Kaskas NM, Ma X, Chaudhery S, Lian T, Moore-Medlin T, et al. Confocal Laser Endomicroscopy in the Detection of Head and Neck Precancerous Lesions. Otolaryngol Head Neck Surg. 2014 Apr 3;151(1):73–80.

290. Jain RK. Normalization of tumor vasculature: an emerging concept in antiangiogenic therapy. Science. 2005 Jan 7;307(5706):58–62.

291. Alander JT, Kaartinen I, Laakso A, Pätilä T, Spillmann T, Tuchin V V, et al. A review of indocyanine green fluorescent imaging in surgery. Int J Biomed Imaging. 2012 Jan;2012:940585.

292. Rubbia-Brandt L, Giostra E, Brezault C, Roth AD, Andres A, Audard V, et al. Importance of histological tumor response assessment in predicting the outcome in patients with colorectal liver metastases treated with neo-adjuvant chemotherapy followed by liver surgery. Ann Oncol. 2007 Feb 1;18(2):299–304.

293. Vermeulen PB, Colpaert C, Salgado R, Royers R, Hellemans H, Van Den Heuvel E, et al. Liver metastases from colorectal adenocarcinomas grow in three patterns with different angiogenesis and desmoplasia. J Pathol. 2001/10/24. 2001;195(3):336–42.

294. Fukumura D, Jain RK. Tumor microvasculature and microenvironment: targets for anti-angiogenesis and normalization. Microvasc Res. 2007 Jan;74(2–3):72–84.

295. Stoeltzing O, Liu W, Reinmuth N, Parikh A, Ahmad SA, Jung YD, et al. Angiogenesis and antiangiogenic therapy of colon cancer liver metastasis. Ann Surg Oncol. 2003 Aug;10(7):722–33.

296. Martirosyan NL, Cavalcanti DD, Eschbacher JM, Delaney PM, Scheck AC, Abdelwahab MG, et al. Use of in vivo near-infrared laser confocal endomicroscopy with indocyanine green to detect the boundary of infiltrative tumor. J Neurosurg. 2011 Dec;115(6):1131–8.

297. Schindl MJ, Redhead DN, Fearon KCH, Garden OJ, Wigmore SJ. The value of residual liver volume as a predictor of hepatic dysfunction and infection after major liver resection. Gut. 2005 Feb;54(2):289–96.

298. Kulaylat MN, Gibbs JF. Thermoablation of colorectal liver metastasis. J Surg Oncol. 2010 Jun 15;101(8):699–705.

299. Schulz P, Dierkes C, Wiedenmann B, Grötzinger C. Near-Infrared Confocal Laser Endomicroscopy Detects Colorectal Cancer via an Integrin αvβ3 Optical Probe. Mol Imaging Biol. 2015;17(4):450–60.

300. Eser S, Messer M, Eser P, von Werder A, Seidler B, Bajbouj M, et al. In vivo diagnosis of murine pancreatic intraepithelial neoplasia and early-stage pancreatic cancer by molecular imaging. Proc Natl Acad Sci U S A. 2011 Jun 14;108(24):9945–50.

301. Meining A, Frimberger E, Becker V, Von Delius S, Von Weyhern CH, Schmid RM, et al. Detection of cholangiocarcinoma in vivo using miniprobe-based confocal fluorescence microscopy. Clin Gastroenterol Hepatol. 2008 Sep;6(9):1057–60.

302. Liu H, Li Y-Q, Yu T, Zhao Y-A, Zhang J-P, Zhang J-N, et al. Confocal endomicroscopy for in vivo detection of microvascular architecture in normal and malignant lesions of upper gastrointestinal tract. J Gastroenterol Hepatol. 2008

Jan;23(1):56–61.

303. Hurlstone DP, Baraza W, Brown S, Thomson M, Tiffin N, Cross SS. In vivo real-time confocal laser scanning endomicroscopic colonoscopy for the detection and characterization of colorectal neoplasia. Br J Surg. 2008 May;95(5):636–45.

304. Goetz M, Fottner C, Schirrmacher E, Delaney P, Gregor S, Schneider C, et al. In-vivo confocal real-time mini-microscopy in animal models of human inflammatory and neoplastic diseases. Endoscopy. 2007/04/12. 2007;39(4):350–6.

305. Chambers AF, Groom AC, MacDonald IC. Dissemination and growth of cancer cells in metastatic sites. Nat Rev Cancer. 2002 Aug;2(8):563–72.

306. Frese KK, Tuveson DA. Maximizing mouse cancer models. Nat Rev Cancer. Nature Publishing Group; 2007 Sep 1;7(9):645–58.

307. Johnson SP, Ogunlade O, Zhang E, Laufer J, Rajkumar V, Pedley RB, et al. Photoacoustic tomography of vascular therapy in a preclinical mouse model of colorectal carcinoma. In: Oraevsky AA, Wang L V., editors. SPIE BiOS. International Society for Optics and Photonics; 2014. p. 89431R.

308. Rees M, Tekkis PP, Welsh FK, O'Rourke T, John TG. Evaluation of long-term survival after hepatic resection for metastatic colorectal cancer: a multifactorial model of 929 patients. Ann Surg. 2007/12/25. 2008;247(1):125–35.

309. Abo T, Nanashima A, Tobinaga S, Hidaka S, Taura N, Takagi K, et al. Usefulness of intraoperative diagnosis of hepatic tumors located at the liver surface and hepatic segmental visualization using indocyanine green-photodynamic eye imaging. Eur J Surg Oncol. 2014 Oct 18;

310. Allen PJ, Ronald P, Kingham TP, Kemeny N, Blumgart LH, Jarnagin WR, et al. Resection Margin and Survival in 2368 Patients Undergoing Hepatic Resection for Metastatic Colorectal Cancer. 2015;262(3).

311. Knavel EM, Brace CL. Tumor ablation: common modalities and general practices. Tech Vasc Interv Radiol. 2013 Dec;16(4):192–200.

312. Herbold T, Wahba R, Bangard C, Demir M, Drebber U, Stippel DL. The laparoscopic approach for radiofrequency ablation of hepatocellular carcinoma--indication, technique and results. Langenbecks Arch Surg. 2013 Jan;398(1):47–53.

313. Frich L. Non-invasive thermometry for monitoring hepatic radiofrequency ablation. Minim Invasive Ther Allied Technol. 2006 Jan;15(1):18–25.

314. Goldberg SN, Dupuy DE. Image-guided Radiofrequency Tumor Ablation: Challenges

and Opportunities—Part I. J Vasc Interv Radiol. 2001 Sep;12(9):1021–32.

315. Chen W, Zhuang H, Cheng G, Torigian DA, Alavi A. Comparison of FDG-PET, MRI and CT for post radiofrequency ablation evaluation of hepatic tumors. Ann Nucl Med. 2013 Jan;27(1):58–64.

316. Kuehl H, Antoch G, Stergar H, Veit-Haibach P, Rosenbaum-Krumme S, Vogt F, et al. Comparison of FDG-PET, PET/CT and MRI for follow-up of colorectal liver metastases treated with radiofrequency ablation: initial results. Eur J Radiol. 2008 Aug;67(2):362–71.

317. Mariani a, Kwiecinski W, Pernot M, Balvay D, Tanter M, Clement O, et al. Real time shear waves elastography monitoring of thermal ablation: in vivo evaluation in pig livers. J Surg Res. Elsevier Inc; 2014 May 1;188(1):37–43.

318. Wang C-P, Wang H, Qu J-H, Lu Y-Y, Bai W-L, Dong Z, et al. Tumour seeding after percutaneous cryoablation for hepatocellular carcinoma. World J Gastroenterol. 2012 Dec 7;18(45):6587–96.

319. Bruners P, Pandeya GD, Levit E, Roesch E, Penzkofer T, Isfort P, et al. CT-based temperature monitoring during hepatic RF ablation: feasibility in an animal model. Int J Hyperthermia. 2012 Jan;28(1):55–61.

320. Nikfarjam M, Muralidharan V, Malcontenti-Wilson C, McLaren W, Christophi C. Impact of blood flow occlusion on liver necrosis following thermal ablation. ANZ J Surg. 2006;76(1–2):84–91.

321. Nakazawa T, Kokubu S, Shibuya A, Ono K, Watanabe M, Hidaka H, et al. Radiofrequency ablation of hepatocellular carcinoma: correlation between local tumor progression after ablation and ablative margin. AJR Am J Roentgenol. American Roentgen Ray Society; 2007 Feb 23;188(2):480–8.

322. Rhim H, Lim HK. Radiofrequency ablation of hepatocellular carcinoma: pros and cons. Gut Liver. 2010 Sep;4 Suppl 1:S113-8.

323. Becker V, von Delius S, Bajbouj M, Karagianni A, Schmid RM, Meining A. Intravenous application of fluorescein for confocal laser scanning microscopy: evaluation of contrast dynamics and image quality with increasing injection-to-imaging time. Gastrointest Endosc. 2008 Aug;68(2):319–23.

324. Demura Y, Ishikawa N, Hirano Y, Inaki N, Matsunoki A, Watanabe G. Transrectal robotic natural orifice translumenal endoscopic surgery (NOTES) applied to intestinal anastomosis in a porcine intestine model. Surg Endosc. 2013 Dec;27(12):4693–701.

325. Flora E Della, Wilson TG, Martin IJ, O'Rourke N a, Maddern GJ. A review of natural

orifice translumenal endoscopic surgery (NOTES) for intra-abdominal surgery: experimental models, techniques, and applicability to the clinical setting. Ann Surg. 2008 Apr;247(4):583–602.

326. Schols RM, Lodewick TM, Bouvy ND, van Dam GM, Dejong CHC, Stassen LPS. Application of a new dye for near-infrared fluorescence laparoscopy of the ureters: demonstration in a pig model. Dis Colon Rectum. 2014 Mar;57(3):407–11.

327. Evers DJ, Westerkamp AC, Spliethoff JW, Pully V V, Hompes D, Hendriks BHW, et al. Diffuse reflectance spectroscopy: toward real-time quantification of steatosis in liver. Transpl Int. 2015 Apr;28(4):465–74.

328. Yoon WJ, Daglilar ES, Fernández-del Castillo C, Mino-Kenudson M, Pitman MB, Brugge WR. Peritoneal seeding in intraductal papillary mucinous neoplasm of the pancreas patients who underwent endoscopic ultrasound-guided fine-needle aspiration: the PIPE Study. Endoscopy. 2014 May;46(5):382–7.

329. Fong ZV, Tanabe KK. The clinical management of hepatocellular carcinoma in the United States, Europe, and Asia: A comprehensive and evidence-based comparison and review. Cancer. 2014;(617).

330. Martin RCG, Kwon D, Chalikonda S, Sellers M, Kotz E, Scoggins C, et al. Treatment of 200 Locally Advanced (Stage III) Pancreatic Adenocarcinoma Patients With Irreversible Electroporation. Ann Surg. 2015;262(3):486–94.

331. Macchi EG, Tosi D, Braschi G, Gallati M, Cigada A, Busca G, et al. Optical fiber sensors-based temperature distribution measurement in ex vivo radiofrequency ablation with submillimeter resolution. J Biomed Opt. International Society for Optics and Photonics; 2014 Jan 1;19(11):117004.

332. Clancy NT, Arya S, Qi J, Stoyanov D, Hanna GB, Elson DS. Polarised stereo endoscope and narrowband detection for minimal access surgery. Biomed Opt Express. 2014 Nov 3;5(12):4108.

333. Howell DC, Howell, C. D. Median Absolute Deviation. In: Wiley StatsRef: Statistics Reference Online. Chichester, UK: John Wiley & Sons, Ltd; 2014.

334. Martin Bland J, Altman D. STATISTICAL METHODS FOR ASSESSING AGREEMENT BETWEEN TWO METHODS OF CLINICAL MEASUREMENT. Lancet. 1986 Feb;327(8476):307–10.

335. Hall AR, Dhillon AP, Green AC, Ferrell L, Crawford JM, Alves V, et al. Hepatic steatosis estimated microscopically versus digital image analysis. Liver Int. 2013 Jul;33(6):926–35.

336. Mari JM, Xia W, West SJ, Desjardins AE. Interventional multispectral photoacoustic imaging with a clinical ultrasound probe for discriminating nerves and tendons: an ex vivo pilot study. J Biomed Opt. 2015;20(11):110503.

337. Wang L V, Hu S. Photoacoustic tomography: in vivo imaging from organelles to organs. Science. 2012 Mar 23;335(6075):1458–62.

338. Forner A, Llovet JM, Bruix J. Hepatocellular carcinoma. Lancet. Elsevier Ltd; 2012;379(9822):1245–55.

339. Athanasopoulos P, Mastoraki A, Papalois A, Nastos C, Kondi-Pafiti A, Kostopanagiotou G, et al. Expression of Inflammatory and Regenerative Genes in a Model of Liver Ischemia/Reperfusion and Partial Hepatectomy. J Investig Surg. 2016;29(2):67–73.

340. Aoki T, Murakami M, Yasuda D, Shimizu Y, Kusano T, Matsuda K, et al. Intraoperative fluorescent imaging using indocyanine green for liver mapping and cholangiography. J Hepatobiliary Pancreat Sci. Japan; 2010 Sep;17(5):590–4.

341. Aubakir B, Nurimbetov B, Tursynbek I, Varol HA. Vital sign monitoring utilizing Eulerian video magnification and thermography. Proc Annu Int Conf IEEE Eng Med Biol Soc EMBS. 2016;2016–Octob:3527–30.

342. Wadhwa N, Rubinstein M, Durand F, Freeman WT. Phase-based video motion processing. ACM Trans Graph. ACM; 2013 Jul 1;32(4):1.

343. Haralick RM. Statistical and structural approaches to texture. Proc IEEE. 1979;67(5):786–804.

344. Marana ANN, Valestin SA, Costa LF, Lotufo RA. Estimation of crowd density using image processing. IEEE Colloq Image Process Secur Appl. IEE; 1997;1997:11–11.

345. Arfken. Discrete Orthogonality -- Discrete Fourier Transform. 1985;

346. Simonoff JS. Smoothing Methods in Statistics. Springer New York; 1996. 356 p.

347. Barron JL, Fleet DJ, Beauchemin SS. Performance of optical flow techniques. Int J Comput Vis. Kluwer Academic Publishers; 1994 Feb;12(1):43–77.

348. Clements LW, Collins JA, Weis JA, Simpson AL, Kingham TP, Jarnagin WR, et al. Deformation correction for image-guided liver surgery: An intraoperative assessment of fidelity. Surgery. 2017 Sep;162(3):1–11.

349. Aoki T, Murakami M, Koizumi T, Kusano T, Fujimori A, Enami Y, et al. Preoperative Tattooing for Precise and Expedient Localization of Landmark in Laparoscopic Liver Resection. J Am Coll Surg. 2015 Nov;221(5):e97–101.

350. Chandra S, Hayashibe M, Thondiyath A. Dominant component in muscle fatigue induced hand tremor during laparoscopic surgical manipulation. In: 2014 36th Annual International Conference of the IEEE Engineering in Medicine and Biology Society. IEEE; 2014. p. 6539–42.

351. Amir-khalili A, Peyrat J, Abinahed J, Al-alao O. Auto Localization and Segmentation of Occluded Vessels in Robot-Assisted Partial Nephrectomy. Med Image Comput Comput Interv – MICCAI 2014. 2014;

352. Muller A, Petrusca L, Auboiroux V, Valette PJ, Salomir R, Cotton F. Management of respiratory motion in extracorporeal high-intensity focused ultrasound treatment in upper abdominal organs: Current status and perspectives. Cardiovasc Intervent Radiol. 2013;36(6):1464–76.

353. Rickey DW, Picot PA, Christopher DA, Fenster A. A wall-less vessel phantom for Doppler ultrasound studies. Ultrasound Med Biol. 1995 Jan;21(9):1163–76.

354. Machado MAC, Surjan RC, Basseres T. The laparoscopic Glissonian approach is safe and efficient when compared with standard laparoscopic liver resection : Results of an observational study over 7 years. 2016;1–9.

355. Ogiso S, Conrad C, Araki K, Nomi T, Anil Z, Gayet B. Laparoscopic Transabdominal With Transdiaphragmatic Access Improves Resection of Difficult Posterosuperior Liver Lesions. Ann Surg. 2015;00(00):1.

356. Machado MAC, Surjan RC. Intrahepatic Glissonian Approach for Single-Port. 2014;24(8):534–7.

357. Soubrane O, de Rougemont O, Kim K-H, Samstein B, Mamode N, Boillot O, et al. Laparoscopic Living Donor Left Lateral Sectionectomy: A New Standard Practice for Donor Hepatectomy. Ann Surg. 2015 Nov;262(5):757-61; discussion 761-3.

358. Cauchy F, Fuks D, Nomi T, Schwarz L, Barbier L, Dokmak S, et al. Risk factors and consequences of conversion in laparoscopic major liver resection. Br J Surg. 2015;n/a-n/a.

359. Peterhans M, vom Berg A, Dagon B, Inderbitzin D, Baur C, Candinas D, et al. A navigation system for open liver surgery: design, workflow and first clinical applications. Int J Med Robot. 2011 Mar;7(1):7–16.

360. Polignano FM, Quyn AJ, De Figueiredo RSM, Henderson N a., Kulli C, Tait IS. Laparoscopic versus open liver segmentectomy: Prospective, case-matched, intention-to-treat analysis of clinical outcomes and cost effectiveness. Surg Endosc Other Interv Tech. 2008;22(12):2564–70.

361. Abu Hilal M, Di Fabio F, Syed S, Wiltshire R, Dimovska E, Turner D, et al. Assessment of the financial implications for laparoscopic liver surgery: A single-centre UK cost analysis for minor and major hepatectomy. Surg Endosc Other Interv Tech. 2013;27:2542–50.

362. Aoki T, Murakami M, Koizumi T. Three-Dimensional Virtual Endoscopy for Laparoscopic and Thoracoscopic Liver Resection. J Am Coll Surg. American College of Surgeons; 2015;221(2):e21–6.

363. Mountney P, Stoyanov D, Davison A, Yang G-Z. Simultaneous stereoscope localization and soft-tissue mapping for minimal invasive surgery. Med Image Comput Comput Assist Interv. 2006;9(Pt 1):347–54.

364. Jia Y, Shelhamer E, Donahue J, Karayev S, Long J, Girshick R, et al. Caffe: Convolutional Architecture for Fast Feature Embedding. Proc ACM Int Conf Multimed - MM '14. 2014;675–8.

365. Gibson E, Robu MR, Thompson S, Edwards PE, Schneider C, Gurusamy K, et al. Deep residual networks for automatic segmentation of laparoscopic videos of the liver. Webster RJ, Fei B, editors. International Society for Optics and Photonics; 2017 Mar 3;10135:101351M.

366. Haouchine N, Dequidt J, Peterlik I. Towards an Accurate Tracking of Liver Tumors for Augmented Reality in Robotic Assisted Surgery. … Robot …. 2014;

367. Kleemann M, Deichmann S, Esnaashari H, Besirevic A, Shahin O, Bruch H-P, et al. Laparoscopic navigated liver resection: technical aspects and clinical practice in benign liver tumors. Case Rep Surg. 2012;2012:265918.

368. Araki K, Conrad C, Ogiso S, Kuwano H, Gayet B. Intraoperative ultrasonography of laparoscopic hepatectomy: Key technique for safe liver transection. J Am Coll Surg. American College of Surgeons; 2014;218(2):e37–41.

369. LIU C, FAN S, LO C, CHAN S, TSO W, NG I, et al. Hepatic resection for incidentaloma. J Gastrointest Surg. 2004 Nov 1;8(7):785–93.

370. Chen X, Chen Y, Li Q, Ma D, Shen B, Peng C. Radiofrequency ablation versus surgical resection for intrahepatic hepatocellular carcinoma recurrence: a meta-analysis. J Surg Res. 2015;195(1):166–74.

371. Lodewick TM, Arnoldussen CWKP, Lahaye MJ, van Mierlo KMC, Neumann UP, Beets-Tan RG, et al. Fast and accurate liver volumetry prior to hepatectomy. HPB. 2016 Sep;18(9):764–72.

372. Lang H, Radtke A, Liu C, Frühauf NR, Peitgen HO, Broelsch CE. Extended left

hepatectomy--modified operation planning based on three-dimensional visualization of liver anatomy. Langenbecks Arch Surg. 2004;389(4):306–10.

373. Schneider C, Johnson SP, Walker-Samuel S, Gurusamy K, Clarkson MJ, Thompson S, et al. Utilizing confocal laser endomicroscopy for evaluating the adequacy of laparoscopic liver ablation. Lasers Surg Med. United States; 2016 Mar;48(3):299–310.

374. Zhu Y, Gao W, Zhou Y, Guo Y, Guo F, He Y. Rapid and high-resolution imaging of human liver specimens by full-field optical coherence tomography. J Biomed Opt. 2015 Nov 30;20(11):116010.

375. Zhang HF, Maslov K, Stoica G, Wang L V. Functional photoacoustic microscopy for high-resolution and noninvasive in vivo imaging. Nat Biotechnol. 2006 Jul 25;24(7):848–51.

376. Chang S, Lanctot AC, McCarter MD, Roberts KM, Glueck DH, Dodd GD. The prediction of radiofrequency ablation zone volume using vascular indices of 3-dimensional volumetric colour Doppler ultrasound in an *in vitro* blood-perfused bovine liver model. Br J Radiol. 2017 Feb;90(1070):20160661.

377. Schols RM, Bouvy ND, Masclee AAM, Van Dam RM, Dejong CHC, Stassen LPS. Fluorescence imaging of the extra-hepatic bile ducts during laparoscopic cholecystectomy: Preliminary results of a pilot-study. Surg Endosc Other Interv Tech. Germany; 2013 May;27(5):S33.

378. Bosetti C, Turati F, La Vecchia C. Hepatocellular carcinoma epidemiology. Best Pract Res Clin Gastroenterol. Elsevier Ltd; 2014;28(5):753–70.

379. Lopez A, Zlatev D V, Mach KE, Bui D, Liu J-J, Rouse R V, et al. Intraoperative Optical Biopsy during Robotic Assisted Radical Prostatectomy Using Confocal Endomicroscopy. J Urol. NIH Public Access; 2016 Apr;195(4 Pt 1):1110–7.

380. Goetz M, Kiesslich R. Advances in confocal laser endomicroscopy for the diagnosis of gastrointestinal diseases. Expert Opin Med Diagn. 2009/09/01. 2009;3(5):493–500.

381. Clancy NT, Saso S, Stoyanov D, Sauvage V, Corless DJ, Boyd M, et al. Multispectral imaging of organ viability during uterine transplantation surgery in rabbits and sheep. J Biomed Opt. International Society for Optics and Photonics; 2016 Oct 27;21(10):106006.

382. Lanzafame RJ. Laser safety programs in general surgery. J Laser Appl. Laser Institute of America; 1994 Jun 29;6(2):111–4.

383. Jones G, Clancy NT, Helo Y, Arridge S, Elson DS, Stoyanov D. Bayesian Estimation of Intrinsic Tissue Oxygenation and Perfusion From RGB Images. IEEE Trans Med Imaging. 2017 Jul;36(7):1491–501.

384. Wadhwa N, Rubinstein M, Durand F, Freeman WT. Riesz pyramids for fast phase-based video magnification. 2014 IEEE Int Conf Comput Photogr ICCP 2014. 2014;

385. Adams F, Schoelly R, Schlager D, Schoenthaler M, Schoeb DS, Wilhelm K, et al. Algorithm-Based Motion Magnification for Video Processing in Urological Laparoscopy. J Endourol. 2017;31(6):583–7.

386. Liu YF, Vuong C, Walker PC, Peterson NR, Inman JC, Filho PAA, et al. Noninvasive Free Flap Monitoring Using Eulerian Video Magnification. Case Rep Otolaryngol. Hindawi Publishing Corporation; 2016;2016:9471696.

387. Suwelack S, Röhl S, Bodenstedt S, Reichard D, Dillmann R, dos Santos T, et al. Physics-based shape matching for intraoperative image guidance. Med Phys. 2014;41(11):111901.

388. Sánchez-Margallo FM, Sánchez-Margallo JA, Moyano-Cuevas JL, Pérez EM, Maestre J. Use of natural user interfaces for image navigation during laparoscopic surgery: initial experience. Minim Invasive Ther Allied Technol. Informa UK Limited, trading as Taylor 8 Francis Group; 2017;0(0):1–9.